INTERSTELLAR ORGANIC CHEMISTRY IN THE AGE OF BROADBAND RADIO ASTRONOMY

Joanna Faith Corby
United States

B.A. Astrophysics, Columbia University in the City of New York, 2009

M.S. Astronomy, University of Virginia, 2012

A Dissertation Presented to the Graduate
Faculty of the University of Virginia
in Candidacy for the Degree of
Doctor of Philosophy

Department of Astronomy

University of Virginia
May 2016

Committee Members:

Dr. Anthony J. Remijan
Professor Eric Herbst
Professor Remy Indebetouw
Professor Robert E. Johnson
Professor Maria Cunningham

To Jupiter for drawing me in,

to Saturn for setting me free.

Abstract

This dissertation explores the challenges and advancements introduced by the arrival of new-generation radio telescopes for understanding the physical and chemical structure of the Interstellar Medium (ISM). New-generation broadband radio instruments, and particularly broadband interferometers, provide the opportunity to obtain a comprehensive view of the coupled physical and chemical structure of the interstellar medium (ISM). This is required in order to transform the field of astrochemistry into a predictive science with diagnostic power for astronomy.

However, significant challenges are posed by the new wealth of data, and in order to extract even a reasonable fraction of the capacity of these data sets, automated data handling is necessary. This work addresses the challenge with scripts written to perform automated spectral line fitting and semi-automated line identification in order to fully characterize broadband data sets. Besides providing scientific results from the spectral analysis, the spectral characterization is a required first step needed in order to interpret spatial distribution information. We test the performance of the scripts on spectral line data from 4 to 6 GHz and 30 to 50 GHz towards the most complex spectral line source in the Galaxy, namely the high mass star forming region Sagittarius B2 (Sgr B2).

Additionally, the results of the automated line fitter are coupled with image data to constrain the physical and chemical conditions in gas located in Sgr B2(N). This material contains multiple exotic molecules of prebiotic relevance, and the gas conditions include moderate densities, warm temperatures, and a complex mechanical and radiative environment with shocks and turbulence as well as strong UV, X-ray, and cosmic ray irradiation.

Finally, we utilize broadband single dish and interferometric data to explore the coupled physical and chemical structure of material in diffuse and translucent clouds located in the Galactic Center and disk. The data reveal systematic differences in the chemical content

and physical structure between Galactic Center and disk clouds. Furthermore, interferometric data collected for a different purpose directly observes the inhomogeneous structure of the diffuse and translucent media, opening up new opportunities for understanding the layered physical and chemical structure of the diffuse and translucent ISM.

Acknowledgements

To my mentors: Thank you for your message, for your patience, for your humanity. To Joe, for your confidence in me from well before I knew I deserved it.

To Tony: While I would have done little the same way that you did, I thank you for doing it, for taking me, of all people, on as a student. For accepting with consistent confusion, life as it happens to me. While our styles, our tastes, our interests appear, on some days, perfectly orthogonol, I thank you for granting me the liberty to play with the data and the questions that I found most enticing. I thank you for going out on a limb for me over and over again, often in effort to ship me out of Charlottesville. As you know, my gratitude for this is sincere.

To my family: First, thank you for supporting me when astronomy didn't. Thank you for supporting me always.

To one of you, thank you for teaching me to percieve, for enforcing that I take care of myself, for inspiring me to love endless learning, and pointing out the miriad ways that my training applies. I cannot imagine being surrounded by greater joy and learning.

To others, thank you for demonstrating just how difficult it is to see. For proving that it can be hardest to teach those who are closest. And for the ways that you grow on your own.

Dreaming forward with others still, known and yet unknown: it is by the wicked twists of fate that we seem to barely meet. When most wouldn't, we both look around to find each other. It is then by a very light decision we may move across countries if we must. Let us hold each other sacred. Let us trust each other rightly. Let us always grow to see. And let us get on with it already! Let us build what we know to be true.

Table of contents

Chapter 1

Introduction to Astrochemistry at Radio Wavelengths

1.1 Historical Context

While astronomy is an ancient science, our contemporary understanding of the Universe has been shaped very recently. It inspires awe to note just how young many of the basic tenants of modern astronomy are. For example, only in the mid-1920's did it become apparent that objects existed outside of our Galaxy (Hubble 1926), opening up entirely new realms of astronomical research, including galaxy formation and evolution and cosmological evolution. It is even more recently that astronomers have amassed observational evidence for other extreme states of matter and forms of energy, including neutron stars (Shklovsky 1967; Hewish et al. 1968), black holes (Sargent et al. 1978; Young et al. 1978), dark matter (Zwicky 1933; Rubin & Ford 1970), and dark energy (Riess et al. 1998). Yet these states are now integral to our cosmological perspective.

Another paradigm shift has resulted from the development of radio antenna technology in the 1930's. Prior to this time, astronomy research was most closely focused on starlight visible at optical, near-infrared, and UV wavelengths, and on mid-infrared emission from planets and other solar system bodies. With the advent of radio telescopes we began to see a new set of physical processes that are as essential to the nature of the universe as are stars. Whereas stars shine brightest at optical wavelengths, radio telescopes are sensitive to interstellar gas. As a result, radio telescopes have made very significant contributions to our understanding of the interstellar medium (ISM), the gas and dust that fills galaxies. It is now apparent that the ISM is critically involved in the formation of stars, the evolution of galaxies and their central black holes, and even the formation of life.

Still less than 50 years ago, it was first discovered that polyatomic molecules exist in the ISM, and this discovery has yet again drastically altered the way we conceive of our Universe and our origins within it. Before their detection, it was generally assumed that space was inhospitable to polyatomic molecules. Under the extremely low densities (the

densest regions of the ISM are $\sim$1 trillion times less dense than the air we breathe), it was believed that molecules should not form in great yield. If they did manage to form, common reasoning suggested they should not survive the harsh UV, X-ray, and cosmic ray (CR) irradiation. Observations demonstrated this to be incorrect.

In 1968, a group led by Charles H. Townes detected the first interstellar polyatomic molecule, namely ammonia (NH_3), through spectral line emission at radio wavelengths (Cheung et al. 1968). A year later, interstellar formaldehyde (H_2CO) was discovered (Snyder et al. 1969), proving that simple organic molecules form and survive in the extreme conditions of interstellar space. By the mid 1970s, new interstellar molecules were being detected at an average rate of four per year, and this rate has been sustained through today. Thus, we have now directly detected more than 190 molecules, predominantly using radio telescopes. While the known chemical inventory involves many household molecules (for instance, ammonia, formaldehyde, and acetic acid or vinegar), many of the detected molecules are highly unstable and are not present in considerable amounts on earth. The ISM is increasingly believed to hold the seeds of life; essential prebiotic species (probable precursors to biomolecules) have been detected (e.g. Rubin et al. 1971; Lovas et al. 2006; Remijan et al. 2002; Loomis et al. 2013), and biomolecules including amino acids are believed to be present (Garrod 2013), just beyond the detection limit of the last generation of telescopes. Besides providing access to the molecular inventories in interstellar regions, the spectral lines produced by molecules provide tools for understanding the physics of interstellar gas clouds, providing measurements of the systematic and internal motion within clouds and of the physical temperatures and densities.

1.2 (Not Yet) Understanding Interstellar Chemistry

Since these detections, great strides have been made towards accounting for the observed chemistry by constructing networks of reactions believed to be important in the ISM and applying approximate models of a gas cloud's evolution. The first chemical models appeared shortly after polyatomic species began being detected (Solomon & Klemperer 1972; Aannestad 1973; Herbst & Klemperer 1973) and have grown to consider many thousands of chemical reactions involving hundreds of molecules. In the past 25 years, the models have expanded to include reactions on the surfaces of dust grains and the ice mantles that cover them (Hasegawa et al. 1992; Garrod et al. 2008). Most of the complex organic molecules observed in the ISM are believed to be formed on the ice mantles that coat the grains. Although the models can account for the observed abundances of some molecules in a few environments under reasonable assumptions about the cloud's evolution, they cannot yet provide a comprehensive understanding of the chemistry, and have not produced notable predictions that have been confirmed observationally. Rather, the model predictions have in some cases been refuted by observations (Garrod et al. 2008; Garrod 2013; McGuire et al. 2015). Nonetheless, the chemical models provide a noteable framework that may prove powerful for making predictions and interpreting observed chemical abundances as constraints to the models improve.

Many different issues may contribute to the shortcomings of the chemical models, and I highlight two. First, there is an incredible amount of uncertainty in the reaction rates, activation energies, and branching ratios. As different reactions occur in the ISM than on Earth, reaction kinetics, including reaction rates, activation energies, and branching ratios, have been measured for an extremely small number of relevant reactions; this is among the many symptoms of the strong terrestrial bias that the discipline of chemistry has. However, our incapacity to explain observed molecular abundances is now spawning

rapid expansion in theoretical and laboratory astrochemistry research, with growing interest in high-level kinetics theory for relevant reactions, and in designing new laboratory setups. In fact, multiple laboratories have recently or will very soon become operational in order to test ice surface chemistry under varying radiative conditions (Ioppolo et al. 2013; Allodi et al. 2013; Paardekooper et al. 2014), chemistry on bare carbonaceous or silicate surfaces (e.g. Loeffler et al. 2016, and references therein), and radical-driven gas phase kinetics (C. Endres 2015, private communication). As the measurements from these experiments become available, they can be included in models. Perhaps the performance of the models will improve drastically as reaction rates are constrained; perhaps instead, we will learn of qualitatively new processes that need be included.

The second major barrier to understanding may come from our limited observational data. While a substantial amount of observational work has been completed, the parameter-space that has been explored is tiny compared to the amount of information present. Interstellar chemistry is among the most multidimensional problems known in the Universe. The abundance of each of the hundreds of molecules present in an interstellar region is intimately dependent on the abundance history of the numerous other species involved in the formation chemistry. And the abundances can be highly sensitive to the temperatures, densities, and radiation fields in the cloud, each of which may vary substantially over the history of the cloud. This precisely points out the power that astrochemistry may have for astronomy: if we are able to compile a comprehensive and therefore predictive understanding of the chemical pathways and abundance evolution, we will be able to read the history of an astronomical region from its molecular chemistry.

But it is impossible to solve such a multidimensional problem without a sufficient number of constraints and without sufficient precision. At present, this phase space is very poorly filled in; temperatures, densities, radiation fields, and local molecular inventories

are incompletely determined for a handful of astronomical sources and largely unconstrained for hundreds of other potentially interesting objects. Even within the most well studied sources, incredible uncertainties persist. We are, at present, obtaining incredible observations that illucidate the structure of the ISM. The observations show, as an example, molecular gas organized in filaments aligned by magnetic fields (Contreras et al. 2016; Rathborne et al. 2015). The data show streaming motion along these structures (Peretto et al. 2013), and shocks and turbulence in stages immediately associated with star formation (Fernández-López et al. 2014; Contreras et al. 2016). The data show substantial inhomogeneities within gas, with neighboring patches having different temperatures and densities, and very different abundances (Guélin et al. 2008; Corby et al. 2015). They show us that it is not reasonable to adopt average abundances over the distinct regions, as the average values are not truly representative of the conditions in either. Therefore our models attempt to account for abundances that are not present.

The recent observational results therefore imply that in order to make progress towards understanding the chemistry, we require high spatial resolution observations capable of resolving the distinct environments, and we require precise measurements of the abundances of many different molecules. Again, further extra-dimensionalizing the problem, each abundance measurement requires observing multiple transitions of the molecule and treating the excitation appropriately. Thankfully, we stand on the brink a vast expansion in our capacity to achieve this. A new generation of radio telescopes have very recently become available, providing tremendous increases in the simultaneous bandwidths of telescopes.

1.3 New-Generation Broadband Radio Instruments

Data obtained through broadband radio astronomy can truly revolutionize our understanding of interstellar chemistry and physics. In the last five years, multiple broadband instruments have become available, many of which are currently in the final stages of commissioning. Among these are existing single dish telescopes (which provide poor spatial resolution but greater sensitivity to extended emission) with upgraded spectrometers and/or receivers, including the Robert C. Byrd Green Bank Telescope, the Effelsberg Telescope, and the 30–meter telescope of the Institut de Radioastronomie Millimétrique (IRAM). Additionally, many radio interferometers (which provide high spatial resolution measurements), including the Karl G. Jansky Very Large Array (VLA) and the Australia Telescope Compact Array (ATCA), have undergone upgrades that increase the simultaneous bandwidth capabilities by $\gtrsim$2 orders of magnitude; additional existing interferometers will undergo substantial upgrades, including the Plateau de Bure Interferometer (PdBI) which will become the NOrthern Extended Millimeter/sub-millimeter Array (NOEMA). Finally, by an incredible international effort (but mostly by Tony's will alone), the Atacama Large Millimeter/submillimeter Array (ALMA) has made previously impossible science achievable in only minutes of observation. Furthermore, the interferometers can be used in conjunction with one another to cover an incredible span in wavelengths, from a hundred centimeters to 0.3 millimeters, and can have matched spatial resolution over much of this range.

Whereas previously, observations typically targeted only a few spectral lines in one tuning, it is now possible to observe tens up to hundreds of spectral lines at once; it is therefore straightforward to compile information on many hundreds of molecular lines in a reasonable amount of observing time. With the new wealth of information available, however, come new challenges in data analysis. In order to extract a reasonable fraction of

the information present in these data sets, automated methods of data analysis are required. To date, these are not adequately developed, and large scale efforts to provide improved visualization and analysis tools for rich spectral line data cubes are under way (Teuben et al. 2013).

1.4 Astronomical Environments

In this work, I focus on observational data taken towards one of the most exhaustively-studied sources in the Galaxy, namely the high mass star forming region Sagittarius B2 (Sgr B2), located in the Central Molecular Zone of the Galaxy. Yet, as the work demonstrates, we have a highly incomplete understanding of this source, with major gaps in our observational constraints on the structure at high spatial resolution. In the spectra towards Sgr B2, we additionally observe diffuse clouds (with low densities and warm temperatures) and translucent clouds (with moderate densities and incomplete shielding of UV radiation) that intersect the line-of-sight. Many of the clouds observed are also located in the Central Molecular Zone of the Galaxy, and others are located in the Galactic spiral arms.

1.4.1 The Central Molecular Zone

The Milky Way's Galactic Center is a fascinating and bewildering environment. As it is, by a significant margin, the most proximate galactic nucleus, it provides our most detailed view of the central region of a galaxy. We have incredible observational data on this region, and the new-generation instruments provide immense potential for understanding the physics and chemistry in the Galactic Center. In this region, we observe star formation in the immediate vicinity of a supermassive black hole (Blank et al. 2016), extended non-thermal radio filaments (Lang et al. 1999), and expanding superbubbles (Ponti et al. 2015),

among many other interesting structures. Magnetic fields are believed to be involved in many of the more bizarre physical features of the Galactic Center. The Galactic Center also hosts Giant Molecular Clouds (GMCs) with extreme physical conditions, including the most massive cloud in the Galaxy, Sagittarius B2 (Sgr B2), which is actively collapsing to form stars, and the highest density cloud, G0.253-0.016 (also called "the Brick"), which appears to be supported against collapse by strong magnetic fields (Rathborne et al. 2015). Our evolving understanding of these systems suggests that GMC-scale star formation proceeds differently in the Galactic Center than in the disk, perhaps only occuring at the positions of resonances like the X-2 orbit (Molinari et al. 2011, Longmore et al. in prep).

The central 300 pc of the Galaxy is also commonly referred to as the Central Molecular Zone (CMZ) as the molecular gas surface density in this region is enhanced by about a factor of a hundred over that present outside of this region (Morris & Serabyn 1996). In addition to CO, emission from C_2H, HCO^+, HCN, and HNC entirely fill the observed area of the CMZ (Jones et al. 2012). While the highest brightness temperature emission occurs at the positions of GMCs, most of the area is not associated with larger molecular clouds. While larger clouds exhibit circular motion around the central position, the multitude of weaker emission sources exhibit highly non-circular motions. It remains unclear precisely how this material is structured, but it is clear that the physical conditions are quite distinct in the CMZ than in the Galactic disk. Diffuse clouds in the Galactic Center have cosmic ray ionization rates that are two to four orders of magnitude larger than diffuse clouds in the Galactic disk (Le Petit et al. 2016), and X-rays are more pervasive (Amo-Baladrón et al. 2009). Additionally, widescale shocks and supersonic turbulence are observed to be nearly ubiquitous in the CMZ (Martín-Pintado et al. 2001; Martín et al. 2008). CMZ gas temperatures are measured to be elevated, at 50-80 K (Morris & Serabyn 1996), compared

to molecular gas in the Galactic disk (at 15-25 K). In spite of the high gas density in the CMZ, however, dust temperatures are not coupled to the gas temperatures, with quite low dust temperatures of ∼15-20 K observed throughout the Galactic Center (Ginsburg et al. 2016).

1.4.2 Sagittarius B2

The most massive cloud in the Galactic Center, and in fact in the Galaxy, is Sagittarius B2 (Sgr B2). Sgr B2 is an order of magnitude more massive, at $\sim 3 \times 10^6$ $M_\odot$ (de Vicente et al. 1997), than most star-forming Giant Molecular Clouds. As is expected from its location in the CMZ, Sgr B2 has more extreme physical conditions than any other star forming GMC in the Galaxy, with pervasive shocks, high magnetic field strengths, and strong X-ray and cosmic-ray (CR) irradiation (Crutcher et al. 1996; Terrier et al. 2010; van der Tak et al. 2006).

Due to the high hydrogen column densities, Sgr B2 presents an exceptional case for studying the molecular chemistry, and more than half of all molecules observed in the ISM were first detected in Sgr B2. In fact, Sgr B2 hosts the most diverse and complex molecular chemistry observed anywhere outside of the solar system.

The most line-dense position in Sgr B2 corresponds to the location of the Large Molecule Heimat (LMH; Heimat means home in German) hot core (Snyder et al. 1994). A hot core is a short-lived phase of the gas surrounding massive stars in the process of formation, and is defined by having warm temperatures of $100 < T < 300$ K and high densities of $n > 10^6$ cm^{-3}. Not only is the LMH the most line-dense position in Sgr B2, but it is the most line-rich source observed anywhere in the ISM, and is exceptional amongst hot cores, as it is the most massive and dense hot core in the Galaxy (Belloche et al. 2008).

The LMH and a second, somewhat less prominent hot core termed “h” in this work

are located in the northernmost star-forming core present in Sgr B2, namely Sgr B2(North) (Sgr B2(N)). Whereas the LMH and "h" hot cores produce dust continuum emission at sub-millimeter wavelengths (Qin et al. 2011), Sgr B2's star-forming cores are defined by their radio continuum emission. Namely, the North (N), Main (M), and South (S) cores are each separated by about 45 arcsec (1 degree = 60 arcmin = 3600 arcsec) in the north-south direction (Figure 1.1). The cores consist of clusters of HII regions, in which the strong UV radiation emitted by young, hot (O and B type) stars ionizes the surrounding gas. In total, more than 50 HII regions are observed in Sgr B2, with varying size scales from hypercompact ($\sim$0.1 arcsec $\approx$ 800 AU), to extended ($\gtrsim$5 arcsec $\approx$ 0.2 pc) cometary shaped HII regions (Gaume et al. 1995; De Pree et al. 2015). In Sgr B2(N), two shell-shaped HII regions are apparent, as are four other compact HII regions.

In addition to line emission produced by the LMH and "h" hot cores, spectral line absorption is observed in the foreground of the HII regions at radio wavelengths. While the absorbing molecular gas components have lower line-densities than the hot cores, multiple complex molecules have been observed in this material but not detected in the hot cores (Hollis et al. 2000; Zaleski et al. 2013; Loomis et al. 2013), including arguably the most important molecules yet detected in the ISM from a prebiotic standpoint.

While Sgr B2 has been targeted by spectral line surveys from centimeter to sub-millimeter wavelengths (Turner 1989; Nummelin et al. 1998; Neill et al. 2012; Belloche et al. 2013; Neill et al. 2014), the data and analyses presented in this work have much to contribute to understanding the physics and chemistry of this highly complex region. Most surveys of Sgr B2 have been conducted with single dish telescopes at frequencies $>$ 80 GHz. At these frequencies, there is significant line confusion (a single feature can be assigned to multiple possible known or yet unknown carriers) and line blending (a single feature consists of multiple transitions of known molecules), as the data are line confusion limited rather than

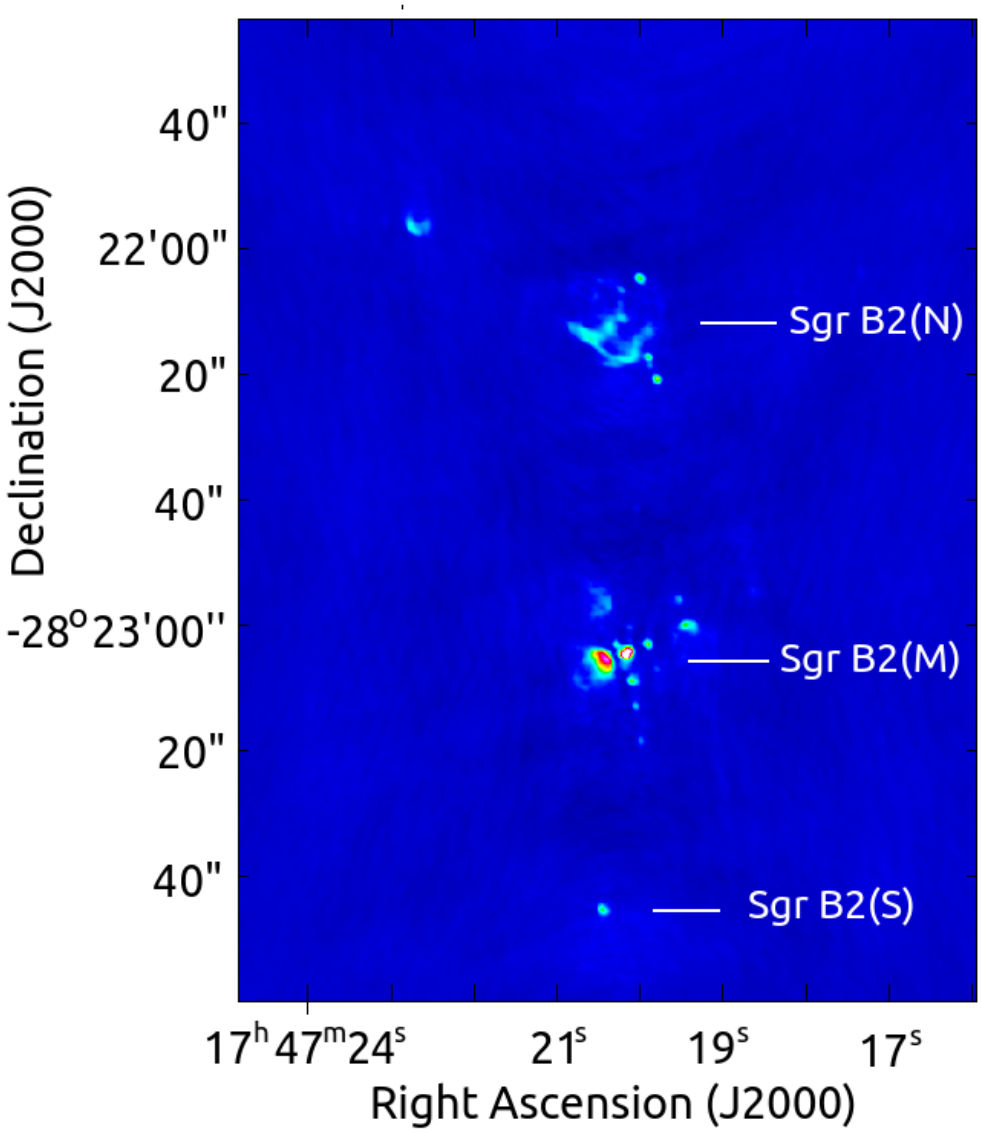

Fig. 1.1 – A continuum image of Sgr B2 at 18 GHz generated with the VLA data described in Section 2.3 shows the positions of the three main cores of star formation in Sgr B2.

noise limited. The centimeter wave spectra of Sgr B2 on the other hand, are noise limited and contain significantly less line confusion and blending, enabling more confident line identifications and measurements of spectral line parameters (i.e. shape, velocity, width, and flux) (McGuire et al. 2012). While the centimeter wave spectrum of Sgr B2(N), as sampled in the PRebiotic Interstellar MOlecular Survey (PRIMOS; Section 2.2), has made tens of important contributions in astrochemistry, only a very small fraction of the information present in the survey has been transferred to scientific journals. Thus, the centimeter wave spectrum is not plagued by the same hurdles as millimeter and sub-millimeter line observations, can be used for different science than higher frequency observations, and is largely unexplored.

Additionally, high spatial resolution ($\theta \lesssim$5 arcsec) observations of Sgr B2 will be critical for understanding the detailed spatial structure of the source. Although many lines have been mapped at low spatial resolution ($\gtrsim$40 arcsec) in the extended envelope of Sgr B2 (Jones et al. 2008, 2011), until very recently, only a few molecular transitions had been imaged with interferometers at the spatial resolution required to resolve the distinct chemical environments in the star forming cores of Sgr B2 ($\lesssim$5 arcsec) (Liu & Snyder 1999; Hollis et al. 2003; Belloche et al. 2008). As it is now possible to construct images of perhaps thousands of spectral features in a reasonable amount of observing time, this is quickly evolving.

1.4.3 The Diffuse and Translucent ISM

The line-of-sight to Sagittarius B2 (Sgr B2) is known to contain diffuse and translucent clouds observable by molecular line absorption against the background continuum of Sgr B2 (Greaves & Nyman 1996). The clouds arise in different regions of the Galaxy, including the Galactic Center, the Bar, and the spiral arm clouds of the Galactic disk. Thus, obser-

vations in this line-of-sight can reveal details of the kinematics, chemical composition, and physical structure of this material, potentially demonstrating systematic differences between different regions of the Galaxy.

Understanding the structure and chemistry of the diffuse interstellar medium (ISM) is essential for understanding the processing of gas within galaxies, as this material is a significant reservoir for the gas in a galaxy (Ferrière 2001). Diffuse clouds refer primarily to material in the Cold Neutral Medium (CNM), in which hydrogen is in its neutral state and physical conditions include low densities of $50 < n < 500$ cm^{-3} and warm temperatures of $80 < T_{kin} < 300$ K. This material contains high abundances of many light hydride molecules, and beyond a considerably small extinction threshold of $A_{\mathrm{V}o} \sim$ 0.2 to 0.4, multiple heavier molecules including c-C_3H_2, CS, and HCN (Snow & McCall 2006). The observed molecular abundances are much greater (by many orders of magnitude for some species) than predicted by standard chemical models. Recent chemical models that include episodic turbulence have improved the predictions substantially, although some molecules remain underpredicted (Godard et al. 2009, 2014).

Translucent clouds are defined as having moderate extinction conditions, with central extinctions of $1 < A_{\mathrm{V}} < 2.5$. In this range, UV irradiation can affect the chemistry significantly, but there is sufficient self-shielding to enable enhanced molecular hydrogen fractions, with more than 50% of the hydrogen atoms in molecular form (Snow & McCall 2006). Translucent clouds are embedded within diffuse clouds, and their physical conditions include higher densities, typically $500 < n < 5000$ cm^{-3}, and lower temperatures than diffuse clouds, of $\sim$25 K. In the Galactic Center however, the translucent clouds can have much higher temperatures, of 50 - 80 K and densities up to 10^4 cm^{-3} (Greaves & Nyman 1996).

Both diffuse and translucent clouds have typically been treated assuming homogeneous

distributions over fairly large size scales, of tens of parsecs for diffuse clouds and $\gtrsim$5 pc for translucent clouds, and the translucent clouds are typically treated as cohesive clouds. The small scale structure of molecular absorption lines has not been well tested, despite observational evidence of substantial clumping in HI clouds due to the presence of "tiny-HI clouds" (Heiles 1997). The broadband datasets produced by new-generation instruments reveal much about the coupled physical and chemical structure of material in the diffuse and translucent ISM.

1.5 Document Structure

This work utilizes broadband radio data at centimeter wavelengths in order to highlight the capabilities and address the challenges presented by new-generation radio instruments. The data are further used in order to advance our understanding of the coupled physical and chemical structure of material in Sgr B2 and in diffuse and translucent clouds along the line-of-sight to Sgr B2. The remainder of the document is structured as follows. Chapter 2 describes the data featured in this work, as the data sets feature in multiple chapters. Chapter 3 describes and demonstrates the performance of automated line fitting and identification routines designed to characterize broadband data sets efficiently. Chapter 4 constrains the physical environment and structure of gas in Sgr B2 that is observed to host exotic molecules of prebiotic importance. Chapter 5 utilizes spectral data to determine molecular abundances and discuss the distribution of small molecules and complex organic molecules in diffuse and translucent clouds in the line-of-sight to Sgr B2, and Chapter 6 discusses the spatial structure of translucent cloud material in the Galactic Center and Bar. Finally, we summarize key results and discuss future prospects for new-generation data sets in Chapter 7.

Chapter 2

Observational Data

Summary Statement

The remaining science chapters utilize three observational data sets all collected towards Sgr B2(N); as the data sets appear in multiple chapters, we describe the data collection and reduction here and refer to it throughout the work. The three data sets were conducted with the Australia Telescope Compact Array (ATCA), the Robert C. Byrd Green Bank Telescope (GBT), and the Karl G. Jansky Very Large Array (VLA). In brief summary, the ATCA data completely covers 29.8 - 50.2 GHz with 3 - 12 arcsec spatial resolution and somewhat poor spectral resolution, varying from 6 to 10 $\mathrm{km\,s^{-1}}$. The PRebiotic Interstellar MOlecular Survey (PRIMOS) conducted with the GBT provides the most sensitive broadband survey at centimeter wavelengths, with nearly complete coverage of the 1 - 50 GHz frequency range. Finally, the VLA data includes selected windows covering nitrile (–C≡N) and imine (–N=H) molecules from 18 to 20.5 GHz with $\sim$1 arcsec spatial and 1 $\mathrm{km\,s^{-1}}$ spectral resolution.

2.1 A 7-mm Band Survey of Sgr B2(N) with the ATCA

We conducted a 7-mm band survey with the ATCA to fully cover the 29.8 to 50.2 GHz range towards Sgr B2(N). The data provide:

1. the largest catalog of radio recombination lines observed with an interferometer.

2. the 30 - 50 GHz spectrum of the most line-rich interstellar source in the Galaxy, namely the LMH hot core.

3. a comprehensive picture of the chemistry, excitation, and kinematic structure of clouds of molecular gas in Sgr B2.

4. new insight into the chemistry and structure of diffuse and translucent clouds clouds observed in the line-of-sight towards Sgr B2.

Continuum images and continuum-subtracted spectral line data cubes are available at http://cdsarc.u-strasbg.fr/viz-bin/qcat?J/MNRAS/. Additionally, spectra extracted from five positions, including the LMH and "h" hot cores and three HII regions are made available at https://github.com/jfc2113/M and in the supplemental material to Corby et al. (2015).

2.1.1 Telescope Configurations

The ATCA observations were conducted with the Compact Array Broadband Backend (CABB) (Wilson et al. 2011) in broadband mode (CFB 1M-0.5k), providing two simultaneous spectra with 2048 channels of 1 MHz width. Eleven different tunings with a separation of 1.85 GHz were required to cover the full 30 - 50 GHz range available with the 7-mm receiver (Table 2.1). The 1 MHz channels provide a velocity resolution of 10 - 6 km s^{-1} from 30 - 50 GHz. Even given the broad linewidths in Sgr B2, the spectral resolution is suboptimal, so that lines may not be Nyquist sampled. However, the broadband mode of the CABB was selected as it makes a line survey over the whole 7-mm band feasible within a relatively short observing time.

Table 2.1 – Log of ATCA observations showing the arrays and CABB tunings.

UT Date	Array	Freq. A1 (GHz)	Freq. A2 (GHz)	Freq. B1 (GHz)	Freq B2 (GHz)
2011 Oct 21	H75	47.40	49.25	43.70	45.55
2013 Apr 3	H214	30.75	32.60	34.45	36.30
2013 Apr 4	H214	38.15	40.00	41.85	43.70

The observations were made in three $\sim$8 hour sessions in 2011 October and 2013 April, with hybrid arrays H75 and H214, respectively, as shown in Table 2.1. In each session, two pairs of tunings were observed, and the 43.70 GHz tuning was repeated in each configura-

tion. The H214 hybrid array enables good (u,v)-coverage of Sgr B2(N), providing sufficient resolution to separate the LMH from the shell-shaped HII regions without losing significant surface-brightness sensitivity. The H75 array is more compact than ideal but this is somewhat countered by using this array for the highest frequency tunings. Resulting angular resolutions, ranging from 3.4 to 13 arcsec are provided in Table 3.1.

The telescope was pointed towards Sgr B2(N) at α = $17^h47^m20\overset{s}{.}4$, δ = $-28^\circ22'12''$ (J2000). We observed a cycle of one minute on the complex-gain calibrator (1714-336), ten minutes on source, one minute on the gain calibrator with one pair of tunings (A1 and A2 in Table 2.1) and then repeated the calibrator-source-calibrator cycle with the second pair of tunings (B1 and B2). The telescope pointing was updated approximately every hour towards the gain calibrator. Uranus and 3C 279 were observed as the primary flux and bandpass calibrators respectively.

2.1.2 Data Reduction

The raw data were reduced into calibrated data cubes using mostly standard techniques of bandpass, absolute flux, and complex gain calibration in the MIRIAD package (Sault et al. 1995). To produce continuum-free line data, the continuum was subtracted in the (u,v)-domain and the fitted continuum was output into separate files. A single continuum image was generated from each of the three observing sessions and deconvolved with the CLEAN algorithm. The CLEAN model was input to determine a phase-only self-calibration solution, which was then applied to the line data and the continuum data. A final continuum image was generated using the CLEAN algorithm from the 7.5 GHz bandwidth data obtained in each observing session.

As this is among the first spectral line surveys completed with a broadband interferometer, we highlight our method for baseline subtraction and challenges for bandpass stability.

We performed baseline subtraction using the MIRIAD task UVLIN, generating a linear fit to the baseline of each 2 GHz tuning in the (u,v)-domain. The continuum images were generated from the continuum solutions output by UVLIN. Because Sgr B2 has a very high line density and because it is difficult to define line-free channels in the (u,v)-domain, we only excluded channels covering strongly masing lines from the fit. As very strong lines covered a small fraction of the bandwidth of each image, this had a very small effect on the continuum subtraction, resulting in a $\sim$1 mJy/beam offset that is $<$0.1% of the continuum level. Such a small effect might be deemed negligible in most data sets, however given the sensitivity of this data, it is non-negligible.

A larger effect was noticed in the form of a baseline wiggle in the images with a maximum amplitude of $<$1.5% of the continuum strength. This resulted from a limited bandpass stability due to the very large bandwidth in each tuning. The bandpass shape is quite complex, and while the selected bandpass calibrator was very strong ($\sim$25 Jy), the strong continuum of Sgr B2 ($\sim$1 Jy) made it difficult to model the continuum to the dynamic range (about 3 orders of magnitude) required. Furthermore, the continuum positions of Sgr B2(N) and (M) are the positions that contain most of the molecular line features, so that the residual continuum preferentially affected areas that are important for the line study.

To correct for these effects, we applied a continuum correction to the data in the image domain. Lines were masked at the 3σ level, and each 2 GHz cube was fitted with a high order polynomial to make a baselevel offset spectrum which was subtracted from the data cube. We describe further processing of the baseline applied to the published spectra in §3.3.1.

We note that the CABB flagged a consistent set of channels in each observation. In the publicly released images, in which the first and last 50 channels of each 2 GHz wide module are cut, the zero-indexed channels affected include channels 0, 1, 78, 106, 206,

462, 590, 718, 974, 1102, 1126, 1230, 1358, 1486, 1742, 1870, and 1947. All data cubes and continuum images are available at the CDS database (Genova et al. 2000) via anonymous ftp to cdsarc.u-strasbg.fr (130.79.128.5) or via http://cdsarc.u-strasbg.fr/viz-bin/qcat?J/MNRAS/. The continuum-subtracted data cubes provided do not have a primary beam correction applied. Models for the ATCA primary beam can be computed from information provided in the ATCA documentation.

The resulting line survey contains over a thousand spectral features towards the most line-dense region of the spectrum, and a few hundred spectral components at the positions of the HII regions. Figure 2.1 shows the spectra observed towards five positions in the ATCA data.

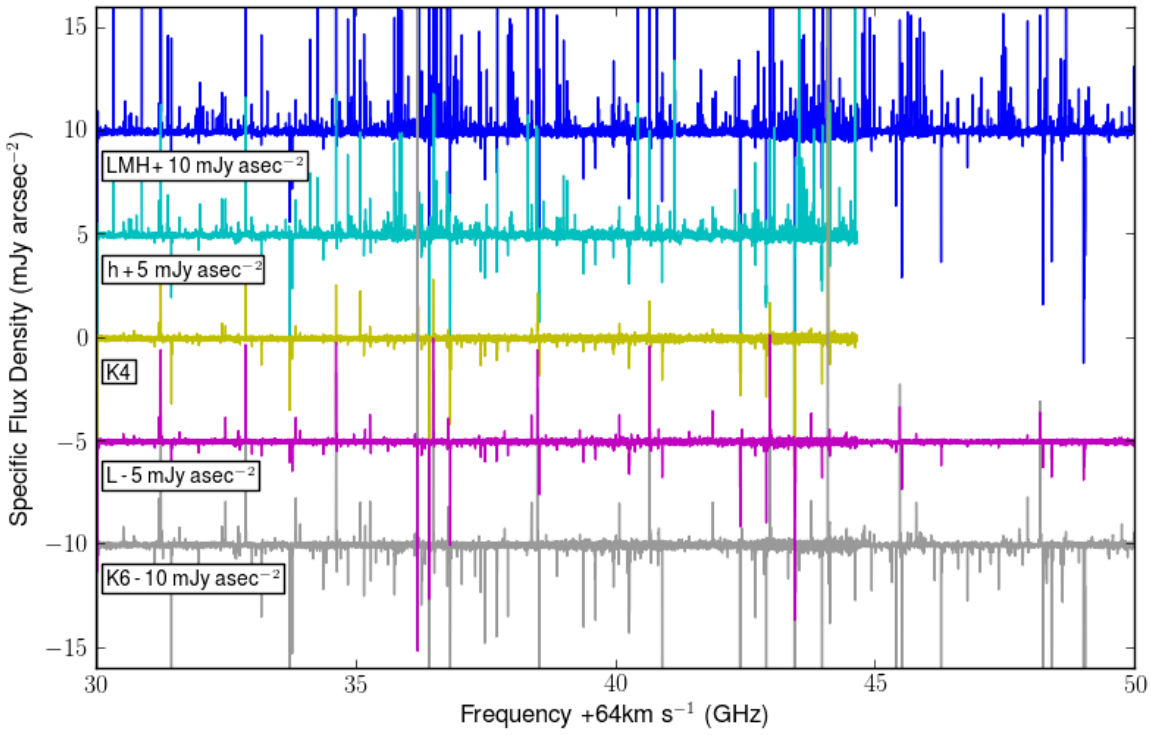

Fig. 2.1 – Spectra observed towards five positions in Sgr B2 demonstrate the line density at 7-mm and the high sensitivity of the ATCA survey.

2.2 The GBT PRIMOS Data

The PRebiotic Interstellar MOlecular Survey (PRIMOS)[1] is a key science project of the GBT that provides the deepest, most frequency-complete centimeter-wave spectral survey completed to date. For all observations, the telescope was pointed towards the position of the Large Molecule Heimat (LMH) at α = $17^h47^m19\overset{s}{.}8$, δ = $-28^\circ22'17''$. The GBT beam, which varies from 13 arcmin at 1 GHz to 15 arcsec at 50 GHz, is sensitive to absorption in the foreground of the free-free continuum structure of Sgr B2(N) as well as emission from the LMH over the full range of frequencies (Figure 2.2). At very low frequencies (of $<$8 GHz), the beam contains Sgr B2(M) as well. Most of the data were collected over the full year of 2007, with some observations performed in 2002, 2005, and 2013. All observations were performed in position switching mode, with an OFF position located 1 degree E in azimuth. Over most of the frequency range (of $>$3 GHz), four spectral windows of 200 MHz bandwidth and 8192 channels were observed simultaneously; 50 MHz windows were observed at frequencies of $<$3 GHz. Most windows were observed for $\sim$10-15 hours, resulting in T_A^* $\sim$5 mK rms noise levels in most of the frequency range.

The data were reduced using standard procedures for position switched data in the GBT data reduction package GBTIDL. For the full C-Band (4 - 6 GHz) data provided in Chapter 3, the data is presented in the T_A^* scale and has been baseline subtracted. At low frequencies observed in the Galactic Center where sources have very strong continuum strengths, very complex baseline patterns are present upon completing standard reduction procedures (Hollis 2005). To improve the baseline subtraction, I wrote a script to perform baseline subtraction by a method that uses a Hodrick-Prescott (HP) filter, described in Schlicht (2009). An HP filter is a commonly used tool for removing long-term growth trends from economics data and is similar in function to a high-pass filter. It is ideal for

[1]PRIMOS is publicly available at http://www.cv.nrao.edu/$\sim$aremijan/PRIMOS/.

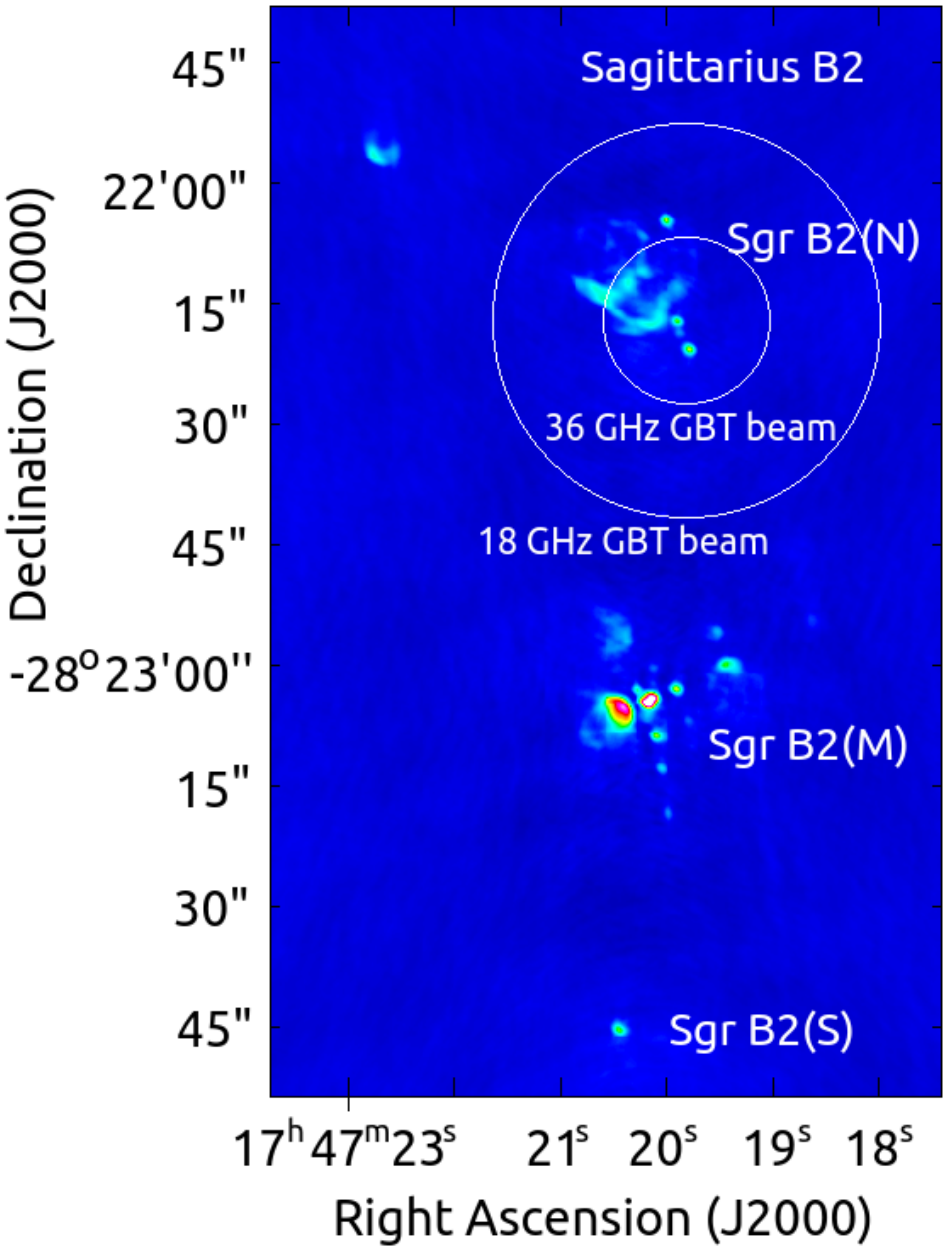

Fig. 2.2 – The FWHM beams of the GBT at 18 and 36 GHz are shown on a continuum image of Sgr B2 at 18 GHz generated with the VLA data described in Section 2.3. The beam fully covers the continuum structure of Sgr B2(N) at 18 GHz, and includes the majority of the structure at 36 GHz.

application to broadband data sets because it does not degrade at the band edges like a polynomial fit, and can fit a broad frequency span at once. The script operates as follows:

1. Determine an approximate baseline shape using the HP filter with a frequency cutoff specified by the user.

2. Determine the root-mean-squared (rms) residual between the data and the baseline solution.

3. Detect spectral lines as channels with higher than 3 σ_{rms} and select a tunable number of neighboring channels.

4. Interpolate over line channels and iterate through steps 1-3 with a higher frequency cutoff. The sensitivity to lines should have improved significantly in this iteration.

5. Edit line selection if desired, before again interpolating over line channels and iterating through steps 1-3 with the same higher frequency cutoff.

6. Subtract the baseline and output data.

The final data selection and baseline subtraction are illustrated in Figure 2.3.

The data used in the diffuse and translucent cloud analysis (Chapter 5) span the full frequency range of the GBT. The absorption profiles are carefully baseline subtracted over the narrow frequency ranges corresponding to about -400 to +250 $\mathrm{km\,s^{-1}}$ using a polynomial solution. For data with very stable baselines (typically Q-Band), we used a 1st order baseline. For data with more highly varying baselines, we usually used a 4th order polynomial fit over a typical velocity range of -400 to +250 $\mathrm{km\,s^{-1}}$. The data was then normalized by the continuum, as the ratio of T_L/T_C is the fundamental value for characterizing the molecular line absorption from the diffuse and translucent clouds. This ratio is independent of

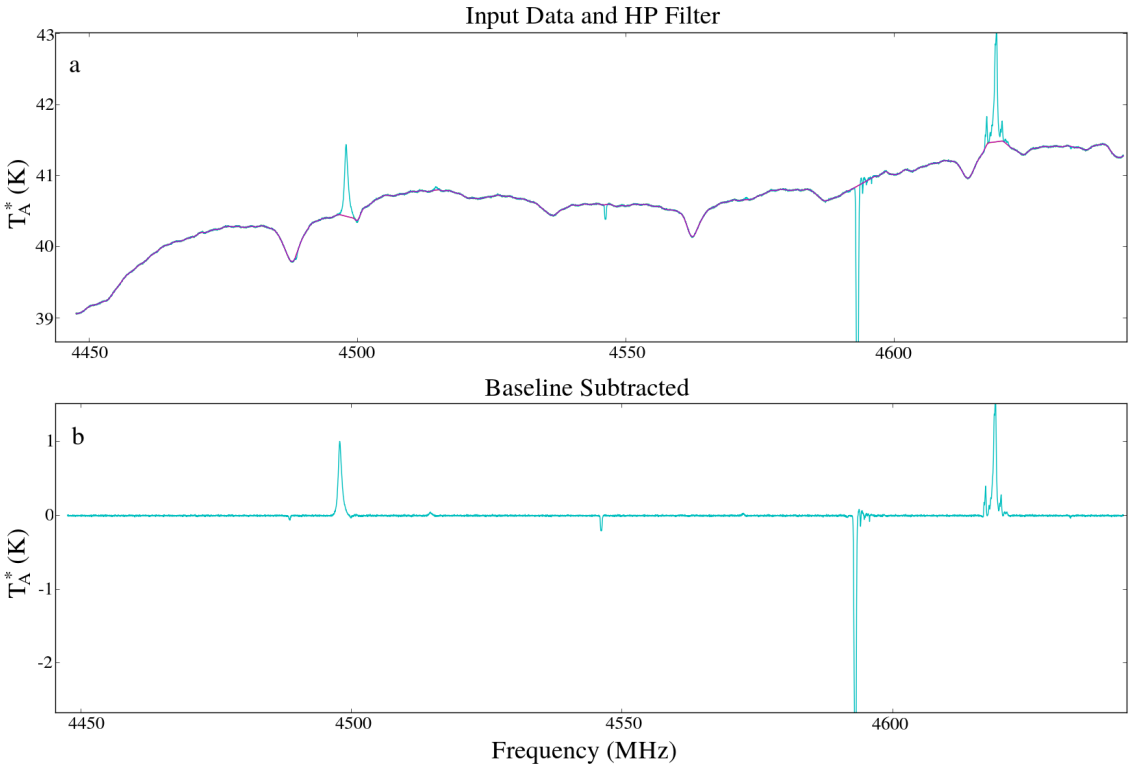

Fig. 2.3 – Baseline subtraction by the Hodrick-Prescott filter in a 200 MHz window of PRIMOS data at 4.5 GHz. **a** includes the raw data in cyan, data with linear interpolation over the frequencies of detected lines in blue, and the baseline determined by the HP filter in red. Panel **b** shows the baseline-subtracted data.

corrections to the atmospheric attenuation and the GBT aperture efficiency, which cancel in the ratio of T_L/T_C .

2.3 K-Band Data with the VLA

Interferometric observations were conducted with the Karl G. Jansky Very Large Array (VLA) towards a single pointing centered on the Large Molecule Heimat (LMH) at α = $17^h47^m19\overset{s}{.}8$, δ = $-28°22'17''$. Observations were conducted in good weather during the move from the CnB to the B array configuration in May 2012. Four hours of on-source observing was completed in six hours of total observing. The quasar source 1331+305 (3C286) was used to calibrate the bandpass and absolute flux. We observed a cycle of four minutes on the complex gain calibrator (J1713-2658), 15 minutes on source and updated the telescope pointing (towards J1743-0350) approximately every hour. The data were calibrated using standard techniques of bandpass, absolute flux, and complex gain calibration with the CASA software package, and the continuum was subtracted in the (u, v)-domain prior to imaging. Phase-only self-calibration solutions were determined with continuum images and applied to the data before performing continuum subtraction in the (u, v)-domain. Imaging was performed using the Cotton-Schwab CLEAN algorithm. To suppress sidelobes and imaging issues related to the strong extended flux in Sgr B2, we applied a Briggs weighting scheme with a robust parameter tending towards natural weighting. Specifically, robust parameters were set to 0.5 for images featured in this body of work, resulting in a $\sim$1 arcsec synthesized beam. This data is thus at significantly higher resolution than the ATCA survey, and is capable of clearly resolving the main structures present in Sgr B2(N).

We used VLA capabilities offered through the Resident Shared Risk Observing program in the 2012 observing cycle to observe 2 $\times$ 1 GHz basebands with 8-bit sampling

at K-Band (18-26 GHz). The correlator was set up in order to cover 13 transitions of nitrile (with -C≡N) and imine (with -N=H) molecules with 1 $\mathrm{km\,s^{-1}}$ channel resolution. The setup included nine subbands placed in the frequency ranges of 18.2 to 19.2 GHz and 19.8 to 20.8 GHz, as illustrated in Figures 2.5 and 2.4. Targeting these lines with matched channel resolution and sensitivity with the VLA prior to the upgrade would have required an order of magnitude longer observing time. Due to the broadband correlator setup utilized, ∼20 additional transitions appear in the final data products. In this dissertation, we feature the line absorption from HC_3N and CH_3CN. Rather than focus on the strong line emission and absorption from Sgr B2 itself, we focus on line absorption from foreground clouds associated with translucent clouds. While the original scientific motivation behind the observation did not include this material, the broadband capabilities enabled a serendipitous observation of the structure of the diffuse and translucent ISM in the Galactic Center (Chapter 6). Prior to the VLA upgrade, spectral line observations targeting the HC_3N and CH_3CN lines would not have covered the translucent cloud absorption. This highlights the significant advancement in the versatility and potential for serendipity when the observations utilize the broadband capabilities of the instruments.

2.4 In the Context of New Generation Data Sets

Each of the three data sets highlights a different aspect of new-generation broadband radio observations. The ATCA data demonstrate the depth and incredible complexity of data that can now be obtained in a very reasonable amount of observing time of 24 hours. More sensitive instruments with higher collecting areas are becoming available, so that similar work can be completed in even less time. While the GBT data featured here were collected with the older GBT spectrometer rather than the VErsatile GBT Astronomical Spectrometer (VEGAS), the broad range of projects that they have been used for (e.g. von

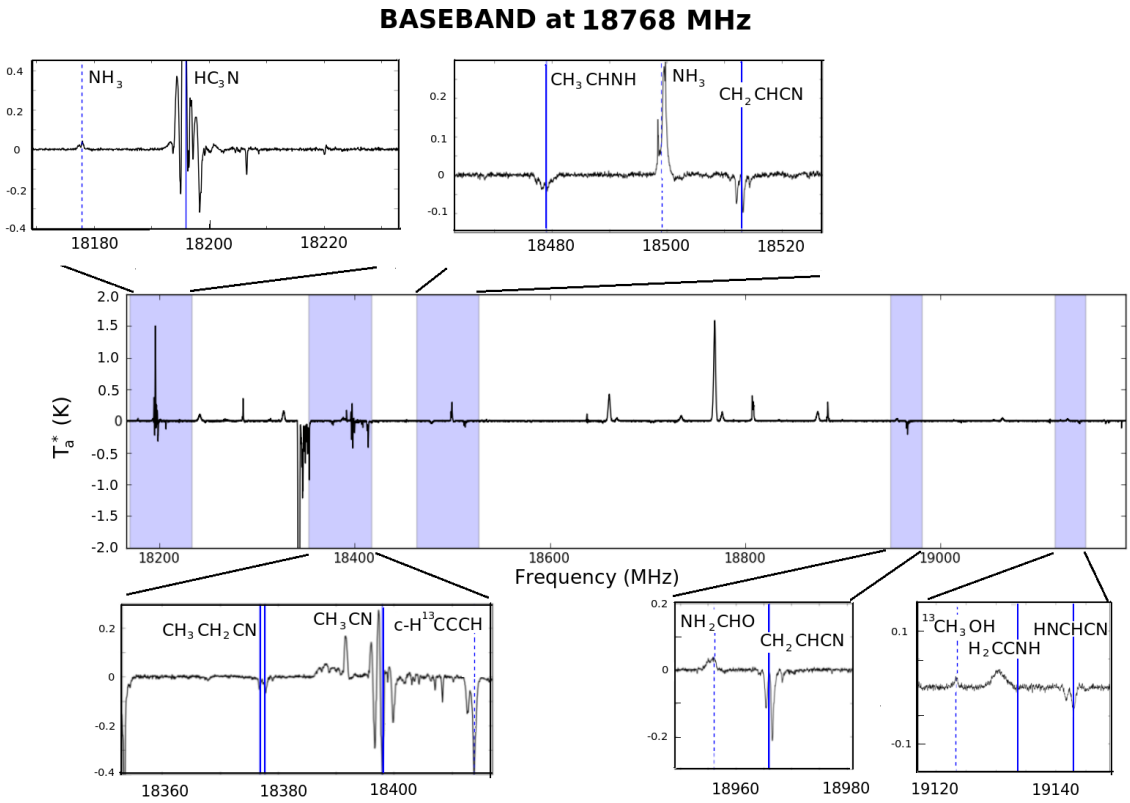

Fig. 2.4 – The baseband and subband coverage of the VLA correlator setup for the BD baseband is illustrated. The data is from the PRIMOS survey, with highlighted segments showing the coverage of the VLA setup. Targeted lines are marked with a solid line, and selected additional lines are shown with a dashed line.

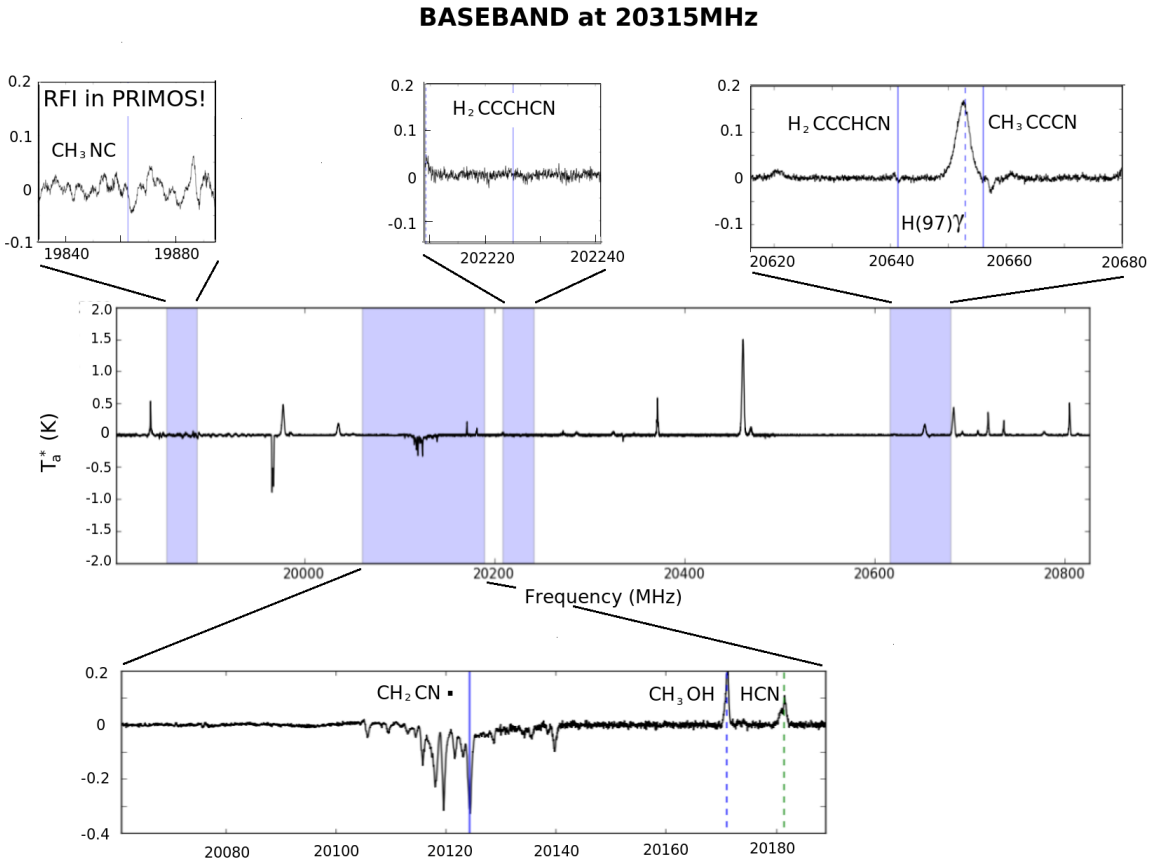

Fig. 2.5 – The baseband and subband coverage of the VLA correlator setup for the AC baseband is illustrated. The data is from the PRIMOS survey, with highlighted segments showing the coverage of the VLA setup. Targeted lines are marked with a solid line, and selected additional lines are shown with a dashed line.

Procházka et al. 2010; Neill et al. 2012; McGuire et al. 2012; Loomis et al. 2013; Faure et al. 2014) demonstrate the versatility of single dish spectral surveys at centimeter wavelengths. With the new instrumentation on the GBT, this data could be collected significantly more efficiently, with more than an order of magnitude reduction in the observing time, and much of the frequency range could be covered even more efficiently with the Effelsberg Telescope. PRIMOS is thus a pathfinder for centimeter-wave spectral surveys. The VLA data was observed using a mode of the correlator that was highly experimental in 2012. Today, it is standard, and in fact, the VLA is capable of obtaining a much greater number of sampled data points, which allows users to easily sample four times the frequency coverage. Yet the observation that we completed would not have been possible ten years ago, and the new capabilities enable new methodologies for observing with an interferometer; the VLA data featured here is among the first interferometric data sets collected that simultaneously targets an entire family of molecules and includes deep images of dozens of lines at high spatial resolution.

Chapter 3

Automated Data Handling of Broadband Interferometric Data

Note: This chapter is adapted from the published work: "An ATCA survey of Sagittarius B2 at 7 mm: chemical complexity meets broad-band interferometry", Corby, J. F., Jones, P. A., Cunningham, M. C., Menten, K. M. et al. (2015), *The Monthly Notices of the Royal Astronomical Society*, 790, 3696.

Abstract

We present scripts written to characterize broadband spectra of complicated spectral line sources. The scripts perform automated spectral line fitting and semi-automated line identification for complex spectra with a detection limit specified by the user. We describe the line-fitting and identification procedures and test their performance on spectra extracted from the positions of three HII regions in a 30 - 50 GHz survey of Sgr B2(N) conducted with the ATCA, and on GBT data at 4 - 6 GHz. The spectra contain recombination line emission and molecular line absorption at multiple velocity components. Towards the most line-dense region characterized in the ATCA data, we detect $\sim$500 spectral line components of which $\sim$90% are confidently assigned to H and He recombination lines and to 53 molecular species and their isotopologues. In this chapter, we report the line identifications and fit parameters, and evaluate the performance of the code by an anlysis of line kinematics.

3.1 Motivation for Full Spectral Characterization

Full spectral characterizations are increasingly requisite for appropriately interpreting radio data, particularly as instruments become more sensitive and have greater broadband capabilities. In order to study the weaker lines in a survey, which comprise the majority of detected lines (Figure 3.1) and often have less obvious molecular carriers, it is necessary to consider the full spectrum in order to mitigate misassignments and verify consistency. In molecule-rich sources, interferometric observations can help to mitigate line confusion and blending, as lines from different molecules can peak at distinct positions, but in order for this to be effective, the spectra must be characterized at each of the positions. Full spectral characterization is even more essential for interferometric data sets containing sources with

complex physical structure. In this case, we would want to characterize spectra extracted from multiple different positions in the field of view, potentially corresponding to distinct physical environments. In order to assign line identifications, we ask questions including:

- Do we detect other lines of the same molecule at the same spatial position?
- Is the upper or lower state energy associated with the transition in the same range as most other detected transitions? If not, is there a reason to expect this transition to be present?
- If the line is from transition A, is the line profile consistent with the kinematics observed in other lines at the same spatial position?

To answer these we characterize the kinematics of the source, the chemical inventory of gas in localized spatial regions and kinematic components, and the excitation of the gas. In a survey containing many lines, we can do so using large number statistics. The spectral characterization is important for doing any further analysis on the data cubes, including making moment 0, moment 1, and moment 2 images of specific lines and interpreting of molecular spatial distributions. This is discussed further in Section 3.6.

3.2 Automated Spectral Line Fitting and Identification

The line fitting routines operate on baseline-subtracted 1-d spectra, containing frequency and intensity axes. The fitting and identification are accomplished in two separate scripts, where the line-identification script utilizes the output of the fitting script. The line fitting script operates by the following basic procedure:

1. Identify "detected" features as those with a single-channel flux $I_{chan} > a\,\sigma_{\rm region}$, where $\sigma_{\rm region}$ is the root-mean-squared (rms) noise of line-free sections of a region's

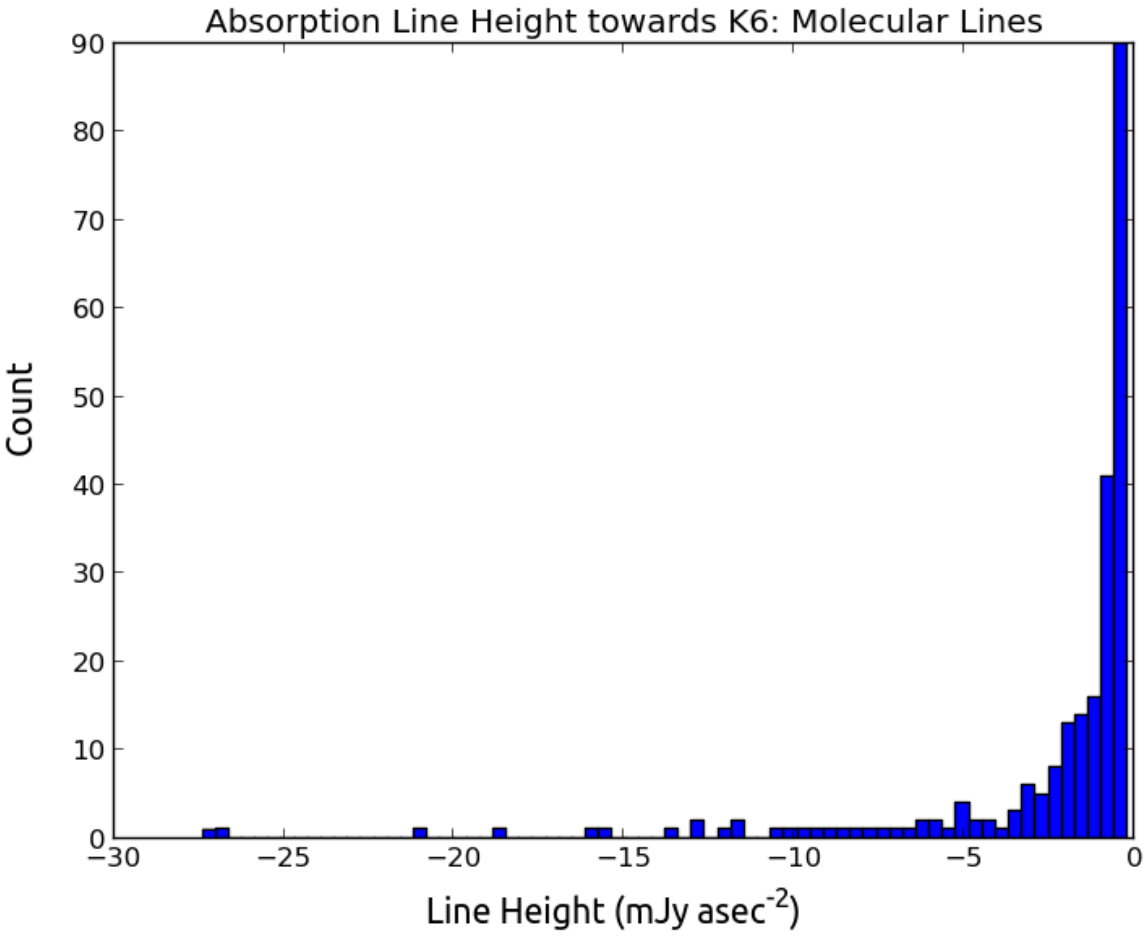

Fig. 3.1 – The distribution of line strengths in the ATCA survey shows that the majority of the spectral lines detected are near the detection limit, while fewer strong features are present.

extracted spectrum and a is a user-specified threshold. The value of $\sigma_{\rm region}$ is determined independently for each frequency tuning, with the spacing between tunings also specified by the user. The fitter selects channels that meet this criteria and 5 channels on either side. In most cases, a threshold of $3.5\,\sigma_{\rm region}$ is recommended, in which case one channel in 2149 should be a false detection assuming perfect baseline subtraction and constant noise within an image.

2. If desired by the user, perform data interpolation within channels selected in step (i), using Fourier-domain zero padding. This is useful for data with poor spectral sampling compared to the source line width, and is recommended for data with fewer than four channels within the full width at half maximum (FWHM) line width. Interpolation will generate data with three channels sampling the frequency range originally covered by a single channel. While the number of independent data points remains the same, this triples the number of points used to constrain the fits, improving the fits significantly for poorly sampled data. For example, if a line profile is sampled by two channels and surrounded by a zero-value baseline, one can imagine many different Gaussian profiles capable of fitting the data perfectly with highly varying heights in particular.

3. Fit one or more Gaussians to each feature iteratively. The spectral line fitter first determines an unconstrained best-fit Gaussian to a spectral line using a least squares routine. The best-fit parameters are then used as input guesses for the least squares fitter to re-fit a single Gaussian to the channels within $0.8 \times$ FWHM of the line center. A cutoff of $0.8 \times$ FWHM is selected in order to minimize the effects of the baseline uncertainty, which preferentially affects line wings. If a 1-component Gaussian shape is appropriate, this includes 94% of the power of the line.

4. Evaluate the 1-component fit against a set of criteria designed to determine whether a multi-component fit is required. The criteria were determined empirically based on performance of the line-fitter applied to spectra from ATCA data from 30 - 50 GHz, and are described in Appendix A; the criteria appear to be robust at centimeter wavelengths based on the application of the code to PRIMOS data at 4 - 6 GHz, (§3.4). If the segment of data meets the criteria, a 2-component fit is determined and evaluated. In the event that neither a 1-component nor a 2-component fit is deemed sufficient, the fitter grabs a slightly different segment to fit and re-attempts both a 1- and 2-component fit. If the result remains insufficient, the reported fit is marked as poor, pointing out where further attention is required.

5. The best 1- or 2-component Gaussian fit is then subtracted from the raw (as opposed to the interpolated) data. If the residual spectrum contains channels with $I_{\rm chan} > a\,\sigma_{\rm region}$, the residual spectrum re-cycles through steps (ii)-(v). Non-Gaussian line shapes (i.e. lines with wing broadening) are fit in this process, so that the iterative solutions do not provide a full characterization of the line shape, but do adequately account for the total flux of the line. The treatment of line wings is discussed further in Appendix A.

6. Compare the Gaussian fit parameters to spectral line catalogue data[1]. At this stage, all lines with reasonable kinematic agreement are output along with the line fit parameters.

[1]All line data were accessed through the online ALMA Spectral Line Catalogue - Splatalogue (available at www.splatalogue.net; Remijan et al. (2007)); original line data were compiled in the Cologne Database for Molecular Spectroscopy (CDMS; Müller et al. 2005); the NASA Jet Propulsion Laboratory catalogue (JPL; Pickett et al. 1998); the National Institute for Standards in Technology (NIST) Recommended Rest Frequencies for Observed Interstellar Molecular Microwave Transitions - 2002 Revision (the Lovas/NIST list; Lovas & Dragoset 2004); and the Spectral Line Atlas of Interstellar Molecules (SLAIM; F. J. Lovas, private communication) and references therein accessible on Splatalogue.

Because a large number of steps were required to obtain the resulting fits, we do not adopt the errors to individual fits. Instead, we utilize the power of broadband line surveys to derive upper limits to the errors empirically from the variation in line parameters amongst a large number of fits (§3.3.2).

The line identification script then operates on this output in order to select the correct line identification based primarily on the source kinematics. The user may also input a set of lines that will be prioritized; these may include recombination lines, strong lines, or lines that may appear at velocities atypical of the source, for example in diffuse or translucent clouds. Because the code is optimized to this dataset, the line-ID component is not very sophisticated, with the primarily kinematics-based rather than chemistry-based consistency checks. The line identification code does not presently include a model for the molecular composition and radiative transfer. This enables us to measure properties of the gas purely empirically, which is particularly appropriate at centimeter wavelengths, where a large number of lines from various molecules have been shown to be non-thermally excited (Menten & van der Tak 2004; McGuire et al. 2012; Faure et al. 2014).

Both the line fitter and line identification scripts are written modularly, enabling adaptation for different datasets. The PYTHON scripts are described in greater detail in Appendix A and available at https://github.com/jfc2113/MicrowaveLineFitter and in the supplemental material to Corby et al. (2015).

3.3 Application to the 7-mm ATCA Survey

3.3.1 Sources and Spectrum Extraction

The ATCA line survey contains of order a thousand spectral lines with significant spatial and kinematic structure. Although line confusion is not as problematic at centimeter

wavelengths as it as at millimeter wavenlengths, line confusion does occur commonly in this data set. Thus, any interpretation of the spectral cube data requires confident line identification and a robust treatment of the source kinematics.

To accomplish this, we apply the automated line fitting and identification scripts to spectra extracted from physically distinct regions of Sgr B2(N). Thus, we first extracted spectra from the elliptical regions shown in Figure 3.2. We extracted spectra over the entire 29.8 - 50.2 GHz bandwidth from a radio continuum peak along the K6 shell-shaped HII region, the cometary HII region L located 35 arcsec NE of Sgr B2(N), and the LMH hot core. In the higher spatial resolution section of the spectrum (from 29.8 - 44.6 GHz due to the observed configurations), we additionally extracted mean spectra towards K4 and "h". Figure 3.2 shows the elliptical regions from which the spectra were extracted and Table 3.2 reports their positions. Note that we did not vary the size of the elliptical regions in different images depending on the beam size. The elliptical regions are typically larger than the beam sizes in the high spatial resolution data (from 29.8 - 44.6 GHz), but smaller than the beam sizes in the low spatial resolution data observed with the compact array configuration (from 44.6 - 50.2 GHz). The spectra are sensitive to the spatial resolution; for example, low spatial resolution data towards the K6 elliptical region includes flux originating on the K5 shell and in the LMH as the regions are poorly resolved. In the case of the spatially isolated source L, the elliptical region from which the spectrum was extracted is similar to the source size of L and well matched to the $\sim$5 arcsec beam size of the high spatial resolution data (Gaume et al. 1995). In the low spatial resolution data, the flux is spread over the larger beam, which has the effect of decreasing the flux in the low spatial resolution section of the spectrum.

After extracting spectra, we interpolated over bad spectrometer channels listed in §2.1.2 using linear interpolation, and performed additional baseline smoothing by applying a

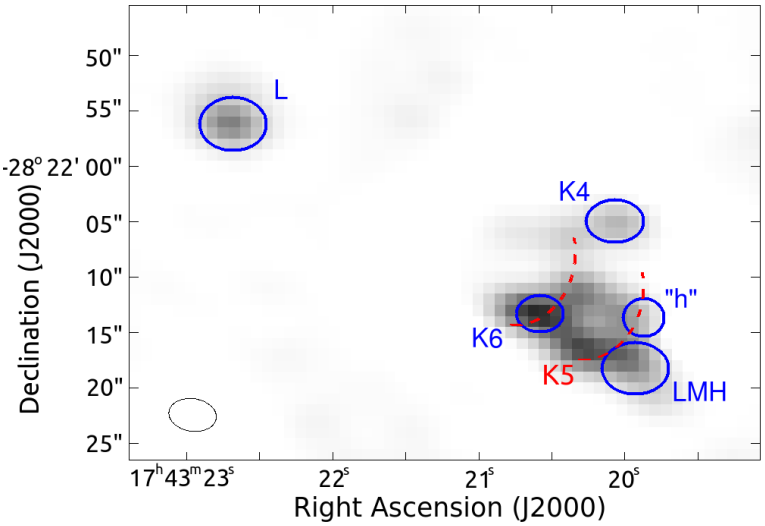

Fig. 3.2 – Continuum image of Sgr B2(N) and L at 40 GHz showing the elliptical regions from which spectra were extracted. The dashed line arcs point out the K5 and K6 shell-shaped HII regions. The synthesized beam shape is shown in the lower left corner.

Table 3.1 – Root mean squared (1σ) noise level in spectra extracted from K6, L, and K4

Center Freq	Beamsize	$\sigma_{\rm RMS}$ (μJy arcsec^{-2})		
(GHz)	arcsec × arcsec	K6	L	K4
30.75	6.3×4.7	58	64	55
32.60	5.9×4.4	54	71	54
34.45	5.7×4.0	61	74	51
36.30	5.2×4.0	70	80	62
38.15	5.1×3.7	72	105	66
40.00	4.7×3.6	100	124	81
41.85	4.6×3.6	82	131	76
43.70	4.4×3.4	132	179	108
45.55	13.0×8.9	53	83	
47.40	11.9×8.7	51	88	
49.25	11.2×8.5	70	148	

Table 3.2 – Coordinates of regions from which spectra were extracted.

Region	Ellipse Shape			
	RA Center	Dec Center	ΔRA (arcsec)	ΔDec (arcsec)
K6	$17^h47^m20\overset{s}{.}58$	-28°22′13″.2	4.9	3.3
L	$17^h47^m22\overset{s}{.}68$	-28°21′56″.1	6.8	4.8
K4	$17^h47^m20\overset{s}{.}07$	-28°22′04″.9	5.9	3.8
LMH	$17^h47^m19\overset{s}{.}93$	-28°22′18″.2	6.8	4.6
"h"	$17^h47^m19\overset{s}{.}87$	-28°22′13″.6	4.1	3.4

Hodrick-Prescott filter to remove a low frequency baseline wiggle (Hodrick & Prescott 1997). Figure 3.3 shows the baseline with and without the HP filter applied. We used a modified version of the HP filter, as described in Schlicht (2009), that can use datasets with segments of missing data. This was useful in order to extrapolate over spectral lines, particularly over broad spectral lines, such as the absorption feature of CH_2CN at 40 230 - 40 270 MHz. Applying the filter achieved a 10 - 25% reduction in the root mean squared (rms) noise in the spectra extracted from different images. This improved the sensitivity of the survey, enabling $\sim$10% more line detections, and also reduced the false detection rate, as sections of the spectrum with poor baseline subtraction were prone to meet the detection criteria without an obvious line.

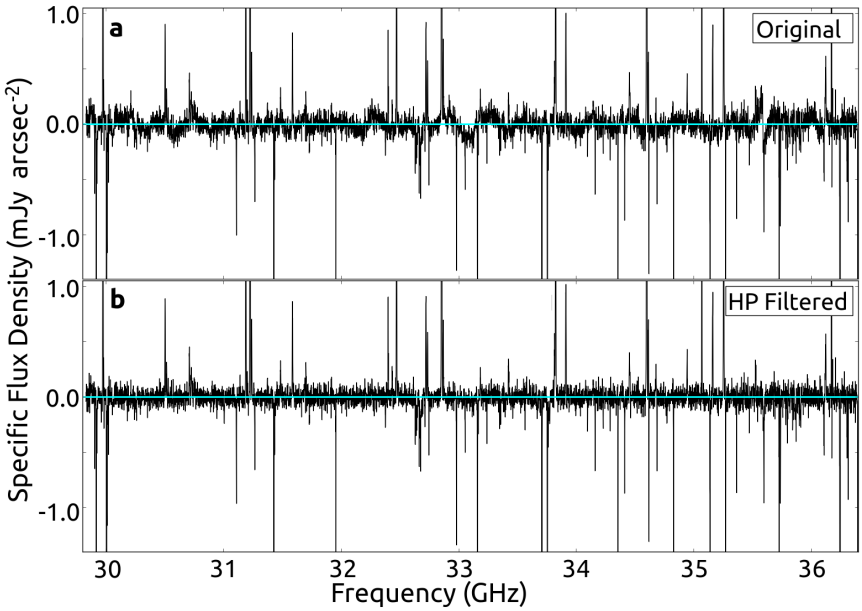

Fig. 3.3 – A segment of the full spectral coverage towards K6. **a.** shows the spectrum extracted from the data cubes and **b.** is the spectrum after baseline removal using a Hodrick-Prescott filter.

We then converted from units of Jy beam^{-1} to mean flux density per square arcsec (or equivalently, specific flux density) in order to inspect images with distinct beam sizes on the same scale. Finally, we performed a primary beam correction to the extracted spec-

tra. We applied the beam correction to the extracted data instead of simply extracting the spectra from beam-corrected images for the following reason. For each image, the standard technique in MIRIAD applies a single primary beam (PB) correction based on the central frequency tuning of the image, and does not include frequency dependence within the image. However, over the 2 GHz bandwidth of each image, frequency-dependence is significant, especially towards L. To compute appropriate frequency-dependent beam corrections, we compared the spectra extracted from the regions in the non-PB corrected cubes to the spectra extracted from the same regions in PB corrected cubes. We fit a fifth order polynomial to the ratio of PB corrected to non-PB corrected data across the 20 GHz of bandwidth. The PB corrections determined from this fit are substantial (up to a factor of 2.6) for L but are very small ($<$1.04) for K4, K6, "h", and the LMH.

Figure 3.4 shows a representative segment of spectra from all five regions from which spectra were extracted. The half power beam widths at all frequency tunings and the rms noise levels in the final extracted spectra are reported in Table 3.1. The supplemental material to Corby et al. (2015) provides the extracted, HP-filtered, and PB-corrected spectra towards all 5 regions, and the line fitting and identification PYTHON code described in §3.2. This material is additionally available at https://github.com/jfc2113/MicrowaveLineFitter.

3.3.2 Spectral Line Results

We report the results of the application of the line fitting and identification scripts to the spectra extracted from K6, L, and K4. Whereas line emission associated with high energy ($E_U \gtrsim 80$ K) transitions is present towards the LMH and "h" (Figure 3.4), the spectra of K6, L, and K4, contain molecular line absorption by primarily low energy ($E_L \lesssim 20$ K) states and additionally hydrogen and helium recombination line emission associated with the HII regions. In addition, molecular line absorption was observed at velocities associated

with diffuse and translucent clouds located in the Galactic Center, Bar, and disk. However, we refrain from further discussion of this material until Chapter 6.

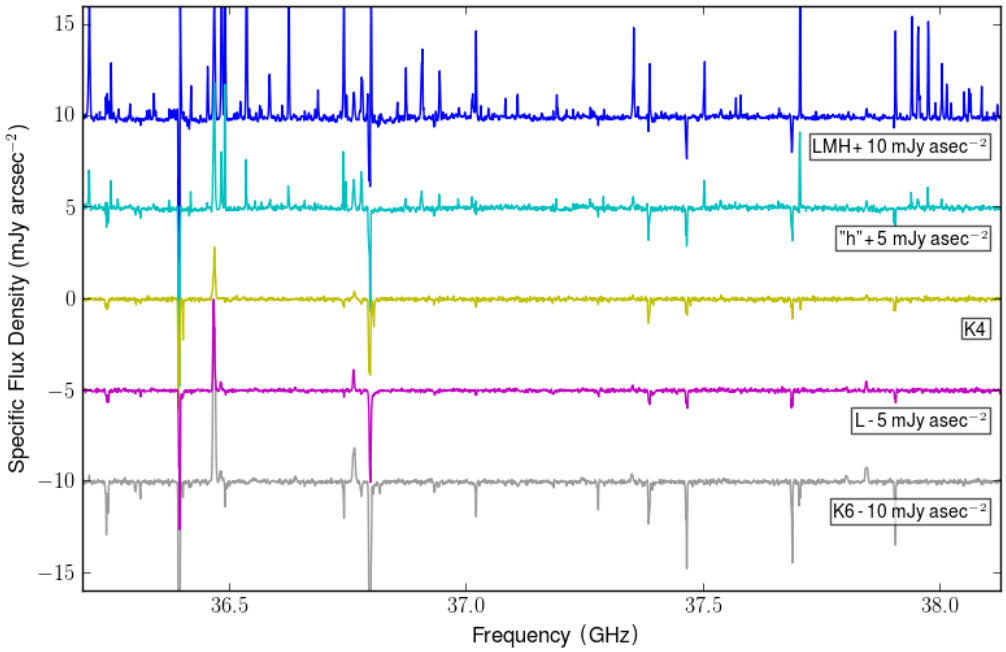

Fig. 3.4 – A representative segment of spectra extracted from all five regions targeted in this study. Whereas the LMH and "h" have line-dense spectra dominated by molecular line emission, K4, L, and K6 have lower line densities with molecular lines observed in absorption and recombination lines in emission.

Of all detected features originating at the positions of K6, L, and K4, ∼90% were confidently assigned to recombination line or molecular carriers. The remaining 10% including unidentified transitions and possible false detections are discussed in Appendix B. Figure 3.5 illustrates the raw data spectrum extracted towards K6 with the output of the line fitter overlaid and line identifications labeled. Figures in this format containing the full spectra towards K6, L, and K4 are provided in Appendix B. Additionally, tables providing line identifications and Gaussian fit parameters, including velocity center, height, width, and integrated flux towards K6, L, and K4 are available in Appendix C. We do not report errors on individual Gaussian fits in the tables, but discuss errors in §3.3.2. As mentioned in

§3.2, lines with wing broadening are approximated by a primary Gaussian component and additional components with lower amplitude. Wing components were required for ∼10% of the lines towards K6, and most of these are attributable to the non-Gaussian shapes of H α lines towards K6; fewer features required wing components towards L and K4. For clarity, we only list the primary Gaussian component parameters in the tables, however, the reported integrated flux values include wing components. It follows that the reported flux is not always equivalent to what you would obtain from the primary Gaussian component alone.

Recombination Line Kinematics

In order to assess the performance of the line fitting and identification routine, the output of the code was evaluated using hydrogen and helium recombination lines towards K6, L, and K4. Recombination lines, particularly at higher principal quantum numbers (n >90), are not well described by simple Gaussian line shapes but exhibit Voigt profiles (von Procházka et al. 2010). The line fitting routine applies only Gaussian shapes, which adequately characterize the bulk motion of ionized gas via the velocity center, particularly because the α and β transitions have lower quantum numbers with less collisional broadening. However, towards K6 in particular, most H α lines require primary components and weaker components to recover the flux in the wings.

The hydrogen and helium 51 - 59 α, 64 - 75 β, 72 - 85 γ, 79 - 93 δ, 85 - 100 ϵ, and 90 - 106 ζ recombination transitions fall in the observed band, enabling measurements of recombination line strengths, widths, and HII region kinematic centers. Figures 3.6 and 3.7 present H and He α and β transitions towards K6, and Figures 3.8 and 3.9 present H and He α transitions towards L and K4 respectively. Each panel shows the H and He data with a single quantum number, with the Gaussian fits reported in Appendix C overlaid. The

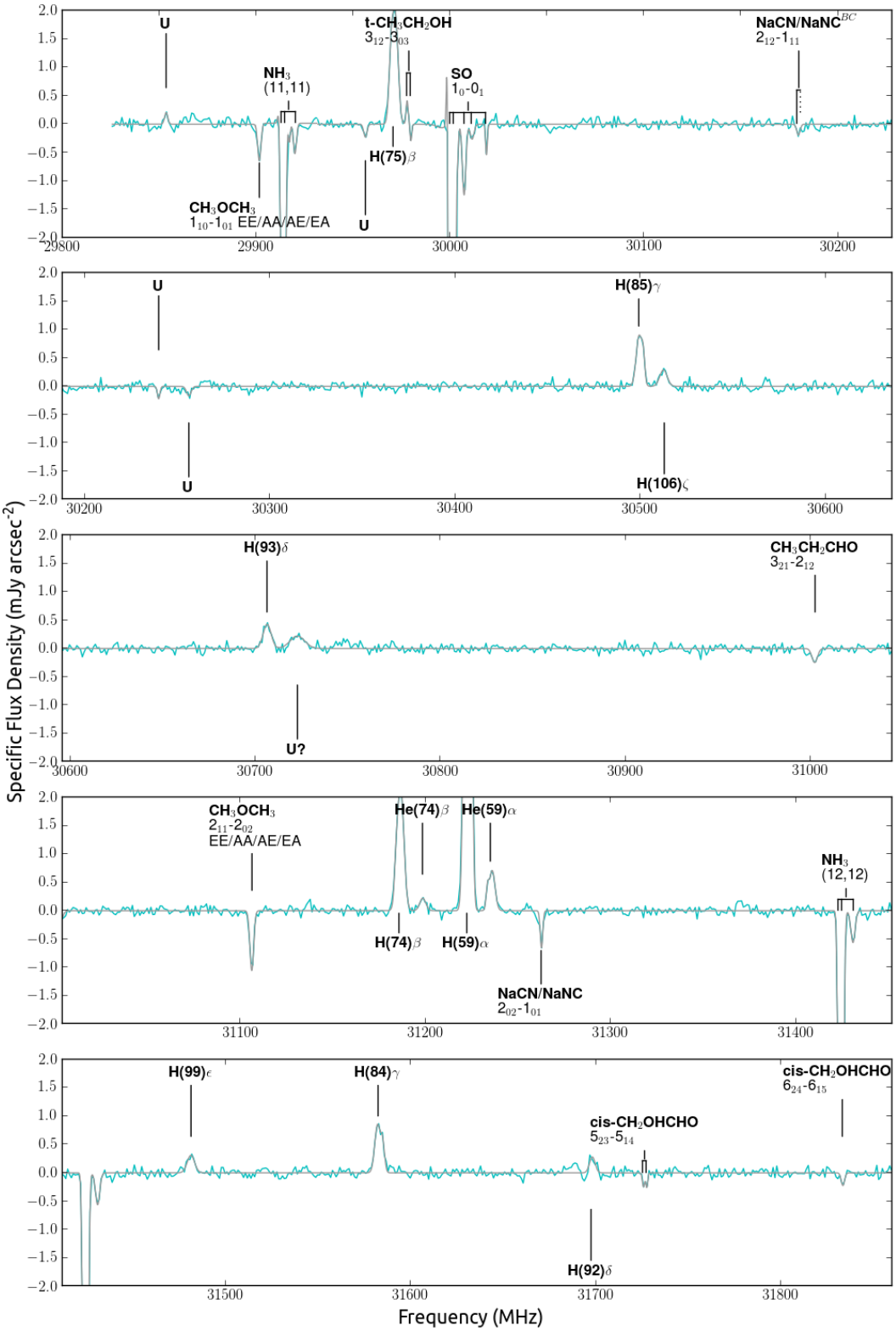

Fig. 3.5 – A sample page of the full data spectrum extracted towards K6 with line identifications labeled and the output of the automated line-fitter overlaid. See Appendix B for full figures for K6, L, and K4.

final panel of each figure shows a composite averaged spectrum overlaid with a fit to the averaged spectrum. The best fits to the averaged spectra are provided in Table 3.3. Additionally, recombination line kinematic measurements generated from H α - γ transitions are provided in Table 3.4 and a histogram of the line centers is shown in Figure 3.10.

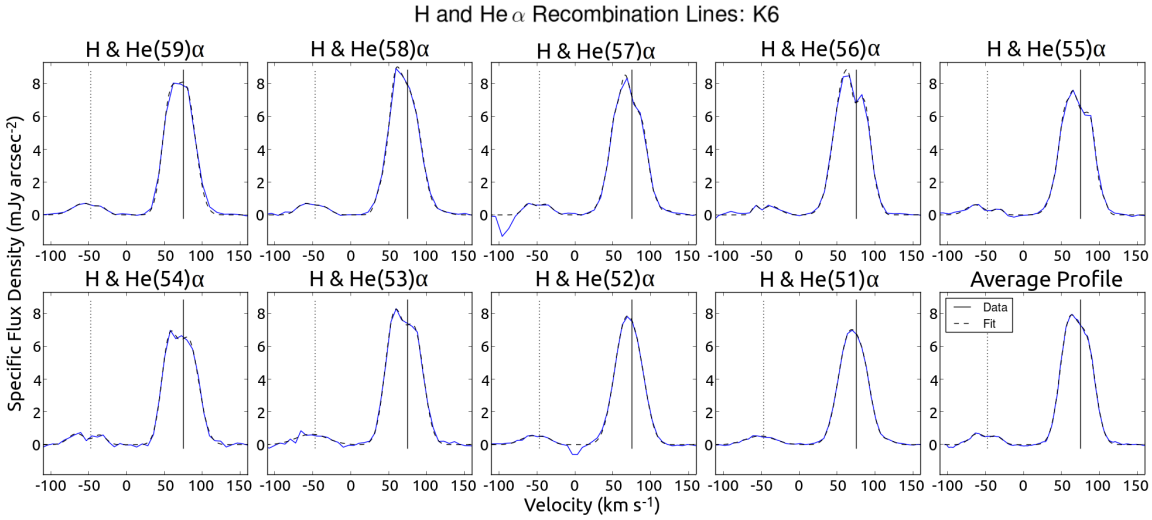

Fig. 3.6 – Hydrogen and Helium α recombination lines towards K6. Profiles of the H(59) - H(53)α transitions, extracted from high spatial resolution data, show a double peaked profile, whereas the H(52) and H(51)α transitions are well fit by a single component. The averaged profile is best fit by a Gaussian centered at 59 km s^{-1} and a weaker component at 84 km s^{-1}. The solid and dashed vertical lines represent the H and He α transitions at 75 km s^{-1} respectively.

Towards K6, the automated line fitting routine detected 64 hydrogen recombination transitions including H α - H ζ and 13 helium transitions including He α - He β lines. The ionized gas towards K6 has two primary velocity components, at $\sim$59 and $\sim$84 km s^{-1} (Figure 3.6). The automated line fitter determined that a 2-component fit is required for all H α transitions and for nearly all H β and He α transitions. Of the 25 unblended H α - γ transitions for which the automated fitting routine used a 2-component fit, it obtained a mean velocity of 58.9 ± 0.8 km s^{-1} and width 28.7 ± 1.1 km s^{-1} for the low velocity component and a mean velocity of 84.7 ± 0.8 km s^{-1} and width 27.2 ± 1.2 km s^{-1} for the high velocity component. The best fits to the composite averaged spectra of H α and H β transi-

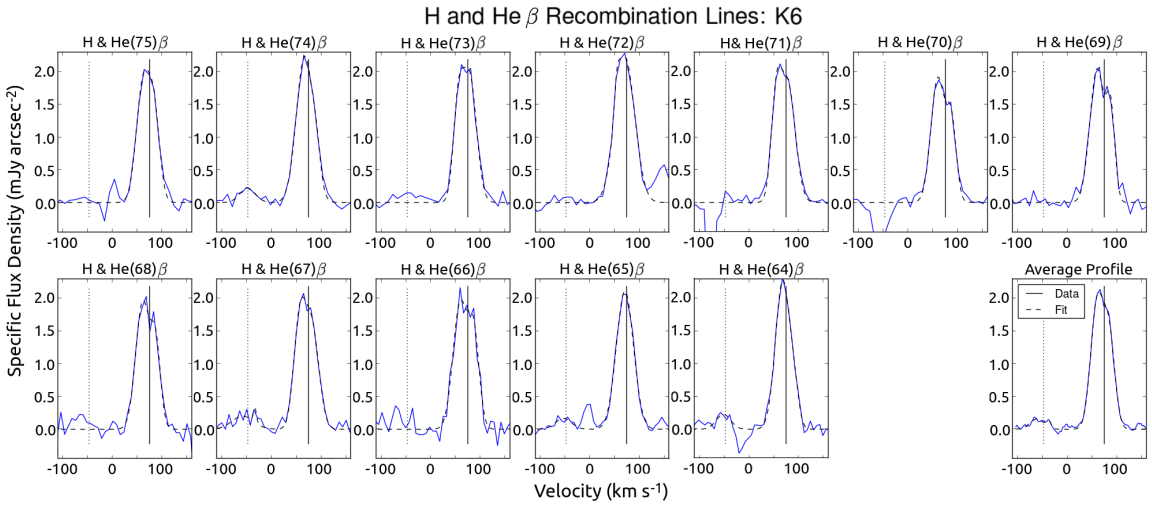

Fig. 3.7 – Hydrogen and Helium β recombination lines towards K6. Profiles of the H(75) - H(66) β transitions, extracted from high spatial resolution data, show a double peaked profile, whereas the H(65) and H(64)β transitions are well fit by a single component. The averaged profile is best fit by a Gaussian centered at 60 km s^{-1} and a weaker component at 84 km s^{-1}. The solid and dashed vertical lines represent the H and He β transitions at 75 km s^{-1} respectively.

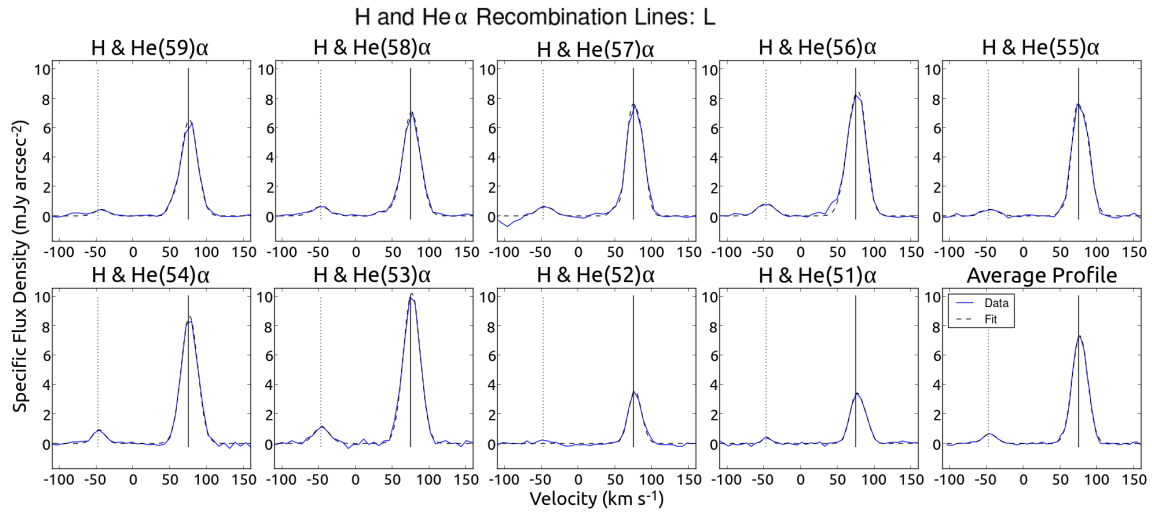

Fig. 3.8 – Hydrogen and Helium α recombination lines towards L are best fit by a Gaussian at 76.5 km s^{-1}. The solid and dashed vertical lines represent the H and He β transitions at 75 km s^{-1} respectively.

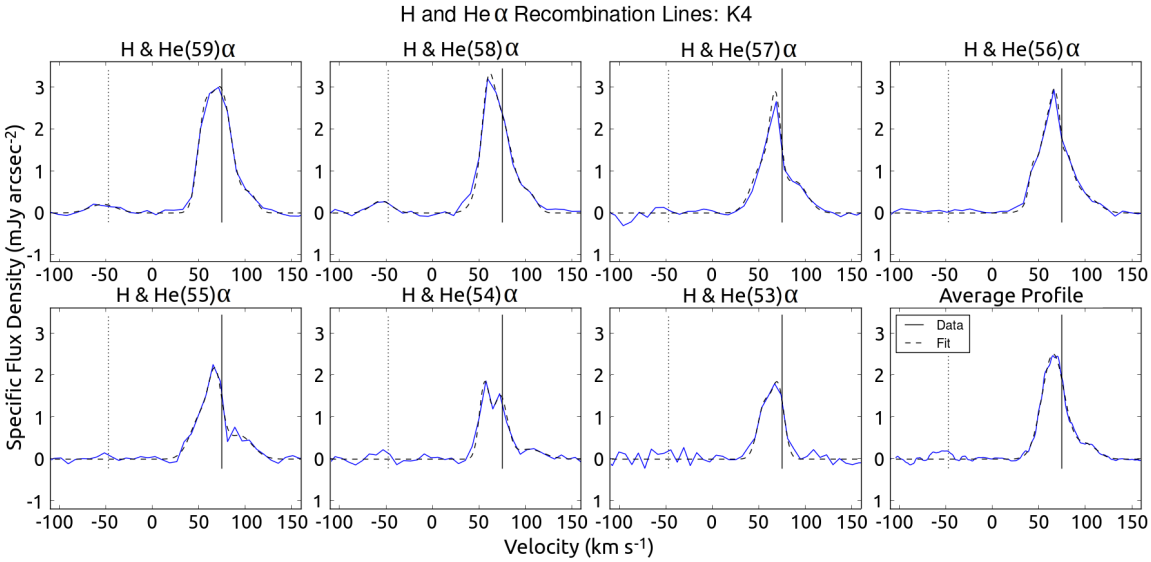

Fig. 3.9 – Hydrogen and Helium α recombination lines towards K4 show unusual line shapes that are highly sensitive to the spatial resolution of the image from which they were extracted. The lines are typically best fit by two primary components. In addition, a weaker wing component appears at $\sim$100 km s^{-1}. The solid and dashed vertical lines represent the H and He β transitions at 75 km s^{-1} respectively.

Table 3.3 – Best fits to the composite average of recombination line transitions. The errors quoted are from the diagonal terms of the covariance matrix. However, the matrices contain significant covariance terms, causing the error to be highly overestimated. Fits to the composite average of Hα and Hβ transitions agree to a precision that is significantly smaller than the covariance matrix output.

Species	Gaussian Component 1			Gaussian Component 2			Height Ratio
	Height (mJy arcsec^{-2})	Velocity (km s^{-1})	Width (km s^{-1})	Height (mJy asec^{-2})	Velocity (km s^{-1})	Width (km s^{-1})	H_1/H_2
K6:							
H α	7.1±1.0	59.3±3.1	28.0 ±3.9	5.7 ±1.1	83.6±3.7	27.0±4.4	1.37
H β	1.9 ± 1.2	59.7 ± 17	30.0 ± 24	1.4 ± 1.9	84.2 ± 20	27.2 ± 21	1.25
He α	0.67 ± 0.28	60.7 ± 10	23.5 ± 21	0.51 ± 0.35	85.6 ± 12	19.8 ± 23	1.31
L:							
H α	7.3 ±0.3	76.6 ±0.4	24.9 ±1.0				
H β	2.0 ±0.3	76.5 ±1.6	25.3±3.8				
He α	0.63 ± 0.27	76.1 ± 4.8	22.4 ± 11				
K4:							
H α	2.5 ± 0.3	65.0 ± 2.5	28.4 ± 5.8	0.35 ± 0.26	100.3 ± 17	27.8 ± 44	7.1

Table 3.4 – Mean parameters and standard errors of fits to Hα - γ transitions. Parameters are calculated from 1-component fits towards L, 2-component fits towards K6, and 1-component fits towards K4.

Region	Number of Fits	Gaussian Component 1		Gaussian Component 2		Height Ratio
		Velocity ($\mathrm{km\,s^{-1}}$)	Width ($\mathrm{km\,s^{-1}}$)	Velocity ($\mathrm{km\,s^{-1}}$)	Width ($\mathrm{km\,s^{-1}}$)	H_1/H_2
K6	25	58.9 ± 0.8	28.7 ± 1.1	84.7 ± 0.8	27.2 ± 1.2	1.36 ± 0.10
L	26	76.3 ± 0.2	26.3 ± 0.7			
K4	14	66.2 ± 0.5	32.1 ± 1.4			

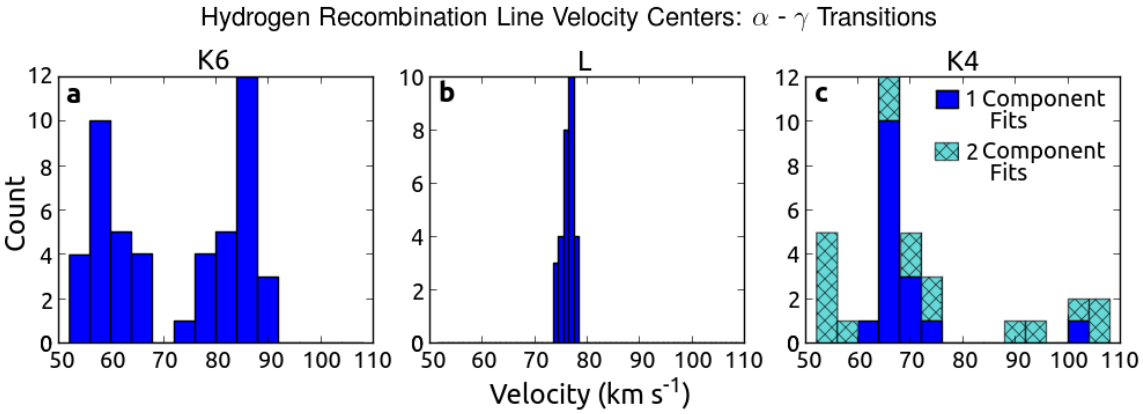

Fig. 3.10 – Velocity center of H α - γ transitions fit towards L, K6, and K4. **a.** includes transitions towards K6 that were fit with 2 Gaussian components; **b.** includes unblended transitions towards L; **c.** includes all transitions towards K4. Components with $v > 80$ $\mathrm{km\,s^{-1}}$ towards K4 are fitting a high velocity wing that is not a primary components of the line profile.

tions are both consistent with these parameters (Table 3.3). As explored in Chapter 4, the line shapes are sensitive to the spatial resolution, due to the spatial and kinematic structure present in the data cubes. As is evident in Figures 3.6 and 3.7, hydrogen recombination transitions at higher spatial resolution, (namely the H(56) - (53)α and H(70) - (66)β transitions) have more pronounced double-peaked line shapes than the moderate resolution transitions (H(59) - (57)α and H(75) - (71)β), which in turn are more double-peaked than the lowest resolution transitions (H(52) - (51)α and H(65) - (64)β).

Towards L, the automated line fitting routine detected 52 hydrogen transitions from H α to H ζ and 8 He α lines. As is evident in Figure 3.8, higher specific flux densities are observed in the high resolution data, which covers the H(59) - H(53)α transitions, due to the effect of the varying beam size discussed in §3.3.1. The automated line fitting routine typically fit each recombination line with a single Gaussian. Of 26 unblended 1-component H α - γ lines detected by the automated fitting routine, the mean center velocity is 76.3 ± 0.2 km s^{-1} and width is 26.3 ± 0.7 km s^{-1}, consistent with the Gaussian fit to the composite average spectrum of H α lines (Table 3.3). Towards L, De Pree et al. (1995) reported a recombination line velocity of 75.8 ± 0.3 km s^{-1} and width 31.7 ± 0.7 km s^{-1}, so that the line widths in particular somewhat disagree with the ATCA data. This is a result of the differences in spatial resolution. In the ATCA observations, L appears as a single unresolved source; on the other hand, the higher spatial resolution observations in De Pree et al. (1995) treat L and L13.30 located $\sim$3 arcsec E as separate sources. Towards L13.30, de Pree et al. obtain a velocity of 76.5 ± 1.2 km s^{-1} and width 20.6 ± 2.8 km s^{-1}. Our line parameters are intermediate between those of the two unresolved sources.

Recombination lines are weaker towards K4 compared to K6 and L. As a result, primarily H α - γ transitions were detected (24 total) and only two He α transitions were detected. As is apparent in Figure 3.9, the line profiles suggest a wing on the high velocity side of

the line center, near 100 $\mathrm{km\,s^{-1}}$. Of the seven H α transitions from 30 - 44.6 GHz, only H(56)α is known to be blended. Of the remaining six H α transitions, four required a 2-component fit to the line emission from 40 - 80 $\mathrm{km\,s^{-1}}$ (Figures 3.9 and 3.10). The other two H α transitions (namely H(57) and H(55)α) did not meet the criteria for 2-component fits, but 2-component fits appear more appropriate and the reported fits are adjusted from the output of the line fitter. The H α line shapes appear to vary substantially towards K4, suggesting a complex kinematic structure resulting in a line shape that is sensitive to the beam size and precise placement of the elliptical region. This is further discussed in the following chapter.

Although most of the H α transitions required a 2-component fit (primary) and a weaker component in the high velocity wing (secondary), the composite line profile is adequately fit by 1-component primary Gaussian fit at 65 $\mathrm{km\,s^{-1}}$ and a weaker wing component (secondary) on the high velocity side at 100 $\mathrm{km\,s^{-1}}$, as reported in Table 3.3. Using fits to H β and H γ lines determined by the line fitter, we find that a 1-component treatment of the recombination lines towards K4 has a velocity center of 66.2 ± 0.5 $\mathrm{km\,s^{-1}}$ and width of 32.1 ± 1.4 $\mathrm{km\,s^{-1}}$. The values we determine are in mild disagreement with those reported by De Pree et al. (1995), who report a velocity of 63.9 ± 0.8 $\mathrm{km\,s^{-1}}$ and a width 36.0 ± 1.9 $\mathrm{km\,s^{-1}}$. This may be because we are looking at different regions of K4. We determined the shape and placement of the elliptical region towards K4 based on the continuum structure as sampled at 40 GHz by the ATCA, which is offset by $\sim$1 arcsec SE of the continuum peak at 22 GHz observed by De Pree et al. (1995). This is, again reflecting a complex kinematic structure, with a kinematic gradient across the K4 HII region; this effect can be accounted for the image data presented in the following chapter.

Molecular Line Kinematics in Sgr B2

Towards all three regions, molecular lines were typically detected at two primary velocity components separated by $\sim$20 km s^{-1}. Figure 3.11 shows a histogram of the 25th - 90th percentile Gaussian fit parameters of identified molecular lines, and Table 3.5 presents the mean fit parameters, characterizing the kinematic structure of molecular gas towards these positions.

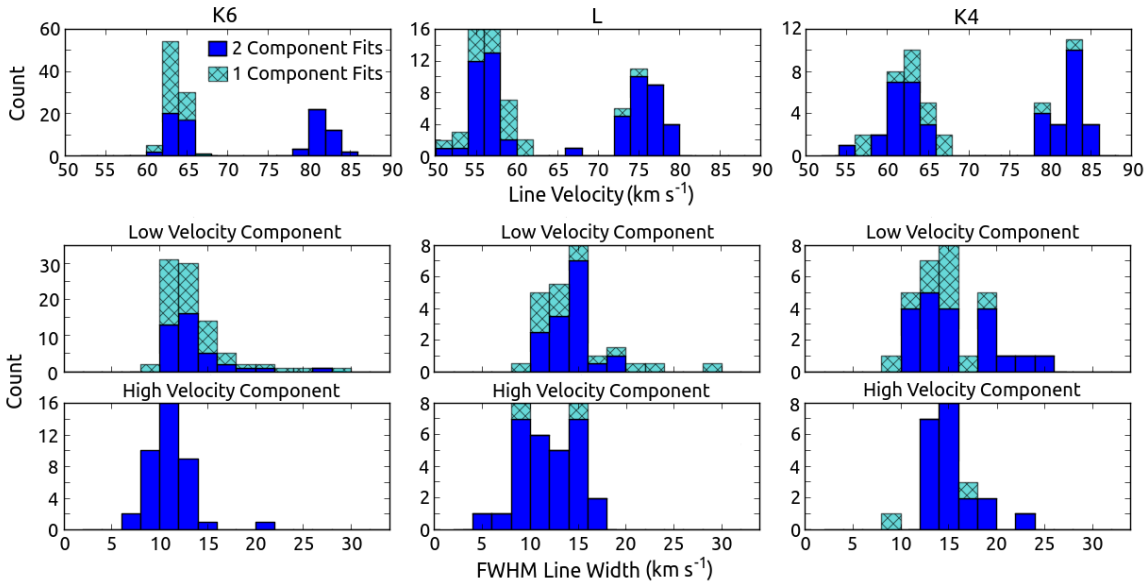

Fig. 3.11 – Kinematic parameters of molecular line fits output by the automated line fitter. 1-component fits shown include fits with a signal-to-noise ratio in the 25th to 90th percentile of all unblended 1-component fits. 2-component fits shown include unblended transitions in which the low velocity component has a signal-to-noise ratio in the 25th to 90th percentile of the low velocity components of all 2-component lines.

Error Estimation

While many sources of error exist, calibration errors (including absolute flux calibration and amplitude error from gain calibration) are small and fairly independent of frequency and position. The main sources of error with which we are concerned include:

Table 3.5 – Kinematic measurements of molecular gas towards K6, L, and K4 from lines in the 25th - 90th percentile signal-to-noise ratio.

Region	Low Velocity Component			High Velocity Component			Height Ratio*
	N Fits	Velocity ($\mathrm{km\,s^{-1}}$)	Width ($\mathrm{km\,s^{-1}}$)	N Fits	Velocity ($\mathrm{km\,s^{-1}}$)	Width ($\mathrm{km\,s^{-1}}$)	H_1/H_2
K6	90	63.5 ± 0.1	13.1 ± 0.3	39	81.9 ± 0.2	11.0 ± 0.3	3.2 ± 0.3
L	47	56.3 ± 0.2	14.1 ± 0.4	29	75.9 ± 0.3	12.0 ± 0.6	1.6 ± 0.3
K4	30	61.8 ± 0.5	14.9 ± 0.7	20	82.0 ± 0.5	15.3 ± 0.6	1.0 ± 0.1

*The height ratio is determined from lines that have both a high and low velocity component.

1. Spectral lines that are barely, or in some cases not, Nyquist sampled have poorly constrained Gaussian line parameters. While the precision of line center and width measurements are obviously limited, this introduces a $\sim$10 - 15% uncertainty to the line height. We adopt a 12.5% error to the line height for unblended lines. It additionally introduces substantial covariance in the fit parameters of 2-component lines that are not well resolved. This applies to the 2-component recombination lines towards K6 and K4 and to molecular lines that are broad due to saturation or blended hyperfine components.

2. The baseline uncertainty, typically of order 0.05 mJy $\mathrm{arcsec^{-2}}$, can increase the number of false detections and affect the best-fit Gaussian shapes. While we minimized the baseline residual using a Hodrick-Prescott filter (Hodrick & Prescott 1997), it is impossible to obtain a fully residual-free baseline, and the remaining baseline can affect low signal-to-noise transitions significantly. This contributes uncertainty in line heights and can artificially broaden the best-fit Gaussian. As discussed in §3.2, we minimize the latter effect by fitting only the region within 0.8 $\times$ FWHM of line center.

3. Frequency-dependent variations in noise level in data from a single spectral tuning can generate false detections. Noise can also contribute significantly to error for low signal-to-noise detections, particularly because the data is not Nyquist sampled.

4. The spectrum extracted from a region can contain flux generated at a different spatial position in low spatial resolution data. This applies primarily to the low spatial resolution data (from 44.6 - 50.2 GHz) in the spectrum of K6, which contains flux arising in the LMH and "h". This effect is discussed further in Appendix B.

5. Towards the three regions that we characterize in this work, we observe molecular gas with two primary kinematic components separated by $\sim$20 km s^{-1}. For a few low signal-to-noise transitions, the data does not significantly disagree with a single Gaussian profile, so the line fitting routine returns a single fit at a velocity that is intermediate between the two velocity components. We indicate fits for which we suspect this has occured with "BC" for blended components. In these cases, the Gaussian parameters are unreliable, but the qualitative statement of transition detection stands. As a primary aim of the study is to demonstrate the functionality of the line fitting code, we correct few instances of this. However, researchers interested in the separate contributions from the two gas cloud components should re-fit these with the velocities and widths fixed to the mean values determined by the scripts.

Because there are many sources of uncertainty and a large number of lines detected in the survey, the simplest method for evaluating the error is to derive it from the fits themselves. To do so, we assume that line radiation from all thermal molecular line transitions originates at a consistent set of central velocities for each targeted spatial region, setting an upper limit on the typical error of fits. With very few high signal-to-noise exceptions, this assumption is supported by the data, as typical differences from the mean center velocity are significantly smaller than the channel widths of 6 - 10 km s^{-1}.

Using molecular line transitions with signal-to-noise ratios (determined as the ratio of the Gaussian fit height to the noise level in the extracted spectrum) in the 25th - 90th percentile range, we determine the standard deviation of the line velocity centers and widths.

The 25th - 90th percentile range excludes the strongest lines which typically have wing broadening and the weakest quartile (with a signal-to-noise ratio $\lesssim 5.4$) which is preferentially affected by baseline issues and noise. The distributions of velocity centers and line widths towards all three regions is shown in Figure 3.11. Using 129 unblended transitions towards K6 that fall in our target signal-to-noise window (including 51 1-component transitions and 39 2-component transitions) we determine the standard deviation of the center velocity to be $\sigma_v = 1.1$ km s^{-1} and the standard deviation of the velocity width to be $\sigma_{\Delta v} = 2.3$ km s^{-1}. The standard deviations of both parameters are significantly lower than the channel resolution of 6 - 10 km s^{-1}, indicating that the method performs rather well given the limits of the dataset. We adopt $\sigma_v = 1.1$ km s^{-1} and $\sigma_{\Delta v} = 2.3$ km s^{-1} as 1σ errors on the fit parameters of 1-component lines and spectrally resolved 2-component lines with a signal-to-noise ratio $>$5.4. This includes unblended 1- and 2-component molecular lines and 1-component recombination lines. These values are consistent with the standard deviations of the parameters fit to high signal-to-noise recombination lines towards L (Figure 3.10 b), further justifying their validity.

For 2-component recombination lines in which the components are not spectrally resolved, we determine $\sigma_v = 3.6$ km s^{-1} and $\sigma_{\Delta v} = 4.9$ km s^{-1} from 17 H α and β lines towards K6, and line height errors of each component are estimated at $\sim$25%. Compared to molecular lines, 2-component recombination lines have larger errors because the two velocity components are poorly resolved, having line widths in excess of the velocity separation by $\left(\frac{\Delta v_1 + \Delta v_2}{2} > v_2 - v_1\right)$. While a 1-component fit does a poor job of matching these profiles, a 2-component fit contains significant covariance between the six fit parameters. Errors of the velocity center and width are approximately 40% higher for 2-component Hγ and δ lines, and the line heights have a $\sim$40% estimated error.

Table 3.6 summarizes the errors of the fit parameters that are adopted in this work and recommended for further use of the ATCA results. Because the errors are significantly smaller than the channel spacing, it appears that the code produces good results. Errors could be evaluated by a similar method in other data sets. Further statistics including the false detection rate and the number of fits that were poor or required adjustment are provided in the Appendices to this chapter.

Table 3.6 – Recommended errors to fits to the ATCA data output by the automated line fitter.

Line Type	S:N Regime	σ_v ($\mathrm{km\,s^{-1}}$)	$\sigma_{\Delta v}$ ($\mathrm{km\,s^{-1}}$)	σ_{Height} (%)
2-Component Recombination Lines				
Primarily H α & H β	S:N $>$15	3.6	4.9	25
Primarily H γ, H δ & Heα	5 $<$ S:N $<$ 15	5.0	6.9	40
1-Component Recombination Lines	S:N $>$5.4	1.1	2.3	12.5
1- & 2-Component Molecular Lines	S:N $>$5.4	1.1	2.3	12.5

3.4 Application to GBT PRIMOS Data from 4 - 6 GHz

To further test the performance of the scripts, we applied them to C-Band data collected with the GBT with higher spectral resolution of 1.5 $\mathrm{km\,s^{-1}}$, sufficient to resolve the features. We do not provide an analysis of the line kinematics and errors, but can comment that the typical center velocities and line widths obtained are similar to the results of the ATCA data. The center velocities of line absorption features are at $\sim$64 and $\sim$82 $\mathrm{km\,s^{-1}}$, similar to what was observed towards K6 and K4, while FWHM line widths of 15 - 20 $\mathrm{km\,s^{-1}}$ are observed in the low velocity component and widths of 10 - 15 $\mathrm{km\,s^{-1}}$ are observed in the high velocity component. We provide figures showing the full C-Band spectrum (Figures 3.12 - 3.16) with the fit overlaid and line identifications annotated. As we have tested the performance at 4 GHz and at up to 50 GHz on data sets with quite different spectral resolutions, the code appears to be robust at centimeter wavelengths. Thus,

the criteria established for determining whether a 1-component fit is adequate for a feature or whether a 2-component fit is required, as well as the algorithm for selecting an optimal range to consider for the fit both appear to be robust.

3.5 Limitations to Code Applicability

To date, the code has not been tested on deep spectral surveys at higher frequencies (mm, sub-mm, and THz frequencies), particularly in sources like Sgr B2 with high molecular diversities. Many higher frequency surveys are confusion-limited rather than noise limited, so that the code must handle many overlapping components. It is quite possible that the algorithm will perform well under these conditions as written. It is also possible that the code might need to be adjusted in order to fit a larger number of Gaussians simultaneously. Fitting a higher number of Gaussians is trivial in theory; however it would be challenging to establish a set of criteria by which the code determines whether a 2-component fit is sufficient or if a 3-component, or perhaps a 4-component fit is needed. Clearly, this could take us down a rabbit hole leading to over-fitting data. Thus, we prefer to fit no more than two components simultaneously, and instead prefer to adjust the sensitivity limit considered for the fit. For some highly complex line profiles in the ATCA data, the fit results are not closely representative of the source kinematics. We expect that the code will perform well at higher frequencies, returning an accurate characterization of the source kinematics and line identities, if the specified detection threshold is greater than the confusion limit. With a lower detection threshold, the kinematics returned for weaker lines may not be reliable, however it may still be useful for line-identification.

Additionally, the line fitter applies only Gaussian shapes to the line fits. For sources with common self-absorption or P Cygni profiles, the line identifications should perform reasonably, while the measurements of the source kinematics may not be reliable. Ob-

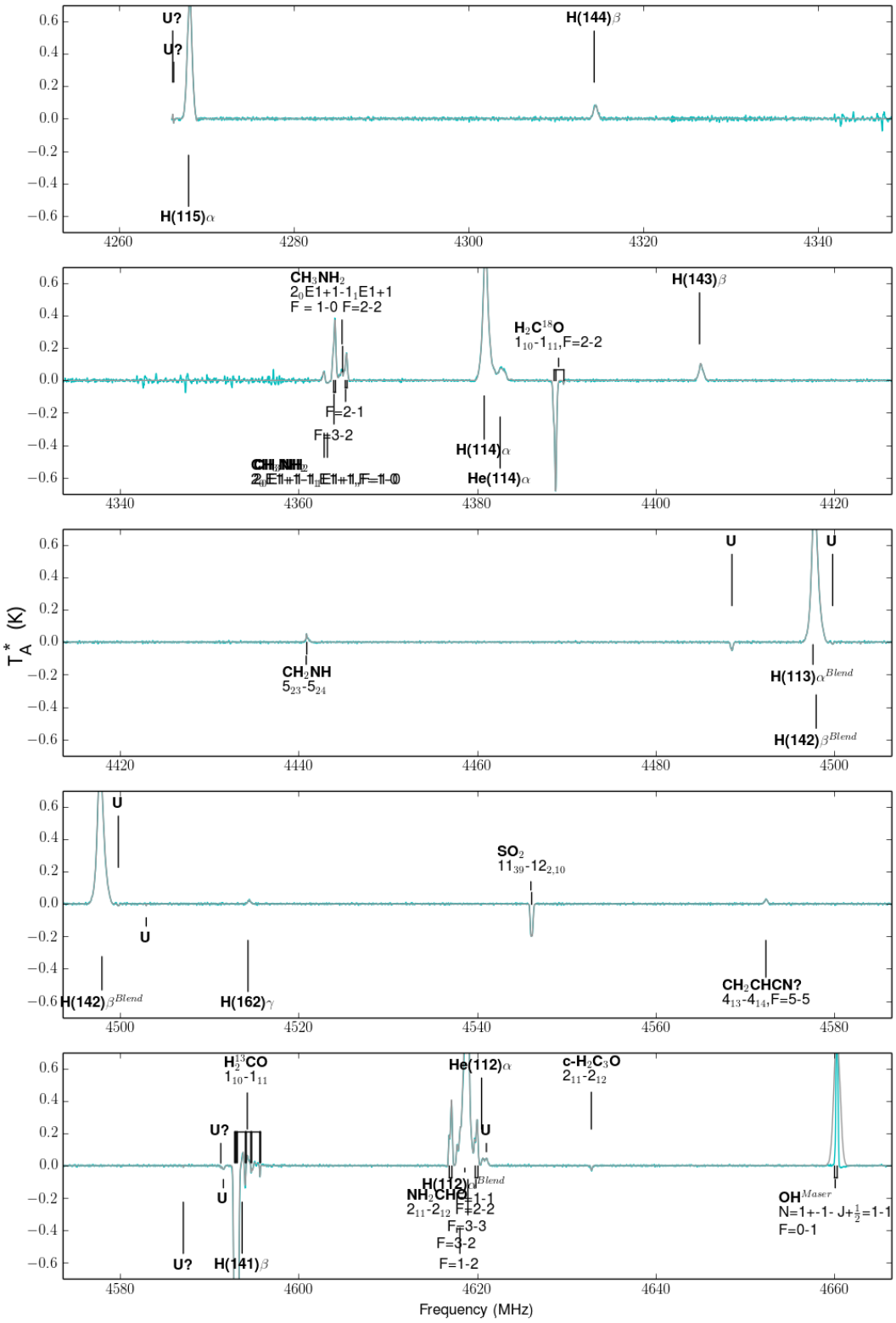

Fig. 3.12 – The C-Band spectrum from PRIMOS data with line identifications labeled and the output of the automated line-fitter overlaid.

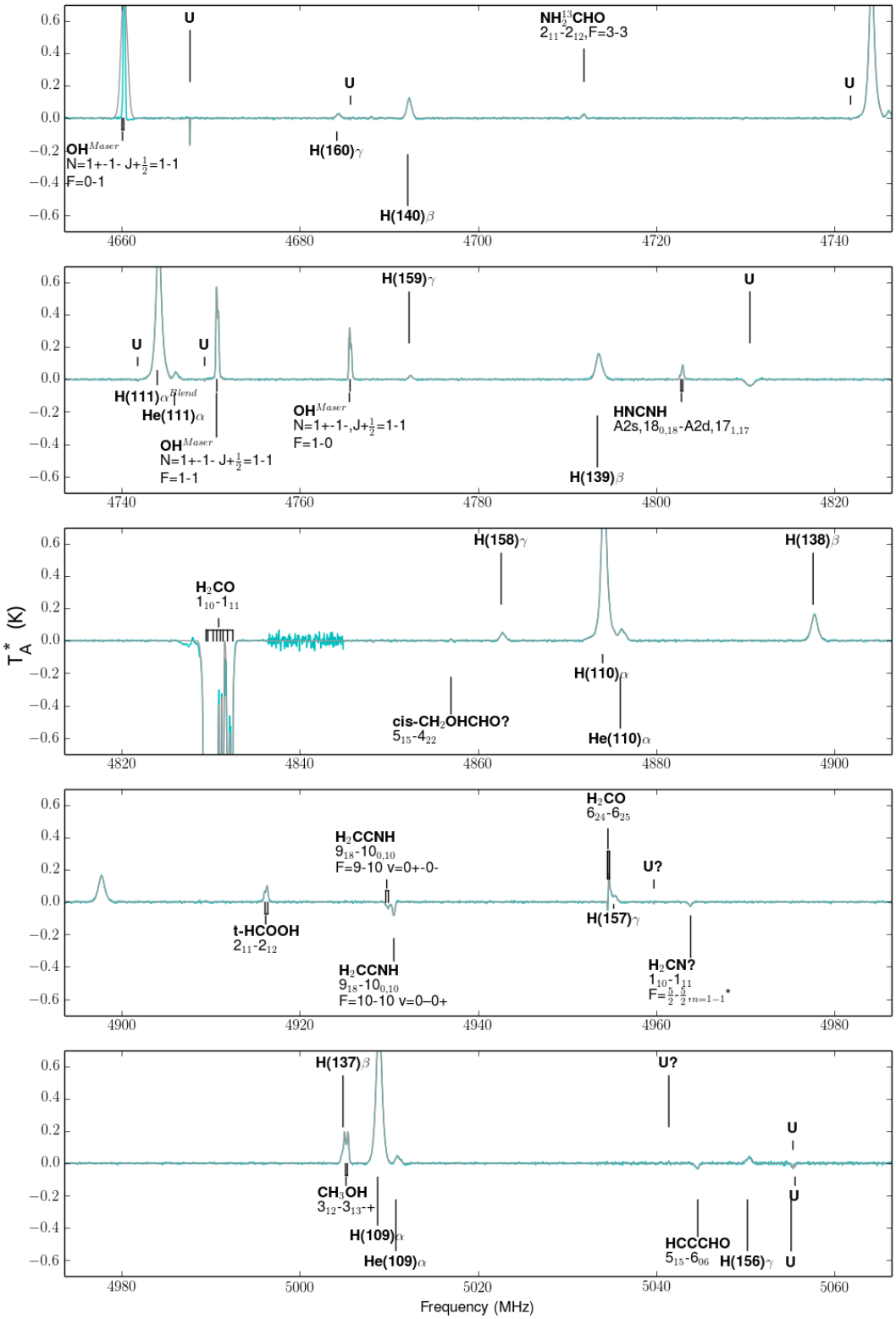

Fig. 3.13 – The C-Band spectrum from PRIMOS data with line identifications labeled and the output of the automated line-fitter overlaid.

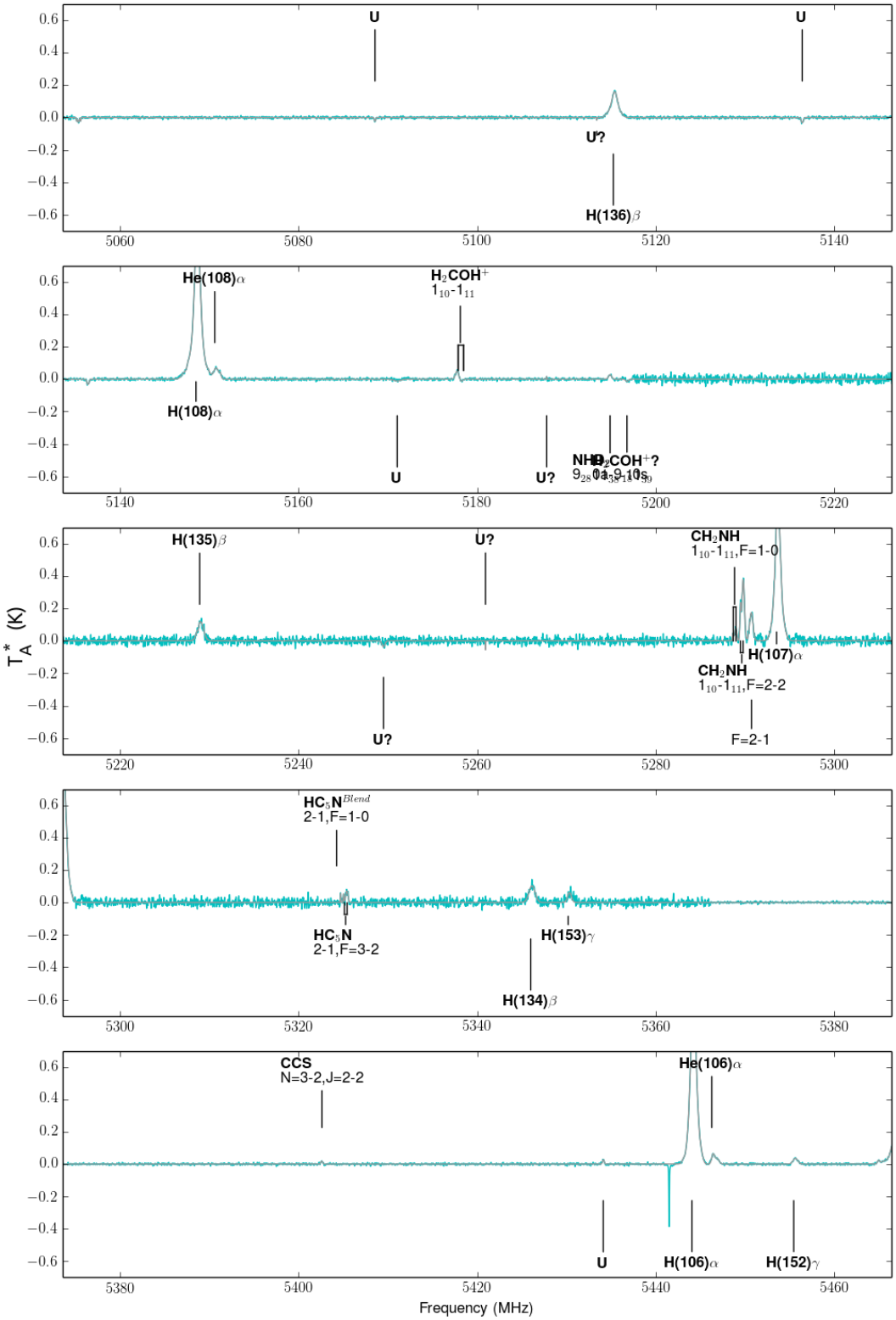

Fig. 3.14 – The C-Band spectrum from PRIMOS data with line identifications labeled and the output of the automated line-fitter overlaid.

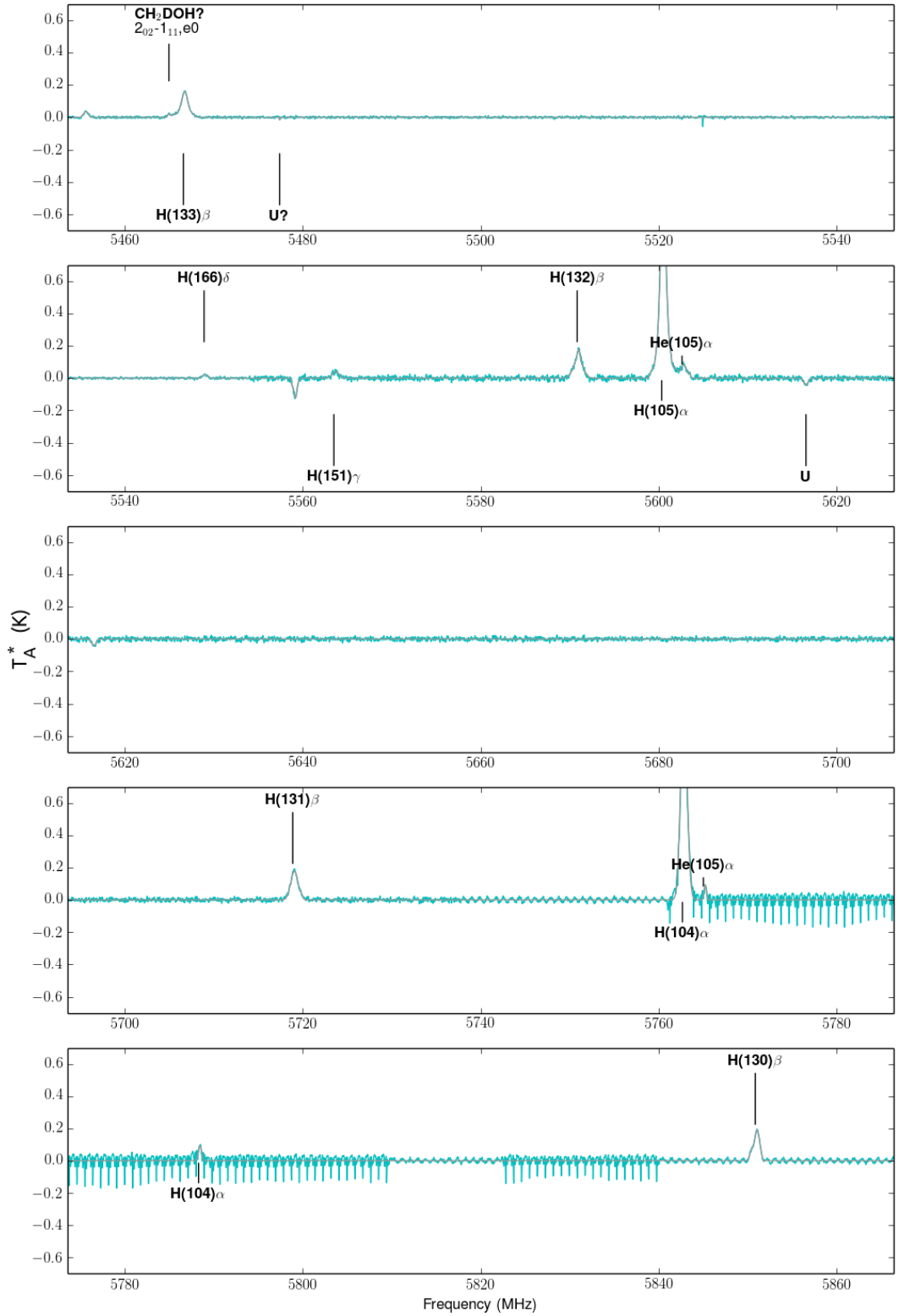

Fig. 3.15 – The C-Band spectrum from PRIMOS data with line identifications labeled and the output of the automated line-fitter overlaid.

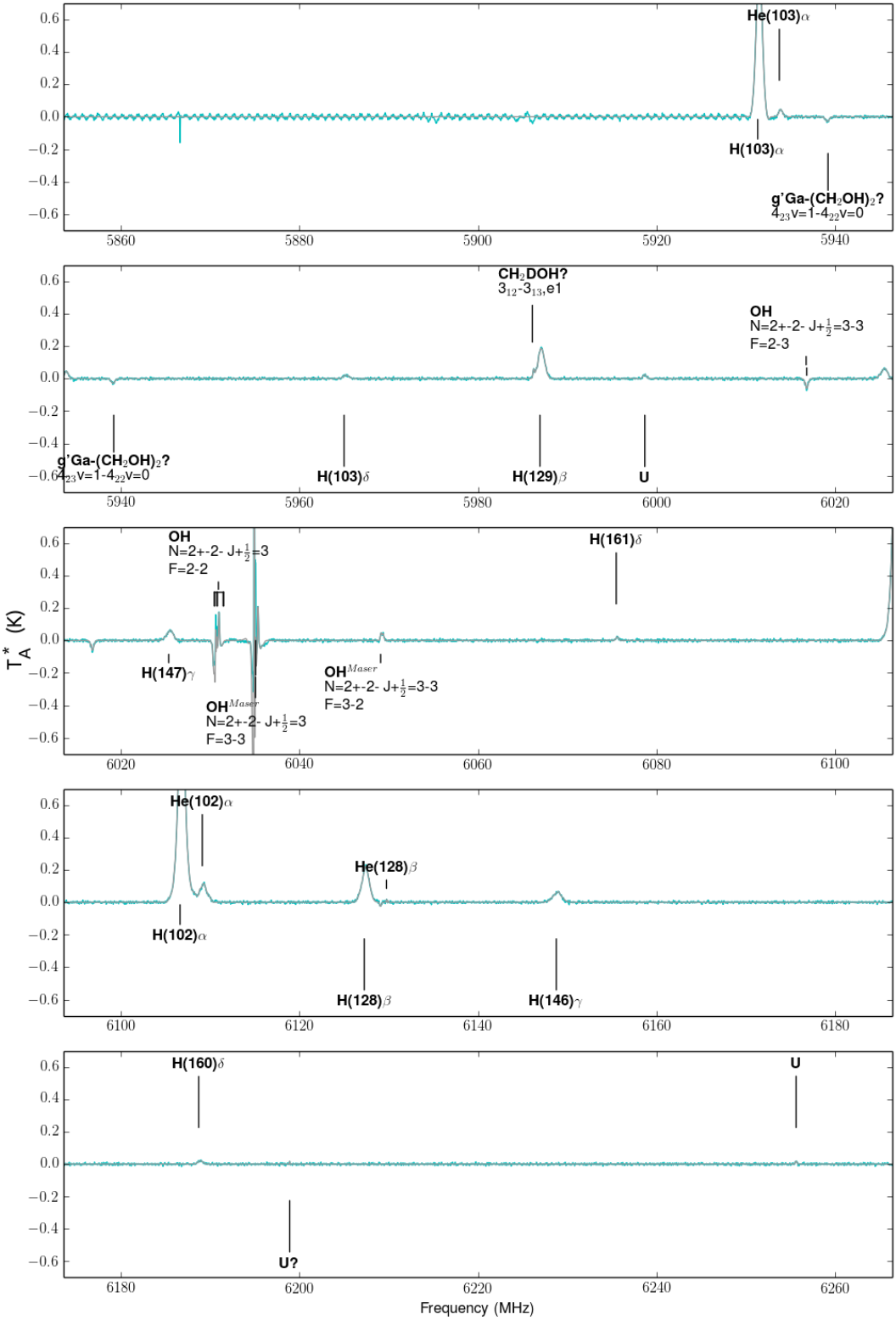

Fig. 3.16 – The C-Band spectrum from PRIMOS data with line identifications labeled and the output of the automated line-fitter overlaid.

viously, this depends on the shape of the profile, including the relative widths of the absorption and emission components. The fitter would also not be appropriate for sources characterized by pronounced two-horned profiles, although it would be reasonably straightforward to adapt the fitter to allow for a two-horned profile.

3.6 Future Directions

Full spectral characterizations are requisite for correctly interpreting data cubes, and ideally, this or a similar code could interface with the data cubes directly. Up to this point, the ATCA data have been inspected only via these few extracted spectra. One could imagine applying a similar system to every pixel of the data cubes, or to improve the sensitivity, to the mean spectrum within a beam-sized region around each pixel.

To first demonstrate the importance of the full spectral characterization for even simple analyses of data cubes, we consider the construction of momemt images in the case of Sgr B2. For Sgr B2 and other sources with complex chemistry, multiple physical environments and complex kinematic structures, moment 0 (integrated intensity), moment 1 (center velocity), and moment 2 (line width) images can misrepresent the data if constructed naively. Moment 1 and moment 2 maps are particularly difficult for transitions with multiple kinematic components, particularly if the kinematics shift over the field. A moment 1 map of a line in the ATCA data, for example, would return neither +64 nor +82 $\mathrm{km\,s^{-1}}$ over most of the absorbing gas, but an intermediate velocity, unless we isolated only the radiation from a single component. If for instance, we hoped to make a moment 1 image of the low velocity gas, it would not be possible to make a single moment 1 image that includes both L and Sgr B2(N) due to the shifted velocity field. This is also problematic for moment 0 images. For example, it is not particularly meaningful to show a moment 0 image over a velocity range that contains multiple distinct velocity components with different chemical environments,

as this would not be representative of the line radiation in either environment. Furthermore, if we wish to make a moment 0 map from a molecular line detected in the absorbing gas, a moment 0 map constructed naively may contain line radiation produced in the hot core by a different molecule entirely, and thus will not be representative of the transition distribution. The problems become even more complicated for lines with hyperfine structure.

However, these problems could be addressed by interfacing code the full-spectral characterization code with the data cubes. With a simple interface, the code would at minimum point out where it is and is not fair to construct moment images. Moreover, it would offer the possibility of constructing images of the fit solutions. This would enable filtering of interloping lines and correctly accounting for the radiation from a specific component. One can imagine cataloguing the identifications in a way that it could be straightforward to view moment images of multiple transitions of a single molecule, or to perform stacking for molecules with very weak transitions.

Whether the code featured here or code of a different composition is interfaced with the image plane, these issues must be tackled in order to utilize even a reasonable fraction of the data produced by new-generation radio interferometers; automation will be critical for obtaining a comprehensive view of astrochemistry.

3.7 Conclusions

We developed spectral line fitting and line identification scripts written in PYTHON. While the scripts can be applied over narrow frequency ranges, they are capable of handling broadband data to provide a full spectral characterization. The code provides purely empirical results rather than comparing with a model, as this was deemed most appropriate at centimeter wavelengths where line radiation is often nonthermal, and performs line identification by comparing with output generated by Splatalogue or another line catalog after

minor formatting. The code is described in §3.2, released in Appendix A, and available at https://github.com/jfc2113/MicrowaveLineFitter and in the supplemental material to Corby et al. (2015).

The code was applied to spectra towards Sgr B2(N), as observed at 4 - 6 GHz with the GBT and at 30 - 50 GHz with the ATCA. In the ATCA data, the scripts were thoroughly tested on spectra extracted from three unique spatial positions, namely K6, L, and K4, characterized by recombination line emission and molecular line absorption at multiple velocity components. The performance of the code was evaluated based on the handling of 65 recombination line profiles and 90 molecular absorption lines, observed against the free-free radio continuum emission. Typical errors on the fits were significantly lower than the channel width in this survey. Approximate errors are summarized in Table 3.6.

While we have not thoroughly analyzed the output of the scripts applied to the 4 - 6 GHz GBT data, we have demonstrated that the kinematics output are consistent with the source kinematics derived from the ATCA data. The fits appear quite reasonable, showing that the algorithms are appropriate when applied over a broad range in frequencies, from 4 to 50 GHz. The code has not yet been tested on high frequency data to determine its utility at the millimeter, sub-mm, and THz wavelengths observed by ALMA.

Future development may include interfacing the code with 3-dimensional data cubes, in order to determine spatial patterns in kinematics, excitation, and chemistry with high number statistics.

3.8 Appendix A: Automated Line Fitter Code Release

All scripts used for automated line fitting and semi-automated line identification are provided in GitHub at https://github.com/jfc2113/MicrowaveLineFitter and in the online supplemental material to Corby et al. (2015). Here, we provide instructions for use includ-

ing a description of the input and output files and system requirements.

The scripts have been tested in IPYTHON version 0.12.1 with PYTHON 2.7.3, NUMPY 1.6.1, and MATPLOTLIB 1.1.1rc. PYTHON 2.7.3 includes the MATH and CSV modules that are used in the scripts.

The packaged file provided in the journal includes eight scripts, spectra characterized in this work, and csv files holding line data. Two of the scripts are run directly, namely 'FullCode.py' is run before 'VelocityFileMaker.py'. After optional adjustments by the user, 'VelocityFileMaker.py' uses the output of 'FullCode.py' to generate a final csv file that contains Gaussian fits to the full spectrum and line identifications. Of the remaining six scripts, five contain modules called in 'FullCode.py'. The modules and their primary purposes include:

- 'LineFind.py' grabs segments of the spectrum that contain lines, detecting "line-channels" with single-channel intensity values greater than $\sigma_{rms}\times$ an input threshold. The module also selects a set number of channels on either side of line-channels. The number of neighboring channels has a default value of 5, but can be adjusted when LineFind is called.

- 'FTinterp.py' interpolates a segment of the spectrum, outputting a spectrum with a factor of 3 improvement in the spectral resolution. It performs the interpolation by Fourier-domain zero padding. This should only be used for data with poor spectral resolution compared to the linewidths.

- 'Gfit.py' provides the most essential functionality; through 'FullCode.py', the function Gfit.GauFit is passed a single segment of the spectrum that contains one or more lines. Gfit.GauFit returns a 1- or 2-component Gaussian fit to a spectral feature within the segment. The script selects a specific portion of the line-containing segment and first attempts a one-component fit. It then follows an algorithm to adjust the section

of the segment used for line-fitting and re-fit 1-component Gaussians. It passes information to 'G2criteria.py', which evaluates the fit against a set of criteria to determine whether a 2-component Gaussian fit is justified. The output of G2criteria determines whether Gfit.GauFit fits a 2-component Gaussian, following an algorithm to adjust the section used for line-fitting and attempting 2-component Gaussian fits.

- 'G2criteria.py' determines if a 2-component Gaussian fit is required. Gfit.GauFit provides G2criteria with information about the data and the best 1-component Gaussian fit achieved; G2criteria then determines if the data differs significantly from the 1-component fit, requiring a 2-component fit. G2criteria takes into account the signal-to-noise ratio of the line in question and the degree to which the data differs from the 1-component Gaussian fit. The primary factors considered include (1) the difference between the position of the absolute maximum of the data and the position of the 1-component Gaussian center; (2) the maximum residual between the data and the fit, compared to the rms noise level at that frequency tuning; (3) the mean residual between the data and the fit, compared to the rms noise level; (4) the width of the fit compared to the typical width of features. The criteria, mostly empirically determined, works very well for the two data sets described here. However, we advise inspecting results obtained on other datasets carefully and adjusting the criteria if needed, as they may change with the parameters of the data.

- 'LineID.py' provides semi-automated line identification of features fit over the full spectrum. FullCode compiles the output of Gfit.py and passes it to LineID, along with one or two csv files containing spectral line catalog data. The input csv files can quickly and easily be output from the ALMA Spectral Line Catalogue - Splatalogue[2] after selecting a set of molecules that might appear in your spectrum.

[2] Available at www.splatalogue.net; Remijan et al. (2007)

FullCode manages the full data spectrum, compiles the results of Gfit.GauFit, and calls LineID to output the data. All of the modules except G2criteria are written to be easily tunable, and the main parameters that users will want to adjust are specified and explained in the first section of FullCode. These parameters include: whether the results should be output; what plots should be produced; the names of input files; whether data interpolation is desired; information about the source including guidelines for appropriate linewidths and line velocities; and information about the data structure (e.g. how many separate data sections are in a single spectrum; in this work, the line-fitter inspected a spectrum including 11 tunings, each of which had different σ_{rms} noise levels. If all tunings have the same noise level in the intensity units you are using, they can be treated as a single section).

FullCode requires a spectrum input in standard ascii format with frequency and baseline subtracted intensity. The file 'K6_fullSpec.txt', provided with the scripts, is in the correct format. If the user chooses to perform line identification, the script requires files containing recombination line or molecular line data output in csv format from any spectral line catalog. The line data should be formatted similarly to the files 'recombLines.csv' and 'molecularLines.csv', provided. If your source has recombination lines, we recommend preserving the file name of 'recombLines.csv', but including lines that are relevant for your frequency range. All csv files read into the code should be text csv files with UNICODE UTF-8 characters and a colon (:) as the field delimiter. The code outputs csv file data with this format as well.

FullCode plots the full data spectrum with the line fits overlaid, marking the locations of lines from the input catalogue data that are near the fit frequency centers. The code can output a csv file containing Gaussian line fits and possible line assignments. This output of FullCode is named ALLFITS_(r).csv, where (r) is the name of the source or region targeted. It contains:

- Gaussian line fit parameters (height, center frequency, and width in frequency units) of all features.

- two measures of the quality of the fit. First, the rms residual between the data and the fit; second, for 1-component fits, the file provides the offset between the frequency at which the data has its maximum absolute value and the Gaussian center frequency. Fits with abnormally large values may be suspect.

- the 'bin' indicates how the line was handled in Gfit.GauFit. Lines with bin = 0 are 1-component fits that were deemed appropriate. Lines with bin = 1 are 2-component fits that were found to be reasonable. For lines with bin = 2, the data significantly differed from the best 1-component fit obtained, however Gfit.GauFit was unable to obtain a reasonable 2-component fit and therefore used the best 1-component fit obtained. These should be inspected and possibly re-fit manually. For bin = 3 lines, the residual between the data and the fit is significantly larger than the noise level of the spectrum. These should be inspected and possibly re-fit manually. Bin = 5 lines are entirely unreasonable, with very broad line widths or unreasonable line heights. They are used as placeholders to enable the code to proceed, and they will need to be re-fit. Of 617 components used to fit the spectrum towards K6, 360 have bin = 0, 242 have bin = 1, 1 has bin = 2, 12 have bin = 3, and 2 have bin = 5.

- possible atomic or molecular carriers of the detected Gaussian features. The output file lists any transitions from the input recombLines.csv and molecularLines.csv files that are within a specified velocity range of the detected features. It does not choose the most probable line at this step, but does so when the second code is run. These can be prioritized before running VelocityFileMaker.py to obtain the final line results.

Upon inspection of the results and manual updates to any bad fits, run VelocityFile-

Maker to generate a final output csv file containing line identifications and Gaussian fit parameters, with parameters listed in velocity space. VelocityFileMaker generates an output csv file entitled 'velocity_ALL_(r).csv'. The file contains line rest frequencies, species, transitions, Gaussian fit velocities, heights, widths (in velocity units), center frequencies, and line types.

Before running VelocityFileMaker, edit parameters in 'velEDIT.py'. Specify the names of the positions from which you extracted spectra, csv file input names, and velocity ranges that are appropriate for different types of lines, including recombination lines, molecular lines from the primary source, and additional lines observed in absorption by foreground diffuse or translucent clouds. The latter are only relevant in some lines-of-sight.

The code implements primarily kinematics-based consistency checks for line identifications, and can use one or two optional input csv files to prioritize line identifications. In order to minimize mis-identification, the final line-identification process operates on a priority system as follows:

- Priority 1: The code first inspects identified recombination lines for kinematic consistency and consistent line-intensities. This step requires a sufficiently large number of recombination lines to work well ($>$10 high signal-to-noise lines or $>$20 lines recommended), as it derives the mean Gaussian fit parameters and standard deviations in order to evaluate consistency. Lines that are self-consistent with the mean and standard deviations are output as firm line identifications, and assigned a "Line-Type" of either "H Recomb" or "He Recomb". The script is not presently equipped to handle carbon recombination lines or absorption by recombination lines, but could be easily adjusted to do so. Features that are inconsistent with recombination lines include absorption lines, features that are significantly more broad or narrow than the mean, features that are too far from the mean center frequency, and lines that are

significantly too strong or weak (e.g. an H γ line that is as strong as most H α lines). These may be output as tentative line identifications, which the user should inspect for line blending or data issues. If you do not have recombination lines, the code will simply move to Priority 2.

- Priority 2: The user has the option of specifying a file entitled 'strongLines.csv'. (Of course, the file name can be changed per the user's preference). The file "strongLines.csv" contains the strongest lines, which can be firmly identified prior to identifying weaker molecular lines. Lines that fall within the velocity range set in the function vEDIT.strongVrange are output as firmly identified, and assigned "LineType = strong". Verify that the first two columns of your strongLines file are formatted the same as the file included in the package.

- Priority 3: The user can use a file entitled 'SAClines.csv', which indicates which transitions that may be observed in foreground absorption by diffuse and translucent cloud material, often referred to as Spiral Arm Clouds (abbreviated SAC). The foreground absorption components are at velocities that are inconsistent with the targeted cloud, and must be constrained in VelocityEditFile. Lines that fall within the velocity range set in the function vEDIT.SACvRange are output as firmly identified, and assigned the "LineType = SAC". Verify that the first two columns of your SAClines file are formatted the same as the file included in the package.

- Priority 4: The code then assigns remaining lines tentatively assigned in ALLFITS_(r). In cases where multiple transitions are near the Gaussian center frequency, the line with the best kinematic match to the velocity, as specified in VelocityEditFile, is output. While this typically works well at centimeter wavelengths, we recommend inspecting lines that have multiple line entries in ALLFITS_(r), especially at higher

frequency. If the code gets the "wrong" answer at this point, mark the line as blended, and consider only keeping the preferred line in ALLFITS_(r)

- Priority 5: Finally, the code outputs all fits that were not firmly identified in Priorities 1-4. These are given a Line Type of "Unidentified". If a fit was associated with a known transition in ALLFITS_(r), the transition parameters will be output so that the user can decide whether or not to adopt the transition as identified.

While FullCode.py can fit most blended lines well, VelocityFileMaker does not handle identification of blended lines with much sophistication; however the prioritization system significantly improves the likelihood that most of the line radiation can be ascribed to the identified carrier transition. The user is responsible for inspecting the output of ALLFITS_(r) and velocity_ALL_(r) to ensure that any lines that may be blended (which should have multiple transitions listed in ALLFITS_(r)) are handled appropriately.

Within each priority, the script also handles wing components. As described in §3.2, numerous spectral features are non-Gaussian, including recombination lines, strongly masing lines, and optically thick molecular lines. In FullCode, in which the line fitting is conducted, after subtracting a best-fit 1- or 2-component Gaussian fits from the raw data (called the primary component(s)), high signal-to-noise lines may have wing components with intensities exceeding the detection threshold. Such wing features, which are typically weak as compared to the primary 1- or 2-component fit, are fit to the residual. VelocityFileMaker selects these features to prevent them from incorrectly being assigned to other molecular carriers or labelled as unidentified. Wing features are selected based on (1) their separation from the primary line component as compared to the width of the primary line component and (2) their height as compared to the primary line component. If a feature meets either of the following criteria, it is identified as a wing of an identified line and the velocity is calculated with respect to the rest frequency of that line. The criteria include:

1. $\frac{H_{\text{Feature}}}{H_{\text{Primary}}} < 0.22$ and $v_{\text{Feature}} - v_{\text{Primary}} < \Delta v_{\text{Primary}}$

2. $\frac{H_{\text{Feature}}}{H_{\text{Primary}}} < 0.05$ and $v_{\text{Feature}} - v_{\text{Primary}} < 1.5 \times \Delta v_{\text{Primary}}$,

for the line heights, velocity centers, and FWHM widths H, v, and $\Delta v_{\text{Primary}}$, respectively. These are assigned "LineType = wing". Within each priority, VelocityFileMaker identifies the primary components, which must be consistent with the kinematic information input, and then selects any wings associated with these lines. As such, the recombination lines and wings of recombination lines are identified, followed by designated "strong lines" and the wings of strong lines, etc.

3.9 Appendix B: Full Spectra and Line Identification Figures

The raw data spectra extracted towards K6, L, and K4 are provided with the output of the line fitter overlaid and line identifications labeled. All data are frequency shifted to the nominal source velocity of +64 km s^{-1}. The following conventions are used in all figures. Tentative identifications are noted with a '?', as are unidentified lines suspected to be artifacts. Strong masing transitions are marked with '$Maser$', blended lines are marked with '$Blend$', and line fits that have been adjusted from the output of the line fitter are marked with 'Adj'. In cases where the line-fitter determined a 1-component fit that we suspect to be a 2-component transition with insufficient signal-to-noise to be identified as such by the fitter, the species is marked with 'BC'.

For cases in which a transition has blended spectral structure (such as blended transitions of A and E states), the listed transition indicates what components are expected to be blended, with the first listed component corresponding to the state that is strongest or best matches the expected source velocity. The transition listed first sets the rest frequency in Column 1 in the table provided in Appendix C.

Recombination lines are marked at 75, 76, and 64 km s^{-1} for K6, L, and K4, respectively. Identified molecular line components are marked at the following velocity components:

K6: Primary velocity components are at 64 and 82 km s^{-1}; translucent cloud components are at 6, -30, -73, and -106 km s^{-1}.

L: Primary: 56 and 76 km s^{-1}; translucent cloud: 35, 20, -5, -35, -75, and -106 km s^{-1}.

K4: Primary: 62 and 82 km s^{-1}; translucent cloud: 2 km s^{-1}.

Tentatively identified velocity components of firmly identified transitions are marked with a dashed pointer. For lines identified in the high velocity gas but not in the low velocity gas, the low velocity component is marked with a dotted line. Figure 3.17 illustrates these conventions.

3.9.1 Notes on U-lines, Tentative U-lines, and Line Contamination

The figures and tables in Appendices B and C include firmly identified features, contamination from flux originating from other locations on the image ("contam"), tentatively identified features (marked with a "?"), unidentified lines (marked with "U" in figures and tables and referred to as U-lines), and tentative U-lines (marked with "U?" in figures and tables and referred to as "U?-lines").

Nearly all instances of line contamination are present in the spectrum of K6 and are lines that originate in the LMH or "h" hot cores. In spectra extracted from the high spatial resolution data (29.8 to 44.6 GHz), the hot cores are sufficiently separated from the elliptical region placed on K6. As a result, the line emission from the hot cores does not generate artifacts in the spectra towards the regions characterized here for frequencies $\nu < 44.6$ GHz. In this region of the spectrum, we have carefully inspected the images and spectra to verify that strong lines in the hot cores do not have imaging artifacts including negative bowls that are detected in K6, K4, and L. In the spectra extracted from the low resolution data (towards K6 and L), no imaging artifacts are observed towards L, while 30 imaging artifacts are present in the spectrum of K6. The authors have carefully inspected the images and spectra to verify that these are properly handled. The instances of contamination occur more frequently in the lowest resolution image (from 44.6 - 46.5 GHz) than in any other image, as would be expected. In cases where line absorption is observed towards K6 and line emission is produced in the LMH and/or "h", the line profiles in the low resolution

spectra will not be representative of the true line flux towards K6. For this reason, we excluded low resolution spectra from the analysis of line ratios.

In addition to the imaging artifacts towards K6, a single feature is labeled as contamination towards L in the high spatial resolution portion of the spectrum. The methanol masing transition at 36 GHz appears as an absorption feature in the spectrum of L. Inspecting the image however, it is clear that imaging artifacts are implicated, as the very strong masing transition has limited dynamic range and image fidelity. We have inspected the images and spectra to ensure that the masing features identified towards K4 and K6 appear to arise from these regions. No instances of line contamination were observed towards K4.

Tentative U-lines (U?-lines) are features that meet the detection threshold, but upon inspecting the spectra and images, the authors remain unconvinced that a real line is present. As noted in §3.2, with the established threshold of 3.5σ, one channel in 2149 line-free channels should meet the detection threshold assuming perfect baseline subtraction and frequency-independent noise within each tuning. With minor baseline residuals, it is reasonable to expect an average of $\sim$1 falsely detected feature per tuning. In the spectra of K6 and L, composed of 11 tunings, we report 11 and 10 U?-lines respectively consistent with this expectation; in the spectrum of K4, composed of 7 tunings, we report 11 U?-lines. The number in emission and absorption are similar, as would be expected for random noise and baseline variations.

As is typical of line surveys of Sgr B2, unidentified transitions are detected in the spectra towards all three positions. However, while a large fraction of detected lines are unidentified in most surveys of the LMH hot core (see e.g. Belloche et al. 2013; Nummelin et al. 1998), roughly 90% of all detected features are confidently assigned towards K6, L, and K4. Of the 496 features detected towards K6 (excluding contamination from the LMH and “h”), 89% are confidently assigned, while tentative assignments, U-lines, and U?-lines

compose 2, 7, and 2% of the detected features, respectively. Towards K6, three of the U-lines are observed at two velocity components, with velocities consistent with the 64 and 82 $\mathrm{km\,s^{-1}}$ components characterized in §3.2. An additional 23 lines are observed in absorption at a single velocity component, and 4 are observed in emission. The fraction of U-lines in emission is thus $\sim$12%, significantly larger than the 1% and 2.5% observed for firmly assigned molecular lines (excluding the methanol masing transitions) in the low and high velocity gas, respectively.

Towards L, 93% of the 273 detected features (excluding contamination) are firmly identified. Tentative assignments, U-lines, and U?-lines compose 2.6, 1.1, and 3.7% of the transitions, respectively. Only three U-lines are reported towards L, and all are in absorption. Two of the three U-lines in L are detected in absorption towards K6, and the third does not meet the detection threshold in K6, but a clear absorption feature is present towards K6. Excluding recombination lines and U?-lines, all detected molecular lines are in absorption towards L. Neither strong maser transitions nor weakly masing transitions are detected towards L.

Of the 192 lines detected towards K4, 90% are firmly identified; tentative assignments, U-lines, and U?-lines compose 1.6, 2.6, and 5.8% respectively. Weak masing constitutes 3 and 2% of the firmly identified molecular lines in the low and high velocity gas, respectively, in K4, and one of the five U-lines observed towards K4 appears in emission. Two of the absorbing U-lines detected in K4 are also detected in K6, but K4 and L have no U-lines in common with one another. It is possible that the U-line observed in emission towards K4 is produced by H_2CS at the same velocity as the methanol masers towards K4.

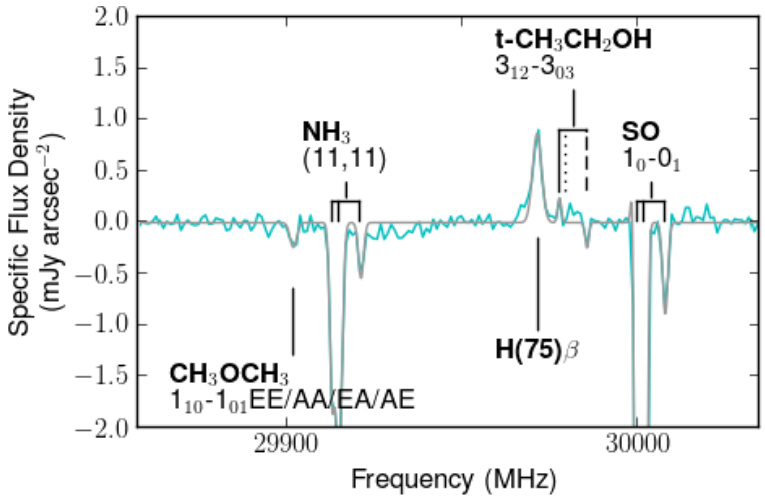

Fig. 3.17 – A segment of the spectrum towards K4 illustrates the marking conventions used in this appendix. The t-CH_3CH_2OH transition is firmly detected at 82 km s^{-1}, indicated by the solid line pointer. No emission or absorption is detected at 62 km s^{-1}, although this component is typically the most prominent. The dotted line marks 62 km s^{-1} , at which we surprisingly detect no line radiation. Additionally, a 2 km s^{-1} component is tentatively detected, producing a dashed pointer. The transitions of SO and NH_3 each have three firmly identified velocity components marked by pointers at 82, 62, and 2 km s^{-1}. The position of CH_3OCH_3 at 62 km s^{-1}is marked by the single pointer at 62 km s^{-1}. Pointers for recombination lines are at 65 km s^{-1}.

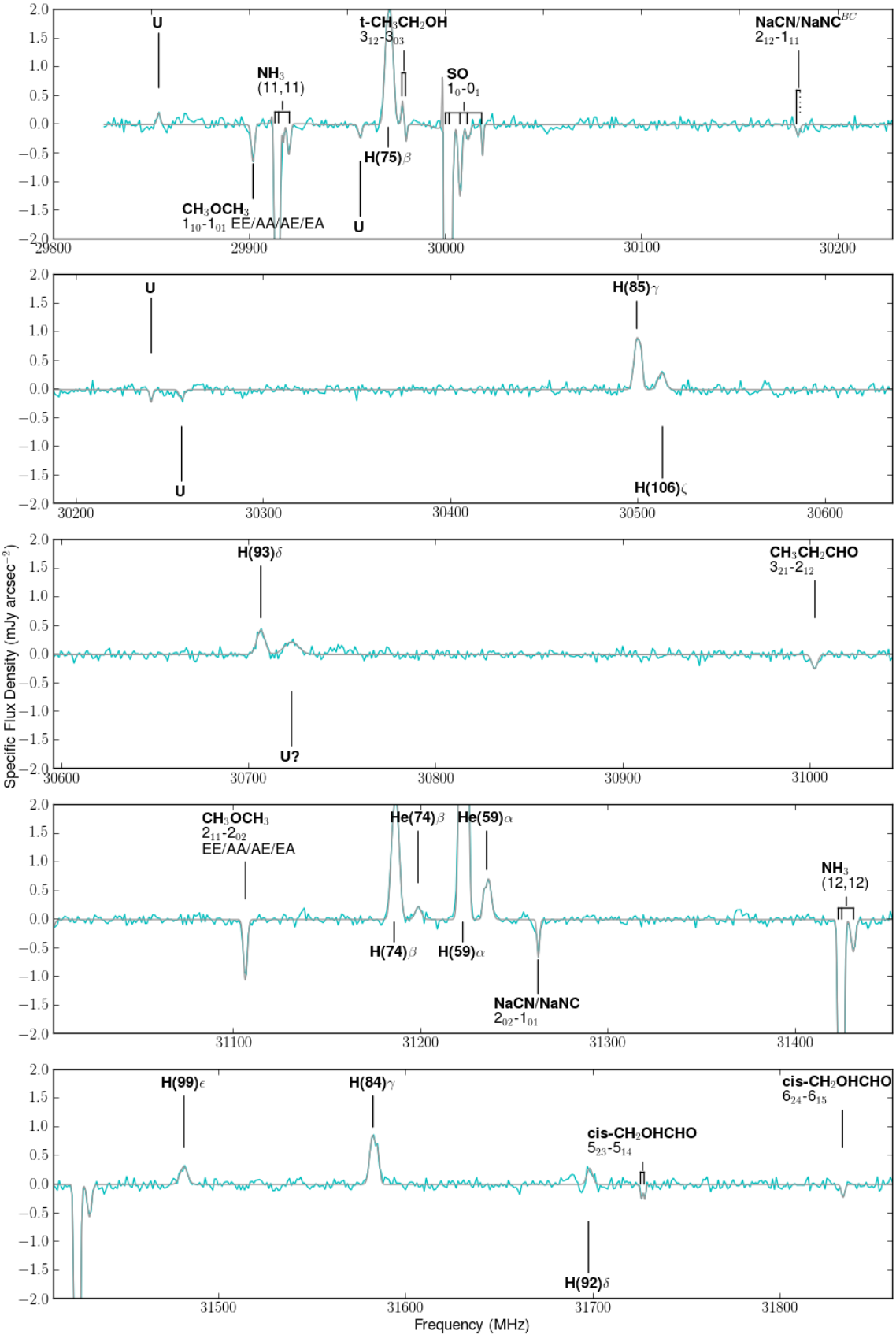

Fig. 3.18 – Spectrum Towards K6.

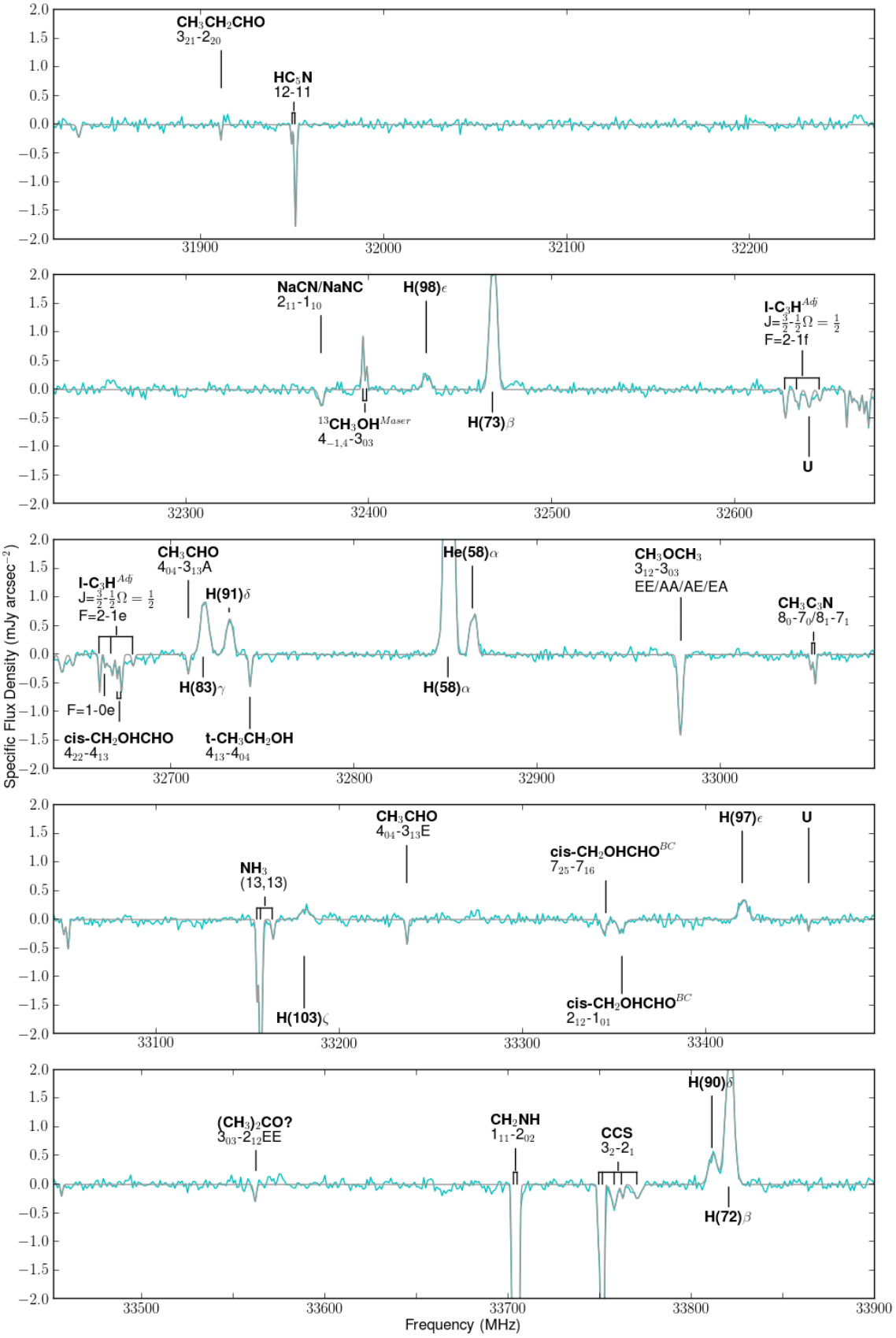

Fig. 3.19 – Spectrum Towards K6.

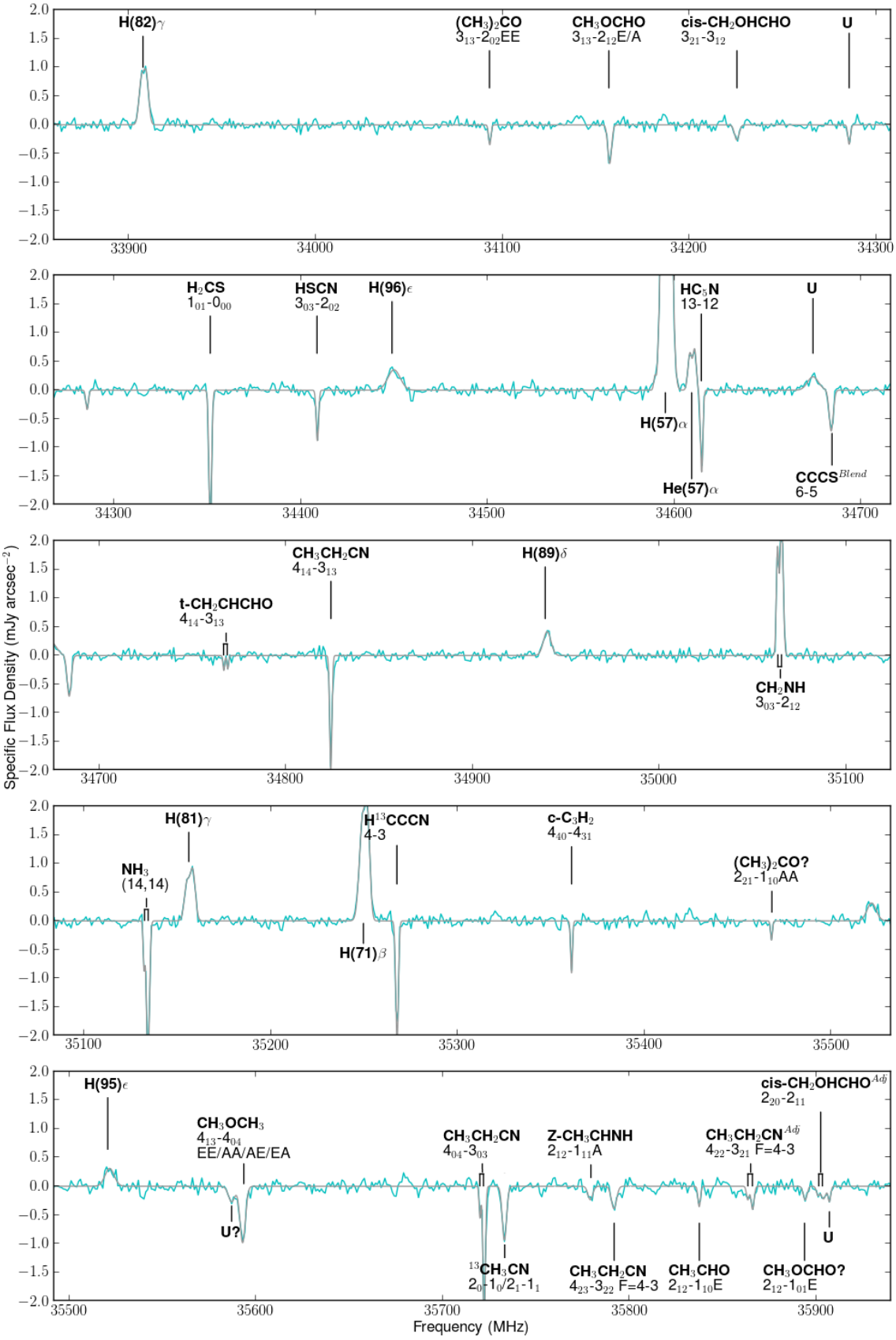

Fig. 3.20 – Spectrum Towards K6.

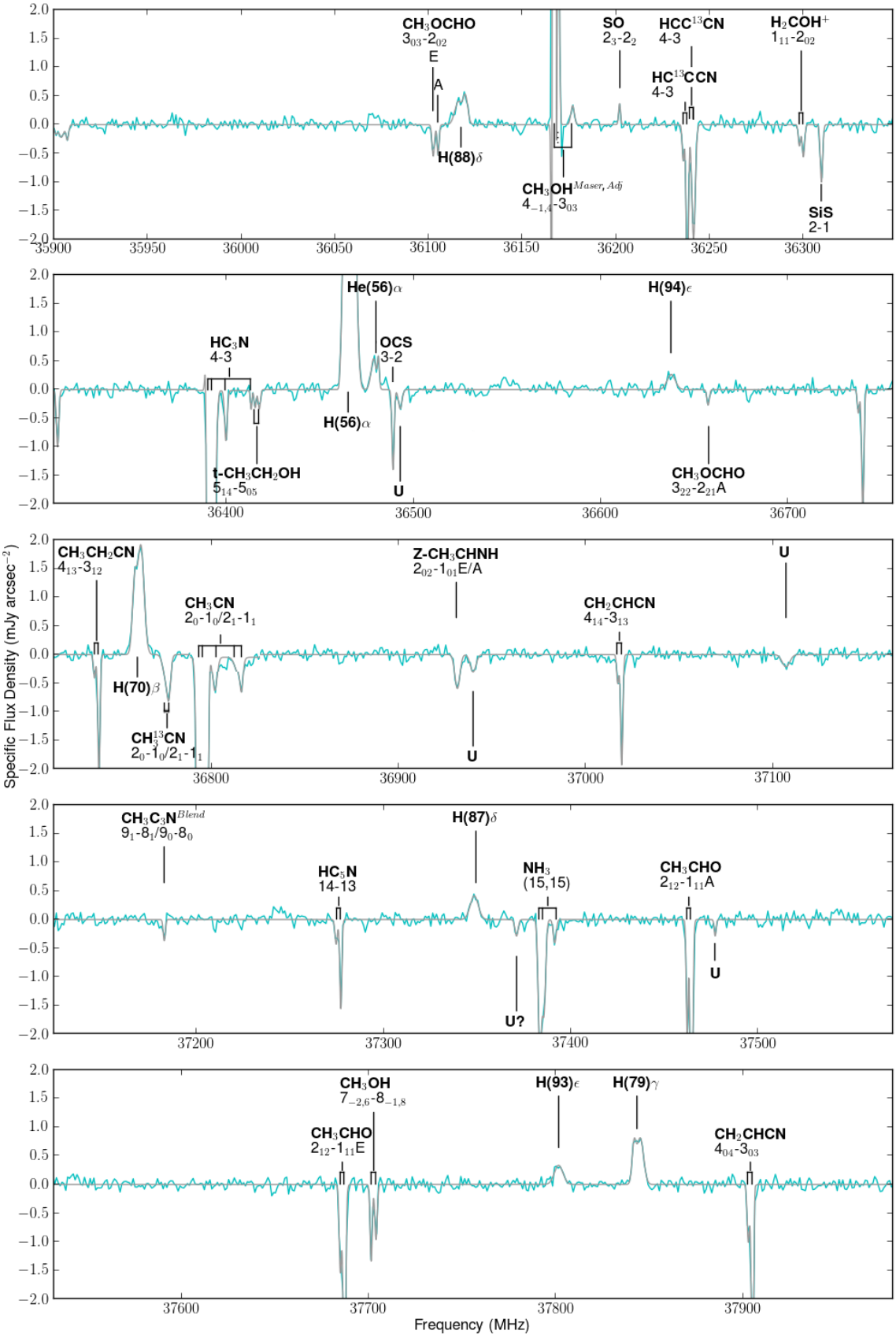

Fig. 3.21 – Spectrum Towards K6.

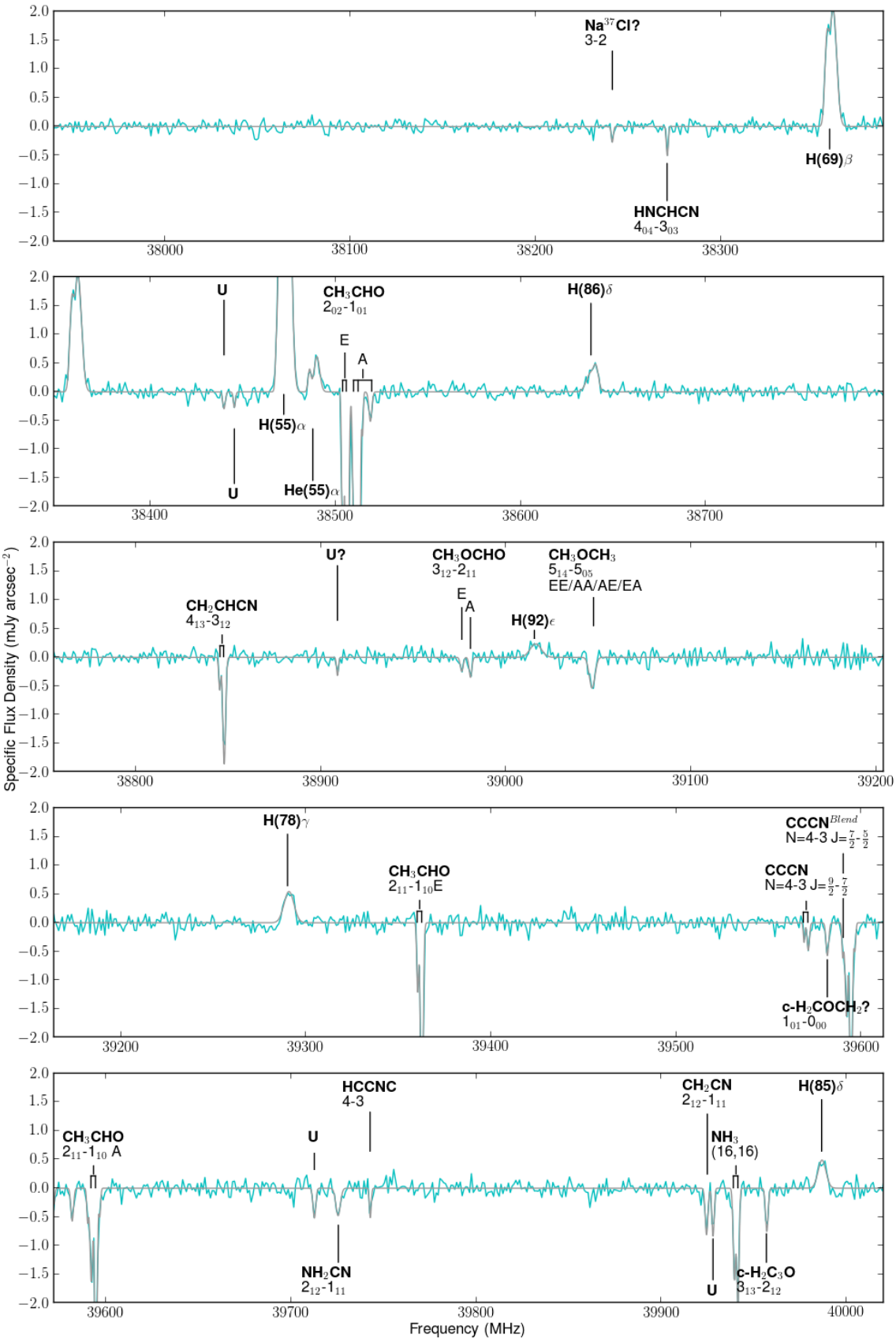

Fig. 3.22 – Spectrum Towards K6.

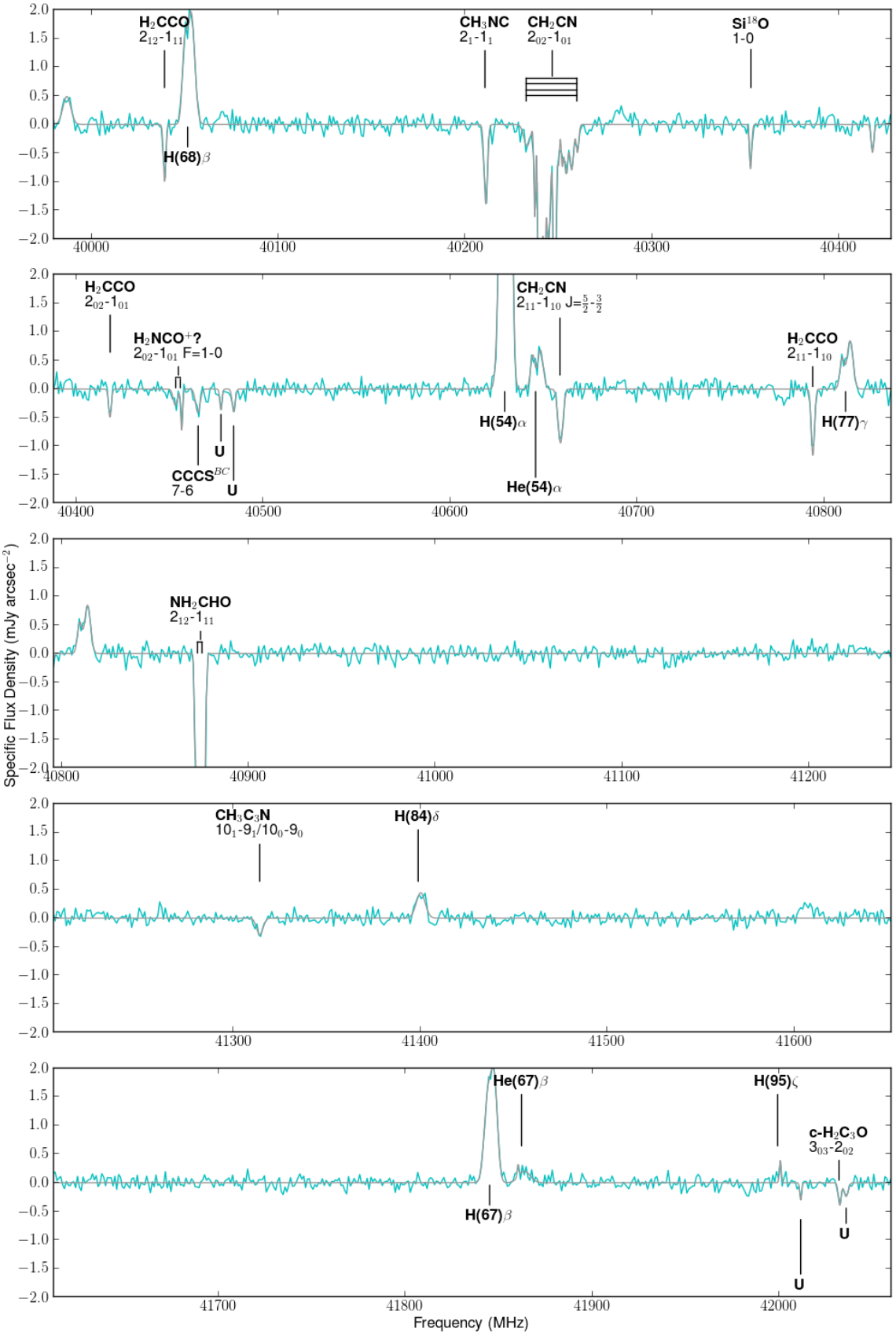

Fig. 3.23 – Spectrum Towards K6.

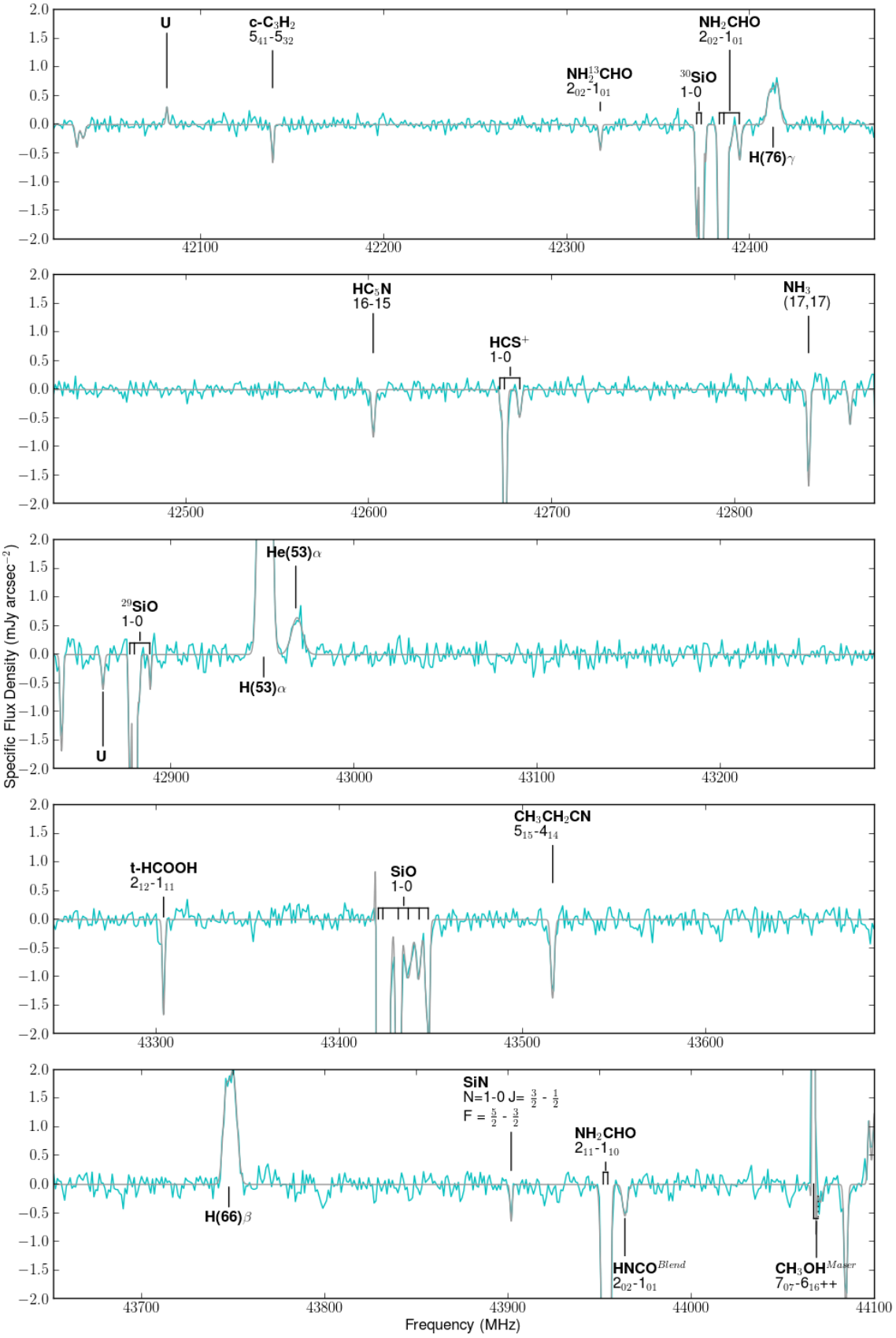

Fig. 3.24 – Spectrum Towards K6.

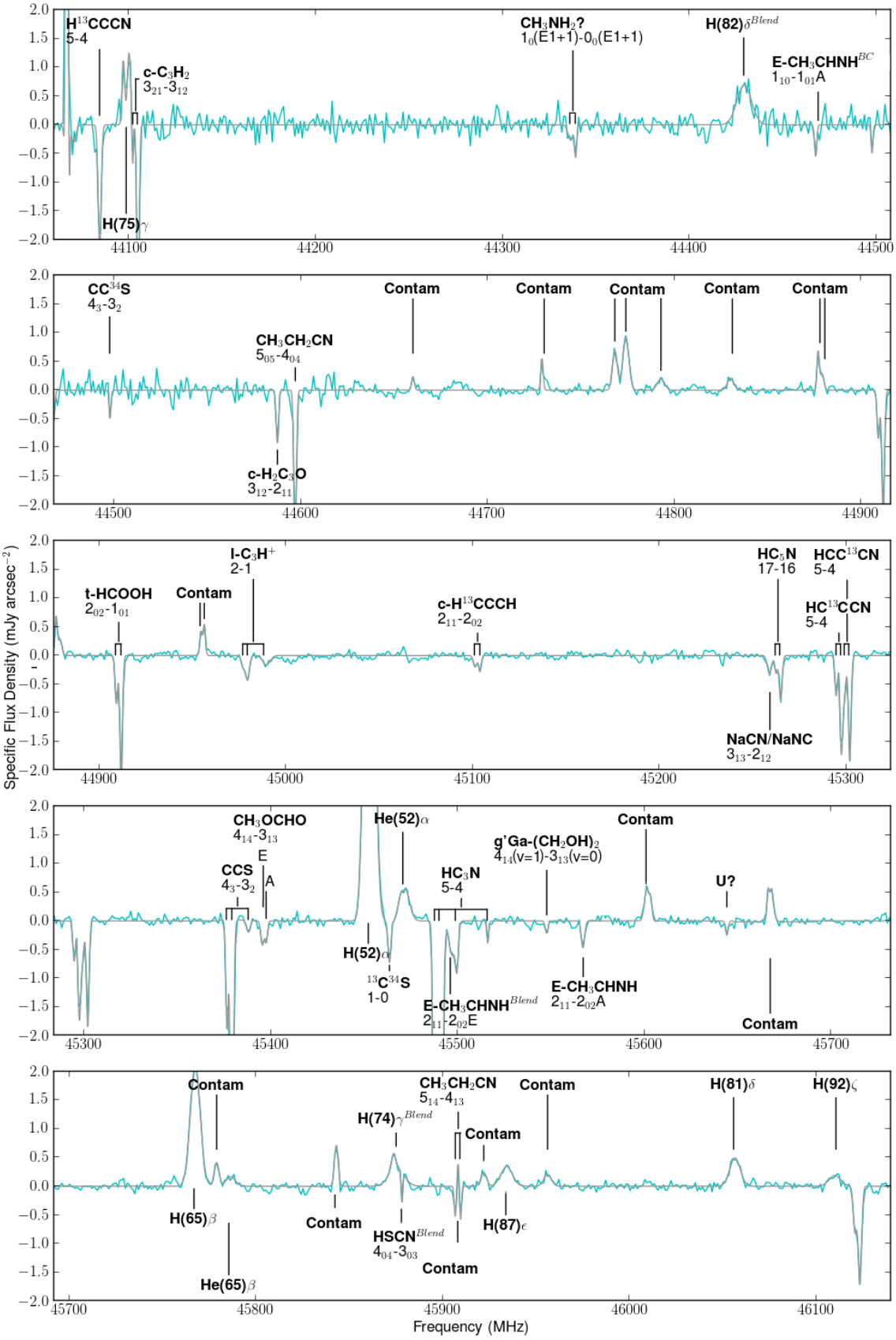

Fig. 3.25 – Spectrum Towards K6.

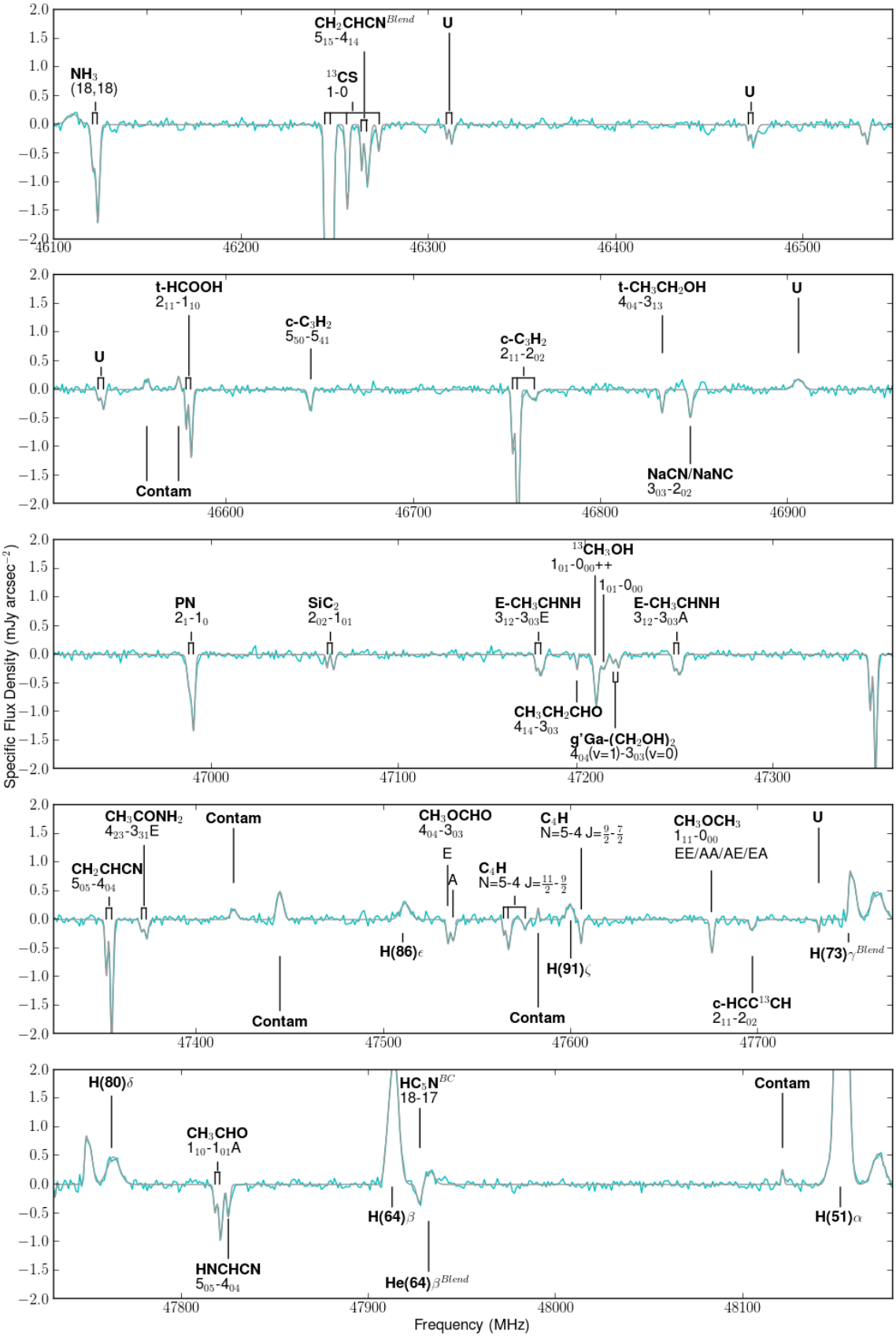

Fig. 3.26 – Spectrum Towards K6.

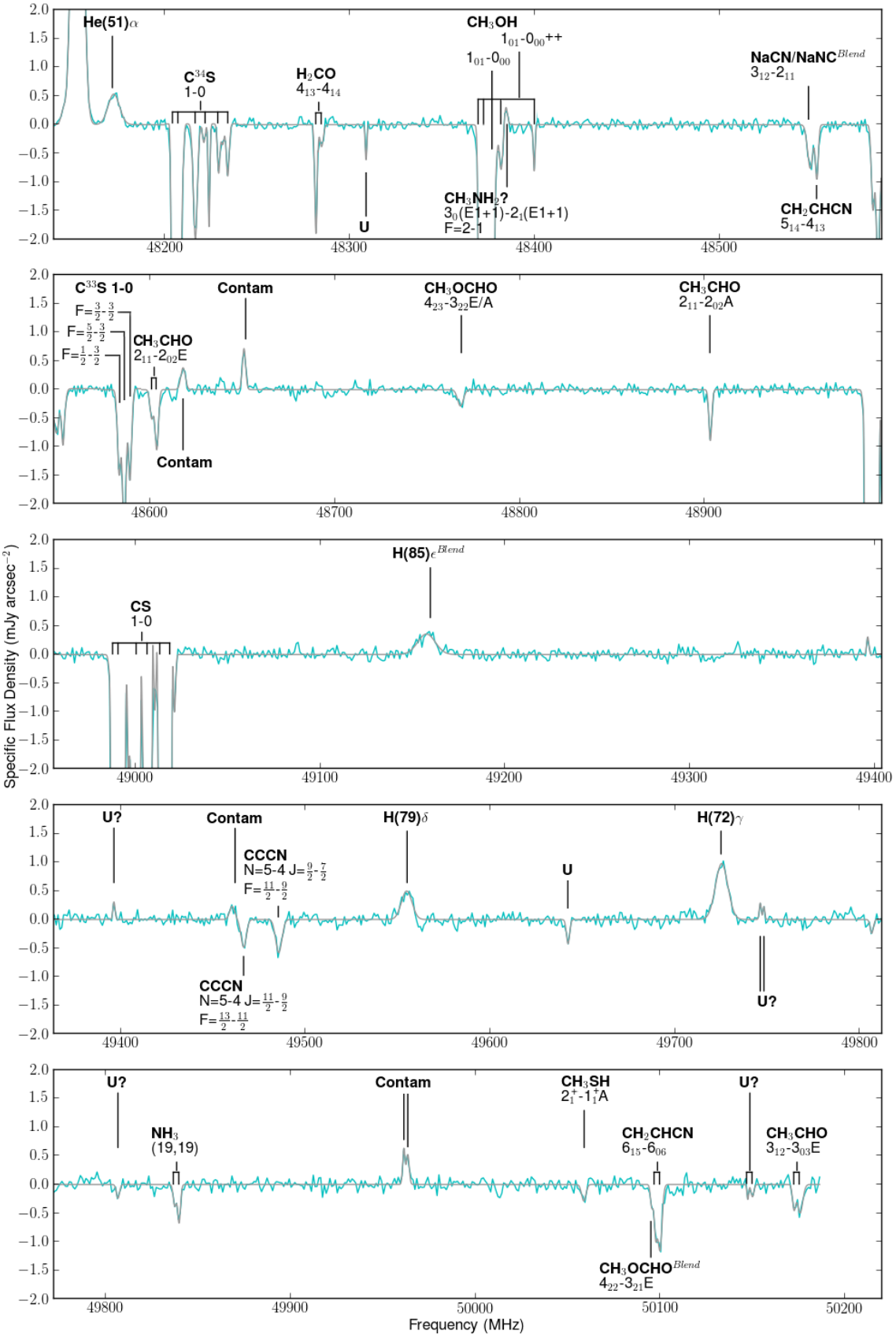

Fig. 3.27 – Spectrum Towards K6.

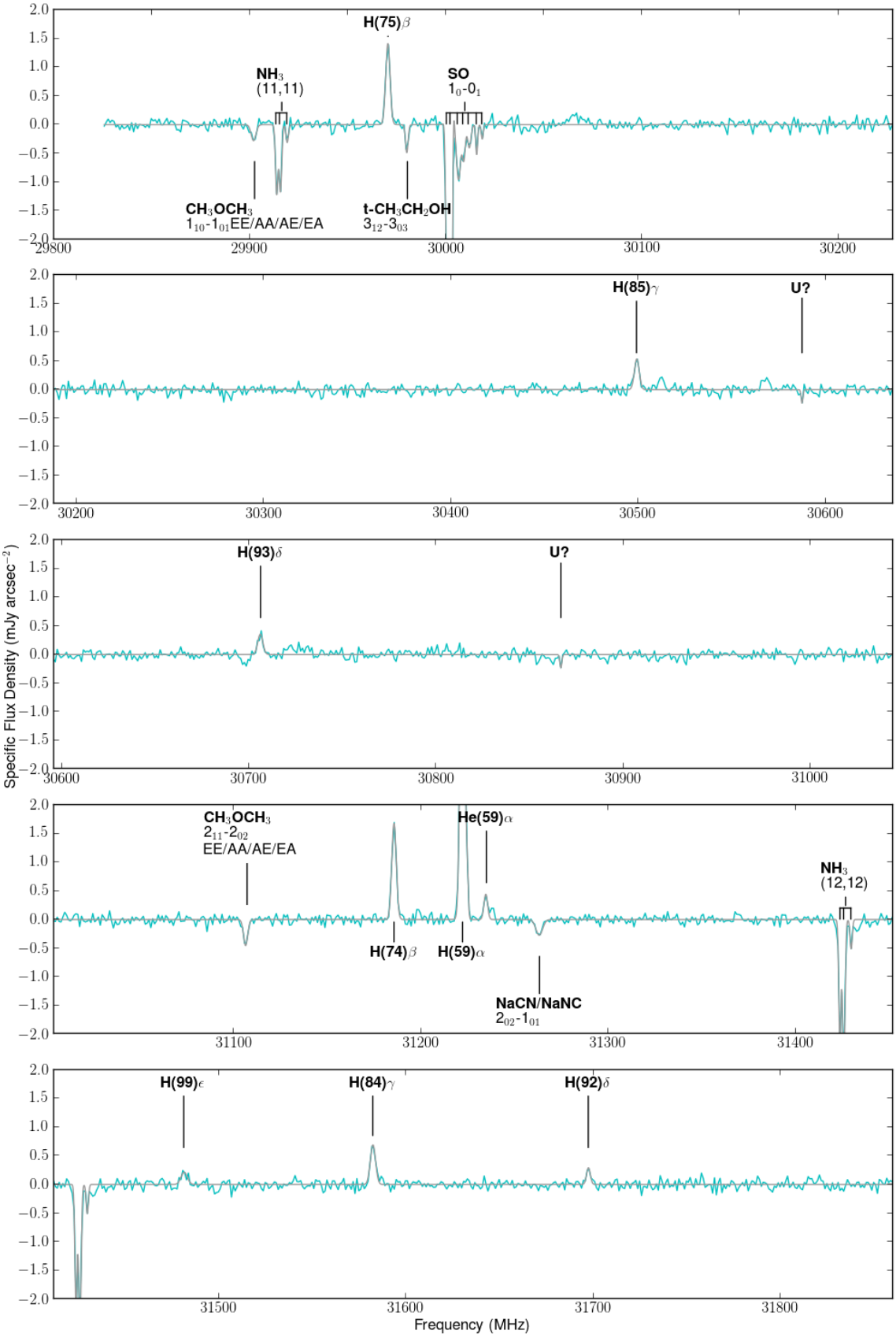

Fig. 3.28 – Spectrum Towards L.

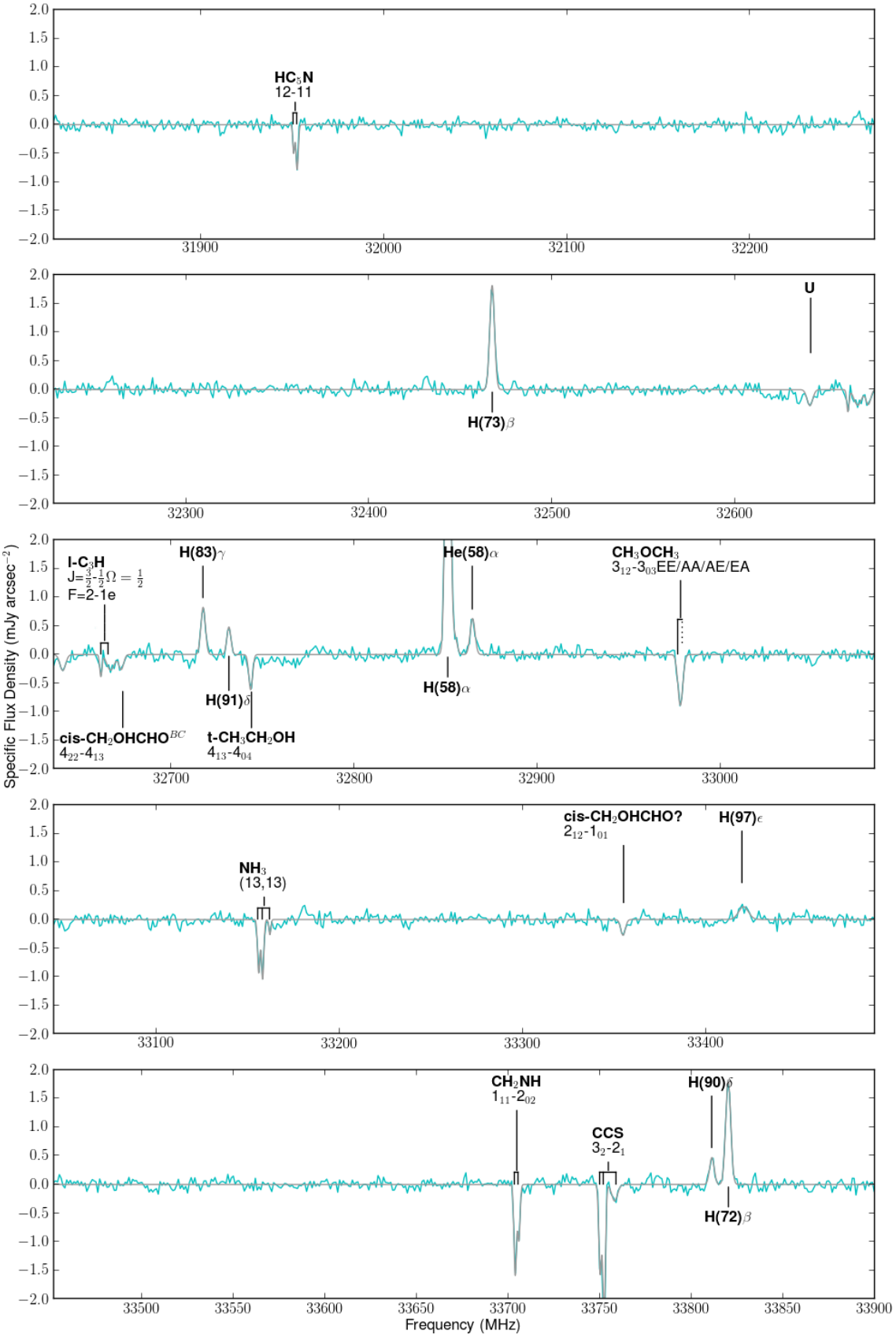

Fig. 3.29 – Spectrum Towards L.

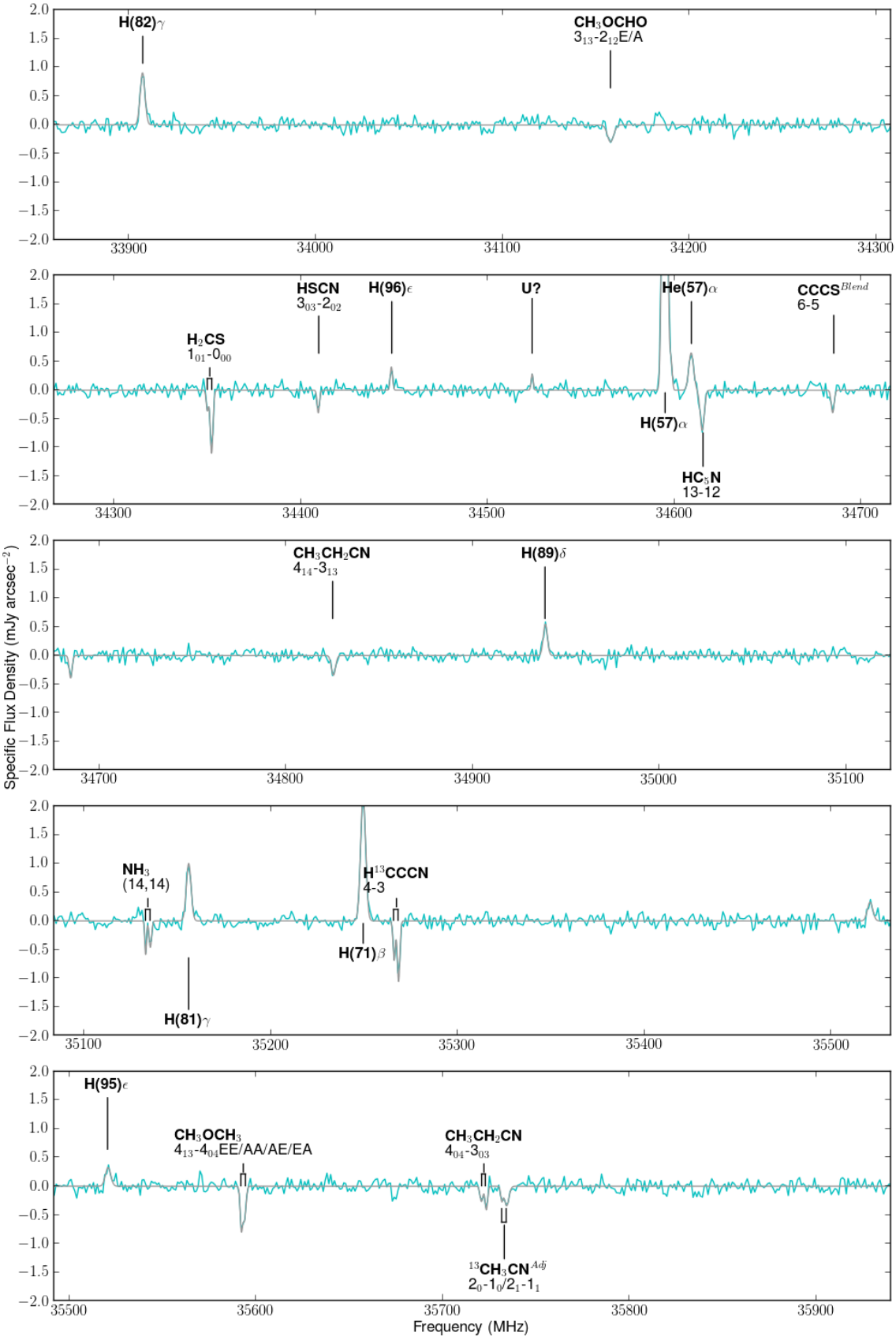

Fig. 3.30 – Spectrum Towards L.

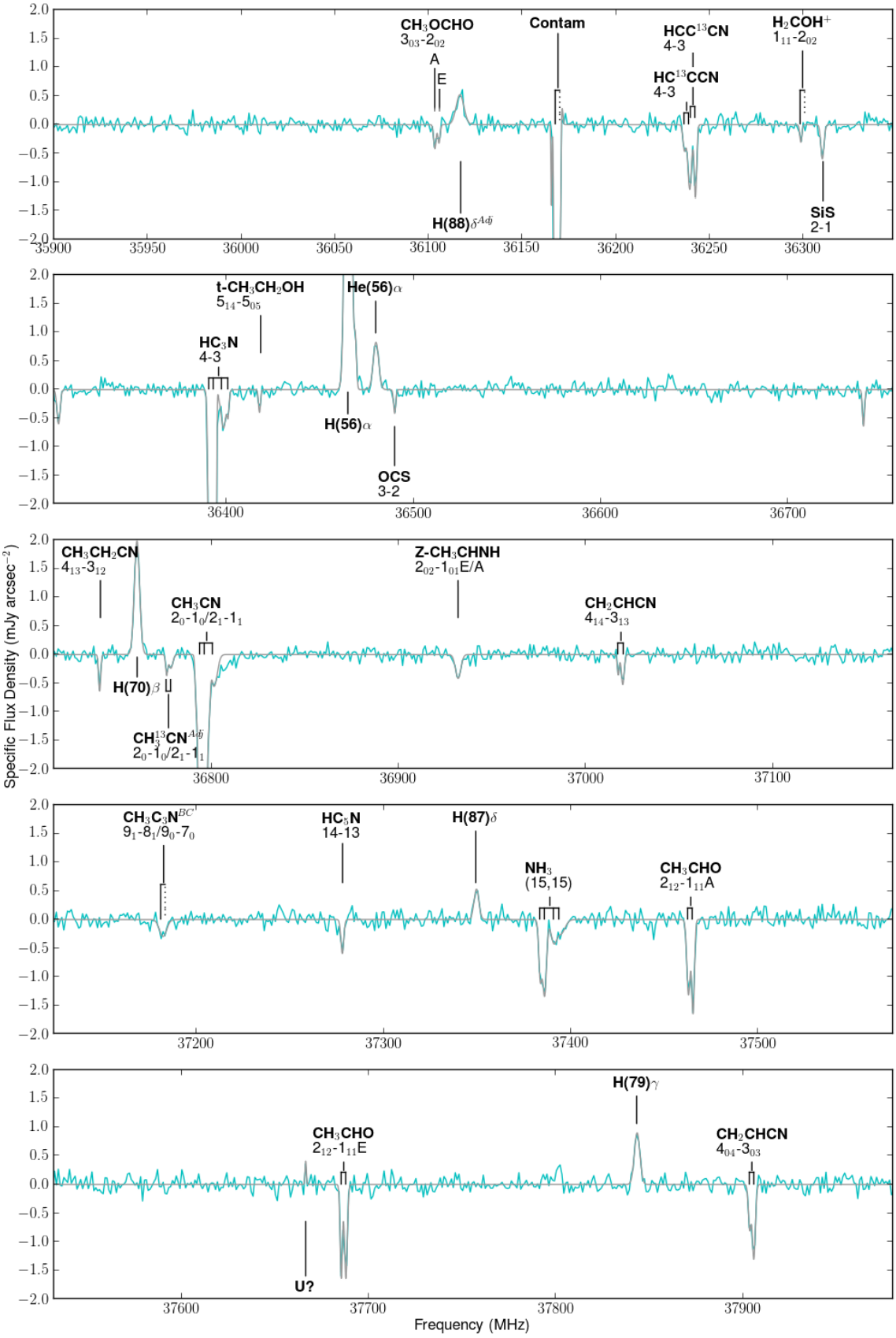

Fig. 3.31 – Spectrum Towards L.

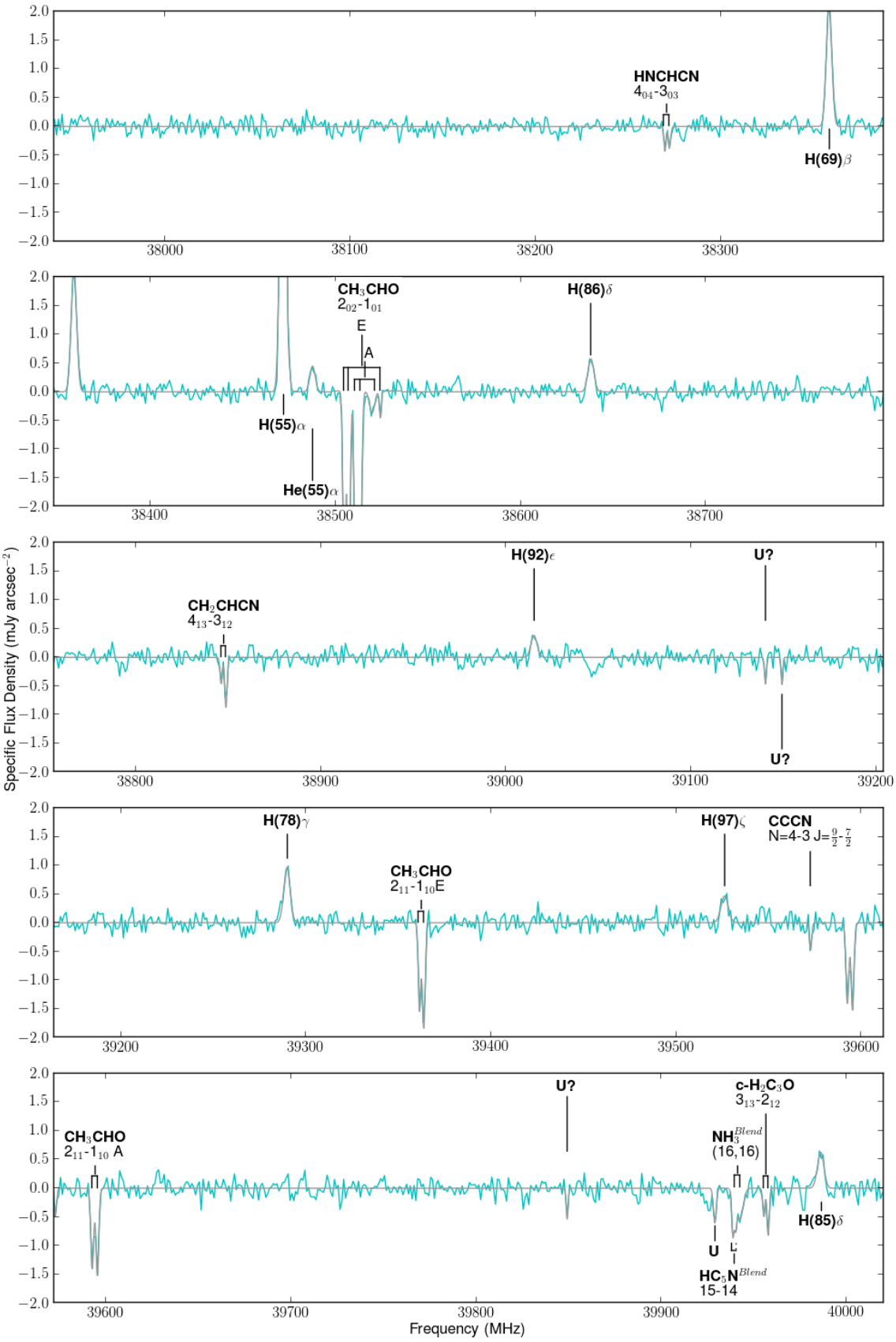

Fig. 3.32 – Spectrum Towards L.

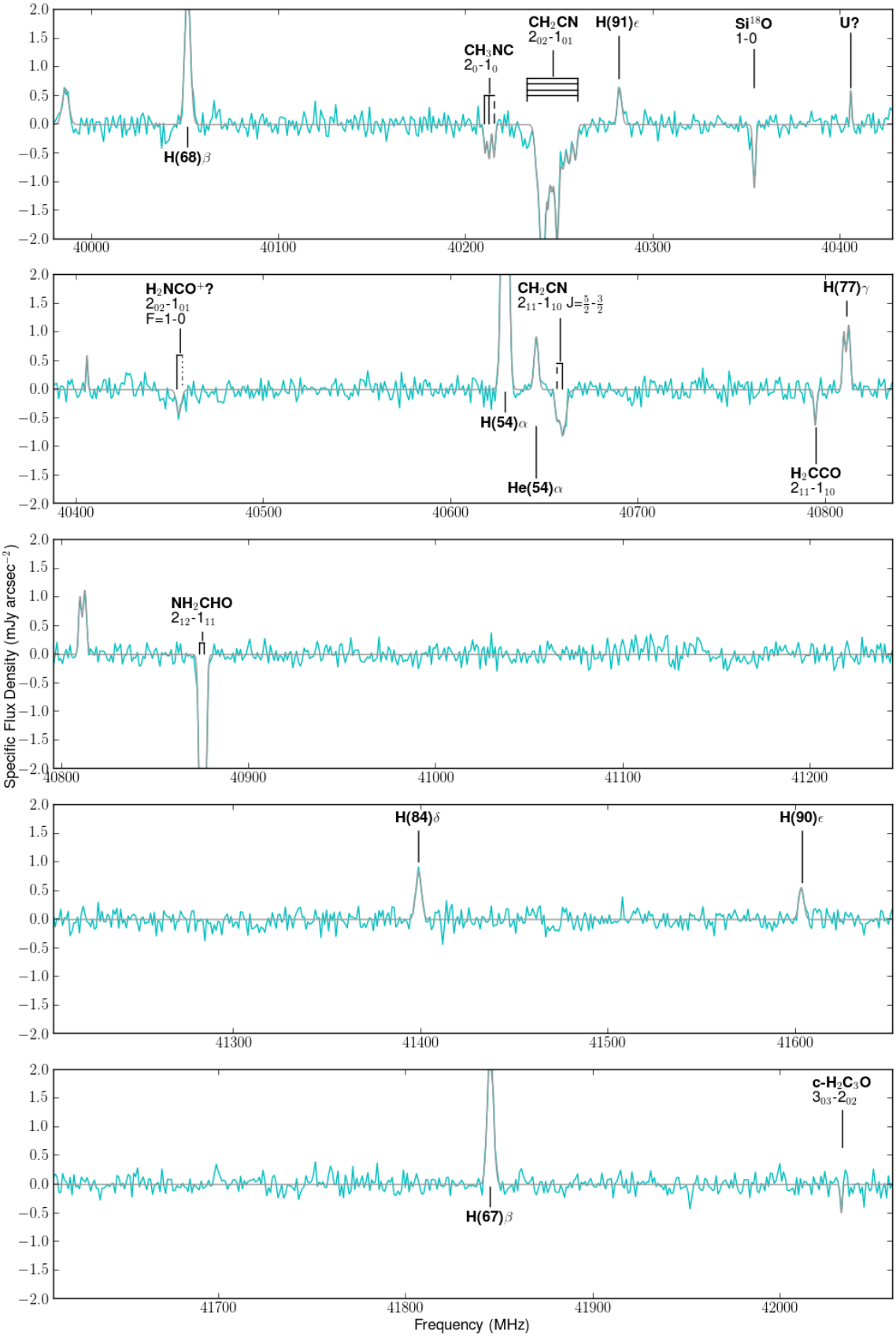

Fig. 3.33 – Spectrum Towards L.

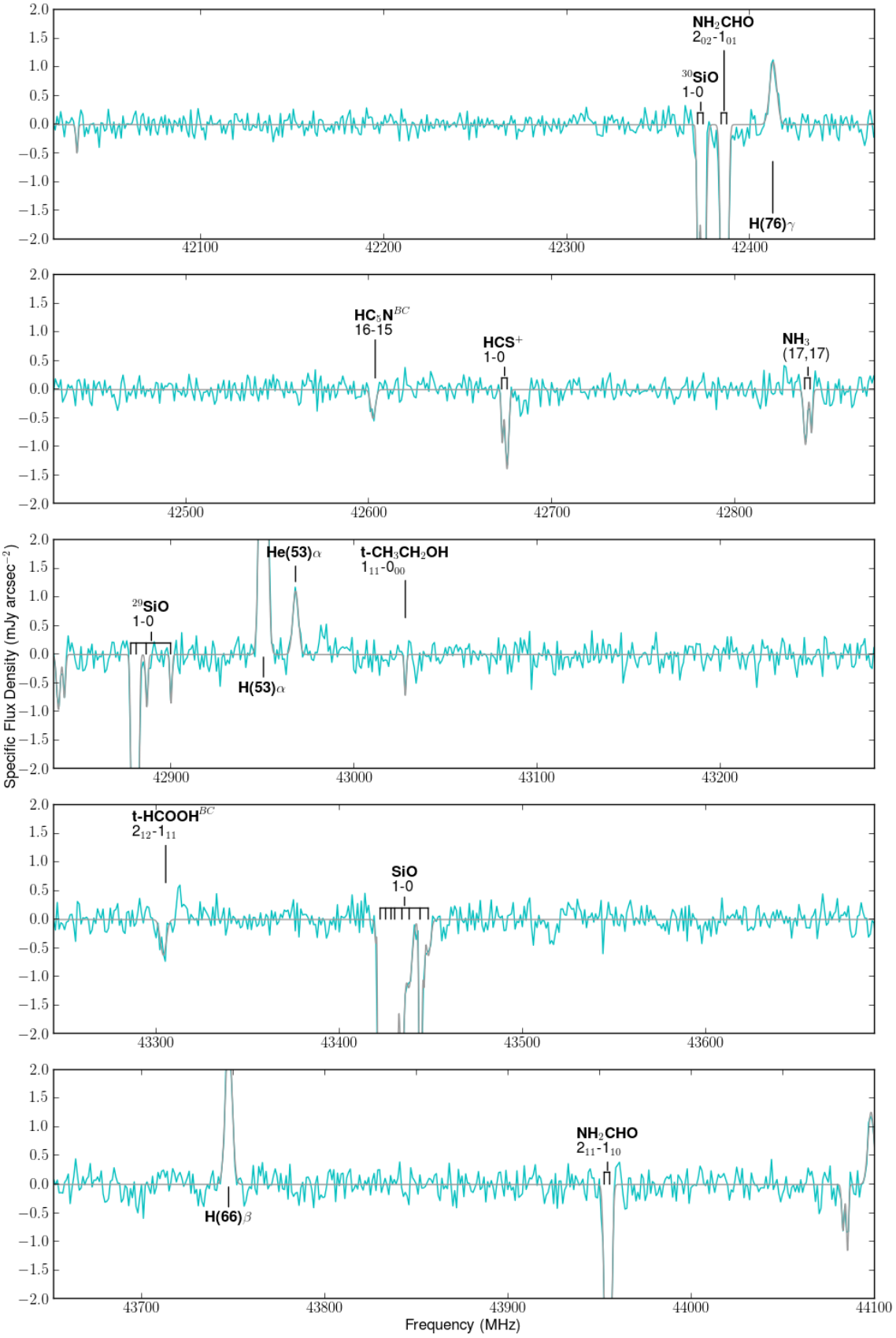

Fig. 3.34 – Spectrum Towards L.

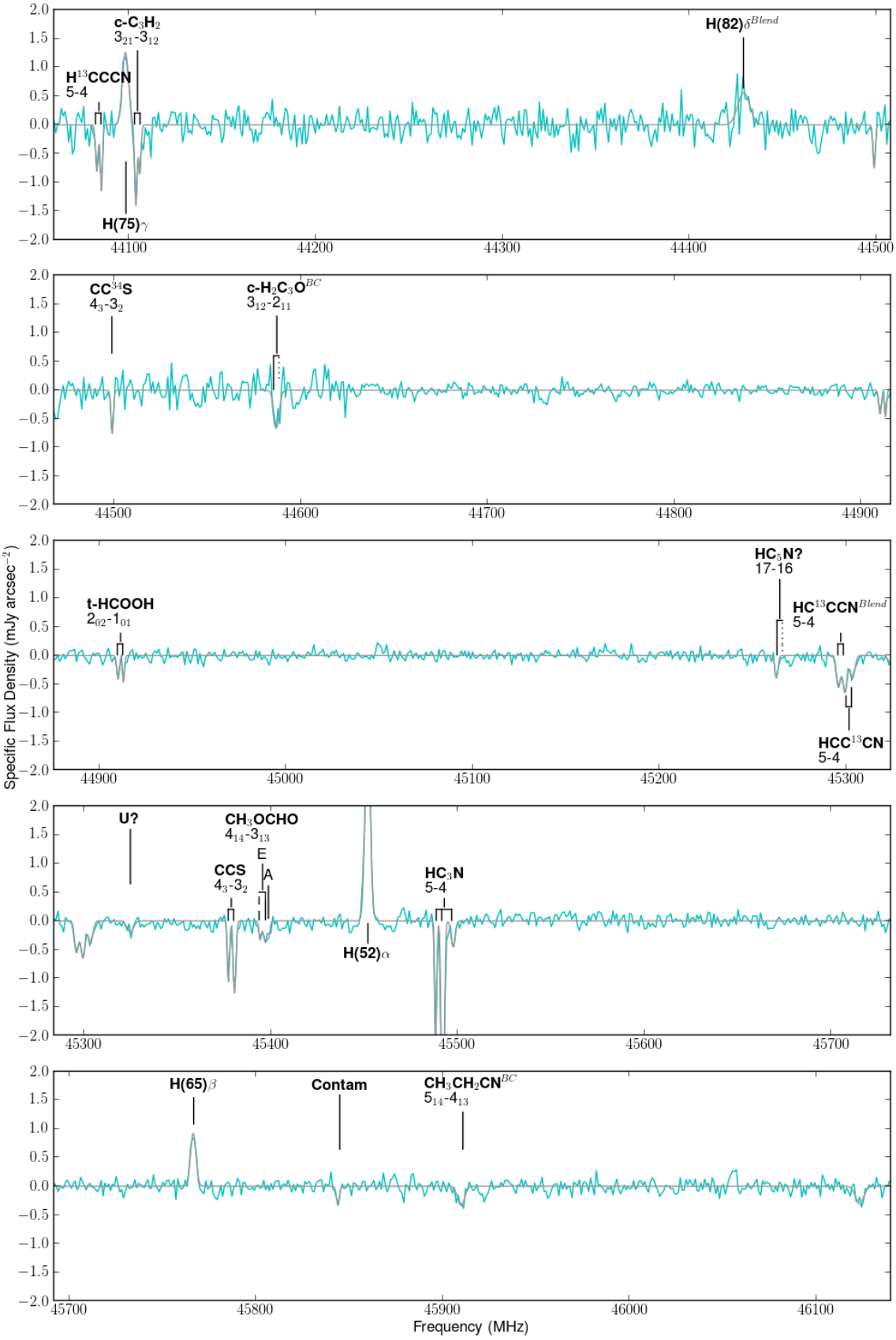

Fig. 3.35 – Spectrum Towards L.

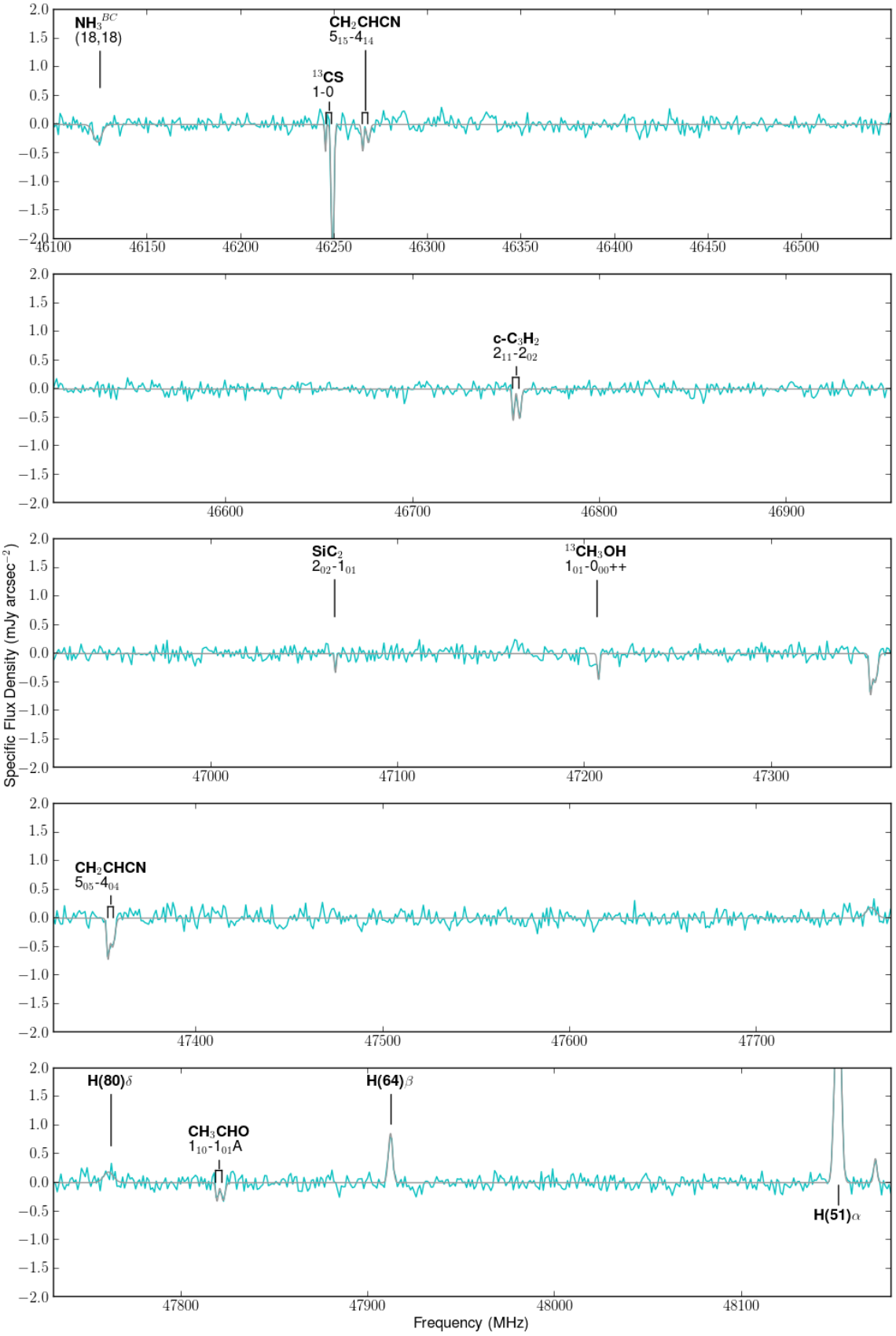

Fig. 3.36 – Spectrum Towards L.

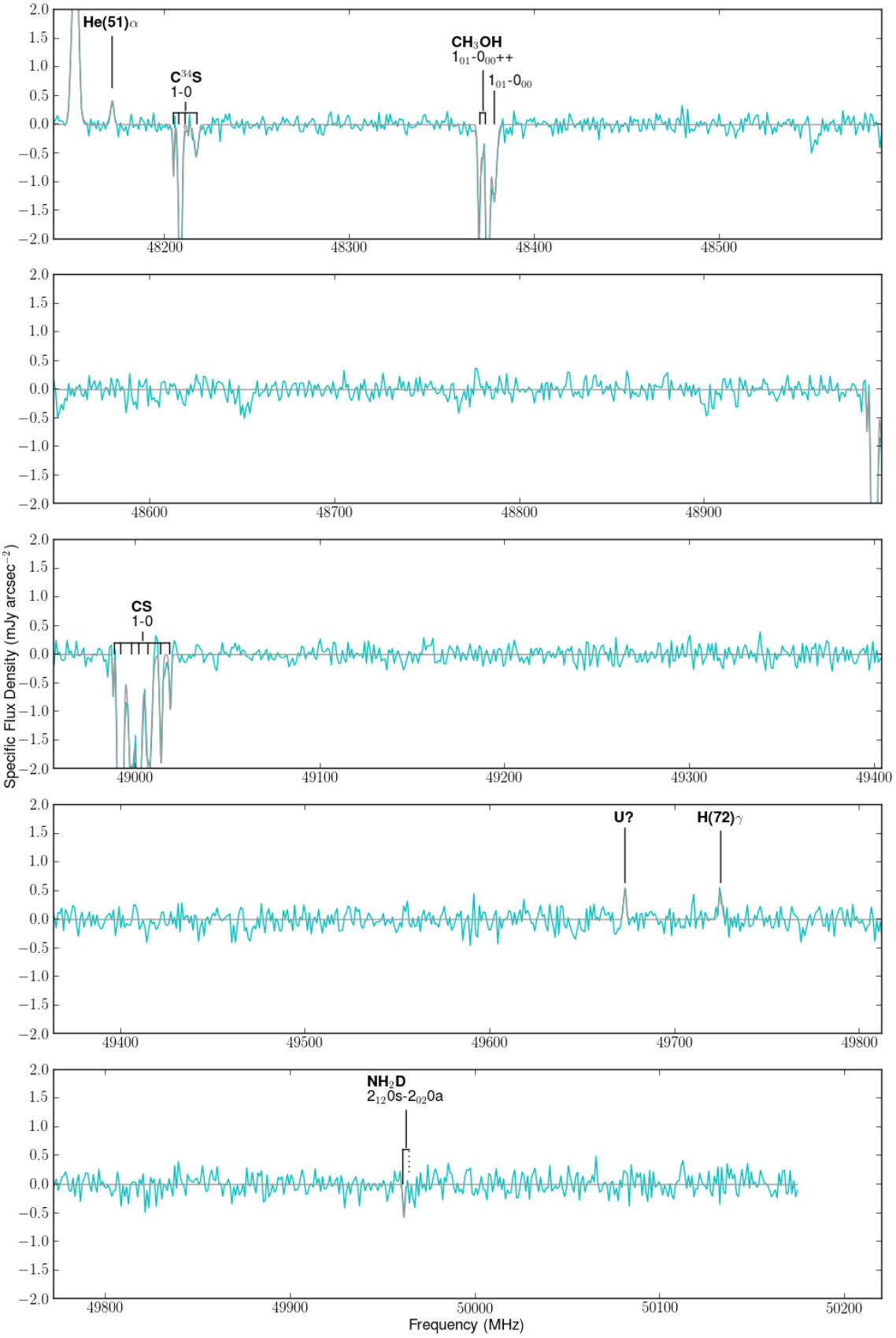

Fig. 3.37 – Spectrum Towards L.

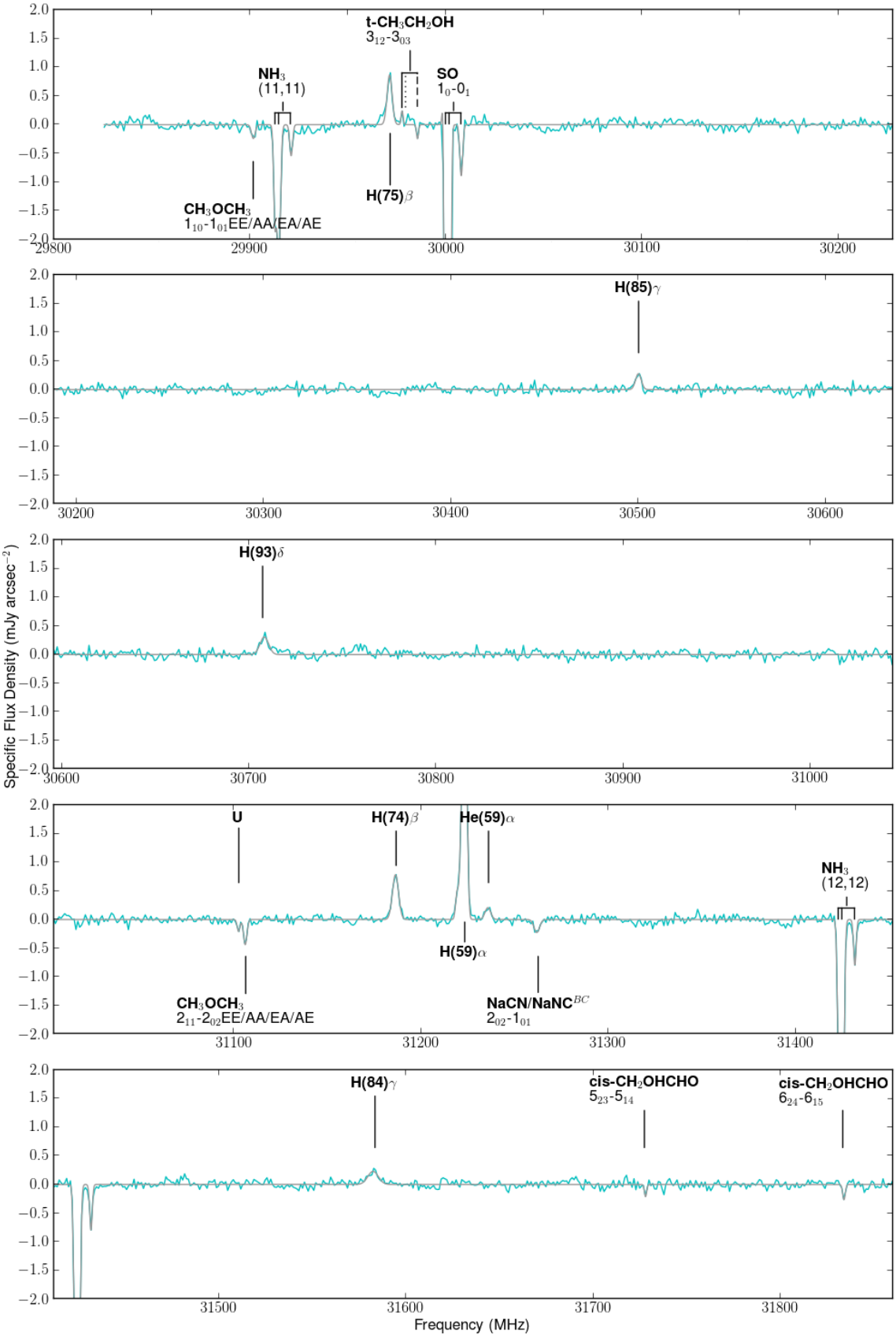

Fig. 3.38 – Spectrum Towards K4.

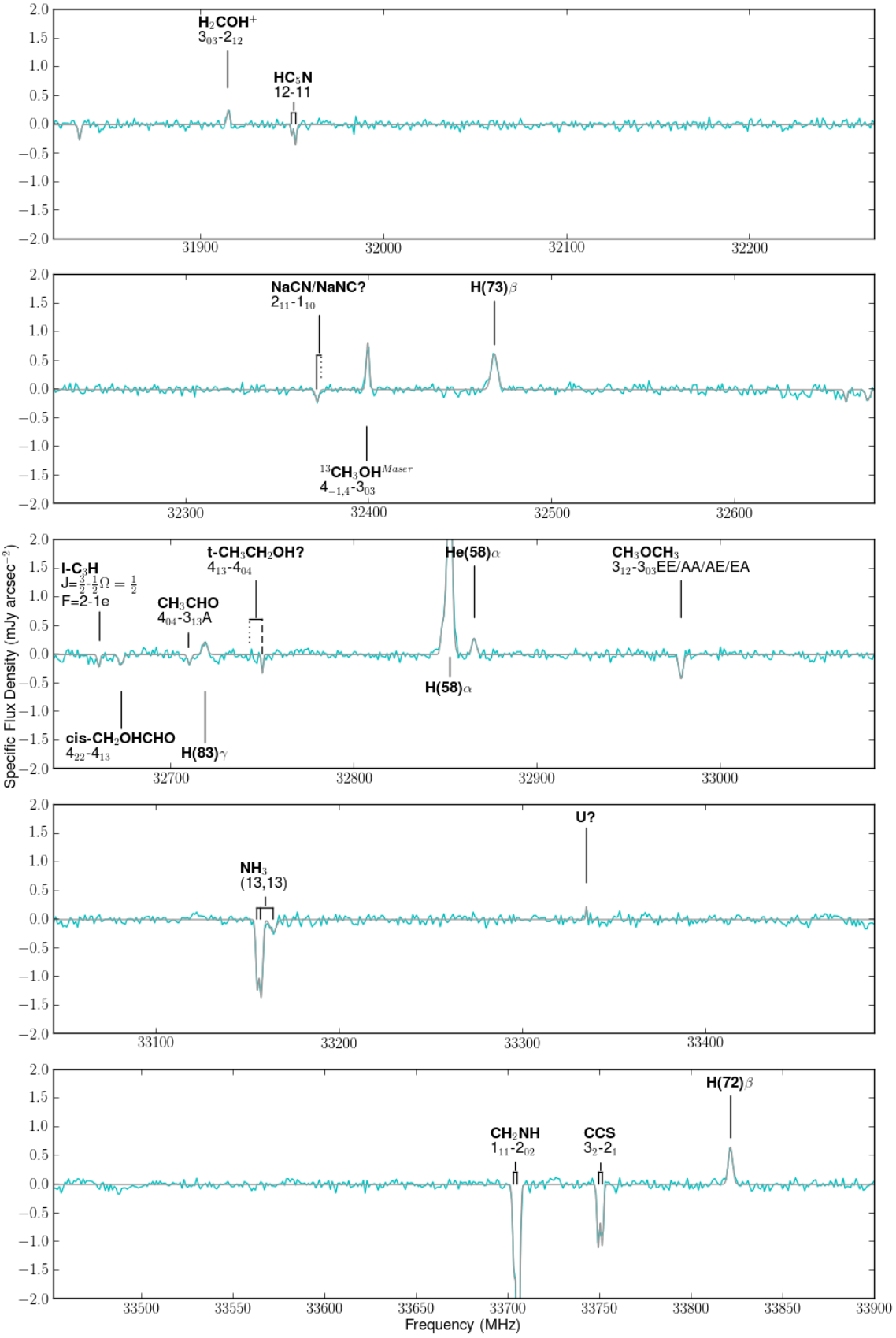

Fig. 3.39 – Spectrum Towards K4.

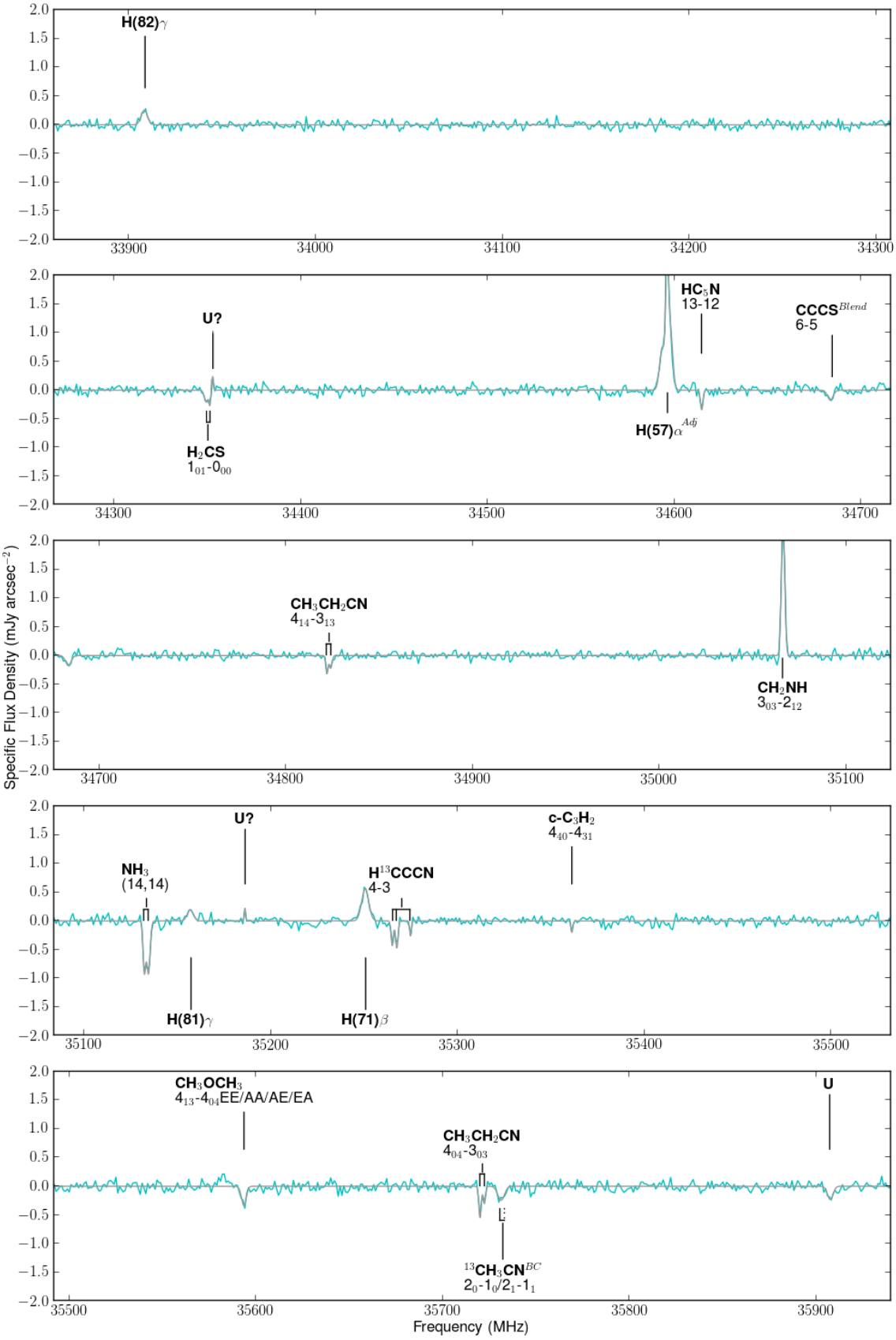

Fig. 3.40 – Spectrum Towards K4.

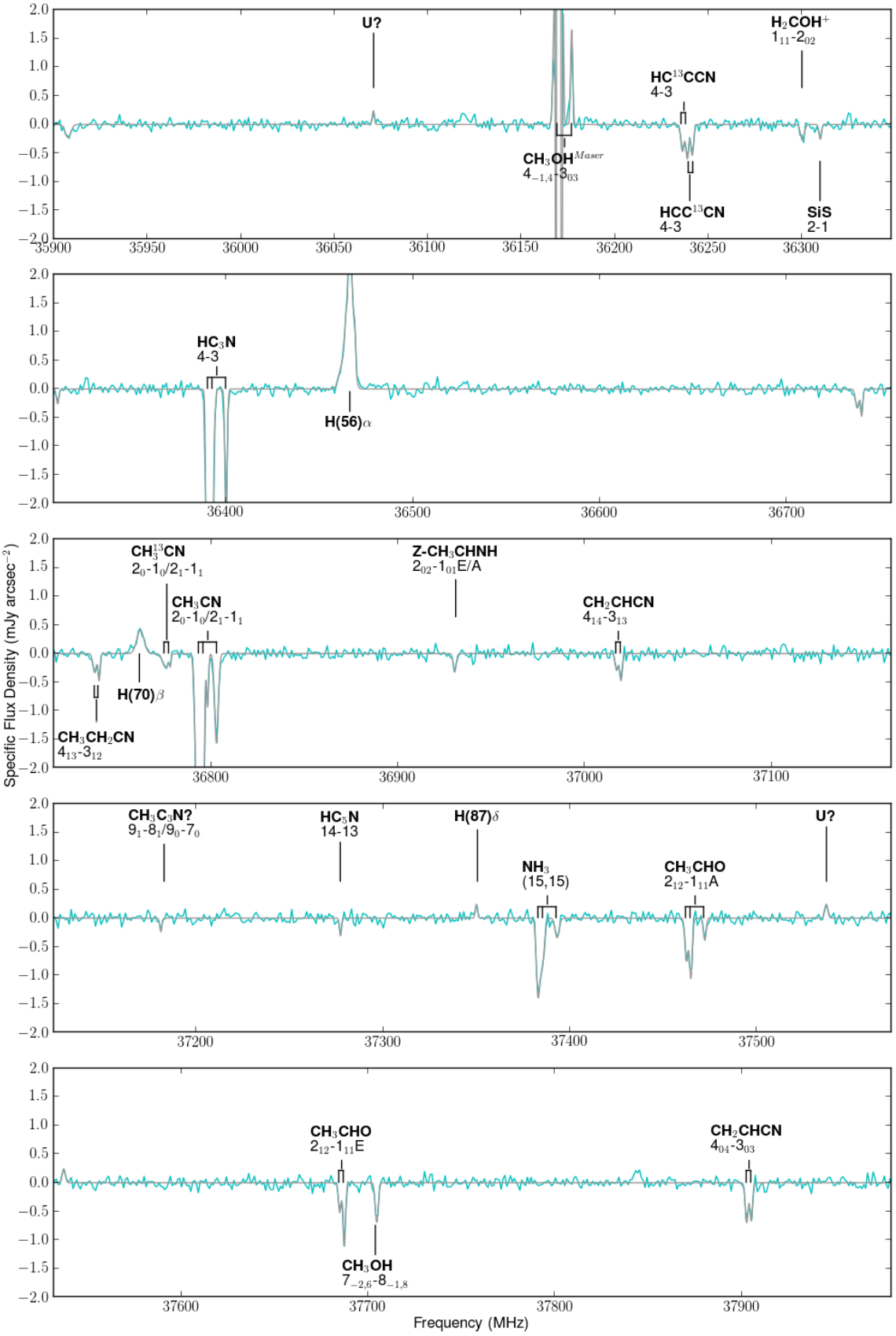

Fig. 3.41 – Spectrum Towards K4.

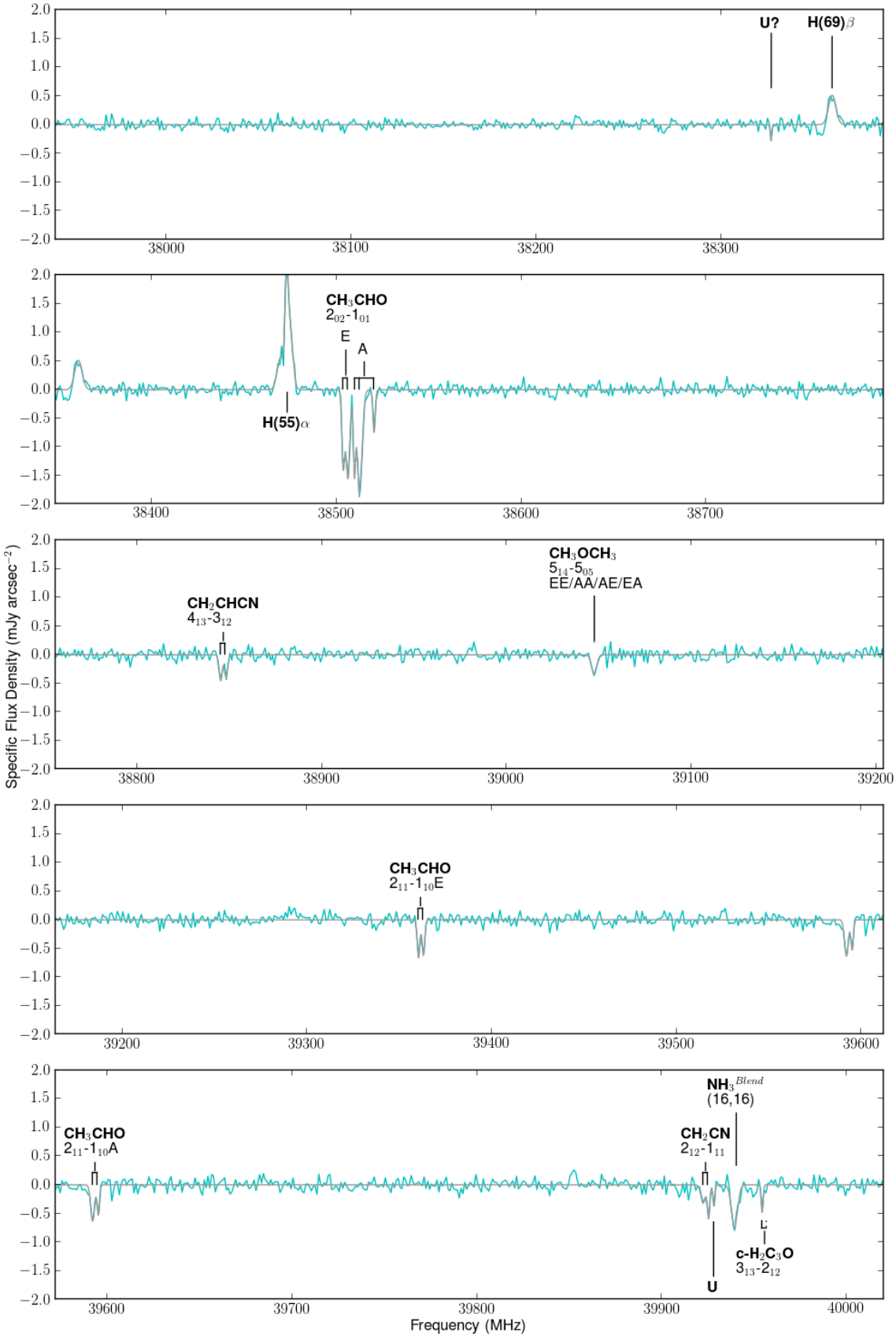

Fig. 3.42 – Spectrum Towards K4.

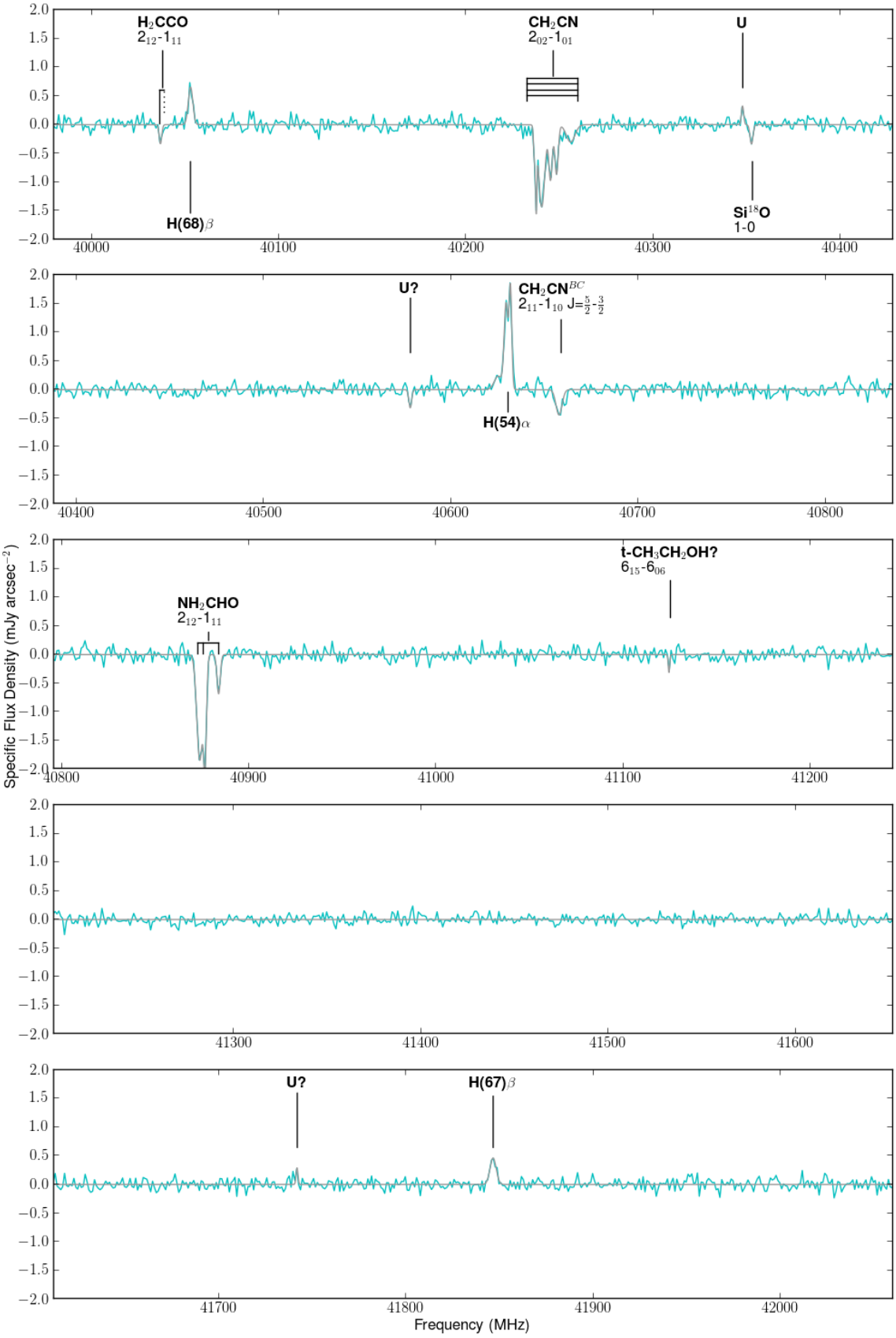

Fig. 3.43 – Spectrum Towards K4.

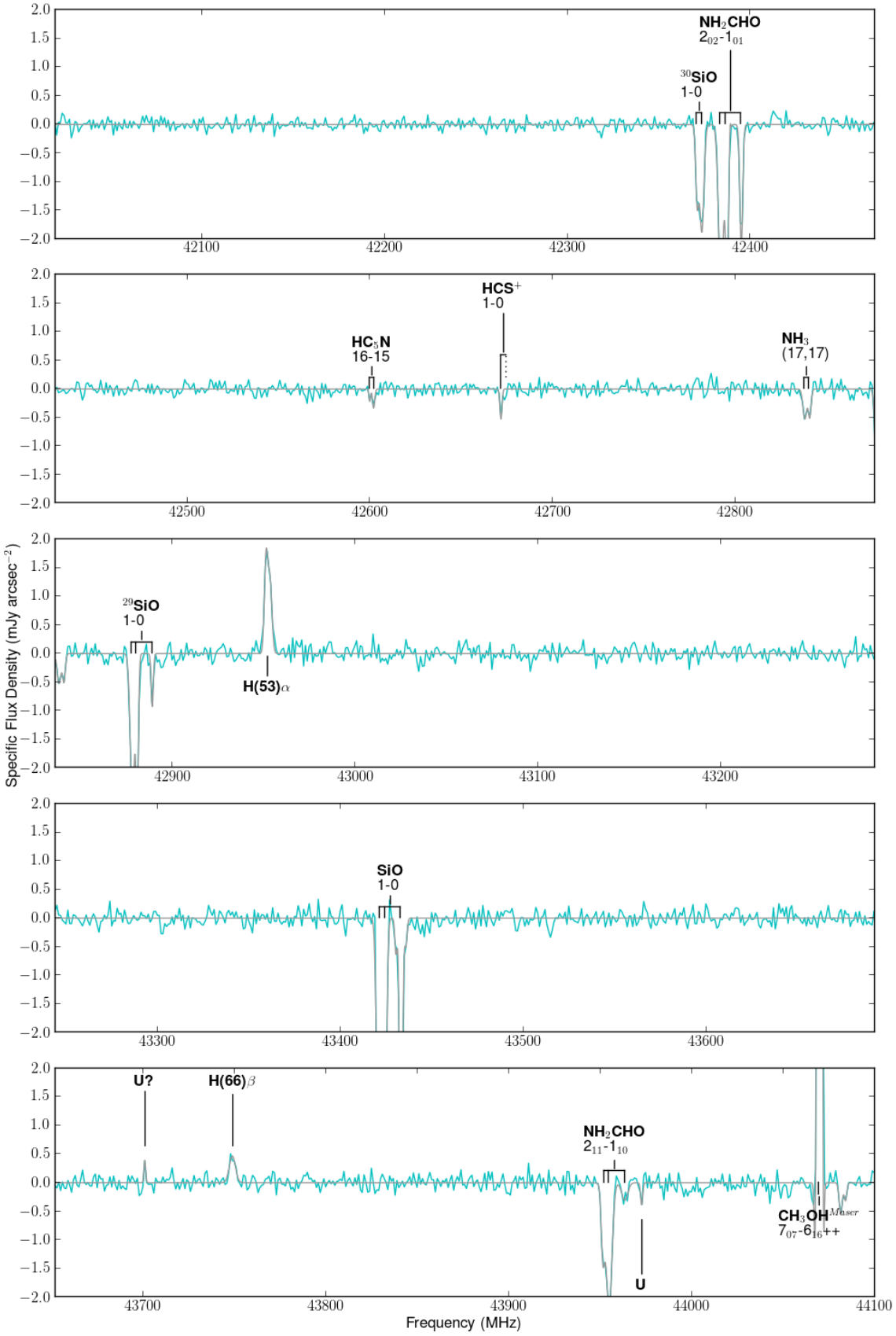

Fig. 3.44 – Spectrum Towards K4.

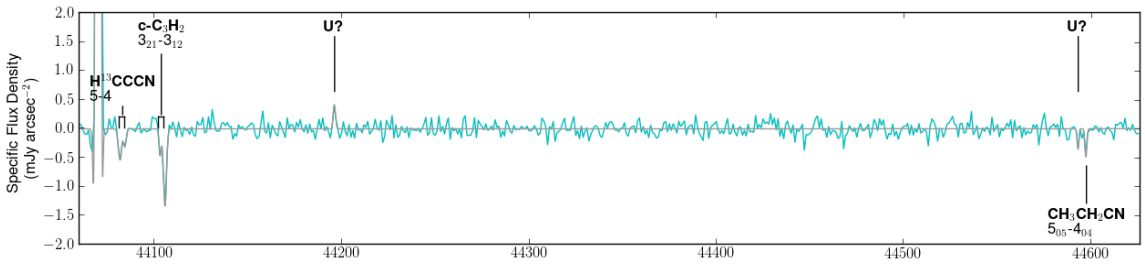

Fig. 3.45 – Spectrum Towards K4.

3.10 Appendix C: Line Identification and Gaussian Fit Tables

Line identifications and Gaussian fit parameters, including velocity center, height, width, and integrated flux towards K6, L, and K4 are provided. The following conventions are used in all tables. Tentative identifications are noted with a '?', as are unidentified lines (U-lines) suspected to be artifacts. Strong masing transitions are marked with '$Maser$', blended lines are marked with 'B', and line fits that have been adjusted from the output of the line fitter are marked with 'Adj'. In cases where the line-fitter determined a 1-component fit that we suspect to be a 2-component transition with insufficient signal-to-noise to be identified as such by the fitter, the species is marked with 'BC'. Footnotes, linked from the velocity column, provide notes on any other notable aspects of lines.

We have applied the following rules to assigning the rest frequencies and velocities to U-lines. U-lines detected towards K6 are treated as follows:

1. 1-component transitions detected towards K6 are assumed to be at a velocity of 64.0 $\mathrm{km\,s^{-1}}$.

2. For 2-component transitions, we assume that the lower velocity component is at 64.0 $\mathrm{km\,s^{-1}}$.

U-lines detected towards L and K4 are treated as follows:

1. If the U-line is detected towards K6, we use the rest frequency determined above.

2. If the U-line is not detected towards K6, we assume the velocity of the low velocity gas component, namely 56 and 62 $\mathrm{km\,s^{-1}}$ for L and K4 respectively.

For cases in which a transition has blended spectral structure (such as blended transitions of A- and E-states), the listed transition indicates what components are expected to

be blended, with the first listed component corresponding to the transition rest frequency in the first column.

Table 3.7 – Line identifications and fit parameters towards K6.

Line Rest Frequency (MHz)	Species	Transition	Velocity (km s^{-1})	Height (mJy × arcsec^{-2})	Width (km s^{-1})	$\int I_v dv$ (mJy arcsec^{-2} × km s^{-1})
29853.31	U	——	64.0	0.20	19.7	4.3
29901.40	CH_3OCH_3	1_{10}-1_{01}	64.2	-0.64	20.2	-13.9
		EE/AA/AE/EA				
29914.49	NH_3	(11,11)	83.4	-2.51	12.5	-29.5
			64.6	-4.96	15.9	-83.5
			11.3	-0.52	18.6	-11.4
29956.11	U	——	64.0	-0.23	20.1	-4.9
29971.48	Hydrogen	H(75)β	84.6	1.20	26.2	33.6
			61.8	1.82	32.3	62.7
29979.38	*t*-CH_3CH_2OH	3_{12}-3_{03}	[1]81.2	0.41	12.5	5.5
			62.0	-0.29	11.5	-3.6
30001.55	SO	1_0-0_1	84.4	-11.73	13.5	-150.3
			64.2	-27.56	15.4	-451.7
			8.9	-1.25	21.2	-30.5
			-32.4	-0.27	22.9	-6.5
			-106.3	-0.54	10.9	-6.3
30180.60	NaCN/NaNC^{BC}	2_{12}-1_{11}	74.4	-0.19	20.4	-4.2
30239.76	U	——	64.0	-0.22	16.1	-3.8
30256.04	U	——	64.0	-0.17	28.6	-5.1
30500.20	Hydrogen	H(85)γ	72.9	0.90	37.3	35.6
			51.1	0.38	18.6	7.5
30513.96	Hydrogen	H(106)ζ	79.1	0.29	46.4	14.4
30707.38	Hydrogen	H(93)δ	74.3	0.43	49.7	22.7
30722.67	U?	——	64.0	0.22	90.9	21.3
31002.30	CH_3CH_2CHO	3_{21}-2_{12}	65.9	-0.25	33.6	-8.9

Continued on next page

Table 3.7 – Line Identifications and Fit Parameters towards K6

Line Rest Frequency (MHz)	Species	Transition	Velocity (km s^{-1})	Height (mJy × arcsec^{-2})	Width (km s^{-1})	$\int I_v dv$ (mJy arcsec^{-2} × km s^{-1})
31106.15	CH_3OCH_3	2_{11}-2_{02}	65.1	-1.06	23.2	-26.1
		EE/AA/AE/EA				
31186.68	Hydrogen	H(74)β	66.8	2.23	39.9	102.6
31199.39	Helium	He(74)β	73.5	0.22	36.9	8.7
31223.31	Hydrogen	H(59)α	78.3	7.51	29.2	233.7
			55.7	5.95	23.1	146.5
31236.04	Helium	He(59)α	89.7	0.32	16.6	5.7
			65.3	0.71	34.8	26.2
31262.33	NaCN/NaNC	2_{02}-1_{01}	62.0	-0.66	15.8	-11.1
31424.94	NH_3	(12,12)	84.5	-2.50	13.3	-35.5
			65.2	-7.30	19.4	-150.5
			8.2	-0.56	25.6	-15.4
31482.38	Hydrogen	H(99)ϵ	75.6	0.31	45.0	14.8
31583.40	Hydrogen	H(84)γ	77.7	0.84	33.4	30.0
			51.2	0.49	23.6	12.2
31698.47	Hydrogen	H(92)δ	68.7	0.28	33.6	10.1
31727.07	*cis*-CH_2OHCHO	5_{23}-5_{14}	77.6	-0.25	13.7	-3.6
			60.9	-0.26	11.7	-3.2
31833.03	*cis*-CH_2OHCHO	6_{24}-6_{15}	61.2	-0.22	20.1	-4.8
31911.20	CH_3CH_2CHO	3_{21}-2_{20}	65.4	-0.27	10.0	-2.9
31951.78	HC_5N	12-11	84.8	-0.34	8.6	-3.1
			64.2	-1.78	12.6	-23.9
32373.67	NaCN/NaNC	2_{11}-1_{10}	62.8	-0.29	28.1	-8.6
32398.56	$^{13}CH_3OH^{Maser}$	$4_{-1,4}$-3_{03}	82.3	0.93	12.6	12.5
			62.8	0.40	10.7	4.6

Continued on next page

Table 3.7 – Line Identifications and Fit Parameters towards K6

Line Rest Frequency (MHz)	Species	Transition	Velocity (km s^{-1})	Height (mJy × arcsec^{-2})	Width (km s^{-1})	$\int I_v dv$ (mJy arcsec^{-2} × km s^{-1})
32432.32	Hydrogen	H(98)ϵ	74.0	0.26	44.3	12.1
32468.48	Hydrogen	H(73)β	78.2	1.92	32.8	66.8
			55.1	1.36	23.8	34.4
32627.30	*l*-C_3H^{Adj}	J=$\frac{3}{2}$-$\frac{1}{2}$ Ω=$\frac{1}{2}$ F=2-1f	63.7	-0.50	17.2	-9.2
			14.5	-0.16	12.0	-2.1
			[2]-2.5	-0.31	18.8	-6.1
32640.21	U	——	[3]64.0	-0.31	26.2	-8.7
32627.30	*l*-C_3H	J=$\frac{3}{2}$-$\frac{1}{2}$ Ω=$\frac{1}{2}$ F=2-1f	-108.5	-0.20	21.1	-4.5
32660.65	*l*-C_3H^{Adj}	J=$\frac{3}{2}$-$\frac{1}{2}$ Ω=$\frac{1}{2}$ F=2-1e	62.6	-0.66	11.7	-8.3
32663.38	*l*-C_3H^{Adj}	J=$\frac{3}{2}$-$\frac{1}{2}$ Ω=$\frac{1}{2}$ F=1-0e	61.8	-0.19	10.5	-2.1
32660.65	*l*-C_3H^{Adj}	J=$\frac{3}{2}$-$\frac{1}{2}$ Ω=$\frac{1}{2}$ F=2-1e	17.4	-0.20	24.8	-5.3
			[4]-2.1	-0.33	14.7	-5.2
32672.52	*cis*-CH_2OHCHO	4_{22}-4_{13}	83.8	-0.42	12.1	-5.4
			62.3	-0.63	16.0	-10.8
32660.65	*l*-C_3H	J=$\frac{3}{2}$-$\frac{1}{2}$ Ω=$\frac{1}{2}$ F=2-1e	-105.6	-0.20	15.5	-3.3
32709.18	CH_3CHO	4_{04}-3_{13}A	63.8	-0.34	15.3	-5.6
32718.50	Hydrogen	H(83)γ	66.7	0.92	45.5	46.0
32732.67	Hydrogen	H(91)δ	71.7	0.62	40.6	26.8
32742.82	*t*-CH_3CH_2OH	4_{13}-4_{04}	62.5	-0.56	15.1	-9.0
32852.20	Hydrogen	H(58)α	83.7	5.60	27.2	169.2
			60.0	8.10	28.0	244.9
32865.58	Helium	He(58)α	83.5	0.52	25.5	14.2
			60.3	0.65	23.4	16.1
32978.23	CH_3OCH_3	3_{12}-3_{03}	66.5	-1.41	25.0	-37.5
		EE/AA/AE/EA				

Continued on next page

Table 3.7 – Line Identifications and Fit Parameters towards K6

Line Rest Frequency (MHz)	Species	Transition	Velocity (km s^{-1})	Height (mJy × arcsec^{-2})	Width (km s^{-1})	$\int I_v dv$ (mJy arcsec^{-2} × km s^{-1})
33051.62	CH_3C_3N	8_0-7_0/8_1-7_1	85.6	-0.27	12.8	-3.7
			64.7	-0.52	13.6	-7.4
33156.85	NH_3	(13,13)	83.1	-1.40	11.7	-17.4
			64.7	-3.52	14.7	-54.9
			3.8	-0.35	16.2	-6.0
33181.67	Hydrogen	H(103)ζ	68.4	0.18	54.8	10.5
33236.47	CH_3CHO	4_{04}-3_{13}E	62.4	-0.43	13.4	-6.2
33345.23	*cis*-CH_2OHCHO^{BC}	7_{25}-7_{16}	72.5	-0.26	25.9	-7.1
33354.01	*cis*-CH_2OHCHO^{BC}	2_{12}-1_{01}	68.1	-0.23	37.7	-9.1
33420.88	Hydrogen	H(97)ϵ	68.2	0.34	49.7	18.2
33455.99	U	——	64.0	-0.21	11.8	-2.6
33562.12	$(CH_3)_2CO$?	3_{03}-2_{12}EE	[5]68.3	-0.30	16.0	-5.1
33704.82	CH_2NH	1_{11}-2_{02}	82.1	-5.77	14.5	-89.3
			63.2	-8.11	15.9	-137.5
33751.37	CCS	3_2-2_1	83.7	-0.87	10.8	-10.0
			64.0	-5.79	17.7	-107.5
			7.3	-0.41	30.6	-10.7
			-34.5	-0.24	15.4	-4.0
			-105.7	-0.24	39.5	-10.2
33812.37	Hydrogen	H(90)δ	69.8	0.53	46.8	26.5
33821.51	Hydrogen	H(72)β	70.3	2.22	46.9	116.9
33908.67	Hydrogen	H(82)γ	82.4	0.77	27.4	22.3
			59.2	0.84	26.4	23.5
34092.97	$(CH_3)_2CO$	3_{13}-2_{02}EE	62.7	-0.35	13.3	-4.9
34156.88	CH_3OCHO	3_{13}-2_{12}E/A	60.1	-0.67	21.2	-15.2

Continued on next page

Table 3.7 – Line Identifications and Fit Parameters towards K6

Line Rest Frequency (MHz)	Species	Transition	Velocity (km s^{-1})	Height (mJy × arcsec^{-2})	Width (km s^{-1})	$\int I_v dv$ (mJy arcsec^{-2} × km s^{-1})
34225.47	*cis*-CH_2OHCHO	3_{21}-3_{12}	64.9	-0.26	25.3	-7.1
34285.54	U	——	64.0	-0.34	14.3	-5.2
34351.45	H_2CS	1_{01}-0_{00}	63.8	-2.46	14.7	-38.5
34408.63	HSCN	3_{03}-2_{02}	62.3	-0.88	13.2	-12.4
34450.03	Hydrogen	H(96)ϵ	65.7	0.36	67.9	25.7
34596.38	Hydrogen	H(57)α	90.0	3.08	18.9	70.3
			64.5	8.28	37.5	332.2
34610.48	Helium	He(57)α	82.9	0.65	21.7	14.9
			61.0	0.68	17.8	12.9
34614.38	HC_5N	13-12	62.4	-1.43	13.5	-20.5
34674.19	U	——	64.0	0.23	59.2	14.8
34684.37	$CCCS^B$	6-5	[6]67.8	-0.71	22.4	-16.9
34768.97	*t*-CH_2CHCHO	4_{14}-3_{13}	83.5	-0.26	9.3	-2.6
			65.2	-0.24	9.5	-2.4
34824.07	CH_3CH_2CN	4_{14}-3_{13}	64.6	-1.98	12.4	-26.1
34940.09	Hydrogen	H(89)δ	66.0	0.42	40.7	18.2
35065.73	CH_2NH	3_{03}-2_{12}	[1]85.7	1.82	13.1	25.3
			[1]67.0	2.37	17.0	42.9
35134.30	NH_3	(14,14)	83.7	-0.79	9.6	-8.0
			65.7	-2.54	16.1	-43.5
35157.27	Hydrogen	H(81)γ	83.8	0.64	27.7	18.7
			57.3	0.87	27.9	25.7
35250.77	Hydrogen	H(71)β	78.2	1.79	35.4	67.5
			54.5	1.42	24.1	36.5
35267.41	$H^{13}CCCN$	4-3	63.4	-2.09	14.4	-32.1

Continued on next page

Table 3.7 – Line Identifications and Fit Parameters towards K6

Line Rest Frequency (MHz)	Species	Transition	Velocity (km s^{-1})	Height (mJy × arcsec^{-2})	Width (km s^{-1})	$\int I_v dv$ (mJy arcsec^{-2} × km s^{-1})
35360.93	*c*-C_3H_2	4_{40}-4_{31}	64.1	-0.91	10.2	-9.8
35468.17	$(CH_3)_2CO$?	2_{21}-1_{10}AA	[7]65.8	-0.34	10.2	-3.7
35521.88	Hydrogen	H(95)ϵ	66.8	0.31	49.1	16.3
35586.91	U?	——	64.0	-0.27	34.5	-10.0
35593.41	CH_3OCH_3	4_{13}-4_{04}	60.8	-0.98	28.9	-30.3
		EE/AA/AE/EA				
35722.21	CH_3CH_2CN	4_{04}-3_{03}	83.3	-0.55	9.7	-5.7
			64.8	-2.49	12.4	-32.7
35733.12	$^{13}CH_3CN$	2_0-1_0/2_1-1_1	65.4	-0.94	22.6	-22.7
35779.25	*Z*-CH_3CHNH	2_{12}-1_{11}A	66.6	-0.24	25.3	-6.3
35791.73	CH_3CH_2CN	4_{23}-3_{22} F=4-3	64.9	-0.39	27.4	-11.4
35837.33	CH_3CHO	2_{12}-1_{10}E	64.6	-0.36	13.5	-5.1
35865.83	$CH_3CH_2CN^{Adj}$	4_{22}-3_{21} F=4-3	85.3	-0.24	14.1	-3.5
			63.8	-0.41	15.8	-6.8
35893.63	CH_3OCHO?	2_{12}-1_{01}E	[8]61.0	-0.24	20.0	-5.1
35903.32	*cis*-CH_2OHCHO^{Adj}	2_{20}-2_{11}	85.0	-0.15	16.3	-2.6
			60.1	-0.22	25.1	-5.9
35906.98	U	——	64.0	-0.26	13.8	-3.8
36102.22	CH_3OCHO	3_{03}-2_{02}E	62.3	-0.55	12.8	-7.5
36104.79	CH_3OCHO	3_{03}-2_{02}A	62.2	-0.54	10.9	-6.2
36118.53	Hydrogen	H(88)δ	86.4	0.40	37.5	16.0
			55.1	0.47	24.9	12.5
36169.29	$CH_3OH^{Maser,Adj}$	$4_{-1,4}$-3_{03}	82.9	182.10	9.2	1614.3
			1.5	0.33	17.9	6.6
36202.04	SO	2_3-2_2	[9]64.9	0.37	10.1	3.9

Continued on next page

Table 3.7 – Line Identifications and Fit Parameters towards K6

Line Rest Frequency (MHz)	Species	Transition	Velocity ($\mathrm{km\,s^{-1}}$)	Height (mJy $\times$ arcsec^{-2})	Width ($\mathrm{km\,s^{-1}}$)	$\int I_v dv$ (mJy arcsec^{-2} $\times$ $\mathrm{km\,s^{-1}}$)
36237.99	$HC^{13}CCN$	4-3	81.4	-0.63	10.5	-7.0
			[10]63.3	-2.95	11.9	-37.4
36241.44	$HCC^{13}CN$	4-3	64.0	-1.99	18.0	-38.1
36299.95	H_2COH^+	1_{11}-2_{02}	80.4	-0.37	11.4	-4.5
			62.8	-0.56	12.6	-7.5
36309.63	SiS	2-1	62.9	-1.00	12.9	-13.8
36392.32	HC_3N	4-3	82.5	-9.27	11.3	-102.3
			62.8	-21.17	16.4	-370.7
			3.6	-0.89	13.9	-20.8
			-107.2	-0.34	8.0	-3.0
36417.24	*t*-CH_3CH_2OH	5_{14}-5_{05}	80.1	-0.31	11.0	-3.7
			62.0	-0.34	11.8	-4.3
36466.26	Hydrogen	H(56)α^B	[11]87.3	5.15	20.1	115.2
			[11]60.2	8.66	34.5	317.6
36481.12	Helium	He(56)α	84.7	0.54	27.1	15.6
			63.9	0.48	9.6	4.9
36488.81	OCS	3-2	[12]62.8	-1.40	11.5	-17.1
36492.76	U	——	64.0	-0.33	19.0	-6.7
36638.68	Hydrogen	H(94)ϵ	73.6	0.26	42.2	11.9
36657.47	CH_3OCHO	3_{22}-2_{21}A	65.9	-0.27	12.4	-3.6
36739.67	CH_3CH_2CN	4_{13}-3_{12}	82.0	-0.41	10.7	-4.7
			62.6	-2.11	11.6	-26.0
36761.72	Hydrogen	H(70)β	87.1	1.16	23.4	29.0
			59.6	1.89	32.7	65.9
36777.28	$CH_3^{13}CN$	2_0-1_0/2_1-1_1	76.1	-0.44	30.7	-14.4

Continued on next page

Table 3.7 – Line Identifications and Fit Parameters towards K6

Line Rest Frequency (MHz)	Species	Transition	Velocity (km s^{-1})	Height (mJy × arcsec^{-2})	Width (km s^{-1})	$\int I_v dv$ (mJy arcsec^{-2} × km s^{-1})
			64.2	-0.50	17.3	-9.2
36795.47	CH_3CN	2_0-1_0/2_1-1_1	79.3	-8.75	21.4	-199.7
			64.1	-18.38	18.2	-355.9
			12.4	-0.63	22.9	-43.8
			-89.4	-0.28	34.1	-10.3
			-103.6	-0.47	14.6	-7.4
36930.70	*Z*-CH_3CHNH	2_{02}-1_{01}E/A	59.2	-0.59	25.8	-16.3
36939.70	U	——	64.0	-0.30	29.0	-9.4
37018.92	CH_2CHCN	4_{14}-3_{13}	79.7	-0.50	10.9	-5.8
			62.8	-1.93	11.5	-23.6
37106.79	U	——	64.0	-0.21	38.3	-8.7
37182.66	$CH_3C_3N^B$	9_1-8_1/9_0-7_0	[13]63.4	-0.37	10.8	-4.3
37276.99	HC_5N	14-13	83.4	-0.43	12.2	-5.6
			63.6	-1.56	10.7	-17.7
37350.57	Hydrogen	H(87)δ	82.1	0.42	40.5	17.9
37370.88	U?	——	64.0	-0.29	16.1	-4.9
37385.12	NH_3^B	(15,15)	[14]78.4	-2.33	16.1	-39.8
			[14]60.8	-1.61	17.2	-29.4
			14.5	-0.41	15.2	-6.6
37464.17	CH_3CHO	2_{12}-1_{11}A	80.8	-2.03	10.1	-20.9
			63.3	-4.84	12.8	-64.4
37476.99	U	——	[15]64.0	-0.29	9.9	-3.0
37686.87	CH_3CHO	2_{12}-1_{11}E	80.4	-1.53	11.8	-19.2
			62.6	-4.47	12.7	-58.4
37703.70	CH_3OH	$7_{-2,6}$-$8_{-1,8}$	83.4	-1.34	10.8	-15.5

Continued on next page

Table 3.7 – Line Identifications and Fit Parameters towards K6

Line Rest Frequency (MHz)	Species	Transition	Velocity ($\mathrm{km\,s^{-1}}$)	Height (mJy $\times$ $\mathrm{arcsec^{-2}}$)	Width ($\mathrm{km\,s^{-1}}$)	$\int I_v dv$ (mJy $\mathrm{arcsec^{-2}}$ $\times$ $\mathrm{km\,s^{-1}}$)
			62.8	-0.96	12.1	-12.4
37802.79	Hydrogen	H(93)ϵ	75.2	0.33	42.7	15.2
37844.59	Hydrogen	H(79)γ	87.6	0.64	19.6	13.4
			61.2	0.81	33.6	29.0
37904.85	CH_2CHCN	4_{04}-3_{03}	81.0	-1.00	11.7	-12.4
			63.2	-3.64	11.9	-44.0
38241.47	$Na^{37}Cl$?	3-2	64.1	-0.27	10.2	-3.0
38271.02	*E*-HNCHCN	4_{04}-3_{03}	63.0	-0.51	9.7	-5.3
38360.27	Hydrogen	H(69)β	87.4	1.26	20.2	27.0
			60.0	2.04	34.9	75.8
38439.65	U	——	64.0	-0.29	12.6	-3.9
38445.25	U	——	64.0	-0.27	10.4	-3.0
38473.36	Hydrogen	H(55)α	88.7	4.26	19.6	91.7
			62.6	7.63	34.6	281.1
38489.04	Helium	He(55)α	88.8	0.38	14.4	5.8
			58.0	0.62	28.0	18.4
38506.04	CH_3CHO	2_{02}-1_{01}E	81.1	-3.27	9.8	-33.6
			63.4	-8.42	13.3	-113.7
38512.11	CH_3CHO	2_{02}-1_{01}A	81.1	-2.89	12.5	-38.1
			63.1	-9.58	12.6	-125.5
			12.5	-0.51	14.6	-13.4
38639.30	Hydrogen	H(86)δ	74.4	0.33	44.9	16.0
			52.7	0.29	23.1	7.2
38847.73	CH_2CHCN	4_{13}-3_{12}	82.6	-0.57	9.6	-5.8
			63.7	-1.86	13.4	-26.5

Continued on next page

Table 3.7 – Line Identifications and Fit Parameters towards K6

Line Rest Frequency (MHz)	Species	Transition	Velocity ($\mathrm{km\,s^{-1}}$)	Height (mJy $\times$ arcsec^{-2})	Width ($\mathrm{km\,s^{-1}}$)	$\int I_v dv$ (mJy arcsec^{-2} $\times$ $\mathrm{km\,s^{-1}}$)
38908.94	U?	——	64.0	-0.32	9.1	-3.1
38976.13	CH_3OCHO	3_{12}-2_{11}E	64.3	-0.25	14.2	-3.7
38980.81	CH_3OCHO	3_{12}-2_{11}A	63.9	-0.35	13.4	-5.0
39016.76	Hydrogen	H(92)ϵ	69.6	0.24	54.2	13.6
39047.30	CH_3OCH_3	5_{14}-5_{05}	69.9	-0.54	27.7	-15.8
		EE/AA/AE/EA				
39291.42	Hydrogen	H(78)γ	69.2	0.55	48.0	27.8
39362.50	CH_3CHO	2_{11}-1_{10}E	81.0	-1.20	8.9	-11.4
			63.9	-4.21	12.0	-53.7
39571.33	CCCN	N=4-3 J=$\frac{9}{2}$-$\frac{7}{2}$	81.1	-0.34	7.7	-2.8
			64.1	-0.48	11.1	-5.7
39581.58	c-H_2COCH_2?	1_{01}-0_{00}	63.6	-0.57	12.9	-7.9
39590.21	$CCCN^B$	N=4-3 J=$\frac{7}{2}$-$\frac{5}{2}$	[16]66.0	-0.57	8.2	-5.0
39594.29	CH_3CHO	2_{11}-1_{10}A	81.8	-1.63	13.0	-22.5
			63.1	-3.67	11.7	-49.9
39712.47	U	——	64.0	-0.52	13.2	-7.4
39725.38	NH_2CN	2_{12}-1_{11}	64.7	-0.48	21.7	-11.1
39742.55	HCCNC	4-3	62.9	-0.51	8.9	-4.9
39924.77	CH_2CN	2_{12}-1_{11}	67.1	-0.81	13.0	-11.2
39927.87	U	——	[17]64.0	-0.84	10.7	-9.6
39941.41	NH_3^B	(16,16)	[18]79.0	-1.58	11.6	-19.6
			64.7	-2.06	10.8	-23.7
39956.70	c-H_2C_3O	3_{13}-2_{12}	62.4	-0.75	12.7	-10.2
39988.02	Hydrogen	H(85)δ	73.5	0.49	37.6	19.6
40039.02	H_2CCO	2_{12}-1_{11}	63.4	-0.99	12.2	-12.9

Continued on next page

Table 3.7 – Line Identifications and Fit Parameters towards K6

Line Rest Frequency (MHz)	Species	Transition	Velocity ($\mathrm{km\,s^{-1}}$)	Height (mJy × $\mathrm{arcsec^{-2}}$)	Width ($\mathrm{km\,s^{-1}}$)	$\int I_v dv$ (mJy $\mathrm{arcsec^{-2}}$ × $\mathrm{km\,s^{-1}}$)
40052.88	Hydrogen	H(68)β	87.4	1.20	23.0	29.3
			60.9	1.94	33.1	68.3
40210.49	CH_3NC	2_1-1_1	60.6	-1.39	15.9	-23.4
40232.80	CH_2CN	2_{02}-1_{01} J=$\frac{3}{2}$-$\frac{1}{2}$	[19]62.6	-0.38	29.6	-12.0
		F1=$\frac{3}{2}$-$\frac{1}{2}$ F=$\frac{5}{2}$-$\frac{3}{2}$				
40239.70	CH_2CN	2_{02}-1_{01} J=$\frac{5}{2}$-$\frac{3}{2}$	[19]83.3	-1.53	8.2	-12.8
		F1=$\frac{7}{2}$-$\frac{5}{2}$ F=$\frac{7}{2}$-$\frac{5}{2}$	[18]62.8	-4.76	16.7	-81.6
40242.22	CH_2CN	2_{02}-1_{01} J=$\frac{5}{2}$-$\frac{3}{2}$	[19]63.4	-2.56	9.5	-26.0
		F1=$\frac{5}{2}$-$\frac{3}{2}$ F=$\frac{5}{2}$-$\frac{3}{2}$				
40244.34	CH_2CN	2_{02}-1_{01} J=$\frac{5}{2}$-$\frac{3}{2}$	[19]63.1	-2.16	18.3	-42.0
		F1=$\frac{5}{2}$-$\frac{3}{2}$ F=$\frac{7}{2}$-$\frac{5}{2}$				
40247.54	CH_2CN	2_{02}-1_{01} J=$\frac{3}{2}$-$\frac{1}{2}$	[19]62.2	-3.63	12.5	-48.1
		F1=$\frac{5}{2}$-$\frac{3}{2}$ F=$\frac{5}{2}$-$\frac{3}{2}$				
40249.34	CH_2CN	2_{02}-1_{01} J=$\frac{3}{2}$-$\frac{3}{2}$	[19]60.1	-0.66	9.2	-6.5
		F1=$\frac{5}{2}$-$\frac{3}{2}$ F=$\frac{5}{2}$-$\frac{5}{2}$				
40251.86	CH_2CN	2_{02}-1_{01} J=$\frac{3}{2}$-$\frac{3}{2}$	[19]64.4	-0.64	9.5	-6.5
		F1=$\frac{5}{2}$-$\frac{3}{2}$ F=$\frac{5}{2}$-$\frac{5}{2}$				
40253.88	CH_2CN	2_{02}-1_{01} J=$\frac{3}{2}$-$\frac{1}{2}$	[19]63.9	-0.85	17.1	-15.5
		F1=$\frac{5}{2}$-$\frac{3}{2}$ F=$\frac{3}{2}$-$\frac{3}{2}$				
40256.79	CH_2CN	2_{02}-1_{01} J=$\frac{3}{2}$-$\frac{1}{2}$	[19]62.9	-0.79	17.5	-14.7
		F1=$\frac{3}{2}$-$\frac{3}{2}$ F=$\frac{5}{2}$-$\frac{5}{2}$				
40259.84	CH_2CN	2_{02}-1_{01} J=$\frac{3}{2}$-$\frac{3}{2}$	[19]62.8	-0.48	12.4	-6.4
		F1=$\frac{3}{2}$-$\frac{5}{2}$ F=$\frac{3}{2}$-$\frac{5}{2}$				
40352.77	$Si^{18}O$	1-0	65.1	-0.77	10.6	-8.8
40417.95	H_2CCO	2_{02}-1_{01}	64.7	-0.49	12.8	-6.7

Continued on next page

Table 3.7 – Line Identifications and Fit Parameters towards K6

Line Rest Frequency (MHz)	Species	Transition	Velocity (km s^{-1})	Height (mJy × arcsec^{-2})	Width (km s^{-1})	$\int I_v dv$ (mJy arcsec^{-2} × km s^{-1})
40455.62	H_2NCO^+?	2_{02}-1_{01} F=1-0	84.7	-0.28	20.1	-6.0
			59.7	-0.71	8.9	-6.7
40465.01	$CCCS^{BC}$	7-6	65.3	-0.41	21.1	-9.2
40477.24	U	——	64.0	-0.36	10.5	-4.1
40484.03	U	——	64.0	-0.40	14.3	-6.1
40630.50	Hydrogen	H(54)α	81.5	6.30	31.6	211.9
			55.4	5.76	23.8	145.9
40647.06	Helium	He(54)α	86.6	0.58	20.0	12.4
			56.1	0.68	25.7	18.6
40658.60	CH_2CN	2_{11}-1_{10} J=$\frac{5}{2}$-$\frac{3}{2}$	61.7	-0.94	22.8	-22.9
40793.84	H_2CCO	2_{11}-1_{10}	63.3	-1.16	15.2	-18.8
40812.95	Hydrogen	H(77)γ	88.7	0.53	20.7	11.7
			57.5	0.85	27.4	24.7
40875.44	NH_2CHO	2_{12}-1_{11}	80.1	-5.32	15.9	-98.4
			62.4	-7.41	12.5	-102.1
41313.99	CH_3C_3N	10_1-9_1/10_0-9_0	63.8	-0.29	29.2	-9.0
41400.26	Hydrogen	H(84)δ	65.2	0.44	40.6	19.2
41846.55	Hydrogen	H(67)β	81.4	1.52	33.1	53.7
			56.3	1.60	28.4	48.4
41863.60	Helium	He(67)β	88.5	0.21	7.6	1.7
			63.9	0.20	51.8	11.1
42000.64	Hydrogen	H(95)ζ	65.0	0.39	8.2	3.4
42011.43	U	——	64.0	-0.30	8.8	-2.8
42031.94	c-H_2C_3O	3_{03}-2_{02}	61.3	-0.39	13.1	-5.5
42035.74	U	——	64.0	-0.24	18.0	-4.6

Continued on next page

Table 3.7 – Line Identifications and Fit Parameters towards K6

Line Rest Frequency (MHz)	Species	Transition	Velocity ($\mathrm{km\,s^{-1}}$)	Height (mJy $\times$ arcsec^{-2})	Width ($\mathrm{km\,s^{-1}}$)	$\int I_v dv$ (mJy arcsec^{-2} $\times$ $\mathrm{km\,s^{-1}}$)
42081.49	U	——	64.0	0.31	9.9	3.3
42139.19	*c*-C_3H_2	5_{41}-5_{32}	63.3	-0.66	10.0	-7.1
42318.18	$NH_2^{13}CHO$	2_{02}-1_{01}	63.8	-0.45	10.9	-5.2
42373.34	^{30}SiO	1-0	81.4	-1.96	11.2	-23.4
			63.1	-10.02	10.6	-117.5
42386.06	NH_2CHO	2_{02}-1_{01}	80.4	-6.15	13.9	-91.3
			62.5	-13.66	12.9	-187.0
			6.0	-0.62	14.2	-14.5
42414.09	Hydrogen	H(76)γ	85.8	0.58	28.5	17.7
			58.9	0.67	26.0	18.6
42602.15	HC_5N	16-15	63.3	-0.83	13.4	-11.9
42674.19	HCS^+	1-0	81.8	-0.33	7.4	-2.6
			64.4	-4.12	13.2	-57.8
			8.4	-0.49	15.8	-8.2
42839.92	NH_3	(17,17)	63.5	-1.68	11.5	-20.6
42862.60	U	——	64.0	-0.61	12.0	-7.8
42879.94	^{29}SiO	1-0	82.1	-3.06	9.2	-28.9
			64.3	-12.73	11.6	-154.9
			4.8	-0.61	8.3	-13.5
42951.97	Hydrogen	H(53)α	84.2	6.67	28.5	202.1
			56.7	7.66	27.8	226.9
42969.47	Helium	He(53)α	70.2	0.65	49.2	33.8
43303.71	*t*-HCOOH	2_{12}-1_{11}	64.2	-1.67	10.6	-18.8
43423.85	SiO^{Adj}	1-0	83.8	-14.45	9.8	-137.4
			62.5	-25.83	26.0	-707.5

Continued on next page

Table 3.7 – Line Identifications and Fit Parameters towards K6

Line Rest Frequency (MHz)	Species	Transition	Velocity (km s^{-1})	Height (mJy × arcsec^{-2})	Width (km s^{-1})	$\int I_v dv$ (mJy arcsec^{-2} × km s^{-1})
			15.3	-2.99	11.5	-38.7
			3.1	-6.16	10.3	-67.5
			-28.4	-1.02	31.0	-33.8
			-67.9	-1.03	20.7	-22.8
			-99.3	-1.66	17.0	-30.1
			-108.1	-1.48	7.9	-12.4
43516.19	CH_3CH_2CN	5_{15}-4_{14}	64.4	-1.37	15.2	-22.2
43748.95	Hydrogen	H(66)β	86.9	1.38	25.9	38.0
			59.1	1.91	34.0	69.2
43901.51	SiN	N=1-0 J= $\frac{3}{2}$ - $\frac{1}{2}$ F = $\frac{5}{2}$ - $\frac{3}{2}$	64.0	-0.64	9.3	-6.3
43954.45	NH_2CHO	2_{11}-1_{10}	78.3	-4.96	21.0	-110.8
			61.7	-7.95	13.4	-113.3
43963.04	$HNCO^B$	2_{02}-1_{01}	[20]60.0	-0.55	20.2	-11.9
44069.48	CH_3OH^{Maser}	7_{07}-6_{16}++	83.2	35.09	7.6	244.6
44084.17	$H^{13}CCCN$	5-4	63.5	-2.18	13.2	-30.5
44100.09	Hydrogen	H(75)γ	85.3	1.11	11.3	13.3
			64.9	1.25	14.7	19.6
44104.78	c-C_3H_2	3_{21}-3_{12}	83.5	-0.80	6.3	-5.3
			64.1	-3.89	10.0	-41.3
44338.89	CH_3NH_2?	1_0E1+1-0_0E1+1	81.1	-0.26	21.5	-6.0
			62.6	-0.53	8.8	-5.0
44430.71	$Hydrogen^B$	H(82)δ	[21]73.2	0.70	61.6	45.6
44469.22	E-CH_3CHNH^{BC}	1_{10}-1_{01}A	[22]74.9	-0.54	9.8	-5.6
44497.60	$CC^{34}S$	4_3-3_2	62.7	-0.49	8.1	-4.2

Continued on next page

Table 3.7 – Line Identifications and Fit Parameters towards K6

Line Rest Frequency (MHz)	Species	Transition	Velocity (km s^{-1})	Height (mJy × arcsec^{-2})	Width (km s^{-1})	$\int I_v dv$ (mJy arcsec^{-2} × km s^{-1})
44587.40	*c*-H_2C_3O	3_{12}-2_{11}	64.0	-0.92	10.6	-10.3
44596.99	CH_3CH_2CN	5_{05}-4_{04}	64.5	-2.80	10.8	-32.1
44659.99	Contam	——	64.0	0.24	11.8	3.0
44730.27	Contam	——	71.8	0.55	10.0	5.9
44768.91	Contam	——	69.5	0.71	20.1	15.0
44773.87	Contam	——	62.9	0.94	24.8	24.8
44792.73	Contam	——	64.0	0.20	31.0	6.5
44831.00	Contam	——	70.3	0.21	27.1	6.0
44878.10	Contam	——	72.0	0.66	10.0	7.0
44879.04	Contam	——	64.0	0.28	15.7	4.7
44911.75	*t*-HCOOH	2_{02}-1_{01}	81.1	-0.84	10.9	-9.7
			63.9	-2.23	11.1	-26.4
44955.78	Contam	——	75.9	0.41	10.1	4.4
			64.0	0.54	10.0	5.7
44979.54	*l*-C_3H^+ ^{Adj}	$_{2-1}$	80.0	-0.21	15.0	-3.3
			64.7	-0.42	15.2	-6.8
			-2.4	-0.16	30.5	-5.3
45103.87	*c*-$H^{13}CCCH^{Adj}$	2_{11}-2_{02}	81.0	-0.20	14.4	-3.1
			64.0	-0.28	10.8	-3.2
45259.08	NaCN/NaNC	3_{13}-2_{12}	65.2	-0.32	17.5	-5.9
45264.72	HC_5N	17-16	79.2	-0.31	10.7	-3.5
			63.0	-0.77	12.4	-10.2
45297.35	$HC^{13}CCN$	5-4	82.3	-0.70	10.5	-7.8
			64.1	-1.64	11.6	-20.2
45301.71	$HCC^{13}CN$	5-4	81.7	-0.67	12.9	-9.2

Continued on next page

Table 3.7 – Line Identifications and Fit Parameters towards K6

Line Rest Frequency (MHz)	Species	Transition	Velocity (km s^{-1})	Height (mJy × arcsec^{-2})	Width (km s^{-1})	$\int I_v dv$ (mJy arcsec^{-2} × km s^{-1})
			62.9	-1.84	11.2	-21.9
45379.03	CCS	4_3-3_2	81.2	-1.86	10.1	-19.9
			64.2	-6.03	12.4	-77.8
			5.2	-0.20	15.9	-3.3
45395.79	CH_3OCHO^B	4_{14}-3_{13}E	[23]66.4	-0.42	13.6	-6.1
45397.38	CH_3OCHO	4_{14}-3_{13}A	63.3	-0.36	10.1	-3.9
45453.72	Hydrogen	H(52)α	84.7	3.28	28.3	99.0
			64.6	6.79	33.2	240.0
45463.42	$^{13}C^{34}S$	1-0	63.8	-0.73	12.3	-9.5
45472.24	Helium	He(52)α	85.9	0.19	17.1	3.5
			66.1	0.55	35.5	20.7
45490.34	HC_3N	5-4	81.0	-8.94	12.2	-115.9
			63.1	-15.77	14.7	-246.3
45495.97	*E*-CH_3CHNH^B	2_{11}-2_{02}E	[24]57.2	-0.60	25.8	-16.5
45490.34	HC_3N	5-4	3.4	-0.72	12.1	-12.6
			-105.3	-0.38	8.1	-3.3
45547.64	*g'Ga*-$(CH_2OH)_2$	4_{14}v=1-3_{13}v=0	64.4	-0.21	11.9	-2.7
45566.66	*E*-CH_3CHNH	2_{11}-2_{02}A	61.8	-0.47	14.2	-7.1
45600.79	Contam	——	61.6	0.59	18.7	11.8
			47.2	0.31	10.8	3.6
45644.07	U?		64.0	-0.23	11.3	-2.8
45667.55	Contam	——	73.6	0.47	9.8	5.0
			61.1	0.56	15.2	9.0
45768.44	Hydrogen	H(65)β	70.5	2.11	40.7	91.5
45778.89	Contam	——	64.0	0.41	19.5	8.5

Continued on next page

Table 3.7 – Line Identifications and Fit Parameters towards K6

Line Rest Frequency (MHz)	Species	Transition	Velocity (km s^{-1})	Height (mJy × arcsec^{-2})	Width (km s^{-1})	$\int I_v dv$ (mJy arcsec^{-2} × km s^{-1})
45787.10	Helium	He(65)β	68.5	0.17	37.9	6.7
45842.95	Contam	——	64.0	0.72	15.2	11.7
45876.67	Hydrogen^B	H(74)γ	[25]84.7	0.25	16.1	4.4
			[25]73.8	0.34	59.4	21.8
45877.81	HSCN^B	4_{04}-3_{03}	62.1	-0.53	7.0	-4.0
45909.51	$CH_3CH_2CN^B$	5_{14}-4_{13}	[26]82.9	-0.53	8.1	-4.5
			[26]72.9	0.39	7.1	2.9
			[26]63.8	-0.58	6.9	-4.3
45921.88	Contam	——	64.0	0.24	22.4	5.8
45935.39	Hydrogen	H(87)ϵ	71.9	0.34	47.3	17.3
45956.07	Contam	——	64.0	0.21	30.9	6.9
46057.33	Hydrogen	H(81)δ	70.1	0.50	42.9	22.6
46112.17	Hydrogen	H(92)ζ	79.0	0.19	47.7	9.4
46123.30	NH_3	(18,18)	81.2	-0.79	13.6	-11.4
			64.1	-1.69	14.2	-25.5
46247.56	^{13}CS	1-0	81.1	-3.54	10.9	-41.1
			64.3	-11.24	14.4	-172.0
			5.6	-1.48	13.1	-24.2
46266.93	CH_2CHCN^B	5_{15}-4_{14}	[27]81.8	-0.79	9.3	-7.8
			[27]61.3	-1.03	16.9	-18.6
46247.56	^{13}CS	$_{1-0}$	-103.2	-0.47	11.8	-5.9
46312.34	U	——	81.3	-0.25	7.8	-2.1
			64.0	-0.33	12.8	-4.5
46473.52	U	——	82.5	-0.23	7.8	-1.9
			64.0	-0.33	22.0	-7.8

Continued on next page

Table 3.7 – Line Identifications and Fit Parameters towards K6

Line Rest Frequency (MHz)	Species	Transition	Velocity ($\mathrm{km\,s^{-1}}$)	Height (mJy $\times$ $\mathrm{arcsec^{-2}}$)	Width ($\mathrm{km\,s^{-1}}$)	$\int I_v dv$ (mJy $\mathrm{arcsec^{-2}}$ $\times$ $\mathrm{km\,s^{-1}}$)
46534.34	U	——	80.8	-0.19	11.7	-2.4
			64.0	-0.35	12.8	-4.7
46557.44	Contam	——	64.0	0.18	19.5	3.7
46574.40	Contam	——	64.0	0.23	12.3	3.0
46581.23	*t*-HCOOH	2_{11}-1_{10}	81.3	-0.69	8.5	-6.3
			64.5	-1.19	11.5	-14.5
46645.05	*c*-C_3H_2	5_{50}-5_{41}	65.9	-0.37	15.9	-6.2
46755.61	*c*-C_3H_2	2_{11}-2_{02}	81.5	-1.11	10.6	-12.6
			64.2	-2.79	12.9	-38.3
			11.1	-0.18	31.0	-5.9
46832.80	*t*-CH_3CH_2OH	4_{04}-3_{13}	64.7	-0.41	11.7	-5.1
46847.73	NaCN/NaNC	3_{03}-2_{02}	63.5	-0.49	15.4	-8.0
46905.49	U	——	64.0	0.18	38.1	7.4
46990.54	PN	N = 1-0 J=2-1	[28]78.4	-0.64	17.5	-11.8
			64.7	-1.21	12.0	-15.5
47064.81	SiC_2	2_{02}-1_{01}	83.6	-0.24	8.6	-2.2
			61.6	-0.27	11.8	-3.3
47176.01	*E*-CH_3CHNH^{Adj}	3_{12}-3_{03}E	80.8	-0.21	8.3	-1.9
			64.5	-0.35	21.6	-8.1
47195.10	CH_3CH_2CHO	4_{14}-3_{03}	63.2	-0.27	8.4	-2.4
47205.21	$^{13}CH_3OH$	1_{01}-0_{00}++	61.9	-0.88	16.9	-15.8
47209.55	$^{13}CH_3OH$	1_{01}-0_{00}	63.9	-0.26	18.6	-5.2
47217.41	*g'Ga*-$(CH_2OH)_2$	4_{04}v=1-3_{03}v=0	82.2	-0.16	11.7	-2.0
			64.2	-0.23	12.1	-3.0
47249.91	*E*-CH_3CHNH	3_{12}-3_{03}A	82.1	-0.22	10.5	-2.4

Continued on next page

Table 3.7 – Line Identifications and Fit Parameters towards K6

Line Rest Frequency (MHz)	Species	Transition	Velocity (km s^{-1})	Height (mJy × arcsec^{-2})	Width (km s^{-1})	$\int I_v dv$ (mJy arcsec^{-2} × km s^{-1})
			63.4	-0.36	23.7	-9.0
47354.65	CH_2CHCN	5_{05}-4_{04}	81.8	-0.98	9.9	-10.3
			63.9	-2.19	11.0	-25.6
47373.32	CH_3CONH_2	4_{23}-3_{31}E	80.6	-0.21	12.8	-2.9
			63.6	-0.33	13.8	-4.8
47419.79	Contam	——	63.9	0.18	24.0	4.7
47444.51	Contam	——	64.0	0.49	23.9	12.5
47511.87	Hydrogen	H(86)ϵ	66.6	0.28	37.8	11.3
47534.09	CH_3OCHO	4_{04}-3_{03}E	62.8	-0.41	11.1	-4.9
47536.94	CH_3OCHO	4_{04}-3_{03}A	63.2	-0.38	15.4	-6.2
47566.80	C_4H	N=5-4 J=$\frac{11}{2}$-$\frac{9}{2}$	81.3	-0.26	8.3	-2.3
			65.0	-0.51	14.7	-8.0
			9.2	-0.17	17.2	-3.1
47582.44	Contam	——	64.0	0.20	7.3	1.6
47601.58	Hydrogen	H(91)ζ	78.1	0.26	25.2	7.0
47605.49	C_4H	N=5-4 J=$\frac{9}{2}$-$\frac{7}{2}$	64.7	-0.42	10.4	-4.7
47674.96	CH_3OCH_3	1_{11}-0_{00}	61.9	-0.58	13.1	-8.2
		EE/AA/AE/EA				
47696.89	c-HCC^{13}CH	2_{11}-2_{02}	65.0	-0.19	19.0	-3.9
47732.32	U	——	64.0	-0.22	6.9	-1.6
47749.98	Hydrogen^B	H(73)γ	[29]70.9	0.45	10.0	4.8
			59.1	0.70	24.3	18.1
47764.35	Hydrogen	H(80)δ	68.6	0.48	48.1	24.6
47820.62	CH_3CHO	1_{10}-1_{01}A	81.3	-0.48	10.7	-5.5
			62.4	-0.95	15.7	-15.8

Continued on next page

Table 3.7 – Line Identifications and Fit Parameters towards K6

Line Rest Frequency (MHz)	Species	Transition	Velocity (km s^{-1})	Height (mJy × arcsec^{-2})	Width (km s^{-1})	$\int I_v dv$ (mJy arcsec^{-2} × km s^{-1})
47824.96	*E*-HNCHCN	5_{05}-4_{04}	63.7	-0.56	12.8	-7.7
47914.18	Hydrogen	H(64)β	68.0	2.27	34.9	92.8
47927.28	HC_5N^{BC}	18-17	65.8	-0.34	19.3	-7.0
47933.71	Helium^B	He(64)β	[30]70.4	0.23	34.2	8.3
48120.99	Contam	——	64.0	0.26	9.6	2.7
48153.60	Hydrogen	H(51)α	85.5	3.42	26.0	100.1
			64.0	6.29	32.6	218.0
48173.22	Helium	He(51)α	70.4	0.53	45.0	25.6
48206.94	$C^{34}S$	1-0	81.3	-4.63	11.4	-54.1
			64.3	-12.98	15.4	-213.2
			5.6	-1.99	15.8	-38.1
			-23.1	-0.31	10.1	-3.4
			-40.4	-1.78	7.0	-13.2
			-72.9	-0.84	9.8	-8.8
			-86.2	-0.34	10.7	-3.9
			-103.4	-0.90	11.4	-10.8
48284.52	H_2CO	4_{13}-4_{14}	81.8	-1.90	9.7	-19.2
			63.1	-0.38	13.8	-5.7
48308.75	U	——	64.0	-0.61	6.7	-4.4
48372.46	CH_3OH	1_{01}-0_{00}++	80.8	-2.20	7.3	-17.1
			61.5	-11.79	20.0	-249.5
48376.89	CH_3OH	1_{01}-0_{00}	62.6	-6.59	12.7	-88.8
48372.46	CH_3OH	1_{01}-0_{00}++	6.0	-0.78	14.6	-16.7
48385.60	CH_3NH_2?	3_0E1+1-2_1E1+1 F=2-1	72.1	0.35	11.0	4.1

Continued on next page

Table 3.7 – Line Identifications and Fit Parameters towards K6

Line Rest Frequency (MHz)	Species	Transition	Velocity ($\mathrm{km\,s^{-1}}$)	Height (mJy $\times$ arcsec^{-2})	Width ($\mathrm{km\,s^{-1}}$)	$\int I_v dv$ (mJy arcsec^{-2} $\times$ $\mathrm{km\,s^{-1}}$)
48372.46	CH_3OH	1_{01}-0_{00}++	-105.1	-0.81	7.3	-6.3
48548.22	NaCN/NaNC^B	3_{12}-2_{11}	[31]58.3	-0.76	21.2	-17.2
48552.56	CH_2CHCN	5_{14}-4_{13}	62.8	-0.93	11.2	-11.1
48583.29	$C^{33}S$	1-0 F=$\frac{1}{2}$-$\frac{3}{2}$	65.2	-1.46	12.6	-19.6
48585.92	$C^{33}S$	1-0 F=$\frac{5}{2}$-$\frac{3}{2}$	64.3	-2.70	13.6	-39.2
48589.07	$C^{33}S$	1-0 F=$\frac{3}{2}$-$\frac{3}{2}$	64.6	-1.57	12.5	-20.9
48603.47	CH_3CHO	2_{11}-2_{02}E	80.8	-0.50	13.9	-7.4
			64.0	-1.04	13.2	-14.7
48617.69	Contam	——	64.0	0.38	17.9	7.3
48651.60	Contam	——	69.7	0.72	13.1	10.0
48768.30	CH_3OCHO	4_{23}-3_{22}E/A	66.8	-0.29	22.8	-6.9
48902.83	CH_3CHO	2_{11}-2_{02}A	62.5	-0.89	11.4	-10.8
48990.95	CS	1-0	80.3	-11.93	15.3	-188.6
			61.5	-18.43	23.0	-451.1
			32.7	-1.54	5.5	-1.9
			6.4	-13.54	19.2	-288.5
			-21.6	-3.61	10.1	-36.9
			-38.3	-11.27	11.6	-144.1
			-76.6	-6.29	18.3	-119.6
			-94.1	-3.16	6.1	-16.7
			-105.3	-8.17	11.0	-94.1
49161.34	Hydrogen^B	H(85)ϵ	[32]87.8	0.36	68.4	26.2
49396.29	U?	——	64.0	0.31	8.4	2.7
49461.85	Contam	——	69.0	0.23	19.8	4.8
49466.46	CCCN	N=5-4 J=$\frac{11}{2}$-$\frac{9}{2}$	63.6	-0.48	20.4	-10.5

Continued on next page

Table 3.7 – Line Identifications and Fit Parameters towards K6

Line Rest Frequency (MHz)	Species	Transition	Velocity (km s^{-1})	Height (mJy × arcsec^{-2})	Width (km s^{-1})	$\int I_v dv$ (mJy arcsec^{-2} × km s^{-1})
49485.25	CCCN	N=5-4 J=$\frac{9}{2}$-$\frac{7}{2}$	62.6	-0.58	24.1	-14.8
49556.79	Hydrogen	H(79)δ	76.4	0.50	40.6	21.5
49642.06	U	U-49643.86	[33]64.0	-0.42	12.3	-5.6
49726.70	Hydrogen	H(72)γ	73.0	0.98	47.6	49.6
49746.08	U?	——	64.0	0.29	7.7	2.3
49748.08	U?	——	64.0	0.23	7.0	1.7
49806.46	U?	——	64.0	-0.24	12.1	-3.1
49839.64	NH_3	(19,19)	78.5	-0.38	11.7	-4.7
			64.5	-0.67	10.9	-7.8
49962.84	Contam	——	73.8	0.61	9.0	5.8
			61.0	0.52	10.8	6.0
50058.80	CH_3SH	2_1+-1_1+A	65.3	-0.29	16.5	-5.1
50094.90	CH_3OCHO^B	4_{22}-3_{21}E	61.0	-0.39	10.2	-4.2
50099.91	CH_2CHCN	6_{15}-6_{06}	78.6	-0.84	11.1	-9.9
			64.7	-1.15	15.9	-19.5
50149.90	U?	——	79.1	-0.26	6.6	-1.8
			64.0	-0.22	11.0	-2.5
50175.41	CH_3CHO	3_{12}-3_{03}E	82.0	-0.42	11.7	-5.2
			62.5	-0.50	20.1	-10.7

[1] Weakly masing.

[2] The line-of-sight absorption of the F=(2-1f) transition is blended with the F=(1-1f) transition and the F=(1-0f) transitions.

[3] This could be l-C_3H F=(1-0f) at 10 km s^{-1}or F=(2-1f) at -54 km s^{-1}. The feature is detected towards L and is evident, but not detected towards K4. If this is a U-line, the line should be shifted to 56 or 76 km s^{-1} towards L; however it is not significantly shifted. If the feature is a spiral arm cloud component, we would not expect to see it

Continued on next page

Table 3.7 – Line Identifications and Fit Parameters towards K6

Line Rest Frequency (MHz)	Species	Transition	Velocity ($\mathrm{km\,s^{-1}}$)	Height (mJy × $\mathrm{arcsec^{-2}}$)	Width ($\mathrm{km\,s^{-1}}$)	$\int I_v dv$ (mJy $\mathrm{arcsec^{-2}}$ × $\mathrm{km\,s^{-1}}$)

towards K4 at these velocities, as strong foreground absorption is only detected towards K4 at $\sim$2 $\mathrm{km\,s^{-1}}$.

[4] Blended with the 64 $\mathrm{km\,s^{-1}}$ component of the F=(1-1) transition.

[5] Tentative because the velocity is unusual for this source.

[6] Blended with CH_3OCH_3 2_{20}-3_{13}.

[7] Tentative because the stronger EE transition is not detected.

[8] Tentative because the A-state transition is not detected.

[9] Generally arising from LMH, with some emission in the base of the K5 shell.

[10] The 64 $\mathrm{km\,s^{-1}}$ component of $HC^{13}CCN$ is blended with the 82 $\mathrm{km\,s^{-1}}$ component of $HCC^{13}CN$.

[11] Blended with H(80)γ.

[12] This may be line-of-sight absorption by OCS at $\sim$35 $\mathrm{km\,s^{-1}}$.

[13] Blended with CH_3OCHO 3_{21}-2_{20}.

[14] Blended with CH_3OCHO 3_{21}-2_{21}E.

[15] This may be line-of-sight absorption by CH_3CHO at -39 $\mathrm{km\,s^{-1}}$.

[16] Blended with the wing of CH_3CHO 2_{11}-1_{10}E.

[17] Detected in K6, L, and K4.

[18] Blended with HC_5N J=(15-14).

[19] Multiple hyperfine components are blended.

[20] Possibly blended with NH_2CHO at $\sim$0 $\mathrm{km\,s^{-1}}$.

[21] Blended with H(88)ϵ.

[22] Unusual velocity, perhaps due to poor S:N or baseline issues.

[23] May be blended with line-of-sight absorption of CCS.

[24] Blended with line-of-sight absorption of HC_3N.

[25] Blended with HSCN 4_{04}-3_{03} towards K6.

[26] Due to line emission from 'h' (at 73 $\mathrm{km\,s^{-1}}$) and the LMH, the line profile is not representative of the gas kinematics towards K6.

Continued on next page

Table 3.7 – Line Identifications and Fit Parameters towards K6

Line Rest Frequency (MHz)	Species	Transition	Velocity ($\mathrm{km\,s^{-1}}$)	Height (mJy $\times$ arcsec^{-2})	Width ($\mathrm{km\,s^{-1}}$)	$\int I_v dv$ (mJy arcsec^{-2} $\times$ $\mathrm{km\,s^{-1}}$)
[27] Blended with line-of-sight absorption of ^{13}CS.						
[28] Blended with the N=1-0 J=1-1 transition.						
[29] Blended with CH_3CHO 1_{10}-1_{01}E.						
[30] Blended with HC_5N J=(18-17).						
[31] Blended with the 82 $\mathrm{km\,s^{-1}}$ component of CH_2CHCN.						
[32] Blend of H(85)ϵ, H(90)ζ, and CH_3OCHO 4_{31}-3_{03}E.						
[33] This is at 74.9 $\mathrm{km\,s^{-1}}$ with respect to a U-line at 49643.86 MHz in the LOVAS catalog.						

Table 3.8 – Line identifications and fit parameters towards L.

Line Rest Frequency (MHz)	Species	Transition	Velocity ($\mathrm{km\,s^{-1}}$)	Height (mJy $\times$ arcsec^{-2})	Width ($\mathrm{km\,s^{-1}}$)	$\int I_v dv$ (mJy arcsec^{-2} $\times$ $\mathrm{km\,s^{-1}}$)
29901.40	CH_3OCH_3	1_{10}-1_{01}EE/AA/AE/EA	[1]61.2	-0.28	28.7	-8.5
29914.49	NH_3	(11,11)	74.0	-1.21	14.9	-19.2
			54.9	-1.16	15.3	-19.0
			20.2	-0.31	14.5	-4.8
29971.48	Hydrogen	H(75)β	76.6	1.42	26.2	39.5
29979.38	*t*-CH_3CH_2OH	3_{12}-3_{03}	59.1	-0.49	15.8	-8.2
30001.55	SO	1_0-0_1	73.7	-4.10	17.1	-70.1
			56.1	-8.86	14.2	-133.1

Continued on next page

Table 3.8 – Line Identifications and Fit Parameters towards L

Line Rest Frequency (MHz)	Species	Transition	Velocity ($\mathrm{km\,s^{-1}}$)	Height (mJy × arcsec^{-2})	Width ($\mathrm{km\,s^{-1}}$)	$\int I_v dv$ (mJy arcsec^{-2} × $\mathrm{km\,s^{-1}}$)
			16.7	-0.96	26.1	-18.0
			-10.4	-0.59	17.4	-10.9
			-38.1	-0.40	20.1	-8.7
			-75.6	-0.52	11.4	-6.3
			-104.3	-0.25	11.8	-3.1
30500.20	Hydrogen	H(85)γ	74.6	0.54	29.8	17.0
30586.57	U?	——	56.0	-0.24	11.2	-2.8
30707.38	Hydrogen	H(93)δ	77.1	0.36	31.3	11.9
30865.74	U?	——	56.0	-0.23	12.0	-3.0
31106.15	CH_3OCH_3	2_{11}-2_{02}EE/AA/AE/EA	[1]63.6	-0.46	25.3	-12.3
31186.68	Hydrogen	H(74)β	75.6	1.68	27.2	48.7
31223.31	Hydrogen	H(59)α	76.3	6.55	26.3	189.8
31236.04	Helium	He(59)α	79.1	0.44	22.0	10.3
31262.33	NaCN/NaNC	2_{02}-1_{01}	57.5	-0.27	40.4	-11.8
31424.94	NH_3	(12,12)	76.8	-2.15	13.4	-30.7
			57.0	-2.58	14.9	-41.0
			19.4	-0.51	13.4	-7.3
31482.38	Hydrogen	H(99)ϵ	73.5	0.21	37.6	8.6
31583.40	Hydrogen	H(84)γ	75.3	0.69	31.2	23.0
31698.47	Hydrogen	H(92)δ	75.2	0.29	22.3	6.9
31951.78	HC_5N	12-11	73.9	-0.49	10.6	-5.6
			56.3	-0.78	14.0	-11.7
32468.48	Hydrogen	H(73)β	76.5	1.82	28.3	54.8
32640.21	U	——	59.9	-0.28	33.2	-9.9
32660.65	*l*-C_3H	J=$\frac{3}{2}$-$\frac{1}{2}$ Ω=$\frac{1}{2}$ F=2-1e	57.0	-0.38	13.3	-5.4

Continued on next page

Table 3.8 – Line Identifications and Fit Parameters towards L

Line Rest Frequency (MHz)	Species	Transition	Velocity ($\mathrm{km\,s^{-1}}$)	Height (mJy × $\mathrm{arcsec^{-2}}$)	Width ($\mathrm{km\,s^{-1}}$)	$\int I_v dv$ (mJy $\mathrm{arcsec^{-2}}$ × $\mathrm{km\,s^{-1}}$)
			[2]7.7	-0.27	44.1	-12.7
32672.52	*cis*-CH_2OHCHO^{BC}	4_{22}-4_{13}	63.5	-0.26	28.1	-7.7
32718.50	Hydrogen	H(83)γ	75.2	0.83	26.5	23.3
32732.67	Hydrogen	H(91)δ	76.1	0.48	24.1	12.3
32742.82	*t*-CH_3CH_2OH	4_{13}-4_{04}	60.2	-0.61	21.9	-14.3
32852.20	Hydrogen	H(58)α	75.8	7.08	27.3	214.5
32865.58	Helium	He(58)α	74.4	0.63	28.5	19.1
32978.23	CH_3OCH_3	3_{12}-3_{03}EE/AA/AE/EA	[1]67.0	-0.89	28.8	-27.2
33156.85	NH_3	(13,13)	74.9	-0.93	13.9	-13.7
			55.6	-1.04	14.3	-15.8
			19.8	-0.26	11.7	-3.3
33354.01	*cis*-CH_2OHCHO?	2_{12}-1_{01}	58.6	-0.27	26.6	-7.8
33420.88	Hydrogen	H(97)ϵ	68.3	0.22	56.0	13.3
33704.82	CH_2NH	1_{11}-2_{02}	73.8	-1.58	14.4	-24.3
			55.9	-0.97	14.0	-14.4
33751.37	CCS	3_2-2_1	75.3	-1.55	15.4	-25.4
			56.1	-2.26	15.2	-36.7
			5.1	-0.29	33.1	-10.2
33812.37	Hydrogen	H(90)δ	75.1	0.47	26.2	13.1
33821.51	Hydrogen	H(72)β	77.0	1.83	29.1	56.5
33908.67	Hydrogen	H(82)γ	76.9	0.91	26.6	25.7
34156.88	CH_3OCHO	3_{13}-2_{12}E/A	56.2	-0.30	34.8	-11.0
34351.45	H_2CS	1_{01}-0_{00}	77.7	-0.35	12.3	-4.6
			57.6	-1.10	15.4	-18.0
34408.63	HSCN	3_{03}-2_{02}	58.2	-0.40	12.9	-5.4

Continued on next page

Table 3.8 – Line Identifications and Fit Parameters towards L

Line Rest Frequency (MHz)	Species	Transition	Velocity ($\mathrm{km\,s^{-1}}$)	Height (mJy × $\mathrm{arcsec^{-2}}$)	Width ($\mathrm{km\,s^{-1}}$)	$\int I_v dv$ (mJy $\mathrm{arcsec^{-2}}$ × $\mathrm{km\,s^{-1}}$)
34450.03	Hydrogen	H(96)ϵ	77.7	0.41	12.8	5.5
34522.90	U?		56.0	0.28	11.2	3.4
34596.38	Hydrogen	H(57)α	[3]85.2	4.80	17.5	89.5
			[3]71.5	6.37	17.9	128.6
34610.48	Helium	He(57)α	77.2	0.65	25.9	17.9
34614.38	HC_5N	13-12	59.7	-0.70	22.0	-16.4
34684.37	$CCCS^B$	6-5	[4]61.1	-0.39	16.0	-6.7
34824.07	CH_3CH_2CN	4_{14}-3_{13}	52.3	-0.34	22.3	-8.2
34940.09	Hydrogen	H(89)δ	74.4	0.55	22.3	13.0
35134.30	NH_3	(14,14)	76.3	-0.59	9.3	-5.8
			54.7	-0.46	13.6	-6.7
35157.27	Hydrogen	H(81)γ	75.5	1.00	25.4	27.2
35250.77	Hydrogen	H(71)β	76.4	2.18	26.8	62.1
35267.41	$H^{13}CCCN$	4-3	76.6	-0.69	12.2	-8.9
			56.4	-1.06	13.9	-15.7
35521.88	Hydrogen	H(95)ϵ	73.5	0.33	28.4	9.9
35593.40	CH_3OCH_3	4_{13}-4_{04}EE/AA/AE/EA	[1]74.9	-0.73	12.9	-10.0
			60.8	-0.58	15.7	-9.8
35722.21	CH_3CH_2CN	4_{04}-3_{03}	76.9	-0.27	15.4	-4.3
			55.1	-0.41	13.8	-6.0
35733.12	$^{13}CH_3CN^{Adj}$	2_0-1_0/2_1-1_1	77.3	-0.23	11.8	-2.9
			55.5	-0.34	24.4	-8.9
36102.22	CH_3OCHO	3_{03}-2_{02}A	55.2	-0.42	12.7	-5.7
36104.79	CH_3OCHO	3_{03}-2_{02}E	58.3	-0.32	11.5	-4.0
36118.53	$Hydrogen^{Adj}$	H(88)δ	79.1	0.52	40.6	22.6

Continued on next page

Table 3.8 – Line Identifications and Fit Parameters towards L

Line Rest Frequency (MHz)	Species	Transition	Velocity ($\mathrm{km\,s^{-1}}$)	Height (mJy × arcsec^{-2})	Width ($\mathrm{km\,s^{-1}}$)	$\int I_v dv$ (mJy arcsec^{-2} × $\mathrm{km\,s^{-1}}$)
36169.29	Contam	——	74.9	-17.01	11.7	-239.9
36237.99	HC^{13}CCN	4-3	75.9	-0.44	15.2	-7.1
			[5]52.2	-1.13	20.0	-24.0
36241.48	HCC^{13}CN	4-3	55.9	-1.25	12.7	-16.9
36299.95	H_2COH^+	1_{11}-2_{02}	73.8	-0.31	11.4	-3.7
36309.63	SiS	2-1	58.8	-0.60	16.5	-10.5
36392.32	HC_3N	4-3	73.1	-6.73	14.9	-106.6
			55.8	-13.17	15.2	-213.7
			14.1	-0.67	27.1	-14.5
			-6.1	-0.36	9.7	-3.7
36417.24	*t*-CH_3CH_2OH	5_{14}-5_{05}	61.1	-0.40	10.3	-4.3
36466.26	Hydrogen	H(56)α^B	[6]74.3	7.86	28.6	264.2
36467.94	Hydrogen	H(80)γ	56.4	0.71	11.2	8.5
36481.12	Helium	He(56)α	74.8	0.83	28.0	24.7
36488.81	OCS	3-2	55.8	-0.42	11.3	-5.0
36739.67	CH_3CH_2CN	4_{13}-3_{12}	59.5	-0.64	10.8	-7.4
36761.72	Hydrogen	H(70)β	76.6	1.98	27.1	57.3
36777.28	$CH_3^{13}CN^{Adj}$	2_0-1_0/2_1-1_1	74.1	-0.33	11.2	-3.9
			55.7	-0.24	19.2	-4.9
36795.47	CH_3CN	2_0-1_0/2_1-1_1	72.7	-6.05	21.6	-144.7
			57.4	-6.31	19.5	-130.7
			15.6	-0.55	31.4	-26.4
36930.70	*Z*-CH_3CHNH	2_{02}-1_{01}E/A	55.9	-0.42	27.5	-12.2
37018.92	CH_2CHCN	4_{14}-3_{13}	77.6	-0.35	9.8	-3.7
			58.2	-0.52	14.2	-7.9

Continued on next page

Table 3.8 – Line Identifications and Fit Parameters towards L

Line Rest Frequency (MHz)	Species	Transition	Velocity ($\mathrm{km\,s^{-1}}$)	Height (mJy × $\mathrm{arcsec^{-2}}$)	Width ($\mathrm{km\,s^{-1}}$)	$\int I_v dv$ (mJy $\mathrm{arcsec^{-2}}$ × $\mathrm{km\,s^{-1}}$)
37182.66	$CH_3C_3N^{BC}$	9_1-8_1/9_0-7_0	68.8	-0.30	36.7	-11.6
37276.99	HC_5N	14-13	57.2	-0.59	14.6	-9.2
37350.57	Hydrogen	H(87)δ	72.8	0.53	24.6	13.9
37385.12	NH_3	(15, 15)	76.4	-0.99	15.1	-15.9
			58.0	-1.33	19.1	-27.0
			19.0	-0.36	27.8	-10.8
			-11.3	-0.25	41.6	-11.0
37464.17	CH_3CHO	2_{12}-1_{11}A	75.4	-1.31	16.9	-23.6
			55.8	-1.62	13.8	-23.7
37665.30	U?	——	56.0	0.41	6.7	2.9
37686.87	CH_3CHO	2_{12}-1_{11}E	76.5	-1.63	11.5	-20.0
			57.0	-1.64	14.0	-24.4
37844.59	Hydrogen	H(79)γ	74.2	0.90	27.5	26.4
37904.85	CH_2CHCN	4_{04}-3_{03}	75.5	-0.77	13.3	-10.9
			57.9	-1.30	15.3	-21.2
38271.02	*E*-HNCHCN	4_{04}-3_{03}	73.0	-0.43	9.6	-4.4
			54.0	-0.38	12.5	-5.0
38360.27	Hydrogen	H(69)β	77.4	2.15	27.0	61.9
38473.36	Hydrogen	H(55)α	77.3	7.86	27.2	222.6
38489.04	Helium	He(55)α	76.1	0.45	26.3	12.6
38506.04	CH_3CHO	2_{02}-1_{01}E	75.1	-3.39	13.4	-48.3
			55.9	-4.12	13.4	-58.6
38512.11	CH_3CHO	2_{02}-1_{01}A	76.6	-2.86	12.7	-38.5
			57.5	-4.60	16.0	-78.5
			5.4	-0.37	25.5	-9.9

Continued on next page

Table 3.8 – Line Identifications and Fit Parameters towards L

Line Rest Frequency (MHz)	Species	Transition	Velocity ($\mathrm{km\,s^{-1}}$)	Height (mJy $\times$ arcsec^{-2})	Width ($\mathrm{km\,s^{-1}}$)	$\int I_v dv$ (mJy arcsec^{-2} $\times$ $\mathrm{km\,s^{-1}}$)
38506.04	CH_3CHO?	2_{02}-1_{01}E	-77.0	-0.45	10.1	-4.8
38639.30	Hydrogen	H(86)δ	75.0	0.57	30.0	18.3
38847.73	CH_2CHCN	4_{13}-3_{12}	76.7	-0.46	10.9	-5.3
			56.6	-0.87	11.6	-10.7
39016.76	Hydrogen	H(92)ϵ	76.7	0.38	29.6	12.0
39139.14	U?	——	56.0	-0.46	9.6	-4.7
39148.05	U?	——	56.0	-0.48	8.9	-4.5
39291.42	Hydrogen	H(78)γ	77.4	0.96	30.9	31.7
39362.50	CH_3CHO	2_{11}-1_{10}E	73.3	-1.51	11.7	-18.9
			55.9	-1.84	14.5	-28.3
39527.73	Hydrogen	H(97)ζ	76.4	0.47	35.0	17.3
39571.33	CCCN	N=4-3 J=$\frac{9}{2}$-$\frac{7}{2}$	54.8	-0.48	11.1	-5.6
39594.29	CH_3CHO	2_{11}-1_{10} A	77.9	-1.40	14.2	-21.3
			56.9	-1.52	13.7	-22.2
39847.97	U?	——	56.0	-0.54	9.3	-5.3
39927.87	U	——	[7]56.7	-0.61	14.0	-9.1
39939.57	$HC_5N^{B,Adj}$	15-14	[8]71.1	-0.80	11.6	-9.9
39941.41	$NH_3^{B,Adj}$	(16,16)	[9]73.7	-0.51	10.1	-5.5
			56.3	-0.54	29.5	-16.9
39956.70	c-H_2C_3O	3_{13}-2_{12}	74.3	-0.49	11.0	-5.7
			56.8	-0.82	10.6	-9.3
39988.02	Hydrogen	H(85)δ	79.0	0.63	31.0	20.7
40052.88	Hydrogen	H(68)β	76.6	2.40	26.3	67.3
40211.39	CH_3NC	2_0-1_0	73.7	-0.49	10.1	-5.3
			57.8	-0.59	12.9	-8.2

Continued on next page

Table 3.8 – Line Identifications and Fit Parameters towards L

Line Rest Frequency (MHz)	Species	Transition	Velocity ($\mathrm{km\,s^{-1}}$)	Height (mJy × $\mathrm{arcsec^{-2}}$)	Width ($\mathrm{km\,s^{-1}}$)	$\int I_v dv$ (mJy $\mathrm{arcsec^{-2}}$ × $\mathrm{km\,s^{-1}}$)
			37.8	-0.57	10.6	-6.5
40239.70	CH_2CN^B	2_{02}-1_{01} J=$\frac{5}{2}$-$\frac{3}{2}$	77.1	-0.72	22.0	-16.9
		F1=$\frac{7}{2}$-$\frac{5}{2}$ F=$\frac{7}{2}$-$\frac{5}{2}$	54.2	-2.70	25.1	-72.2
40242.22	CH_2CN^B	2_{02}-1_{01} J=$\frac{5}{2}$-$\frac{3}{2}$	52.4	-0.77	9.1	-7.5
		F1=$\frac{5}{2}$-$\frac{3}{2}$ F=$\frac{5}{2}$-$\frac{3}{2}$				
40244.34	CH_2CN^B	2_{02}-1_{01} J=$\frac{5}{2}$-$\frac{3}{2}$	54.5	-1.13	19.4	-23.3
		F1=$\frac{5}{2}$-$\frac{3}{2}$ F=$\frac{7}{2}$-$\frac{5}{2}$				
40247.54	CH_2CN^B	2_{02}-1_{01} J=$\frac{3}{2}$-$\frac{1}{2}$	56.2	-2.05	18.0	-39.2
		F1=$\frac{5}{2}$-$\frac{3}{2}$ F=$\frac{5}{2}$-$\frac{3}{2}$				
40250.43	CH_2CN^B	2_{02}-1_{01} J=$\frac{3}{2}$-$\frac{3}{2}$	54.0	-0.75	20.6	-16.4
		F1=$\frac{3}{2}$-$\frac{1}{2}$ F=$\frac{1}{2}$-$\frac{1}{2}$				
40253.88	CH_2CN^B	2_{02}-1_{01} J=$\frac{3}{2}$-$\frac{1}{2}$	54.9	-0.67	19.6	-13.9
		F1=$\frac{5}{2}$-$\frac{3}{2}$ F=$\frac{3}{2}$-$\frac{3}{2}$				
40256.79	CH_2CN^B	2_{02}-1_{01} J=$\frac{3}{2}$-$\frac{1}{2}$	52.4	-0.61	15.8	-10.3
		F1=$\frac{3}{2}$-$\frac{3}{2}$ F=$\frac{5}{2}$-$\frac{5}{2}$				
40283.29	Hydrogen	H(91)ϵ	74.2	0.64	20.3	13.8
40352.77	$Si^{18}O$	1-0	55.8	-1.10	12.6	-14.8
40404.39	U?	——	56.0	0.59	8.8	5.6
40455.62	H_2NCO^+?	2_{02}-1_{01} F=1-0	71.8	-0.43	22.8	-10.4
40630.50	Hydrogen	H(54)α	76.6	8.65	26.4	242.5
40647.06	Helium	He(54)α	75.8	0.92	19.6	19.2
40658.60	CH_2CN?	2_{11}-1_{10} J=$\frac{5}{2}$-$\frac{3}{2}$	80.3	-0.43	15.6	-7.2
			55.9	-0.79	28.8	-24.4
40793.84	H_2CCO	2_{11}-1_{10}	59.5	-0.62	11.8	-7.8
40812.95	Hydrogen	H(77)γ	[3]87.7	0.98	12.5	13.0

Continued on next page

Table 3.8 – Line Identifications and Fit Parameters towards L

Line Rest Frequency (MHz)	Species	Transition	Velocity ($\mathrm{km\,s^{-1}}$)	Height (mJy $\times$ arcsec^{-2})	Width ($\mathrm{km\,s^{-1}}$)	$\int I_v dv$ (mJy arcsec^{-2} $\times$ $\mathrm{km\,s^{-1}}$)
			68.9	1.12	16.6	19.9
40875.44	NH_2CHO	2_{12}-1_{11}	74.6	-2.96	15.5	-48.7
			56.0	-3.11	15.1	-49.9
41400.26	Hydrogen	H(84)δ	75.9	0.84	25.9	23.3
41605.24	Hydrogen	H(90)ϵ	80.2	0.56	23.2	13.8
41846.55	Hydrogen^{Adj}	H(67)β	75.8	2.52	26.0	69.6
42031.94	c-H_2C_3O	3_{03}-2_{02}	60.8	-0.49	9.4	-5.0
42373.34	^{30}SiO	1-0	76.2	-3.02	10.6	-34.1
			54.9	-4.35	19.0	-88.2
42386.06	NH_2CHO	2_{02}-1_{01}	72.8	-4.58	15.8	-77.2
			57.7	-7.60	15.6	-126.1
42414.09	Hydrogen	H(76)γ	74.4	1.09	31.6	36.8
42602.15	HC_5N^{BC}	16-15	64.5	-0.50	21.1	-11.3
42674.19	HCS^+	1-0	74.8	-0.90	9.5	-9.1
			56.4	-1.39	15.6	-23.0
42839.92	NH_3	(17,17)	75.6	-0.96	15.6	-15.9
			52.8	-0.75	10.9	-8.7
42879.94	^{29}SiO	1-0	73.6	-3.84	11.9	-48.5
			55.2	-8.43	13.0	-117.0
			17.9	-0.91	10.5	-10.2
			-74.5	-0.85	9.3	-8.4
42951.97	Hydrogen	H(53)α	76.2	10.21	26.9	292.0
42969.47	Helium	He(53)α	75.6	1.11	25.3	29.9
43026.60	t-CH_3CH_2OH	1_{11}-0_{00}	56.4	-0.71	9.0	-6.9
43303.71	t-HCOOH ^{BC}	2_{12}-1_{11}	65.1	-0.62	26.0	-17.2

Continued on next page

Table 3.8 – Line Identifications and Fit Parameters towards L

Line Rest Frequency (MHz)	Species	Transition	Velocity ($\mathrm{km\,s^{-1}}$)	Height (mJy × arcsec^{-2})	Width ($\mathrm{km\,s^{-1}}$)	$\int I_v dv$ (mJy arcsec^{-2} × $\mathrm{km\,s^{-1}}$)
43423.85	SiO	1-0	73.0	-13.30	19.9	-272.2
			53.9	-16.94	14.5	-261.5
			33.5	-3.74	9.2	-32.4
			18.9	-7.45	12.6	-100.0
			-4.4	-2.63	19.9	-55.6
			-31.6	-1.17	26.3	-32.8
			-75.1	-4.24	11.3	-51.0
			-104.8	-0.63	20.4	-21.5
43748.95	Hydrogen	H(66)β	75.5	2.68	28.6	81.6
43954.45	NH_2CHO	2_{11}-1_{10}	72.4	-3.05	17.0	-55.2
			55.7	-3.31	15.3	-53.9
44084.17	$H^{13}CCCN$	5-4	73.5	-0.80	11.6	-9.9
			57.1	-1.15	9.4	-11.5
44100.09	Hydrogen	H(75)γ	78.0	1.26	27.0	36.3
44104.78	c-C_3H_2 ^{B}	3_{21}-3_{12}	[10]71.7	-1.40	10.9	-16.2
			57.2	-0.84	10.1	-9.1
44430.71	Hydrogen^B	H(82)δ	[11]74.9	0.56	50.3	30.2
44497.60	$CC^{34}S$	4_3-3_2	54.9	-0.75	10.4	-8.3
44587.40	c-$H_2C_3O^{BC}$	3_{12}-2_{11}	66.8	-0.64	23.0	-15.8
44911.75	t-HCOOH	2_{02}-1_{01}	75.0	-0.41	10.9	-4.8
			55.7	-0.46	8.8	-4.3
45264.72	HC_5N?	17-16	78.1	-0.40	13.0	-5.5
45297.35	$HC^{13}CCN$	5-4	74.4	-0.55	18.4	-10.8
			[5]50.8	-0.64	17.8	-12.2
45301.71	$HCC^{13}CN$	5-4	53.3	-0.40	19.4	-8.2

Continued on next page

Table 3.8 – Line Identifications and Fit Parameters towards L

Line Rest Frequency (MHz)	Species	Transition	Velocity ($\mathrm{km\,s^{-1}}$)	Height (mJy $\times$ arcsec^{-2})	Width ($\mathrm{km\,s^{-1}}$)	$\int I_v dv$ (mJy arcsec^{-2} $\times$ $\mathrm{km\,s^{-1}}$)
45323.48	U?		56.0	-0.19	26.4	-5.5
45379.03	CCS	4_3-3_2	76.1	-1.06	9.1	-10.3
			54.7	-1.26	11.7	-15.6
45395.79	CH_3OCHO?	4_{14}-3_{13}E	74.5	-0.32	10.2	-3.5
			56.2	-0.37	16.3	-6.4
45397.38	CH_3OCHO	4_{14}-3_{13}A	54.4	-0.22	10.3	-2.4
45453.72	Hydrogen	H(52)α	76.9	3.57	21.2	80.4
45490.34	HC_3N	5-4	78.6	-2.08	9.1	-20.1
			53.3	-4.88	11.3	-58.7
			16.7	-0.46	16.5	-8.0
45768.44	Hydrogen	H(65)β	77.9	0.92	22.6	22.2
45843.57	Contam	——	[12]62.4	-0.33	12.0	-4.3
45909.51	$CH_3CH_2CN^{BC}$	5_{14}-4_{13}	62.5	-0.34	28.3	-10.1
46123.30	NH_3^{BC}	(18,18)	65.0	-0.31	33.8	-11.0
46247.56	^{13}CS	1-0	79.6	-0.47	5.7	-2.8
			54.9	-2.66	10.7	-30.2
46266.93	CH_2CHCN	5_{15}-4_{14}	76.0	-0.46	9.1	-4.4
			56.2	-0.32	12.5	-4.2
46755.61	c-C_3H_2	2_{11}-2_{02}	76.7	-0.55	9.5	-5.6
			55.0	-0.52	13.0	-7.1
47064.83	SiC_2	2_{02}-1_{01}	53.7	-0.33	7.6	-2.7
47205.21	$^{13}CH_3OH$	1_{01}-0_{00}++	51.2	-0.45	9.7	-4.6
47354.65	CH_2CHCN	5_{05}-4_{04}	75.9	-0.65	10.6	-7.3
			60.3	-0.51	18.2	-9.8
47764.35	Hydrogen	H(80)δ	84.7	0.19	39.0	7.7

Continued on next page

Table 3.8 – Line Identifications and Fit Parameters towards L

Line Rest Frequency (MHz)	Species	Transition	Velocity ($\mathrm{km\,s^{-1}}$)	Height (mJy $\times$ arcsec^{-2})	Width ($\mathrm{km\,s^{-1}}$)	$\int I_v dv$ (mJy arcsec^{-2} $\times$ $\mathrm{km\,s^{-1}}$)
47820.62	CH_3CHO	1_{10}-1_{01}A	73.2	-0.32	10.2	-3.5
			52.7	-0.31	15.3	-5.1
47914.18	Hydrogen	H(64)β	78.0	0.86	16.9	15.5
48153.60	Hydrogen	H(51)α	88.9	1.12	16.3	19.5
			75.0	3.25	20.1	69.5
48173.22	Helium	He(51)α	75.5	0.42	12.4	5.5
48206.94	$C^{34}S$	1-0	79.0	-0.91	6.1	-5.9
			55.8	-3.30	12.6	-44.3
			29.8	-0.20	5.3	-1.1
			2.6	-0.55	16.8	-9.8
48372.46	CH_3OH	1_{01}-0_{00}++	79.7	-2.01	9.9	-23.6
			50.4	-4.18	12.7	-58.0
48376.89	CH_3OH	1_{01}-0_{00}	56.2	-1.35	17.6	-25.4
48990.95	CS	1-0	[13]82.7	-0.73	5.3	-4.1
			[13]67.0	-2.63	8.7	-28.7
			53.8	-4.91	11.7	-60.7
			22.6	-2.16	22.6	-51.9
			-2.8	-3.04	18.3	-59.2
			-35.5	-2.18	20.1	-46.7
			-75.8	-1.90	9.8	-19.8
			-106.5	-0.96	8.1	-8.3
49671.55	U?	——	56.0	0.55	10.4	6.1
49726.70	Hydrogen	H(72)γ	77.5	0.49	13.0	6.7
49962.84	NH_2D	2_{12}0s-2_{02}0a	73.5	-0.58	8.1	-4.9

[1] Transitions of CH_3OCH_3 towards L are more kinematically consistent with being the AA transition than the EE

Continued on next page

Table 3.8 – Line Identifications and Fit Parameters towards L

Line Rest Frequency (MHz)	Species	Transition	Velocity ($\mathrm{km\,s^{-1}}$)	Height (mJy × $\mathrm{arcsec^{-2}}$)	Width ($\mathrm{km\,s^{-1}}$)	$\int I_v dv$ (mJy $\mathrm{arcsec^{-2}}$ × $\mathrm{km\,s^{-1}}$)

transition, although the EE transition has a higher quantum line strength. Towards K6 and K4, the EE transitions are more kinematically consistent.

[2] Blended with the F=(1-1) transition.

[3] One of only two recombination line fit with two components towards this source. Possible blending.

[4] Blended with CH_3OCH_3 2_{20}-3_{13}EE & AA.

[5] The 56 $\mathrm{km\,s^{-1}}$ component of $HC^{13}CCN$ is blended with the 76 $\mathrm{km\,s^{-1}}$ component of $HCC^{13}CN$.

[6] Blended with H(80)γ.

[7] Detected in K6, L, and K4.

[8] Blended with NH_3 (16, 16).

[9] Blended with HC_5N J=(15-14).

[10] Blended with H(75)γ.

[11] Blended with H(88)ϵ.

[12] This corresponds to the 9_{36}-$10_{2,8}$ line produced by CH_3OH in the hot cores. The beam pattern falls near L.

[13] The profile of CS is atypical of line profiles towards L. Instead of absorbing components at 56 and 76 $\mathrm{km\,s^{-1}}$, we observe strong absorption at 56 $\mathrm{km\,s^{-1}}$, fairly strong absorption at 67 $\mathrm{km\,s^{-1}}$, and a weak absorption component at 82 $\mathrm{km\,s^{-1}}$. The 76 $\mathrm{km\,s^{-1}}$ component does not appear in absorption.

Table 3.9 – Line identifications and fit parameters towards K4.

Line Rest Frequency (MHz)	Species	Transition	Velocity ($\mathrm{km\,s^{-1}}$)	Height (mJy $\times$ arcsec^{-2})	Width ($\mathrm{km\,s^{-1}}$)	$\int I_v dv$ (mJy arcsec^{-2} $\times$ $\mathrm{km\,s^{-1}}$)
29901.40	CH_3OCH_3	1_{10}-1_{01}EE/AA/EA/AE	62.4	-0.24	22.7	-5.8
29914.49	NH_3	(11,11)	82.9	-1.64	15.9	-27.8
			63.3	-2.49	20.2	-53.4
			0.1	-0.54	17.5	-10.1
29971.48	Hydrogen	H(75)β	67.9	0.87	30.2	27.8
29979.38	*t*-CH_3CH_2OH	3_{12}-3_{03}	[1]83.0	0.24	11.9	3.0
			4.7	-0.25	12.2	-3.2
30001.55	SO	1_0-0_1	83.3	-7.41	15.8	-115.6
			63.7	-9.84	15.6	-163.9
			3.0	-0.89	17.5	-16.6
30500.20	Hydrogen	H(85)γ	66.2	0.28	35.4	10.4
30707.38	Hydrogen	H(93)δ	56.3	0.31	52.9	17.3
31102.23	U	——	62.0	-0.21	16.6	-3.7
31106.15	CH_3OCH_3	2_{11}-2_{02}EE/AA/EA/AE	65.6	-0.44	20.9	-9.8
31186.68	Hydrogen	H(74)β	68.3	0.78	37.0	30.7
31223.31	Hydrogen	H(59)α	104.8	0.42	17.5	7.9
			72.9	2.95	27.6	86.9
			54.7	1.60	16.5	28.1
31236.04	Helium	He(59)α	68.6	0.21	34.3	7.5
31262.33	NaCN/NaNC^{BC}	2_{02}-1_{01}	70.1	-0.23	33.0	-8.0
31424.94	NH_3	(12,12)	82.4	-2.57	16.8	-45.9
			62.1	-3.74	17.8	-70.9
			0.6	-0.80	15.5	-13.2
31583.40	Hydrogen	H(84)γ	74.8	0.23	62.4	15.2
31727.07	*cis*-CH_2OHCHO	5_{23}-5_{14}	[2]57.0	-0.21	13.3	-3.0

Continued on next page

Table 3.9 – Line Identifications and Fit Parameters towards K4

Line Rest Frequency (MHz)	Species	Transition	Velocity ($\mathrm{km\,s^{-1}}$)	Height (mJy × arcsec^{-2})	Width ($\mathrm{km\,s^{-1}}$)	$\int I_v dv$ (mJy arcsec^{-2} × $\mathrm{km\,s^{-1}}$)
31833.03	*cis*-CH_2OHCHO	6_{24}-6_{15}	[2]57.0	-0.27	15.5	-4.4
31914.62	H_2COH^+	3_{03}-2_{12}	[1]60.0	0.25	17.9	4.7
31951.78	HC_5N	12-11	83.3	-0.20	11.1	-2.3
			64.0	-0.35	12.6	-4.7
32373.67	NaCN/NaNC?	2_{11}-1_{10}	83.3	-0.21	20.0	-4.5
32398.56	$^{13}CH_3OH^{Maser}$	$4_{-1,4}$-3_{03}	58.0	0.82	17.9	15.6
32468.48	Hydrogen	H(73)β	65.6	0.62	37.5	24.9
32660.65	*l*-C_3H	J=$\frac{3}{2}$-$\frac{1}{2}$ Ω=$\frac{1}{2}$ F=2-1e	66.9	-0.22	16.4	-3.8
32672.52	*cis*-CH_2OHCHO	4_{22}-4_{13}	65.9	-0.19	25.5	-5.1
32709.18	CH_3CHO	4_{04}-3_{13}A	58.7	-0.17	20.4	-3.7
32718.50	Hydrogen	H(83)γ	66.4	0.22	28.1	6.5
32742.82	t-CH_3CH_2OH?	4_{13}-4_{04}	2.0	-0.33	11.1	-3.9
32852.20	Hydrogen	H(58)α	104.5	0.39	17.7	7.3
			70.3	2.42	33.1	85.5
			59.1	1.44	14.3	22.1
32865.58	Helium	He(58)α	66.7	0.29	25.8	7.9
32978.23	CH_3OCH_3	3_{12}-3_{03}EE/AA/AE/EA	63.6	-0.42	24.3	-10.8
33156.85	NH_3	(13,13)	82.0	-1.16	15.9	-19.8
			62.5	-1.34	18.5	-26.5
			3.3	-0.22	34.5	-8.2
33334.34	U?	——	[3]62.0	0.23	8.1	1.9
33704.82	CH_2NH	1_{11}-2_{02}	79.0	-1.50	16.3	-26.1
			58.9	-3.98	17.4	-73.7
33751.37	CCS	3_2-2_1	84.3	-1.09	14.8	-17.2
			65.1	-1.06	14.9	-16.8

Continued on next page

Table 3.9 – Line Identifications and Fit Parameters towards K4

Line Rest Frequency (MHz)	Species	Transition	Velocity ($\mathrm{km\,s^{-1}}$)	Height (mJy $\times$ arcsec^{-2})	Width ($\mathrm{km\,s^{-1}}$)	$\int I_v dv$ (mJy arcsec^{-2} $\times$ $\mathrm{km\,s^{-1}}$)
33821.51	Hydrogen	H(72)β	66.1	0.65	25.7	17.6
33908.67	Hydrogen	H(82)γ	68.5	0.26	35.8	9.7
34351.45	H_2CS	1_{01}-0_{00}	82.2	-0.21	21.0	-4.7
			65.6	-0.23	9.3	-2.3
34352.53	U?	——	[4]62.0	0.23	8.7	2.1
34596.38	Hydrogen^{Adj}	H(57)α	89.4	0.73	28.9	22.4
			67.6	2.04	13.3	28.9
			55.0	1.20	28.9	36.9
34614.38	HC_5N	13-12	62.4	-0.34	13.7	-5.0
34684.37	$CCCS^B$	6-5	[5]71.9	-0.17	30.4	-5.6
34824.07	CH_3CH_2CN	4_{14}-3_{13}	82.5	-0.31	12.1	-4.0
			65.1	-0.22	14.7	-3.4
35065.73	CH_2NH	3_{03}-2_{12}	[2]60.4	2.44	17.7	45.9
35134.30	NH_3	(14,14)	82.2	-0.88	14.3	-13.3
			63.5	-0.92	18.4	-18.0
35157.27	Hydrogen	H(81)γ	68.2	0.19	32.5	6.7
35185.80	U?	——	62.0	0.22	7.9	1.8
35250.77	Hydrogen	H(71)β	67.1	0.56	37.9	22.5
35267.41	$H^{13}CCCN$	4-3	85.0	-0.43	12.8	-5.8
			64.5	-0.47	13.2	-6.6
			2.1	-0.26	9.5	-2.6
35360.93	c-C_3H_2	4_{40}-4_{31}	62.7	-0.20	10.4	-2.2
35593.40	CH_3OCH_3	4_{13}-4_{04}EE/AA/AE/EA	63.7	-0.34	25.3	-9.1
35722.21	CH_3CH_2CN	4_{04}-3_{03}	83.5	-0.55	12.8	-7.5
			63.8	-0.30	12.2	-4.0

Continued on next page

Table 3.9 – Line Identifications and Fit Parameters towards K4

Line Rest Frequency (MHz)	Species	Transition	Velocity ($\mathrm{km\,s^{-1}}$)	Height (mJy × arcsec^{-2})	Width ($\mathrm{km\,s^{-1}}$)	$\int I_v dv$ (mJy arcsec^{-2} × $\mathrm{km\,s^{-1}}$)
35733.12	$^{13}CH_3CN^{BC}$	2_0-1_0/2_1-1_1	80.2	-0.24	34.9	-9.1
35906.98	U	——	60.4	-0.23	29.6	-7.3
36070.55	U?	——	62.0	0.24	10.9	2.8
36169.29	CH_3OH^{Maser}	$4_{-1,4}$-3_{03}	58.1	617.11	9.2	5263.7
			1.0	1.66	10.9	19.2
36237.95	$HC^{13}CCN$	4-3	78.5	-0.47	16.3	-8.1
			[6]57.3	-0.60	15.1	-9.6
36241.44	$HCC^{13}CN$	4-3	64.3	-0.54	14.5	-8.3
36299.95	H_2COH^+	1_{11}-2_{02}	60.8	-0.28	19.5	-5.8
36309.63	SiS	2-1	62.1	-0.26	12.6	-3.5
36392.32	HC_3N	4-3	83.2	-6.22	12.2	-81.1
			64.3	-5.02	13.5	-72.2
			1.1	-2.33	11.7	-31.9
36466.26	Hydrogen	$H(56)\alpha^B$	[7]101.3	0.34	30.2	11.1
			65.4	2.60	32.6	94.6
36739.67	CH_3CH_2CN	4_{13}-3_{12}	80.3	-0.33	17.8	-6.3
			60.9	-0.46	10.8	-5.3
36761.72	Hydrogen	$H(70)\beta$	61.1	0.41	36.4	16.1
36777.28	$CH_3^{13}CN$	2_0-1_0/2_1-1_1	77.7	-0.25	29.5	-7.7
			57.6	-0.17	8.0	-1.4
36795.47	CH_3CN	2_0-1_0/2_1-1_1	84.4	-4.02	22.4	-95.8
			64.3	-3.94	14.2	-59.5
			4.0	-1.57	18.4	-40.4
36930.70	Z-CH_3CHNH	2_{02}-1_{01}E/A	67.2	-0.32	14.5	-5.0
37018.92	CH_2CHCN	4_{14}-3_{13}	80.0	-0.30	14.2	-4.5

Continued on next page

Table 3.9 – Line Identifications and Fit Parameters towards K4

Line Rest Frequency (MHz)	Species	Transition	Velocity ($\mathrm{km\,s^{-1}}$)	Height (mJy × arcsec^{-2})	Width ($\mathrm{km\,s^{-1}}$)	$\int I_v dv$ (mJy arcsec^{-2} × $\mathrm{km\,s^{-1}}$)
			61.1	-0.47	13.7	-6.9
37182.66	CH_3C_3N?	9_1-8_1/9_0-7_0	72.5	-0.24	10.6	-2.7
37276.99	HC_5N	14-13	62.4	-0.31	10.8	-3.5
37350.57	Hydrogen	H(87)δ	69.0	0.24	11.9	3.1
37385.12	NH_3	(15, 15)	82.7	-1.20	16.8	-21.5
			64.8	-0.86	23.2	-21.3
			-0.1	-0.34	19.9	-7.3
37464.17	CH_3CHO	2_{12}-1_{11}A	78.7	-0.75	15.3	-12.2
			60.0	-1.05	14.2	-15.8
			0.4	-0.39	13.5	-5.5
37536.85	U?		62.0	0.24	15.5	4.0
37686.87	CH_3CHO	2_{12}-1_{11}E	80.6	-0.52	12.8	-7.1
			61.3	-1.11	13.0	-15.4
37703.70	CH_3OH	$7_{-2,6}$-$8_{-1,8}$	56.8	-0.70	15.3	-11.4
37904.85	CH_2CHCN	4_{04}-3_{03} F=4-3	82.5	-0.69	14.2	-10.5
			63.0	-0.67	14.0	-9.9
38326.81	U?	——	62.0	-0.28	7.5	-2.2
38360.27	Hydrogen	H(69)β	64.7	0.51	36.4	19.9
38473.36	Hydrogen^{Adj}	H(55)α	93.1	0.56	32.9	19.7
			67.8	1.54	16.4	27.0
			53.3	1.07	27.9	31.8
38506.04	CH_3CHO	2_{02}-1_{01}E	83.5	-1.31	13.9	-19.3
			63.8	-1.55	19.5	-32.1
38512.11	CH_3CHO	2_{02}-1_{01}A	83.8	-1.35	10.8	-15.4
			[8]61.5	-1.81	24.8	-47.8

Continued on next page

Table 3.9 – Line Identifications and Fit Parameters towards K4

Line Rest Frequency (MHz)	Species	Transition	Velocity ($\mathrm{km\,s^{-1}}$)	Height (mJy × arcsec^{-2})	Width ($\mathrm{km\,s^{-1}}$)	$\int I_v dv$ (mJy arcsec^{-2} × $\mathrm{km\,s^{-1}}$)
			0.7	-0.74	11.3	-8.9
38847.73	CH_2CHCN	4_{13}-3_{12}	83.7	-0.45	15.2	-7.3
			61.0	-0.39	15.9	-6.6
39047.30	CH_3OCH_3	5_{14}-5_{05}EE/AA/AE/EA	63.8	-0.34	24.9	-9.1
39362.50	CH_3CHO	2_{11}-1_{10}E	80.7	-0.66	13.1	-9.2
			60.6	-0.62	13.3	-8.8
39594.29	CH_3CHO	2_{11}-1_{10}A	82.2	-0.63	18.4	-12.4
			58.7	-0.52	11.7	-6.5
39924.77	CH_2CN	2_{12}-1_{11}	82.0	-0.32	21.5	-7.3
			60.1	-0.58	11.8	-7.2
39927.87	U	——	[9]61.7	-0.37	9.5	-3.8
39941.41	NH_3^B	(16,16)	[10]79.8	-0.72	29.3	-22.5
39956.70	c-H_2C_3O	3_{13}-2_{12}	82.3	-0.48	9.4	-4.7
40039.02	H_2CCO	2_{12}-1_{11}	81.3	-0.33	12.3	-4.4
40052.88	Hydrogen	H(68)β	64.8	0.66	21.5	15.0
40239.19	CH_2CN^B	2_{02}-1_{01} J=$\frac{5}{2}$-$\frac{3}{2}$	[11]84.5	-0.53	7.9	-4.4
		F1=$\frac{7}{2}$-$\frac{5}{2}$ F=$\frac{5}{2}$-$\frac{3}{2}$				
40239.70	CH_2CN^B	2_{02}-1_{01} J=$\frac{5}{2}$-$\frac{3}{2}$	[11]81.2	-1.23	6.5	-8.5
		F1=$\frac{7}{2}$-$\frac{5}{2}$ F=$\frac{7}{2}$-$\frac{5}{2}$	[11]59.2	-1.44	28.7	-43.8
40247.54	CH_2CN^B	2_{02}-1_{01} J=$\frac{3}{2}$-$\frac{1}{2}$	[11]82.5	-0.95	16.1	-16.3
		F1=$\frac{5}{2}$-$\frac{3}{2}$ F=$\frac{5}{2}$-$\frac{3}{2}$	[11]58.7	-0.87	15.7	-14.4
40256.79	CH_2CN^{BC}	2_{02}-1_{01} J=$\frac{3}{2}$-$\frac{1}{2}$	[11]71.5	-0.30	40.2	-13.0
		F1=$\frac{3}{2}$-$\frac{3}{2}$ F=$\frac{5}{2}$-$\frac{5}{2}$				
40347.34	U	——	62.0	0.33	10.6	3.7
40352.77	$Si^{18}O$	1-0	66.7	-0.34	14.0	-5.0

Continued on next page

Table 3.9 – Line Identifications and Fit Parameters towards K4

Line Rest Frequency (MHz)	Species	Transition	Velocity ($\mathrm{km\,s^{-1}}$)	Height (mJy × arcsec^{-2})	Width ($\mathrm{km\,s^{-1}}$)	$\int I_v dv$ (mJy arcsec^{-2} × $\mathrm{km\,s^{-1}}$)
40577.83	U?	——	62.0	-0.32	13.3	-4.5
40630.50	Hydrogen	H(54)α	103.3	0.24	37.2	9.3
			72.9	1.47	17.5	27.4
			55.7	1.74	12.9	23.8
40658.60	CH_2CN^{BC}	2_{11}-1_{10} J=$\frac{5}{2}$-$\frac{3}{2}$	[2]71.5	-0.44	28.1	-13.2
40875.44	NH_2CHO	2_{12}-1_{11}	[12]76.6	-1.84	27.3	-53.7
			[2]56.0	-1.68	13.4	-24.0
			2.8	-0.69	15.1	-11.0
41124.95	*t*-CH_3CH_2OH?	6_{15}-6_{06}	68.6	-0.31	6.8	-2.3
41741.37	U?		62.0	0.29	8.5	2.6
41846.55	Hydrogen	H(67)β	65.3	0.46	27.8	13.7
42373.34	$^{30}SiO^{Adj}$	1-0	81.1	-1.32	13.8	-19.4
			63.2	-1.87	18.8	-37.6
42386.06	NH_2CHO^{Adj}	2_{02}-1_{01}	79.1	-2.79	22.5	-68.5
			[2]55.3	-2.61	14.6	-40.3
			0.6	-2.10	13.2	-27.3
42602.15	HC_5N^{Adj}	16-15	80.7	-0.22	7.6	-1.7
			65.7	-0.33	10.0	-3.5
42674.19	HCS^+	1-0	82.5	-0.53	9.4	-5.3
42839.92	NH_3	(17,17)	78.7	-0.52	17.1	-9.5
			60.2	-0.49	12.4	-6.5
42879.94	^{29}SiO	1-0	78.1	-2.62	19.6	-54.6
			59.6	-2.78	10.7	-31.8
			2.2	-0.93	10.0	-9.9
42951.97	Hydrogen	H(53)α	70.6	1.63	15.1	26.2

Continued on next page

Table 3.9 – Line Identifications and Fit Parameters towards K4

Line Rest Frequency (MHz)	Species	Transition	Velocity ($\mathrm{km\,s^{-1}}$)	Height (mJy $\times$ arcsec^{-2})	Width ($\mathrm{km\,s^{-1}}$)	$\int I_v dv$ (mJy arcsec^{-2} $\times$ $\mathrm{km\,s^{-1}}$)
			55.8	1.29	17.7	24.2
43423.85	SiO	1-0	82.9	-6.60	19.8	-139.1
			60.3	-3.28	13.5	-47.2
			1.5	-5.46	12.8	-87.0
43700.42	U?	——	62.0	0.39	7.7	3.2
43748.95	Hydrogen	H(66)β	66.4	0.47	26.7	13.3
43954.45	NH_2CHO	2_{11}-1_{10}	85.3	-1.24	15.4	-20.3
			62.2	-2.26	24.8	-59.6
			[13]3.8	-0.31	26.2	-8.5
43972.23	U		62.0	-0.39	9.4	-3.9
44069.48	$CH_3OH^{Maser,Adj}$	7_{07}-6_{16}++	68.4	12.90	9.7	118.7
			56.7	50.24	9.0	462.2
44084.17	$H^{13}CCCN^{Adj}$	5-4	82.5	-0.54	13.9	-8.0
			64.8	-0.31	11.3	-3.8
44104.78	c-C_3H_2 ^{B}	3_{21}-3_{12}	[14]77.0	-0.46	9.5	-4.7
			59.4	-1.34	12.9	-18.4
44195.58	U?	——	62.0	0.42	9.5	4.3
44592.31	U?	——	62.0	-0.36	7.6	-2.9
44596.99	CH_3CH_2CN	5_{05}-4_{04}	65.0	-0.49	8.3	-4.3

[1] Weakly masing.

[2] Transition is at an unusual velocity for the source.

[3] A U-line at 33332.3 MHz is reported in the LOVAS catalog.

[4] This may be weak masing by H_2CS at $\sim$55 $\mathrm{km\,s^{-1}}$. This velocity is similar to that at which the methanol masing transitions emit towards this source.

[5] Blended with CH_3OCH_3 2_{20}-3_{13}AA & EE.

Continued on next page

Table 3.9 – Line Identifications and Fit Parameters towards K4

Line Rest Frequency (MHz)	Species	Transition	Velocity ($\mathrm{km\,s^{-1}}$)	Height (mJy $\times$ arcsec^{-2})	Width ($\mathrm{km\,s^{-1}}$)	$\int I_v dv$ (mJy arcsec^{-2} $\times$ $\mathrm{km\,s^{-1}}$)

[6] The 62 $\mathrm{km\,s^{-1}}$ component of HC^{13}CCN is blended with the 82 $\mathrm{km\,s^{-1}}$ component of HCC^{13}CN.

[7] Blended with H(80)γ.

[8] Blended with foreground absorption by the E-state transition.

[9] Detected in K6, L, and K4.

[10] Blended with HC_5N J=(15-14).

[11] Multiple hyperfine components are blended.

[12] This contains a bad spectrometer channel that could interfere with the fit.

[13] Possibly blended with HNCO 2_{02}-1_{01}.

[14] Blended with H(75)γ.

Chapter 4

Constraining the Physical Structure and Environment in Sgr B2(N): Insights from an ATCA Survey at 7-mm

Note: This chapter is adapted from the published work: "An ATCA survey of Sagittarius B2 at 7 mm: chemical complexity meets broad-band interferometry", Corby, J. F., Jones, P. A., Cunningham, M. C., Menten, K. M. et al. (2015), *The Monthly Notices of the Royal Astronomical Society*, 790, 3696.

Abstract

We present science results from a 30 - 50 GHz survey of Sagittarius B2(N) conducted with the Australia Telescope Compact Array (ATCA) with 5 - 10 arcsec resolution. The work utilizes the interferometric images and the output of the code presented in Chapter 3 to discuss the kinematics, spatial structure, and physical environment within gas located in Sgr B2. The material of interest appears in absorption against the radio continuum produced by HII regions in Sgr B2(N), and has physical conditions that are poorly constrained. The data reveal that a diverse set of molecules persist in this gas, with 53 molecules detected and additional isotopologues. We discuss three primary results and their implications for the gas. First, the data confirm the presence of extremely subthermal molecular excitation conditions, implying low or moderate densities. Secondly, line radiation spanning the full spectra reveals substantial variation in molecular abundances or line excitation conditions on small spatial scales of $\lesssim$10 arcsec. Third, the spatial distributions of species including *l*-C_3H^+, CS, OCS, SiO, and HNCO indicate that the absorbing gas components likely have high UV-fluxes consistent with a photodissociation region (PDR). We conclude that the confluence of conditions, including strong X-ray, UV, and CR irradiation, in addition to probable shocks may contribute to the observed chemistry. The data suggest that a multitude of organic molecules, including nitriles, aldehydes, alcohols, and imines, either form or persist in these conditions, and observed species provide promising, and in many cases biologically relevant, targets for observations in other PDRs.

4.1 The Known Structure of Sgr B2

As described in §1.4.1, Sgr B2 is the most massive star forming GMC in the Galaxy, and has physical properties that tend to be more extreme than in most star forming clouds.

Particularly, the X-ray flux (Terrier et al. 2010), cosmic ray ionization rate (van der Tak et al. 2006), and magnetic field strength (Crutcher et al. 1996) are $\gtrsim$10 times the strength in Sgr B2 compared to most star forming clouds, and shocks are believed to be pervasive as well (Martín et al. 2008; Minh & Irvine 2006).

Sgr B2 has a complex physical structure with more than 50 known extended, compact, ultra-compact, and hypercompact HII regions embedded in an extended envelope of molecular, atomic, and ionized gas (Gaume et al. 1995; Goicoechea et al. 2003; Jones et al. 2008). The North, Main, and South (Sgr B2(N), (M), and (S)) cores of star formation (Figure 1.1) have v_{LSR} of $\sim$55 - 70 km s^{-1}, and many researchers have suggested that the star formation is triggered by the collision of a cloud of gas at $\sim$80 - 90 km s^{-1} with the main body of Sgr B2 at $\sim$40 km s^{-1} (e.g. Hasegawa et al. 1994; Sato et al. 2000).

Towards the North core of Sgr B2 (Sgr B2(N)), the focus of this study, continuum emission is produced by a complex of HII regions, as observed in Gaume et al. (1995). Two $\sim$10 arcsec (= 0.4 pc) concentric shell-shaped regions – K5 and K6 – are thought to be expanding ionization fronts (Figure 3.2). To the NW of these, the more compact region K4 is thought to be a similar system at an earlier stage of development. Three subarcsecond cores of continuum emission – K1, K2, and K3 – are located to the SW of K5 and K6. Finally, a cometary HII region, L, is located $\sim$35 arcsec NE of the North core.

Molecular gas is observed in the foreground of the HII regions and in extended envelope surrounding the cores (Huettemeister et al. 1995; Jones et al. 2008). Additionally, the LMH hot core is a $\sim$5 arcsec region surrounding K2 that is continuum-free at radio wavelengths, but bright in submillimeter continuum (Miao et al. 1995; Qin et al. 2011). Similarly, the "h" hot core, first identified as a quasi-thermal methanol core (Mehringer & Menten 1997) produces submillimeter continuum emission (Qin et al. 2011) and line emission by many complex organic species (Hollis et al. 2003; Belloche et al. 2013).

4.2 Ionized Gas Structure

In Chapter 3, the results of the automated line fitter demonstrated that recombination line emission in the spectrum of K6 contains two kinematic components, at ∼59 and ∼85 km s^{-1}, each about 28 km s^{-1} wide and therefore poorly resolved. The profiles also proved to be sensitive to the resolution of the image, with profiles sampled at higher spatial resolution having more pronounced separation between the two components. Recombination line emission from L, on the other hand, had very well-behaved kinematics with a single line component that was consistently at 73.6 ± 0.2. The line profiles observed towards K4 were highly sensitive to the spatial resolution, and included two primary components with velocities of $\sim$ 70 and $\sim$ 55 km s^{-1} as well as a wing component at ∼100 km s^{-1}.

The double-peaked structure towards K6 was first reported by De Pree et al. (1995) in an image of the H(66)α transition observed by the VLA with 1.″4 resolution. This work reported a 2-component recombination line profile located internal to the K6 shell at a position roughly 2.5 arcsec north of our selected K6 region. The components were reported at 50 and 93 km s^{-1}, and De Pree et al. (1995) argued that the H(66)α line profile provides a direct detection of the two sides of a shell with an expansion velocity of ∼21 km s^{-1}. In the ATCA data, a double-peaked profile with components at ∼50 and 90 km s^{-1} is observed towards the K6-internal position noted in that work. However, the spatial positions of the peak 50 and 90 km s^{-1} recombination line emission are offset, with the 50 kms component centered on the base of the K6 shell within our K6 elliptical region, and the 90 km s^{-1} gas centered ∼4 arcsec to the NW (Figure 4.1). At the K6 position used in this work, the two components peak at somewhat more intermediate velocities of ∼59 and 85 km s^{-1}. This is consistent with the picture of an expanding shell, as the K6 position on the edge-on shell should exhibit a smaller velocity separation between the two sides of the shell

than at the K6-internal position. As different positions on the edge-on shell are prominent at different velocities, the data are consistent with the ionization front expanding into a clumpy molecular cloud and preferentially illuminating at the position of a clumps on the front and back sides of the shell.

The observed sensitivity of the line profiles to the spatial resolution can also be explained by inspecting this image. In the lower spatial resolution images, emission from the K5 shell contributes significant flux to the spectrum extracted towards K6. The flux originating from the K5 shell is at $\sim$70 km s^{-1}, and therefore fills in the space between the two velocity components at K6.

Similarly, the recombination line emission profiles towards K4 were observed to be highly sensitive to the beam size. The channel maps show a steep velocity gradient across K4 which could account for the differences in line shape, with low velocity emission to the NW and high velocity emission to the SE of K4. The high velocity emission located SE of K4 appears to bridge K4 with the top of the K6 shell. This is a very interesting feature, for which we do not presently offer a sound physical interpretation.

4.3 Molecular Composition of Absorbing Gas Components

We utilize the output of the automated line fitter to characterize the molecular composition of the gas clouds observed towards K4, K6, and L.

Nearly all of the molecular lines detected towards K6, L, and K4 are in absorption against the free-free continuum emission. The following molecular species were detected towards one or more of these regions. Tentative detections are marked with a "(?)".

CS Family: CS, $C^{34}S$, $C^{33}S$, ^{13}CS, $^{13}C^{34}S$, HCS^+, H_2CS, CCS, $CC^{34}S$, OCS, CCCS

Silicon Species: SiO, ^{29}SiO, ^{30}SiO, $Si^{18}O$, SiN, SiS, SiC_2

Other Inorganic Molecules: SO, PN, $Na^{37}Cl$(?)

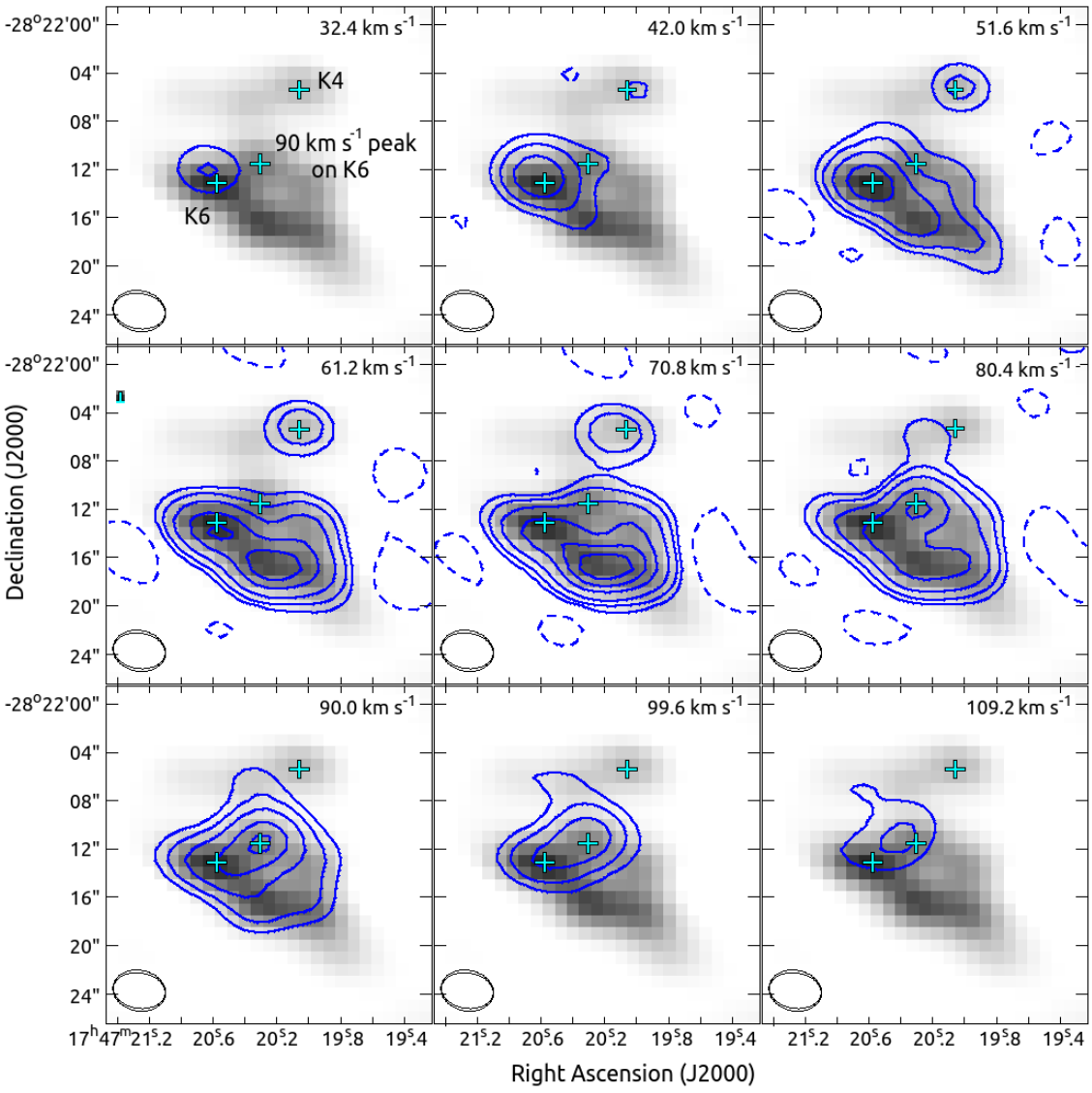

Fig. 4.1 – Channel maps of the H(53)α transition at 42951 MHz shown in contours over the 40 GHz continuum in greyscale. The synthesized beams for the continuum and line images are shown in the lower left corner. The figure shows a strong velocity gradient from the NW to the SE of K4. The crosses mark the center positions of the regions selected for K4 and K6 (at the base of the K6 shell) and indicate the peak position of the 90 $\mathrm{km\,s^{-1}}$ gas. Notice the offset positions of high and low velocity gas on the K6 shell and the velocity gradient observed at K4.

Hydrocarbon Chains: *l*-C_3H, *l*-C_3H^+, C_4H

Ring Species: *c*-C_3H_2, *c*-$H^{13}CCCH$, *c*-$HCC^{13}CH$, *c*-H_2C_3O, *c*-H_2COCH_2

Amines: NH_3, NH_2D, CH_3NH_2(?), NH_2CN, CH_3CONH_2, H_2NCO^+(?)

Isonitriles: CH_3NC, HCCNC

Nitriles: CCCN, HSCN, NaCN/NaNC, CH_2CN, CH_3CN, $CH_3^{13}CN$, $^{13}CH_3CN$, CH_2CHCN, CH_3CH_2CN, HC_3N, $HCC^{13}CN$, $HC^{13}CCN$, $H^{13}CCCN$, HC_5N, CH_3C_3N

Imines: CH_2NH, *E*-CH_3CHNH, *Z*-CH_3CHNH, HNCHCN

Aldehydes: H_2CO, H_2COH^+, CH_3CHO, NH_2CHO, $NH_2^{13}CHO$, CH_3OCHO, *cis*-CH_2OHCHO, *t*-CH_2CHCHO, CH_3CH_2CHO

Alcohols: CH_3OH, $^{13}CH_3OH$, *t*-CH_3CH_2OH, *g'Ga*-$(CH_2OH)_2$

Other Oxynated Species: HNCO, *t*-HCOOH, H_2CCO, CH_3OCH_3, $(CH_3)_2CO$

Other Organic Species: CH_3SH

The molecular inventory of the gas includes that reported in the more extended envelope of Sgr B2 and in the north cloud, an extended cloud of material that peaks 1 arcmin north of the Sgr B2(N) core (Jones et al. 2008, 2011). In a survey conducted with the Mopra telescope over the same frequency range on a 6 arcmin $\times$ 6 arcmin field of view, the species CS, HCS^+, CCS, OCS, SiO, SO, HNCO, $HOCO^+$, HC_3N, HC_5N, CH_3OH, CH_3CN, CH_3CHO, NH_2CHO, CH_2CN, and CH_2NH were detected in extended material around the North and Main cores (Jones et al. 2011). All of these molecules except $HOCO^+$ were detected in the significantly more sensitive ATCA survey, along with an additional $\sim$40 molecular species. We note that the depletion of $HOCO^+$ in the absorbing material is curious and refrain from further interpreting this. In a 3-mm survey conducted with Mopra over a similar field of view as the 7 mm survey, multiple other species detected here were observed to have an extended distribution, including NH_2CN, CH_3OCH_3, CH_3OCHO, *t*-CH_3CH_2OH, *c*-C_3H_2, CH_2CHCN, CH_3CH_2CN, H_2CO, H_2CS, H_2COH^+, and CH_3SH (Jones et al. 2008).

In the ATCA spectra extracted towards K6, L, and K4, molecular lines were primarily detected at two velocity components separated by $\sim$20 km s^{-1} towards all three regions. The kinematics were characterized in the previous chapter, where Figure 3.11 shows a histogram of the 25th - 90th percentile Gaussian fit parameters of identified molecular lines, and Table 3.5 presents the mean fit parameters. K6 and K4 have velocity components centered at 64 and 82 km s^{-1} and 62 and 82 km s^{-1} respectively, whereas L has velocity components at 56 and 76 km s^{-1}. While we do not include a full characterization of the spectra towards the LMH and "h", the spectra of these sources show that line emission from the LMH hot core is at $\sim$64 km s^{-1} and emission from "h" is at 73 km s^{-1}, in agreement with previous observations (Hollis et al. 2003; Belloche et al. 2013). Towards K6, L, and K4, both primary velocity components have median line widths $>$10 km s^{-1}, indicating highly supersonic turbulence.

A larger number of transitions are detected in the low velocity component gas towards all three regions, and the low velocity component has a higher total integrated line intensity in the detected transitions. Towards K6, the total integrated flux absorbed by the 64 km s^{-1} component is a factor of 3.5 times greater than the total flux absorbed by the 82 km s^{-1} component. Towards L and K4, the low and high velocity components typically have more similar line intensities, with total integrated flux ratios of $\frac{\int (T_L)|_{Low}}{\int (T_L)|_{High}}$ = 1.7 and 1.1 respectively. The line height ratios, also tabulated in Table 3.5, show similar values. A larger number of distinct molecules were detected towards the low velocity component gas in K6 than towards any other position or velocity component.

While nearly all molecular lines appear in absorption, a few species exhibit weakly masing transitions that appear in emission. Previous work has demonstrated that the unusual environment in the Galactic Center produces unique excitation conditions (Menten & van der Tak 2004). For some large molecules, the conditions cause inversion of the energy

levels in some low-J lines and anti-inversion in others, leading to weak maser emission in the first scenario and enhanced absorption in the latter (see §1.2 of Menten 2004, and references therein). In the spectra towards K6 and K4, two transitions of CH_2NH are detected, including the $1_{11}-2_{02}$ transition in absorption and the weakly masing $3_{03}-2_{12}$ transition in emission. Both transitions are detected both in the high and low velocity gas components towards K6, with similar morphologies over the K5 and K6 shells (Steber et al. in prep). The maser emission is detected in the low velocity gas towards K4 as well. Additionally, the $3_{12}-3_{03}$ transition of *t*-CH_3CH_2OH is weakly masing in the high velocity gas component (at 82 $\mathrm{km\,s^{-1}}$) towards K6 and K4, and H_2COH^+ 3_{03}-2_{12} appears in emission towards K4. Finally, the $1_{01}-0_{00}$ transition of H_2CS may show weak masing at an offset velocity in the low velocity gas in K4 (see Figure 4.2c), but further investigation would be required to confirm this. No maser emission is detected towards L.

With the exception of ammonia inversion transitions, methanol masing transitions, one transition of H_2CO, and three transitions of *c*-C_3H_2, all detected molecular transitions have lower state energies below 20 K, with most being below 10 K. For many of the detected molecules, the highest quantum line strength transitions that fall in the 30-50 GHz range are between low energy states; however, a number of stronger lines between higher energy states (40 - 80 K) are missing. The gas is therefore rotationally cold. Given the typical temperatures of molecular gas in the Galactic Center ($\gtrsim$70 K) (Ao et al. 2013; Martín et al. 2008, and references therein) and the observed supersonic turbulence, excitation temperatures of T_{Ex} $\sim$10 K are highly subthermal. This result agrees with the conclusions of Huettemeister et al. (1995), which determined that $T_{Ex} < 20\ \mathrm{K} \ll T_{kin}$ in the absorbing gas components, and with multiple recent characterizations of species detected in absorption in Sgr B2(N), which have determined that $T_{Ex} \sim 9$ K (Loomis et al. 2013; Zaleski et al. 2013; McGuire et al. 2013).

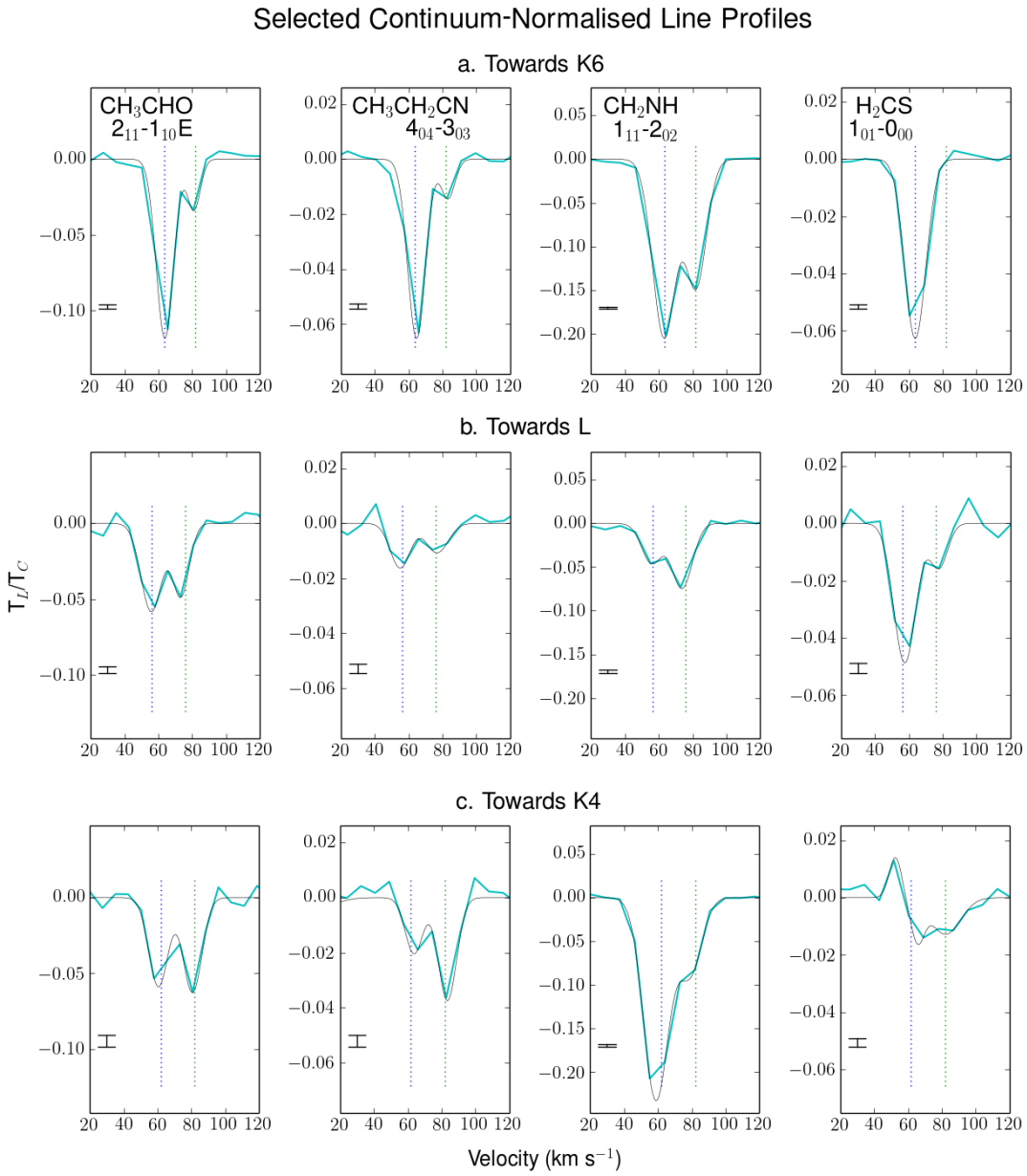

Fig. 4.2 – Line profiles of CH_3CHO, CH_3CH_2CN, CH_2NH, and H_2CS reveal differences in the line optical depth ratios between all spatial positions and all velocity components. The data (cyan) are overlaid with the automated line fits (black), and vertical dotted lines indicate the velocities associated with the low and high velocity gas towards each region. **a.** In K6, while CH_3CHO and CH_3CH_2CN have similar line profiles, the selected transition of CH_2NH has a comparatively enhanced line strength in K6: 82 $\mathrm{km\,s^{-1}}$; the line radiation by H_2CS in the K6: 82 $\mathrm{km\,s^{-1}}$ is significantly depleted to below the detection threshold. Towards L (**b.**) and K4 (**c.**) the line profiles vary significantly, and line strengths do not scale linearly with the strengths observed towards K6. The root-mean-squared noise in the extracted spectra are shown in the lower left corner of each panel.

Additionally, ammonia inversion transitions with lower state energies ranging from 1200 - 3500 K are detected in both velocity components towards K6, L, and K4. Most of these transitions have been reported toward Sgr B2(N) previously with single dish observations (Huettemeister et al. 1995; Flower et al. 1995). Although ammonia inversion lines are useful diagnostics of gas temperature (Ho & Townes 1983; Walmsley & Ungerechts 1983) the very high energy transitions do not likely indicate the kinetic temperature of the molecular gas, as the energy states may be populated due to formation pumping (Lis et al. 2012; E. Bergin 2014, private communication). In work on Sgr B2 using Herschel data from the HEXOS program, Lis et al. (2012) proposed that H_3O^+ and NH_3, which have homologous structures with inversion transitions between metastable energy states, may be excited to very high energy levels by excess energy available from formation in the presence of X-ray radiation. While they favor an X-ray dominated environment for producing observed abundance ratios of H_3O^+ and H_2O, they do not rule out cosmic ray or shock driven chemistry. Regardless of the exact scenario, the high energy ammonia transitions can only be explained with significant energy available in the gas (via X-rays, CRs, or shocks). As such, the ATCA data are decidedly not probing cold material in the two primary velocity components towards K6, K4, and L, providing additional evidence that the gas is extremely subthermally excited.

The presence of two velocity components at multiple positions across the field, the spatial extent of the absorbing gas over the full continuum structure (Figure 4.4a), the similar excitation conditions across the spatial field, and the similarity with the molecular inventory observed in more extended material by Jones et al. (2011, 2008) suggests we may be peering through two extended sheets of gas, perhaps with a kinematic gradient across the field. Previous work has suggested that absorbing gas at $\sim$65 and 82 $\mathrm{km\,s^{-1}}$ is associated with the extended envelope of Sgr B2 (Huettemeister et al. 1995) and is not internal to the

core. If the components are located in the envelope, they would be anywhere from 3 - 10 pc from the cores (Huettemeister et al. 1995), a distance that is significantly larger than the projected distance between the cores, as L and K6 are separated by $\sim$1.3 pc and K4 and K6 are separated by 0.4 pc in the plane of the sky. In this scenario, the extended molecular gas components need not interact directly with the local structure of the core (including expanding HII regions), and it is unclear whether the higher or lower velocity component is closer to the star forming core.

4.3.1 Normalised Spectral Line Ratios: Determining Chemical or Excitation Differences In Absorbing Gas

To determine if the system consists of two extended clouds or if each kinematic component towards each region should be treated as a separate cloud (in which case we would be probing 3 spatial regions $\times$ 2 velocity components = 6 clouds), we inspect the line radiation in each component. If the gas is located in the envelope with significant distance between the cores and the absorbing gas, we expect the gas phase molecular abundances and excitation to be fairly self-consistent in low velocity gas across the spatial field and in high velocity gas across the field. The low velocity gas could be quite distinct from the high velocity gas however, as they are clearly separate clouds.

If two components of gas have identical gas phase abundances and excitation, then the line optical depth ratios of the two gas components should be equivalent for any two lines, such that

$$\left(\frac{\tau_{C2}}{\tau_{C1}}\right)_A = \left(\frac{\tau_{C2}}{\tau_{C1}}\right)_B \pm \text{Error} \tag{4.1}$$

for two gas components C1 and C2 and for spectral lines A and B. The optical depth of an absorption line is related to the measured line and continuum brightness levels by

$$\tau = -ln\left(1 + \frac{T_L}{T_C - [f(T_{Ex}) - f(T_{CMB})]}\right); f(T) = \frac{h\nu/k}{e^{h\nu/kT} - 1} \tag{4.2}$$

$$\tau \approx \frac{-T_L}{T_C - [f(T_{Ex}) - f(T_{CMB})]} \tag{4.3}$$

$$\tau \approx \frac{-T_L}{T_C} \tag{4.4}$$

Equation 2 provides the general equation for absorption line optical depth, while Equation 3 is appropriate for optically thin lines, and Equation 4 is appropriate for optically thin lines when the continuum temperature dominates the excitation and cosmic microwave background temperatures. Towards K6, due to the strong continuum and low excitation temperature, Equation 4 is appropriate for optically thin lines. It follows that the line-to-continuum ratio can be read as the optical depth towards K6. The continuum is somewhat weaker towards L and K4, and as a result, the excitation temperature may contribute non-trivially to the denominator in Equation 3 resulting in a factor offset compared to Equation 4. While the factor varies with frequency for a frequency-dependent continuum temperature, the change is small with frequency in the range of 30-44 GHz. For optically thin lines in all cases therefore, Equation 1 can be rewritten as

$$\left(\frac{(T_L/T_C)_{C2}}{(T_L/T_C)_{C1}}\right)_A = \left(\frac{(T_L/T_C)_{C2}}{(T_L/T_C)_{C1}}\right)_B \pm \text{Error.} \tag{4.5}$$

We refer to the quantity on the left as the normalised line ratio (NLR) of spectral line A with respect to C1 and use the line height generated by the automated line fitter for T_L. In the range of 29.8 to 44.6 GHz, we determine the continuum levels using the continuum images with central frequencies of 33.4 and 40.8 GHz and 7.5 GHz bandwidths. From the two images, we derived a power-law fit to the continuum strength towards K6 and linear fits to the continuum ratios $\frac{(T_C)}{(T_C)_{K6}}$ for L and K4. We estimate that uncertainty in the continuum ratios contributes 10% error to an NLR.

Figure 4.2 shows the profiles of selected transitions of CH_3CHO, CH_3CH_2CN, CH_2NH, and H_2CS. Inspecting the profiles towards K6 (Figure 4.2a), it is clear that the low (64 $\mathrm{km\,s^{-1}}$) and high (82 $\mathrm{km\,s^{-1}}$) velocity components do not show identical gas phase abundances and excitation. The line profiles of CH_3CHO and CH_3CH_2CN appear quite similar,

with the peak line strengths in the high velocity gas being $\sim$25% that in the low velocity gas. In terms of Equation 5,

$$\mathrm{NLR}_{CH_3CHO} \approx \mathrm{NLR}_{CH_3CH_2CN} \approx 0.25$$

for the high velocity gas with respect to the low velocity gas for the two specific transitions. However, the NLR is clearly much higher, at $\sim$70%, for the transition of CH_2NH and much lower for H_2CS. If the line profiles of CH_3CHO and CH_3CH_2CN are typical towards K6, we can therefore say that the high velocity component towards K6 (K6: 82 km s^{-1}) is enhanced in CH_2NH 1_{11} - 2_{02} and depleted in H_2CS $1_{01} - 0_{00}$ relative to the low velocity gas in K6 (K6: 64 km s^{-1}). Towards K6, it follows that significant differences in gas phase abundances and/or excitation exist in the two gas clouds. As the low and high velocity clouds are obviously distinct bodies, this result is not suprising.

More interestingly, the line profiles towards L and K4 look very distinct compared to those in K6. We first compare only the low velocity gas in all three regions. In the CH_3CHO line, the NLRs with respect to K6: 64 km s^{-1} are 50% for the low velocity gas in both L and K4 (L: 56 km s^{-1} and K4: 62 km s^{-1}, respectively). In the line of CH_3CH_2CN, however, absorption by L: 56 km s^{-1} and K4: 62 km s^{-1} is considerably weaker, at $\sim$25 and 30%, respectively. Whereas the low velocity component absorption by CH_2NH is weak in L: 56 km s^{-1} (at $\sim$22% the strength observed in K6), it is very strong in K4. On the other hand, the line of H_2CS is strong in the low velocity gas towards L: 56 km s^{-1} (at $\sim$75% the strength observed in K6), and weak in K4: 62 km s^{-1} (at $\sim$25% the strength observed in K6). From these four lines alone, it is very clear that differences in excitation and/or gas phase molecular abundances exist on small angular scales of $<$10 arcsec.

Comparing the high velocity gas in the three regions produces a similar result. With respect to K6: 82 km s^{-1}, the high velocity components in L and K4 have 40 and 80% deeper

line absorption by CH_3CHO. In the CH_3CH_2CN line, K6: 82 km s^{-1} and L: 76 km s^{-1} have similar line strengths, while the high velocity gas in K4 (K4: 82 km s^{-1}) shows significant enhancement. L: 76 km s^{-1} and K4: 82 km s^{-1} have lower line strengths of CH_2NH 1_{11}-2_{02}, and while H_2CS is undetected in K6: 82 km s^{-1}, it is observed towards L: 76 km s^{-1} and K4: 82 km s^{-1} . This result does not support the hypothesis that the high velocity gas is an extended cloud located in the envelope of Sgr B2.

Utilizing the bandwidth offered by the survey, we compute the NLRs of unblended, confidently assigned absorption lines from multiple distinct molecular families in the segment of the spectrum extracted from high spatial resolution data (from 29.8 - 44.6 GHz). Figure 4.3 provides NLR values with respect to K6: 64 km s^{-1} for spectral lines in each velocity component of each spatial region, plotted against the line-to-continuum ratios of the lines in K6: 64 km s^{-1}. As follows from Equations 2 - 4, the abscissa provides a proxy for the line optical depth in K6: 64 km s^{-1}, while the ordinate is proportional to the line optical depth ratio with respect to K6: 64 km s^{-1} in the indicated gas component. The median NLR is shown by the dashed line with $\pm 3\sigma$ errors shaded around the median. The shaded errors are estimated by 12.5% error on each line height added in quadrature with 10% error introduced by uncertainty in the continuum ratios, resulting in a $\sim$20% total 1σ error. Finally, we note that the apparent slope at the low optical depth side relates to the detection limit in the spectra. Because K6: 64 km s^{-1} has the strongest continuum level, making the spectrum towrads K6 more sensitive to low optical depth lines and also typically has the highest optical depth, lines that are weakly detected towards K6: 64 km s^{-1} are only detected towards other components if they have enhanced line optical depths compared to the median. This does not imply that these points are unreliable, but implies that the lower left corners of the plot cannot be filled in.

We consider the line radiation with respect to the median ratio, as differences in the

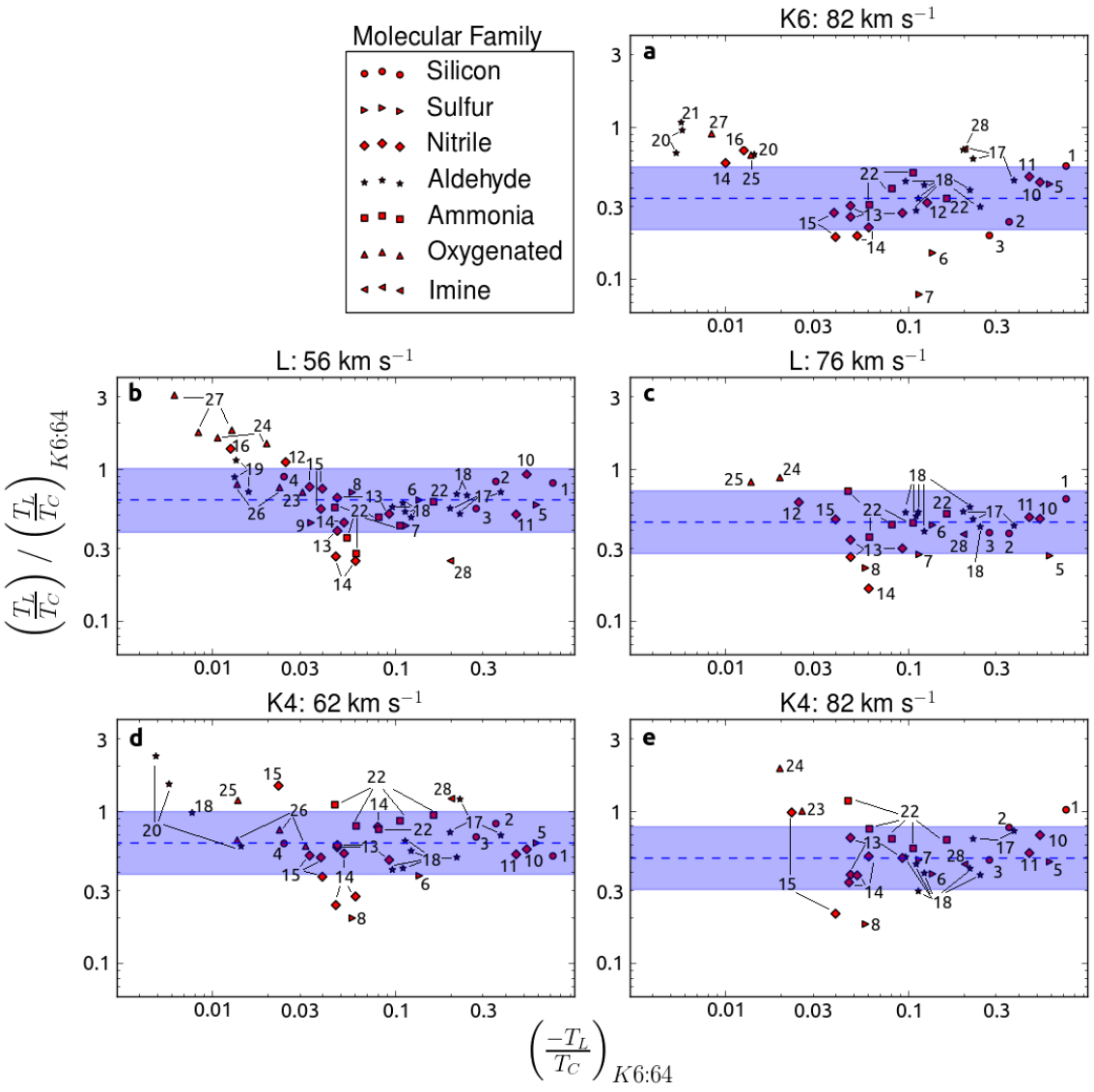

Fig. 4.3 – Normalised line ratios (NLRs) indicate statistically significant differences in gas phase abundances or excitation between different spatial positions. The abscissa shows the line height-to-continuum ratios of lines in K6: 64 km s^{-1}. Under the low excitation temperatures and high background continuum in K6: 64 km s^{-1}, this is a proxy for the line optical depth. The ordinate provides NLRs with respect to K6: 64 km s^{-1}; for optically thin lines, these are proportional to the line optical depth ratio. The dashed lines and shading indicate median ratios and the $\pm 3\sigma$ range. Represented data include transitions from 30 - 44.6 GHz for selected families of molecules. Species are numbered by: 1 - 4 are SiO, ^{29}SiO, ^{30}SiO, and SiS. 5 - 9 are SO, CCS, HCS^+, H_2CS, and OCS. 10 - 16 are nitriles HC_3N, CH_3CN, CH_2CN, CH_2CHCN, CH_3CH_2CN, HC_5N, and CCCN. 17 - 21 are aldehydes NH_2CHO, CH_3CHO, CH_3OCHO, *cis*-CH_2OHCHO, and *t*-CH_2CHCHO. 22 is NH_3. 23 - 27 are other oxygenated species H_2CCO, *c*-H_2C_3O, H_2COH^+, CH_3OCH_3, and *t*-CH_3CH_2OH. 28 is the imine CH_2NH. The slope at low optical depths is related to the detection limit; because K6: 64 km s^{-1} has the highest optical depth, lines that are weakly detected towards K6: 64 km s^{-1} are detected towards other components only if they have higher than the median line optical depth. This implies that the lower left corners of each panel are below the detection threshold.

median NLR (such that median $\neq$ 1) do not necessarily indicate differences in the relative chemical abundances or excitation. Instead the median NLR may correspond to the relative optical depth of molecular gas, and it also holds the factor offset introduced by $[f(T_{Ex}) - f(T_{CMB})]$ in Equation 3 towards L and K4. However, statistically significant differences with respect to the median NLR indicate either (1) excitation differences, with distinct excitation of some molecules, or (2) chemical differences, with different relative gas phase molecular abundances present in distinct gas components. If statistically significant scatter is observed in lines of a single molecule (e.g. differences in the NLR of different lines of CH_3CHO), excitation differences are implicated. Although low excitation conditions are common in the gas components discussed here, differences in the excitation conditions can impact the excitation of different K-states, and weak masing effects may selectively enhance or deplete the populations of certain states (Menten 2004; Faure et al. 2014). Where line excitation is not implicated, the differences are attributable to chemical abundance differences.

Trends in Figure 4.3

Transitions that appear to vary the most between different panels of Figure 4.3 include CH_2NH $1_{11}-2_{02}$, CCS 3_2-2_1, HCS^+ J = (1-0), H_2CS $1_{01}-0_{00}$, and weaker transitions of large aldehyde and O-bearing species. Of these species, CH_2NH is known to be weakly masing at 1 GHz (Godfrey et al. 1973) and is masing in this survey as well; H_2CS has been reported to exhibit non-thermal behavior at cm wavelengths (Sinclair et al. 1973); and transitions of the O-bearing species *t*-CH_3CH_2OH and H_2COH^+ exhibit weak masing in this work. While the lines included in Figure 4.3 appear in absorption and are therefore not themselves masing, the energy state populations may be very sensitive to the physical conditions. Significant effort will be required to determine the excitation conditions re-

sponsible for the observed line strengths, providing powerful constraints on the physical conditions in the gas.

While aware of the presence of non-LTE excitation in these lines, we expect that a few of the trends indicate true gas phase relative abundance differences. In this discussion, relative abundance differences are relative to the median abundance ratio of molecules sampled in two components of gas. In most panels, transitions of CH_3CH_2CN appear consistently below the median value, indicating that K6: 64 $\mathrm{km\,s^{-1}}$ likely has a high gas phase abundance of the species compared to other gas components. Similarly, K6: 64 $\mathrm{km\,s^{-1}}$ likely has enhanced relative abundances of most S-bearing species, with only L: 56 $\mathrm{km\,s^{-1}}$ having NLR values that are similar to the median. As many of the O-bearing species have multiple lines with high NLRs, we expect that these do reflect true abundance differences.

We expected to observe similarity between the low velocity gas towards all three regions and the high velocity gas in the regions, with a distinction apparent between the two sets of spectra. Instead a different trend is present. K6: 64 $\mathrm{km\,s^{-1}}$, L: 56 $\mathrm{km\,s^{-1}}$, and L: 76 $\mathrm{km\,s^{-1}}$ exhibit very similar excitation. This can be seen by inspecting transitions of CH_3CHO, NH_2CHO, and CH_2CHCN in particular. Each of these three molecules has multiple transitions sampled in Figure 4.3, and for each of these species, the NLR values of all transitions show little variation. On the other hand, K6: 82 $\mathrm{km\,s^{-1}}$, K4: 62 $\mathrm{km\,s^{-1}}$, and K4: 82 $\mathrm{km\,s^{-1}}$ show a different pattern of excitation and are more similar to each other than they are to the first set of components. Evidence for this follows from the significant amount of scatter observed in lines of CH_3CHO (K6: 82 $\mathrm{km\,s^{-1}}$), NH_2CHO (K6: 82 $\mathrm{km\,s^{-1}}$ and K4: 62 $\mathrm{km\,s^{-1}}$), CH_2CHCN (K4: 82 $\mathrm{km\,s^{-1}}$), CH_3CH_2CN (K4: 62 $\mathrm{km\,s^{-1}}$), HC_5N (K4: 62 $\mathrm{km\,s^{-1}}$ and K4: 82 $\mathrm{km\,s^{-1}}$), and *cis*-CH_2OHCHO (K4: 62 $\mathrm{km\,s^{-1}}$).

In the first set of components, all lines of NH_2CHO and CH_3CHO, and most transitions of small molecules are consistent with the median NLRs, although NH_3 transitions

show some variability. Observed lines of the S-bearing molecules SO, HCS^+ and H_2CS are comparatively depleted in L: 76 km s^{-1}. Lines of CH_3CH_2CN are depleted in both L: 56 km s^{-1} and L: 76 km s^{-1} relative to K6: 64 km s^{-1}, and lines of CH_2CHCN may be slightly depleted in L: 76. km s^{-1}. On the other hand, multiple lines of O-bearing species, including *c*-H_2C_3O (L: 56 km s^{-1} and L: 76 km s^{-1}), H_2COH^+ (L: 76 km s^{-1}), CH_3OCHO (L: 56 km s^{-1}), and *t*-CH_3CH_2OH (L: 56 km s^{-1}), are enhanced in both components in L. While further analysis is required, this likely indicates higher gas phase abundances of the specified O-bearing species, particularly where multiple lines consistently demonstrate enhancement (i.e. for *c*-H_2C_3O and *t*-CH_3CH_2OH in L: 56 km s^{-1}). Particularly because no maser emission is detected at either component towards L, we do not anticipate that the energy state populations are significantly enhanced or depleted by these processes, further supporting the interpretation of the results as indicating true differences in relative abundances.

In the second set of components, incldluing K6: 82 km s^{-1}, K4: 62 km s^{-1}, and K4: 82 km s^{-1}, we note low line ratios for some S-bearing species including H_2CS, CCS (K6: 82 km s^{-1} and K4: 62 km s^{-1}), and HCS^+ (K6: 82 km s^{-1}). Additionally, CH_3CH_2CN lines are lower than the median NLR towards K6: 82 km s^{-1} and SiO isotopologues have somewhat low values. Towards all three regions, multiple O-bearing species exhibit high NLRs. In K6: 82 km s^{-1}, H_2COH^+, *cis*-CH_2OHCHO, *t*-CH_2CHCHO, *t*-CH_3CH_2OH, and the nitrile species C_3N, exhibit enhanced line radiation relative to the median. In K4: 62 km s^{-1}, *cis*-CH_2OHCHO and H_2COH^+ have high NLRs, and in K4: 82 km s^{-1}, lines of H_2CCO and *c*-H_2C_3O have high NLRs. With respect to one another, K6: 82 km s^{-1} and K4: 82 km s^{-1} exhibit similar excitation (evidenced by NLR values for molecules with multiple line transitions), but very different line strengths for some S-bearing species. With respect to one another, they also show differences in the relative abundances of some aldehyde and

nitrile species, with NLR values that are consistently offset from the median. They additionally show differences in which weak O-bearing transitions are detected, possibly indicating relative abundance differences. K4: 64 km s^{-1} has a very similar molecular inventory to that of K6: 82 km s^{-1}, but the excitation is somewhat distinct. Besides the relative depletion of SiO isotopologues in K6: 82 km s^{-1}, the relative abundances are quite consistent with those in K6: 64 km s^{-1}, indicating that these two regions have similar chemical conditions.

As is clear from this discussion and in agreement with the above discussion of Figure 4.2, Figure 4.3 reveals statistically significant differences from the median values for both velocity components towards all three regions. In fact, by comparing the panels to one another, it is apparent that no two components have consistent line radiation, revealing variability in excitation and relative abundances on small spatial scales. As a result, the gas phase molecular abundances and excitation of the 3 spatial regions $\times$ 2 velocity components should be treated separately. This does not imply that each of the 6 clouds is an entirely localized body, but that sufficient variability is observed so that signals from different positions cannot be combined, particularly for transitions that exhibit greater degrees of variability.

4.3.2 Implications for the Structure of Sgr B2

If the structure of Sgr B2 included two clouds in the envelope that are extended over the continuum structure, we would observe that the molecular abundance ratios and excitation should be self consistent in the low velocity material and in the high velocity material. The low velocity material could show a very distinct pattern from the high velocity gas however. If this were the case, the panels corresponding to low velocity material in Figure 4.3 (panels b and d) should have very few points outside of the shaded 3σ errors. While the

high velocity material (panels a, c, and e) could have points outside of this, the same points should appear outside of the shaded region in all three panels. As is evident from Figures 4.3 and from the discussion above, this is not observed. The differences in line radiation thus indicate that we cannot adopt the most simple treatment of the molecular material, namely as two extended sheets of gas that are not interacting directly with the structure of the core. Instead, we observe significant variation on size scales of $<$30 arcsec, indicating that both the low velocity component and the high velocity component are likely located proximate to the star forming core and are not envelope components.

As K6: 64 km s^{-1} and K4: 62 km s^{-1} components, separated by $<$10 arcsec, show a great deal of differentiation, it does not appear likely that the low velocity gas is located in the extended envelope, removed from the immediate mechanical and radiative environment of the HII regions and embedded sources. The low velocity gas, varying in both excitation and in relative molecular abundance values towards the regions, is instead likely located proximate to the HII regions. The low velocity gas towards K6 and K4 may be part of the same structure, however we argue that the gas is located close to the core and is therefore responding to localised conditions. A similar result was deduced from interferometric observations of FeO towards Sgr B2(M), which observed that the FeO abundance is enhanced in gas observed in absorption against Sgr B2(M) compared to the surrounding area (Furuya et al. 2003); this implies that the material is directly shocked or otherwise affected by the core itself, and therefore is located proximate to the core. Nonetheless, it is well established that the low velocity component absorbing gas in Sgr B2(N) and (M) is part of an extended structure of $\geq$50 arcsec size scale (Huettemeister et al. 1995, and references therein). Therefore the low velocity cloud may be an extended structure ($\gtrsim$ 1 arcmin) located in the immediate viscinity of the cores, creating locally variable gas phase abundances and excitation due to radiative and/or mechanical interactions with HII regions. While Fig-

ure 4.3 demonstrates similarity in excitation between K6: 64 km s^{-1} and L: 56 km s^{-1}, the ATCA data cannot provide direct observational evidence that the L: 56 km s^{-1} gas is part of the same structure as K6: 64 km s^{-1}. Other work has provided some evidence that they are, however (see e.g. Sato et al. 2000, and references therein).

While K6: 82 km s^{-1} and K4: 82 km s^{-1} are more similar to one another, differences nontheless persist. The chemistry and excitation may be localised to a lesser degree than the low velocity gas. While this gas does not appear to be located in the extended envelope, it may be located further from the cores than the low velocity gas in Sgr B2(N). As L: 76 km s^{-1} shows a distinct pattern of excitation and gas phase abundance, it is not obvious in our observations that it is related to the high velocity gas observed towards K6 and K4. However, the work of Hasegawa et al. (1994) and Sato et al. (2000) provides evidence connecting the gas clouds, indicating that the high velocity material may also be part of an extended structure (>40 arcsec). It is plausible however that a very clumpy structure in the envelope, as proposed by Goicoechea et al. (2003), could account for the differences between the high velocity gas in K6 and K4 while allowing the gas to be located in the envelope.

If we adopt this structure, in which the low velocity material is located closest to the HII regions, then the expanding K6 ionization shell would interact mechanically and radiatively with the 64 km s^{-1} molecular gas given the HII region kinematics compiled in Tables 3.3 and 3.4, driving shocks into the system and contributing near-UV radiation to generate a PDR. These conditions could produce the more highly varying line ratios for molecules towards K6. Towards L, the low velocity molecular material would not be expected to mechanically interact with the HII regions given the recombination line kinematics described in §4.2, although it very likely sets the radiative environment.

Furthermore, if the high velocity components are indeed further from the HII regions

than the low velocity components, we may be directly observing the colliding molecular clouds that are triggering star formation in Sgr B2, consistent with the scenario first proposed by Hasegawa et al. (1994). In this scenario, an extended high velocity cloud (at $75 < v_{LSR} < 90$ km s^{-1}) collides with the body of Sgr B2 (at $40 < v_{LSR} < 50$ km s^{-1}), generating star formation in processed material at an intermediate velocity of $55 < v_{LSR} < 70$ km s^{-1}. The observed 2-component molecular gas thus may be a direct observation of remaining material in the high velocity cloud continuing to collide with the processed cloud, a process that may trigger yet more star formation. This scenario is consistent with the observation of molecular line material at $\sim$65 km s^{-1} towards Sgr B2(M) (Huettemeister et al. 1995). However, significant pieces of evidence for this scenario remain missing. For example, there should be observational signatures of a shock at the interface of the colliding gas clouds at a velocity intermediate to the high and low velocity gas components. While the line profile of ^{28}SiO is wing-broadened, the optically thin isotopologues of SiO do not show such a signature. Additionally, to elucidate the interaction between the HII region and the low velocity component molecular gas, high spatial and spectral resolution observations of CI, CII, NI, NII, and OI are required to provide information on the PDR at the surface of the HII region. Notably, however, carbon recombination lines are not observed in this material.

The evidence that the low velocity material is closer to the HII regions remains tenuous however, and additional evidence suggests the situation may be yet more complex. Recombination lines towards K6 have 2-component profiles centered at velocities of 60 and 84 km s^{-1}, while molecular gas is observed at 64 and 82 km s^{-1}. If the K6 shell is an expanding HII region that only interacts mechanically with the low velocity molecular gas, then it is a coincidence that the high velocity molecular gas is at nearly the same velocity as the far side of the expanding shell. Likewise, this scenario requires that the L: 56 km s^{-1} molec-

ular gas component is more closely associated with the HII region (at 77 km s^{-1}) than the L: 76 km s^{-1} molecular gas component. The velocity correspondence between the HII region and the L: 76 km s^{-1} molecular gas may be merely coincidental, however, a deeper look at structure is warranted.

4.4 Selected Molecular Distributions in Sgr B2

Clear evidence of differentiation is present in the data cubes, with most detected molecular transitions observed either in absorption preferentially along the K5 and K6 shells, L, and K4, or in emission towards the LMH and "h" hot cores (Figure 4.4). Figure 4.4 illustrates the two main spatial distributions observed.

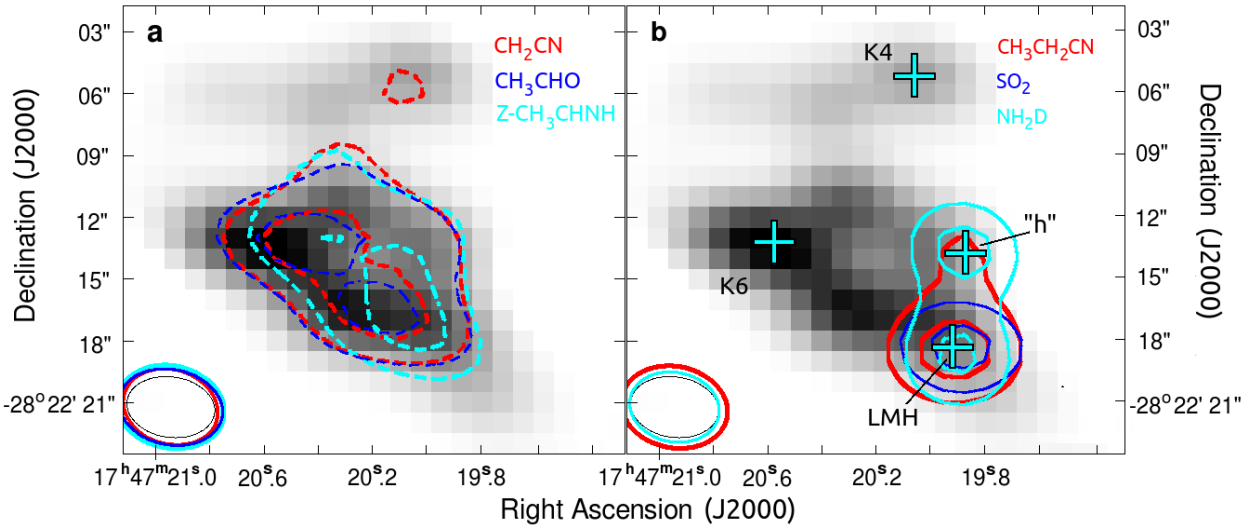

Fig. 4.4 – 40% and 80% integrated line emission contours over 40 GHz continuum illustrate the two most common distributions of molecular line radiation. **a.** CH_2CN (2 - 1), CH_3CHO (2_{02} - 1_{01}), and *Z*-CH_3CHNH (2_{02} - 1_{01}) are observed in absorption (dashed contours) preferentially towards the K5 and K6 shells. **b.** NH_2D (3_{13} - 3_{03}), CH_3CH_2CN (4_{31} - 3_{30}), and SO_2 ($19_{3,18}$ - $18_{3,15}$) are detected in emission towards the LMH hot core, and NH_2D and CH_3CH_2CN are detected in emission towards "h". The central positions of the elliptical regions from which spectra were extracted are indicated by the crosses. The synthesized beam shapes for the continuum (thin black ellipse) and spectral lines (colored ellipses) are shown in the lower left corner.

While most transitions detected towards K6, L, and K4 have spatial distributions similar to the absorption lines in Figure 4.4a, low energy transitions from a handful of detected molecules show simultaneous absorption towards the continuum and emission from one or both hot cores. Transitions of NH_3, HCS^+, CH_3CN, CH_2CHCN, CH_3CH_2CN, HC_3N, NH_2CHO, CH_3OCHO, and CH_3OCH_3 are prominent in absorption in the foreground of the HII regions and in emission from the LMH and usually "h" (notably, NH_2CHO is not detected in "h"). Additionally, detected transitions of OCS, HNCO, and NH_2D produce strong emission towards the LMH and "h" and very weak absorption against the radio continuum. The data also contain multiple instances in which molecules whose spatial distributions might be expected to be correlated exhibit very distinct morphologies.

The molecules SiO and HNCO are widely regarded as excellent shock tracers and therefore might be expected to exhibit similar spatial distributions. Enhanced gas phase abundances of SiO are achieved by grain sputtering upon passage of a shock (Schilke et al. 1997; Caselli et al. 1997; Pineau des Forets et al. 1997), and HNCO is observed to be enhanced in multiple regions that have known shocks (Rodríguez-Fernández et al. 2010; Minh & Irvine 2006; Martín et al. 2008). The spatial distribution of HNCO has been observed to follow that of SiO in multiple sources via observations with single dish telescopes (Zinchenko et al. 2000). However, Figure 4.5 shows that the distributions of transitions between low-energy states of SiO and HNCO in the core of Sgr B2(N) are anti-correlated. The HNCO 2_{02}-1_{01} transition produces very strong line emission in both hot cores, whereas only very weak absorption is detected towards K6 (the absorption contour of HNCO is at 2.5% of the peak emission line strength). On the other hand, for the J = (1-0) transitions of all isotopologues of SiO, the images include absorption against the continuum structure and a negative "bowl" indicating extended emission that could not be recovered with the interferometer. No compact emission by SiO isotopologues is observed towards the "h" hot core. We note

the presence of a weak emission feature on the high velocity wing of ^{28}SiO eminating from the northwest edge of the LMH. Due to the line density towards the LMH and the absence of an emission feature on the low velocity wing, which would be more consistent with the velocity of the LMH, we cannot firmly identify the noted feature as an SiO line.

The distributions indicate chemical differentiation for these two species in Sgr B2(N). HNCO is highly abundant in the LMH and "h" hot cores and depleted in the molecular gas observed against the HII regions; on the other hand, even if the noted wing feature is from SiO, the species has a significantly lower column density in the LMH than in the absorbing gas. Any emission generated by SiO in the LMH is entirely overwhelmed by the absorbing gas components, including in the optically thin transitions of the isotopologues. Although the higher energy states (100 K $<$ E$_L$ $<$ 300 K) of SiO should be preferentially populated in the LMH and "h", Neill et al. (2014) reported the non-detection of SiO in HEXOS data sampling SiO transitions with T $>$160 K. SiO thus appears to be depleted from the gas phase in the LMH and "h" hot cores, but highly abundant in molecular material in the low velocity (50 - 65 km s^{-1}) and high velocity (70 - 85 km s^{-1}) gas observed in absorption towards the HII regions, and in extended material around the core. A similar distribution of gas phase SiO has been observed in the source G34.26+0.15 (G34.26), which contains a hot core, UC HII regions, collimated outflows, and molecular gas interacting with stellar winds (Hatchell et al. 2001; Watt & Mundy 1999). Towards G34.26, SiO was observed to be widespread and highly abundant in the material interacting with stellar winds; it was not detected in the hot core, however (Hatchell et al. 2001).

The spatial distributions of transitions from species in the CS-family present yet another puzzle; whereas transitions of CS, CCS, CCCS, and H_2CS are detected in the absorbing gas with no apparent emission from the hot cores, line radiation from the J = (3-2) transition of OCS shows a similar behavior to that of HNCO (Figure 4.6). Very weak line absorption

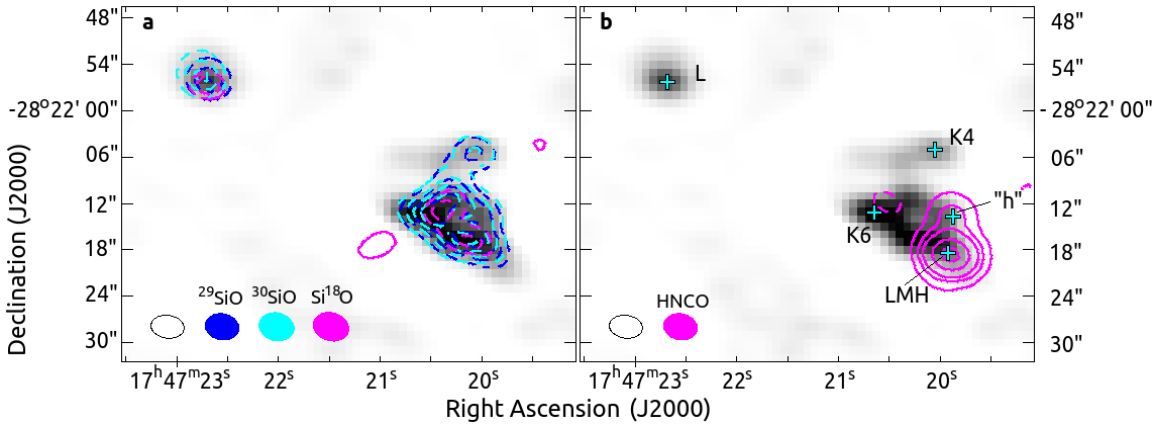

Fig. 4.5 – Integrated line contours of the (1-0) transitions of SiO isotopologues are anticorrelated with the 2_{02}-1_{01} transition of HNCO. **a.** ^{29}SiO, ^{30}SiO, and Si^{18}O are observed in absorption (dashed contours) against the continuum and exhibit no emission associated with the hot cores. **b.** HNCO is present in emission towards the LMH and "h" hot cores. A very weak absorption feature (with a contour at 2.5% of the peak line strength) is detected slightly north of K6. The crosses indicate the center positions of the elliptical regions from which spectra were extracted. The synthesized beams for the continuum and line images are shown in the lower left corner.

by OCS (with the lowest contour at 4.5% of the peak emission) is detected towards K6 and K4, but nearly all of the OCS radiation is emission produced in the hot cores. OCS, like HNCO, is believed to form on grain mantles and has been linked to shock enhancement (Ren et al. 2011; Garozzo et al. 2010). Distinct from other CS-containing species, HCS^+ appears both in absorption against the continuum and in emission from the hot cores.

4.5 Physical Environment in the Absorbing Material: An Integrative View

The detection of SiO, CS, and other CS-bearing species and the depletion of HNCO and OCS in the absorbing molecular material provides insight into the physical environment in the absorbing gas. The strong absorption by SiO likely results from the presence of shocks and supersonic turbulence in the gas, although the enhancement of SiO may instead

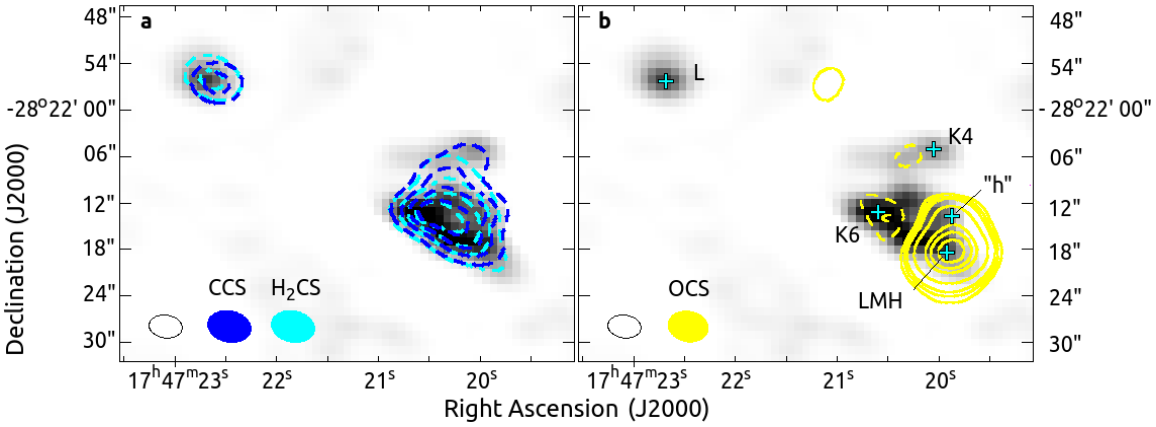

Fig. 4.6 – Integrated line contours of H_2CS (1_{01}-0_{00}), CCS (3_2-3_1), and OCS (3-2). **a.** H_2CS and CCS are observed in absorption (dashed contours) against K4, K5, K6, and L, with no detected emission from hot core regions. Contour levels are at 20, 40, 60, and 80 % of the peak line strength. **b.** OCS appears in emission from the hot core regions, the LMH and "h", with very weak absorption observed towards K6 and near K4. The contour levels are at 4.5, 7, 20, 40, 60, and 80 % of the peak line strength. The crosses indicate the center positions of the elliptical regions from which spectra were extracted. The synthesized beams for the continuum and line images are shown in the lower left corner.

be attributed to the high X-ray flux in this X-ray reflection nebula (Martín-Pintado et al. 2000; Amo-Baladrón et al. 2009). Other CS-bearing species found in the absorbing gas, particularly CCS and CCCS may be formed by chemistry driven by the radical CH (Petrie 1996; Yamada et al. 2002; Sakai et al. 2007), and multiple larger radical species are directly detected in the spectra towards K6, L, and K4 (Appendix B). The presence of radicals typically indicates X-ray or UV irradiation typical of XDRs or PDRs (Danks et al. 1984; Boger & Sternberg 2005; Meijerink et al. 2007).

Further, the ratio of HNCO to CS may be an excellent diagnostic of the radiative environment. Using a limited sample of Galactic Center clouds, in which shocks are believed to be ubiquitous, Martín et al. (2008) demonstrated that the HNCO:CS abundance ratio is high ($\sim$70) in non-PDR shocked regions and an order of magnitude lower in PDRs. While both species can be photodissociated, CS is less easily destroyed by UV radiation and can be replenished by a gas phase reaction of S^+, an abundant ion in PDRs (Drdla

et al. 1989; Sternberg & Dalgarno 1995; Martín et al. 2008). In the Horsehead Nebula, CS is observed to be nearly equally abundant in the PDR and in the dense UV-shielded core (Goicoechea et al. 2006). On the other hand, HNCO is believed to form efficiently on grain mantles (Hasegawa & Herbst 1993) and after being released into the gas phase, it is easily photodissociated by UV radiation (Martín et al. 2008; Roberge et al. 1991). While theoretical work contends that the HNCO:CS ratio is time-dependent and more indeterminate (Tideswell et al. 2010), the very high ratio of CS:HNCO in the absorbing gas provides evidence that this material has an enhanced UV radiation field. Like HNCO, OCS is believed to form on grains, and the species has been directly observed on ice grain mantles (Gibb et al. 2004; Garozzo et al. 2010; Palumbo et al. 2011; Ren et al. 2011). Gas phase OCS is destroyed by near-UV radiation with an even higher photodissociation rate than HNCO (Roberge et al. 1991; Sternberg & Dalgarno 1995; Sato et al. 1995). The nearly complete depletion OCS from the absorbing gas is further evidence for PDR conditions.

As Sgr B2 is known to have a strong and pervasive X-ray flux, it is possible that X-ray radiation instead of UV radiation could destroy HNCO and OCS in the absorbing material. Due to the extremely high densities of the LMH and "h" hot cores (Belloche et al. 2008, 2014), even X-ray radiation is well shielded. However, HNCO and OCS exhibit widespread distributions to the west of the core (Jones et al. 2008). In this material, we expect that the X-ray field is more typical of the bulk of material in Sgr B2. This expectation is consistent with the prevalence of the X-ray tracer CN in the material to the west of the core (Jones et al. 2008). The widespread distributions thus suggest that X-ray radiation is not responsible for destroying HNCO and OCS; as such, we interpret the ATCA distributions of CS, OCS, and HNCO as suggesting the presence of a strong UV radiation field in the absorbing gas.

Additional support for a strong UV radiation field in the absorbing material follows from the results of §4.3. First, the highly subthermal excitation indicates that the material

is sub-critically dense, with densities typical of PDRs. Without an excitation analysis, it is possible to estimate an upper limit of $n \lesssim$ a few $\times 10^5$ cm^{-3} using the critical densities of energy states that had undetected transitions in the 30 - 50 GHz range with high quantum line strengths. Huettemeister et al. (1995) determined an upper limit to the density of the absorbing gas of n $<10^4$ cm^{-3} based on the fact that the HC_3N J = (3-2) transition is in absorption instead of emission, and independently based on an analysis of the (1,1) through (6,6) NH_3 inversion transitions. However, the latter estimate may not hold if the H_3O^+ formation pumping excitation mechanism proposed in Lis et al. (2012) proves effective for NH_3. Densities of $10^3 <$ n $< 10^5$ cm^{-3} are typical of PDRs (Tielens et al. 1993; Hollenbach & Tielens 1997), and densities of n $\approx$ a few $\times 10^5$ cm^{-3} are reasonable in the hot, supremely dense environment at the core of Sgr B2(N). In section §4.3, we determined that both absorbing gas components appear to be local to the star forming cores rather than in the extended envelope material, with the low velocity gas possibly closer to the interface of the HII regions. If the absorbing gas clouds are proximate to the HII regions, it is not only reasonable, but structurally required, that they are or contain PDRs.

Second, the species l-C_3H^+ is detected in the absorbing material, but not in the hot core. To date, l-C_3H^+ has been reported in the literature as firmly detected in the Horsehead Nebula, the Orion Bar, and Sgr B2(N) (Pety et al. 2012; McGuire et al. 2013, 2014b); l-C_3H^+ has also been rigorously detected in three other PDRs, with tentative evidence for its presence in two additional PDRs (B. McGuire 2015, private communication). Further, a deep search towards multiple hot cores, hot corinos, and dark clouds provided no detections of l-C_3H^+ (McGuire et al. 2014b), and while the molecule was observed in the Horsehead PDR, it was not detected in a molecule-rich UV-shielded core in the Horsehead Nebula (Pety et al. 2012). Thus, Sgr B2 is the only source in which l-C_3H^+ has been detected that is not definitively discussed as a PDR. The species is clearly associated with UV-irradiated

gas, and its detection in the low and high velocity gas towards K6 supports the hypothesis that both gas components are PDR sources.

Finally, a few of the organic species detected in the absorbing clouds were recently reported to be highly abundant in a PDR environment (Gratier et al. 2013; Guzmán et al. 2014). CH_3CN, HC_3N, H_2CCO, and CH_3CHO were observed in the Horsehead PDR with abundances enhanced by a factor of 1 - 30 as compared to abundances in the UV-shielded core in the Horsehead. While the species are known to be abundant in multiple distinct environments, their detection in the absorbing material in Sgr B2(N) is consistent with the absorbing material being a PDR.

The data and discussions in this work thus support a structure in which molecular gas at $50 < v_{LSR} < 70$ km s^{-1} is located on the interface of the HII regions at the core of Sgr B2. This gas component is UV-irradiated by the O-stars that power the HII regions, and may mechanically interact with the HII region, particularly towards K6 where the shell-shaped HII region is thought to be expanding. The high velocity cloud ($70 < v_{LSR} < 85$ km s^{-1}) is also close to the core, although it may not be as deeply embedded as the low velocity material. It may be actively colliding with the low velocity cloud consistent with a cloud-cloud collision scenario (Hasegawa et al. 1994), although additional evidence is required to verify this. Based on the detection of *l*-C_3H^+ and the nearly complete depletion of OCS and HNCO, it appears that both absorbing clouds are PDRs. This hypothesis should be further tested via comparison to high spatial and, ideally, high spectral resolution observations of neutral and ionized carbon, sulfur and oxygen.

However, merely calling the gas clouds PDRs is an over-simplification. The clouds contain supersonic turbulence requiring shocks, have a high X-ray flux, and likely have an enhanced cosmic ray flux as compared to most Galactic sources. It is quite possible that a different factor drives the chemistry of different groups of species; for instance, the

strong X-ray flux may produce radicals that drive the chemistry of imine molecules (with an X=N–H group), whereas UV radiation may drive the sulfur and carbon-chain chemistry and selectively destroy certain molecules. Meanwhile, shocks may liberate silicon-bearing species and dust mantle species to be processed in the soup of ionic, atomic, and molecular gas.

Regardless of the physical parameters driving the formation of each species, the extracted spectra suggest that a multitude of organic molecules, including nitriles, aldehydes, alcohols, and imines, either form or persist in the presence of UV irradiation, X-ray radiation, and shocks. While we expect that some of the observed species will not prove ubiquitous in more typical Galactic PDRs, all of the detected species can at least survive moderate UV radiation fields and are promising targets for exploring the chemical complexity in PDRs.

4.6 Conclusions

In this chapter, we have coupled a full-spectrum analysis of spectra extracted from the positions of three HII regions with image data in order to constrain the physical and chemical structure of Sgr B2. We utilized the output of a line-fitting script applied to the three spectra, each of which contains recombination line emission and multiple components of molecular line absorption. In all three spectra, molecular absorption associated with Sgr B2 was observed in two velocity components separated by 20 $\mathrm{km\,s^{-1}}$, although the velocities varied between the different positions.

The molecular inventories of the two velocity components of absorbing gas were determined and the approximate excitation conditions were characterized, showing that the gas clouds that give rise to the absorption are highly subthermally excited ($\mathrm{T}_{Ex} \sim 10$ K $\ll \mathrm{T}_{kin}$). Line radiation was then inspected using the relative line strengths in different gas

components to determine whether the molecular line radiation is self-consistent at distinct spatial positions (Figure 4.3). This methodology can determine the chemical similarity between clouds at different spatial positions or velocities under conditions of similar excitation conditions, and the method could be quantified to further establish the degree of similarity. In the era of broadband spectral line observing, the method could be highly useful for quickly determining if observed clouds are chemically distinct and demonstrating relative enhancement of different families of molecules. The application of this method toward a variety of sources is necessary to determine its utility.

We applied the method to the ATCA data in order to test whether the molecular gas radiation is consistent with an extended distribution that is not interacting with the local structure of the core, as would be expected if the absorbing gas is in the envelope. We determined that in both primary velocity components, the three spatial regions show statistically significant differences in their line radiation, indicating differences in either line excitation or gas-phase molecular abundances. Many of the differences appear to be due to relative gas-phase abundance differences. The molecular gas in the low velocity component proved more highly variable, indicating that it may be subjected to more localized conditions and therefore located deeper within the star-forming core. It may be on the interface of the HII regions, interacting mechanically and radiatively with the structure of the HII regions. In agreement with cloud-cloud collision scenarios, the 82 $\mathrm{km\,s^{-1}}$ gas is likely located further from the core. However, required pieces of observational evidence for the proposed structure remain unavailable, particularly high spatial (few arcsec resolution) and spectral (10 - 25 $\mathrm{km\,s^{-1}}$) resolution images of atomic and ionic lines of carbon, oxygen, and sulfur.

Finally, we discussed the spatial distributions of a few detected molecular species providing evidence for chemical differentiation between species including SiO, HNCO, OCS,

CS, CCS, and additional CS-bearing molecules. We explored the implications of the spatial distributions for the physical environments of the molecular gas. The observed distributions and physical structure indicate that both primary absorbing gas components are likely PDR environments, although shocks, high X-ray fluxes, and high cosmic ray fluxes may have equal influence on the observed chemistry. The data reveal that molecules including (1) silicon-bearing species, (2) sulfur-bearing species, (3) carbon chain molecules, (4) multiple classes of oxygenated species including aldhydes and alcohols, (5) nitrogen species of pre-biotic importance including nitriles and imines are abundant in the exotic PDR environments.

Chapter 5

Molecular Line Absorption by Diffuse and Translucent Clouds in the Line-of-Sight to Sgr B2

Abstract

The 1-50 GHz PRebiotic Interstellar MOlecular Survey (PRIMOS) contains absorption by $\sim$50 molecular lines observed in clouds located in the line-of-sight to Sgr B2(N). The line-of-sight clouds are associated with diffuse and translucent clouds located in the Galactic Center, Bar, and spiral arms in the disk. We measure the column densities and estimate abundances, relative to H_2, of 16 molecules and additional isotopologues observed in this material. We use absorption by optically thin transitions of c-C_3H_2 to estimate the molecular hydrogen columns, and argue that this method is preferable to more commonly used methods. We discuss the kinematic structure and abundance patterns of small molecules including the sulfur-bearing species CS, SO, CCS, H_2CS, and HCS^+; oxygen-bearing molecules OH, SiO, and H_2CO; hydrocarbon molecules c-C_3H_2, l-C_3H, and l-C_3H^+; and complex organic molecules CH_3OH, HC_3N, CH_3CN, CH_3CHO, and NH_2CHO. Finally, we discuss the implications of the observed chemistry for the structure of the gas and dust in the ISM.

Highlighted results include the following. First, whereas gas in the disk has a molecular hydrogen fraction of 0.4, clouds on the outer edge of the Galactic Bar and in or near the Galactic Center have molecular fractions of 0.8 and $\gtrsim$0.9. Second, we suggest that CS has an enhanced abundance within higher density clumps of material in the disk, and therefore may be diagnostic of cloud conditions. If this holds, the diffuse clouds in the Galactic disk contain multiple embedded hyperdensities in a clumpy structure. Thirdly, the considerable abundances of complex organic molecules (COMs) indicate that grain surface chemistry may occur more effectively than previously known.

5.1 Introduction

The diffuse and translucent ISM serves as a significant reservoir for gas in the Galaxy, and is believed to be involved in processes of gas accretion, recycling and feedback from star formation, and in the first stages of molecular cloud formation. Thus, an understanding of this material is essential for understanding the processing of gas in galaxies. Although the first interstellar molecular detections were made in diffuse gas, namely CH, CH^+, and CN (Swings & Rosenfeld 1937; McKellar 1940; Douglas & Herzberg 1941), the diffuse ISM was not expected to have a very rich molecular chemistry, and recent observations have proven surprising. While our picture of the physical and chemical structure of the diffuse ISM continues to evolve, the chemistry reveals three primary phases with blurred boundaries. First, the most diffuse material produces absorption primarily by light hydride species (e.g. Gerin et al. 2010; Qin et al. 2010; Indriolo et al. 2015). The absorption components tend to be broad $\Delta \mathrm{v} \gtrsim 15$ km s^{-1}, indicating large spatial extents, and estimated physical conditions include low densities ($50 < n < 300$ cm^{-3}), high temperatures ($80 < T < 300$ K) (Snow & McCall 2006), and low molecular hydrogen fractions $\left(f(\mathrm{H_2}) = \frac{2N_{\mathrm{H_2}}}{N_{\mathrm{H\,I}}+2N_{\mathrm{H_2}}} < 0.1\right)$ (Indriolo et al. 2015; Snow & McCall 2006). In the second phase, heavier molecules appear, including HCN, CS, H_2CO, and c-C_3H_2, but estimated physical conditions still include low densities ($100 < n < 500$ cm^{-3}) and warm temperatures, similar to the more diffuse material (Snow & McCall 2006; Liszt et al. 2006, 2012). Generally, this phase occurs under central extinction conditions of $A_{\mathrm{V}o} \gtrsim 0.2$ mag (implying a total extinction $A_{\mathrm{V}} \gtrsim 0.4$), and higher molecular hydrogen fractions, of $f(\mathrm{H_2}) \approx 0.4$, are observed (Liszt et al. 2012). The third phase includes embedded regions of enhanced density including translucent clouds, which are defined as having central extinctions of $1 < A_{\mathrm{V}o} < 2.5$ (Snow & McCall 2006). The kinematic signatures of these include absorption over the same general velocity range as the diffuse material, but with more narrow

features. Galactic disk translucent clouds have densities of order 5×10^3 cm^{-3} and cool temperatures of $15 < T < 30$ K. In Galactic Center translucent clouds, densities may be higher, up to 10^4 cm^{-3} (Greaves et al. 1992; Greaves & Williams 1994), and temperatures are much warmer at $50 < T < 90$ K.

Diffuse and translucent clouds are best observed by molecular line absorption against strong continuum sources. Absorption techniques provide the high sensitivity required to detect the very low column densities of most molecules present in diffuse and translucent clouds. Previous absorption studies have investigated molecular abundances and correlations between different species under varying hydrogen column densities. These studies have indicated that certain species including HCO^+, C_2H, and c-C_3H_2 have constant abundances with respect to H_2 (Greaves & Nyman 1996; Liszt et al. 2012), whereas other species, including H_2CO and CS exhibit more variable abundances that do not appear to track closely with the hydrogen column density (Liszt et al. 2006).

In all three phases, standard chemical models underpredict the molecular abundances by multiple orders of magnitude (Lucas & Liszt 2002; Godard et al. 2012), indicating a poor understanding of the physics and chemistry of these regions. Grain surface processes have not typically been implicated in diffuse cloud chemistry, as ice mantles should not form under the low extinction, low density, and warm temperature conditions present, although some models have considered hydrogenation on grain surfaces (Viti et al. 2000; Price et al. 2003; Hocuk et al. 2016). In higher optical depth translucent clouds, with $A_{\mathrm{V}o} \gtrsim 2$ under a standard interstellar radiation field, grain chemistry may become more important (Tielens & Allamandola 1987), although this depends on the precise conditions present. Chemical models incorporating turbulence dissipation, where material is heated and compressed periodically, produce model predictions that are more consistent with observations for light hydride species in diffuse clouds (Godard et al. 2009, 2012). Yet much work remains in

order to understand the coupled physics and chemistry within the diffuse and translucent media, including the physical and chemical exchange between the three phases.

Furthermore, the diffuse and translucent gas in the Galactic Center appears to be systematically different from that observed in the disk by multiple measures. Besides the temperature and density differences noted above, observations have indicated very high abundances of H_3^+ with a very high filling factor (of nearly 1) (Oka et al. 2005) and a larger fractional volume filled by translucent clouds in the Galactic Center compared to the disk, due largely to the extreme amount of gas mass in the Galactic Center (Morris & Serabyn 1996). CR ionization rates in diffuse gas in the Galactic Center have been measured to be enhanced by 1 to 3 orders of magnitude compared to the disk (Le Petit et al. 2016; Indriolo et al. 2015), and significantly higher X-ray fluxes are also present (Amo-Baladrón et al. 2009). It is not precisely known how this affects the chemistry in these regions, although chemical models typically predict lower molecular abundances in high CR flux conditions due to molecular dissociation (e.g. Quan et al. 2016).

In this chapter, I present absorption profiles by sixteen molecules and additional isotopologues in the line-of-sight to Sgr B2(N), as measured by the GBT PRIMOS data, which provide a highly sensitive spectrum towards Sgr B2 described in §2.2. While absorption and emission associated with Sgr B2 spans the velocity range of +40 to +90 $\mathrm{km\,s^{-1}}$, diffuse and translucent clouds believed to be located in the Galactic Center, Bar, and spiral arms are observed in the range of -130 to +40 $\mathrm{km\,s^{-1}}$. While the exact locations of most of the cloud components are not very confidently known, the following guidelines are helpful for interpreting abundance patterns. Features in the velocity range of -130 to -55 $\mathrm{km\,s^{-1}}$ are believed to be located within 1 kpc of the Galactic Center, and although some of the material at 0 $\mathrm{km\,s^{-1}}$ is presumably local to the Orion Arm, most of the absorption from -10 to +20 $\mathrm{km\,s^{-1}}$ is also generated near the Galactic Center. Amongst the most prominent

features, the -106 km s^{-1} cloud is associated with the Expanding Molecular Ring (EMR) that spans the Galactic Center and marks the outer edge of the CMZ at a 200 to 300 pc galactocentric distance (Whiteoak & Gardner 1979); the -73 km s^{-1} cloud is suggested to be part of the 1-kpc disk located deep within the Galactic Bar (Wirström et al. 2010); and while some researchers have suggested that the $\sim$0 km s^{-1} component consists of ejecta from Sgr B2 (Wirström et al. 2010), multiple observations have shown that this feature is widespread across the Galactic Center, and is a rather unique system containing molecular line absorption and weak recombination line emission across the Galactic Center (Jones et al. 2012; Royster & Yusef-Zadeh 2014), as well as weak masing in the viscinity of Sgr B2(N) (Corby et al. 2015). The gas from -55 to -35 km s^{-1} is associated with gas in the near 3-kpc arm located on the outer edge of the Galactic Bar, while the material from -35 to -10 km s^{-1} is believed to arise in a spiral arm in the disk at a Galactocentric distance of $\sim$4 kpc (Whiteoak & Gardner 1979; Wirström et al. 2010).

The remainder of the chapter is organized as follows. In §5.2, we present the line profiles (§5.2.1), cloud kinematics (§5.2.2), and measured column densities and abundances (§5.2.3). In §5.3, we discuss the method for molecular hydrogen column estimation. In §5.5 and §5.6, we discuss observed molecular abundances for small molecules and large molecules respectively, and implications for the cloud structures, before concluding in §5.7.

5.1.1 Molecular Excitation and the Line-to-Continuum Ratio

The densities in diffuse and translucent clouds are insufficient to excite molecules much beyond the CMB temperature, and excitation temperatures within this material are observed to span the range of 2.7 K $\lesssim T_{ex} \lesssim$4 K (Greaves & Williams 1994; Linke et al. 1981). As

a result, the equation for line optical depth reduces to

$$\tau = -ln(1 + \mathrm{T}_L/\mathrm{T}_C),$$

for baseline subtracted line strength T_L absorbing against a continuum source of strength T_C. The value T_L/T_C fully characterizes the line optical depth, and I therefore show all data in this scale. This scale additionally provides higher precision measurements, as many sources of calibration error that typically apply to single dish radio data cancel in this ratio, including atmospheric opacity corrections, telescope efficiencies, and absolute flux calibrations.

5.2 Results

In observations toward Sgr B2(N), two absorption components are associated with Sgr B2 itself, at +64 and +82 km s^{-1} (Huettemeister et al. 1995; Corby et al. 2015). We assume that line absorption and emission in the range of +40 to +90 km s^{-1} is from Sgr B2 and refrain from further discussing this material, instead focusing on the molecular composition of clouds observed in the velocity range of -126 to +38 km s^{-1}, associated with material in the line of sight to Sgr B2. Throughout this chapter, we assume that excitation conditions in all absorbing components are equivalent and characterized by T_{ex} = 3 K. This assumption has been validated in the line-of-sight to Sgr B2(M) for CS (Greaves & Williams 1994), and has been widely adopted for studies of diffuse and translucent clouds in line-of-sight absorption (e.g. Nyman 1984; Greaves & Nyman 1996; Lucas & Liszt 1993). The assumption is further validated in Section 5.2.3, in which we explore the line excitation of molecules sampled by multiple transitions in the PRIMOS data. By assuming equivalent excitation in all line-of-sight clouds, it is possible to directly compare column densities in

different clouds from a single line profile.

5.2.1 Spectral Profiles

In the 1-50 GHz spectrum obtained by PRIMOS, foreground absorption is detected from $\sim$50 molecular transitions of 17 molecules and six isotopologues. The transitions are between low energy states (typically E_L <10 K), and are produced by OH, CS, SO SiO, NH_3, CCS, HCS^+, H_2CS, *l*-C_3H, *l*-C_3H^+, *c*-C_3H_2, H_2CO, CH_3OH, CH_3CN, HC_3N, CH_3CHO, NH_2CHO, and detected isotopologues of these species. In this section, we present the results for all observed molecules except for NH_3, whose absorption in the metastable transitions should be treated in a different analysis. Table 5.1 lists transitions that were observed in line-of-sight absorption with sufficient signal-to-noise and baseline stability to enable a fair characterization. For all listed transitions, we fit Gaussian components over the velocity range of -126 to +38 $\mathrm{km\,s^{-1}}$ using the FITGAUSS function provided in the GBTIDL data reduction package and/or with a Gaussian fitting function constructed by the authors. We attempted to use as few Gaussian components as could account for the line profile to within the noise level and we determined errors as the square root of the diagonal entries of the covariance matrix. Gaussian fits are overlaid on all spectral profiles shown in the paper, and individual Gaussian components are shown with a dashed profile. For transitions with resolvable hyperfine structure or A/E splitting, including *l*-C_3H (J=$\frac{3}{2}$-$\frac{1}{2}$, $\Omega = \frac{1}{2}$), HC_3N (2-1) and (3-2), CH_3CN (1-0), CH_3CHO (1_{01}-0_{00}) and (2_{02}-1_{01}), and NH_2CHO (1_{01}-0_{00}), we fit the primary hyperfine component and assumed that the satellite lines have the same line shape with the height set by the relative line strengths of the satellite and primary features. All line profiles listed in Table 5.1 are shown in Appendix A with Gaussian fits overlaid.

Figure 5.1 shows the absorption profiles and Gaussian component fits to selected lines

Table 5.1 – Summary of molecular lines observed in line-of-sight absorption

Molecule	Transition	Frequency (MHz)	E_L (K)	θ_B (arcsec)	Catalogue
OH	J=$\frac{3}{2}$ Ω=$\frac{3}{2}$ F=1^+-2^-	1612.2310(2)	0.0026		JPL
OH	J=$\frac{3}{2}$ Ω=$\frac{3}{2}$ F=1^+-1^-	1665.4018(2)	0.00		JPL
OH	J=$\frac{3}{2}$ Ω=$\frac{3}{2}$ F=2^+-2^-	1667.3590(2)	0.0026		JPL
c-C_3H_2	1_{10} - 1_{01}	18343.143(2)	2.350	40.3	CDMS
c-C_3H_2	2_{20} - 2_{11}	21587.4008(3)	8.672	34.3	JPL
c-C_3H_2	2_{11} - 2_{02}	46755.610(2)	6.428		CDMS
c-H^{13}CC$_2$H	1_{10} - 1_{01}	18413.8248(7)	2.291	40.1	CDMS
H_2CO	1_{10} - 1_{11}	4829.660(1)	15.163		JPL
H_2CO	2_{11} - 2_{12}	14488.479(1)	21.922	51.1	JPL
H_2CO	3_{12} - 3_{13}	28974.805(10)	32.059		JPL
$H_2^{13}CO$	1_{10} - 1_{11}	4593.0885(1)	15.12649		JPL
$H_2^{13}CO$	2_{11} - 2_{12}	13778.8041(2)	21.72296		JPL
^{28}SiO	1 - 0	43423.76(5)	0.000	17.0	CDMS
^{29}SiO	1 - 0	42879.949(3)	0.000	17.3	CDMS
^{30}SiO	1 - 0	42373.427(5)	0.000	17.5	CDMS
SO	1_0 - 0_1	30001.58(10)	0.000		CDMS
CS	1 - 0	48990.955(2)	0.000		CDMS
C^{34}S	1 - 0	48206.941(2)	0.000		CDMS
CCS	$N_J = 1_2$ - 2_1	22344.031(1)	0.533	33.1	CDMS
CCS	$N_J = 2_3$ - 1_2	33751.370(1)	1.606		CDMS
HCS^+	1 - 0	42674.195(1)	0.000		CDMS
H_2CS	1_{01} - 0_{00}	34351.43(2)	0.000		CDMS
l-C_3H^+	1 - 0	22489.864(2)	0.00		CDMS
l-C_3H^+	2 - 1	44979.544(3)	1.079		CDMS
l-C_3H	J=$\frac{3}{2}$ - $\frac{1}{2}$ Ω=$\frac{1}{2}$ F= 2 - 1 f	32627.297(2)	0.00086		CDMS
l-C_3H	J=$\frac{3}{2}$ - $\frac{1}{2}$ Ω=$\frac{1}{2}$ F= 2 - 1 e	32660.645(2)	0.00086		CDMS
CH_3OH	2_{02} - 3_{-13}	12178.597(4)	19.504		CDMS
CH_3OH	2_{11} - 3_{03}	19967.3961(2)	27.053		CDMS
CH_3OH	1_{01} - 0_{00}++	48372.4558(7)	0.000		CDMS
$^{13}CH_3OH$	2_{02} - 3_{-13}	14782.27(5)	19.196		CDMS
HC_3N	2 - 1 F = 3-2	18196.3104(10)	0.437		CDMS
HC_3N	3 - 2	27294.289(10)	1.310		CDMS
HC_3N	4 - 3	36392.324(10)	2.620		CDMS
HC_3N	5 - 4	45490.3138(5)	4.366		CDMS
CH_3CN	1_0-0_0 F=2-1	18397.9960(1)	0.000		JPL
CH_3CN	2_0-1_0 F=3-2	36795.5670(1)	8.029		JPL
CH_3CHO	1_{01} - 0_{00} E	19262.141(1)	0.098	38.4	JPL
CH_3CHO	1_{01} - 0_{00} A	19265.137(1)	0.00	38.4	SLAIM
CH_3CHO	2_{12} - 1_{11} A	37464.168(20)	3.167		JPL
CH_3CHO	2_{12} - 1_{11} E	37686.868(20)	3.225		JPL
CH_3CHO	2_{02} - 1_{01} E	38506.035(3)	1.022		SLAIM
CH_3CHO	2_{02} - 1_{01} A	38512.081(3)	0.923		SLAIM
CH_3CHO	2_{11} - 1_{10} E	39362.504(20)	3.314		JPL
CH_3CHO	2_{11} - 1_{10} A	39594.287(20)	3.218		JPL
NH_2CHO	1_{01} - 0_{00} F=2-1	21207.3338(2)	0.00	34.8	CDMS
NH_2CHO	2_{11} - 1_{11}	40875.4416(2)	3.962		CDMS
NH_2CHO	2_{02} - 1_{01}	42386.0590(2)	1.018	17.5	CDMS

of OH and c-C_3H_2. The profile of OH (J=$\frac{3}{2}$ Ω=$\frac{3}{2}$ F=2^+-2^-) at 1667 MHz includes very broad line components, many of which have $\Delta v \gtrsim 20$ km s^{-1}, and the absorption fully covers the velocity range of -120 to +40 km s^{-1} with no absorption-free channels. While the OH (J=$\frac{3}{2}$ Ω=$\frac{3}{2}$ F=1^+-1^-) transition at 1665 MHz is extremely similar to the profile of the 1667 MHz transition (Appendix A), the (J=$\frac{3}{2}$ Ω=$\frac{3}{2}$ F=1^+-2^-) line profile at 1612 MHz appears somewhat different. The 1612 MHz transition has a higher line strength in the -40 km s^{-1} cloud and weaker absorption in the velocity range of -90 to -60 km s^{-1}, as discussed in §5.2.4. While the line absorption at 1612 MHz also fully covers the velocity range of -120 to +40 km s^{-1} and contains broad ($\Delta v \gtrsim 10$ km s^{-1}) Gaussian components over this range, lower line width features, of $3 \lesssim \Delta v \lesssim 10$ km s^{-1}, are superposed on the broad line absorption. In contrast to the broad line widths of the 1667 MHz OH transition in particular, absorption by c-C_3H_2 consists of comparatively narrow features, leaving segments of the spectrum without detectable absorption. In this profile, many narrow components (with $\Delta v \lesssim 3$ km s^{-1}) are superposed on moderately broad components with $3 \lesssim \Delta v \lesssim 10$ km s^{-1}.

In the line absorption by c-C_3H_2, at least ten line-of-sight absorption components are clearly distinguishable, peaking at velocities from -106 to +25 km s^{-1}. Throughout this section, we treat these features independently and refer to these clouds by their approximate center velocities. The center velocities and velocity ranges considered are provided in Table 5.2. Due to the nearly constant abundance of c-C_3H_2 in diffuse and translucent gas (Liszt et al. 2012), we use this species as a diagnostic for the total column of H_2 and compare the profiles of other species to c-C_3H_2. We further discuss the validity of this in §5.3.1.

Figure 5.2 shows high signal-to-noise transitions of H_2CO, CS, and SO. H_2CO and CS are detected in the same ten velocity components as c-C_3H_2, while SO is detected in all components with the exception of the -92 km s^{-1} cloud. Line absorption by c-C_3H_2 and

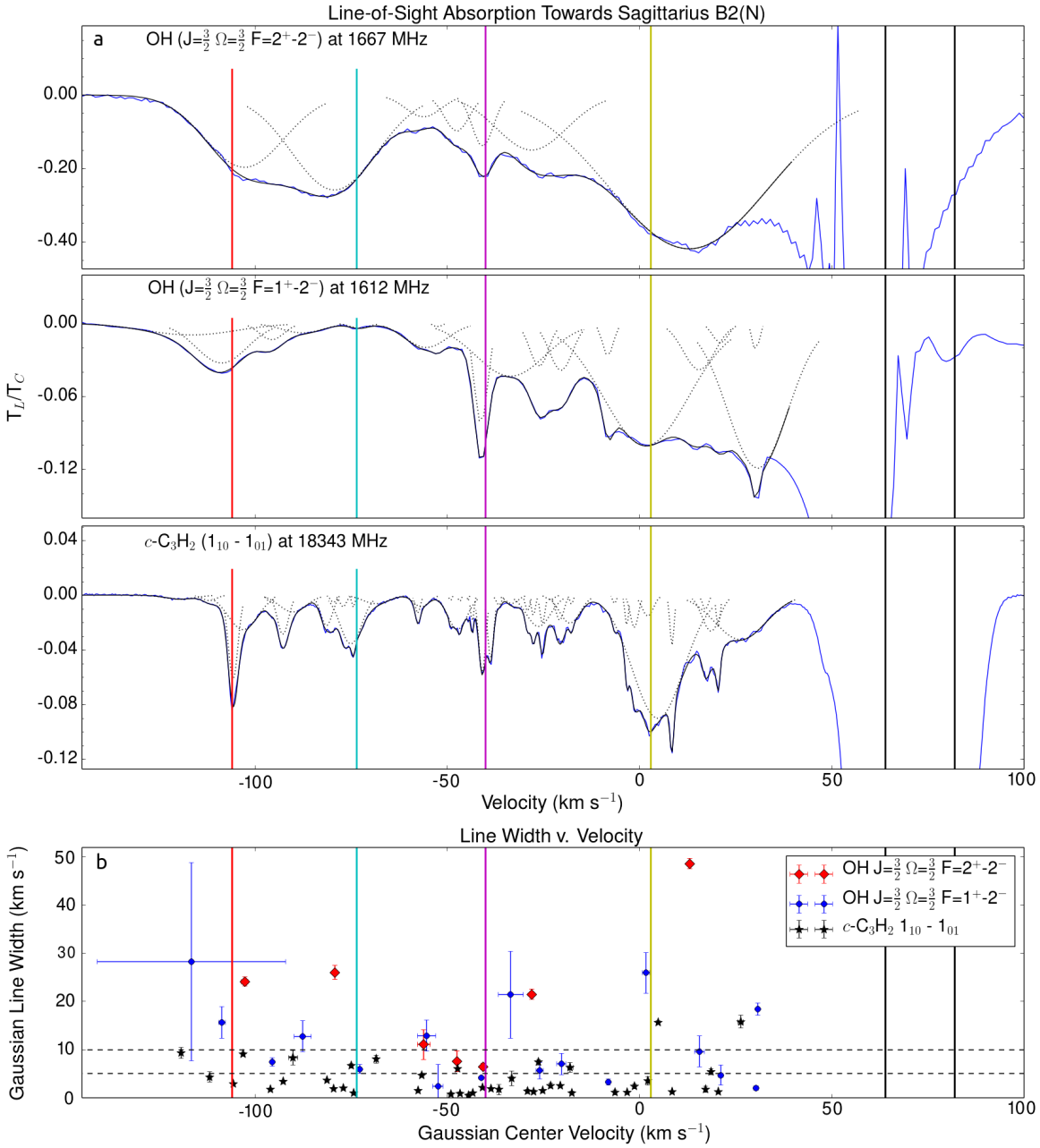

Fig. 5.1 – **a.** Line-of-sight profiles of OH and c-C_3H_2 are plotted in blue with individual Gaussian fit components shown with black dashed lines and the complete Gaussian fit overlaid in solid black. **b.** Gaussian fit parameters of center velocity and line width for individual Gaussian components fit to the profiles of OH and c-C_3H_2. Horizontal dashed lines indicate line widths of 10 $\mathrm{km\,s^{-1}}$ and 5 $\mathrm{km\,s^{-1}}$. In all panels, black vertical lines indicate the velocities of line absorption by Sgr B2 at +64 and +82 $\mathrm{km\,s^{-1}}$, and colored lines are located at -106, -73.5, -40, and +3 $\mathrm{km\,s^{-1}}$.

Table 5.2 – Velocity ranges considered for each cloud

Nominal Velocity ($\mathrm{km\,s^{-1}}$)	v_0 ($\mathrm{km\,s^{-1}}$)	v_1 ($\mathrm{km\,s^{-1}}$)
-120	-126	-116
-106	-110	-97.5
-92	-97.5	-86.8
-80	-86.8	-78
-73	-78	-67
-58	-62	-54
-47[1]	-54	-42.5
-40[2]	-42.5	-35
-23	-33	-12
0	-11	11.5
20[3]	11.5	38

[1] For COMs, we use the range of -54 to -44.5.
[2] For COMs, we use the range of -44.5 to -35.
[3] For transitions with significant wings from Sgr B2, we use the range of +11.5 to +20.

H_2CO are fairly similar but have notable differences. Whereas absorption by c-C_3H_2 is of a similar peak line strength in the -92, -73, -40, and -23 $\mathrm{km\,s^{-1}}$ clouds, the peak line strength in H_2CO absorption varies more substantially in these components. In the H_2CO profile, the -73 $\mathrm{km\,s^{-1}}$ and the -23 $\mathrm{km\,s^{-1}}$ components have similar line strengths, whereas the -40 $\mathrm{km\,s^{-1}}$ component is a factor of $\sim$3 stronger and the -92 $\mathrm{km\,s^{-1}}$ cloud is significantly weaker.

The absorption profile of CS (1-0) appears qualitatively distinct from the line profiles of c-C_3H_2 and H_2CO. Whereas c-C_3H_2 and H_2CO exhibit comparatively smooth absorption profiles, CS line absorption is characterized by sharper, more jagged peaks. This is particularly true of the clusters of clouds around -47, -40, and -23 $\mathrm{km\,s^{-1}}$, where CS absorbs in narrow, sharp peaks without as much broad-component absorption as is present in the line profiles of c-C_3H_2 and H_2CO. This is best illustrated by the -47 $\mathrm{km\,s^{-1}}$ gas, in which the line strengths of the narrow features are significantly greater than the strength of the broad absorption component in the CS profile, whereas the opposite is true for c-C_3H_2 and H_2CO. Similarly, absorption by SO (1_0-1_1) has narrow lines with little broad-component

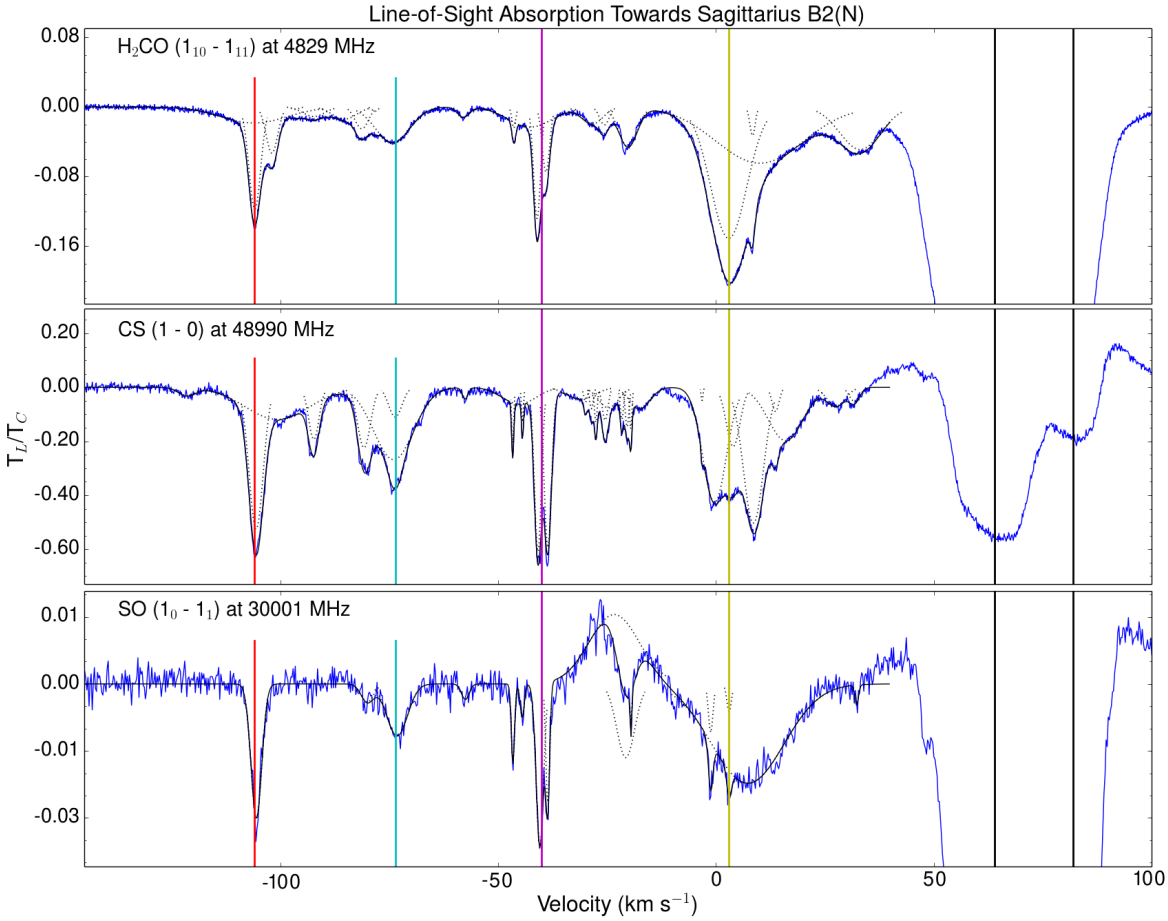

Fig. 5.2 – The absorption profiles of H_2CO, CS, and SO are overlaid by individual best fit Gaussian components (black dotted line) and the sum of best-fit Gaussians (black solid line). Black vertical lines indicate the velocities of line absorption by Sgr B2 at +64 and +82 $\mathrm{km\,s^{-1}}$, and colored lines are located at -106, -73.5, -40, and +3 $\mathrm{km\,s^{-1}}$. In the profile of SO, the dashed-dotted line indicates the 8_{17}^{-} - 8_{18}^{+} transition of CH_3OH at +64 $\mathrm{km\,s^{-1}}$, which appears in emission.

absorption in the -47 and -40 $\mathrm{km\,s^{-1}}$ clouds.

Figure 5.3 includes selected line profiles of CS-bearing molecules. Generally, the profiles of $C^{34}S$ and CCS are similar to one another, with strong line absorption in the -106, -73, -40, and 0 $\mathrm{km\,s^{-1}}$ clouds and narrow peaks characterizing the -47 and -40 $\mathrm{km\,s^{-1}}$ gas. The profiles of H_2CS and HCS^+ appear to be less characterized by deep, narrow absorption features, although this could be because these two profiles do not have sufficient signal-to-noise to permit a full characterization of narrow features. The patterns of absorption are somewhat different for these two species than for CS, $C^{34}S$, and CCS. For H_2CS, little to no absorption is detected at -73 $\mathrm{km\,s^{-1}}$. In the profile of HCS^+, only weak absorption by HCS^+ is observed in the -40 $\mathrm{km\,s^{-1}}$ component whereas CS, $C^{34}S$, CCS, and H_2CS produce strong absorption in this cloud.

Figure 5.4 shows the line profiles of ^{28}SiO and ^{29}SiO. Compared to *c*-C_3H_2, H_2CO, and CS-bearing species especially, the profiles of SiO isotopologues are much smoother and are predominantly characterized by moderately broad components (with $3 \lesssim \Delta v \lesssim 10$ $\mathrm{km\,s^{-1}}$). Strong absorption is present particularly at -73 and 0 $\mathrm{km\,s^{-1}}$.

The line profiles of *l*-C_3H and *l*-C_3H^+ are shown in Figure 5.5. As the transitions of *l*-C_3H have hyperfine structure, we have only fit the primary (F=2-1) line, with these components shown by dashed Gaussian profiles, and we add the hyperfine structure to the total fit (solid black line) as described above. The presence of the hyperfine structure, combined with the somewhat weak signal and line blending, makes it difficult to characterize the line profiles of *l*-C_3H. From the (J=$\frac{3}{2}$ - $\frac{1}{2}$ Ω=$\frac{1}{2}$ F = 2 - 1 *l*=f) line profile at 32 627 MHz, we can confidently characterize the absorption at -106, -92, -80, -73, -40, -23, and 0 $\mathrm{km\,s^{-1}}$. In this line profile, we also notice strong absorption at -57 and -48 $\mathrm{km\,s^{-1}}$, possibly arising from the -58 and -47 $\mathrm{km\,s^{-1}}$ clouds. In the line-of-sight profiles by other molecules in the PRIMOS data, however, absorption by the -58 and -47 $\mathrm{km\,s^{-1}}$ clouds is weaker than ab-

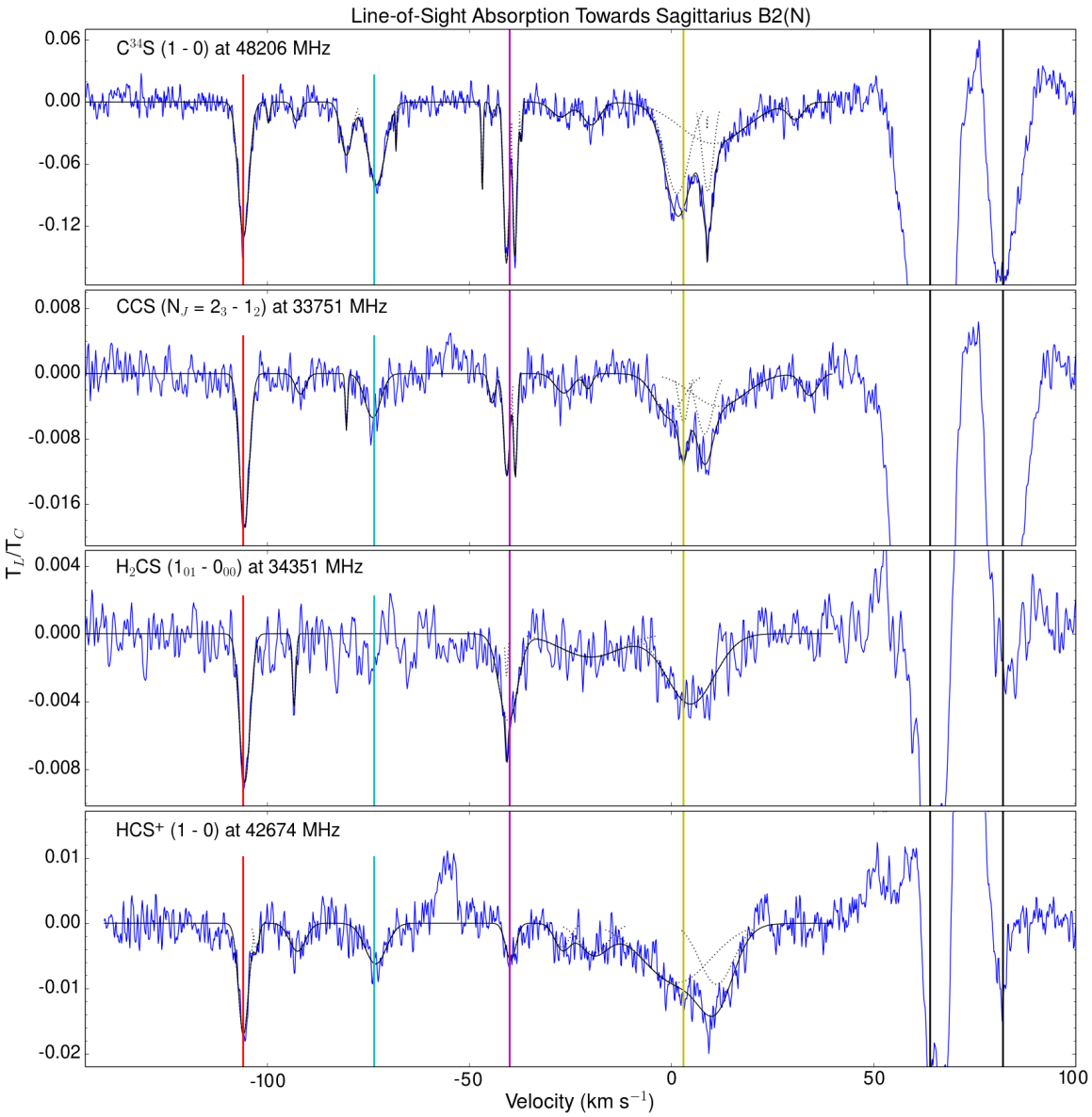

Fig. 5.3 – The absorption profiles of CS-bearing species are overlaid by the best fit Gaussian components (black dotted line) and the sum of best-fit Gaussians (black solid line). Black vertical lines indicate the velocities of line absorption by Sgr B2 at +64 and +82 km s^{-1}, and colored lines are located at -106, -73.5, -40, and +3 km s^{-1}.

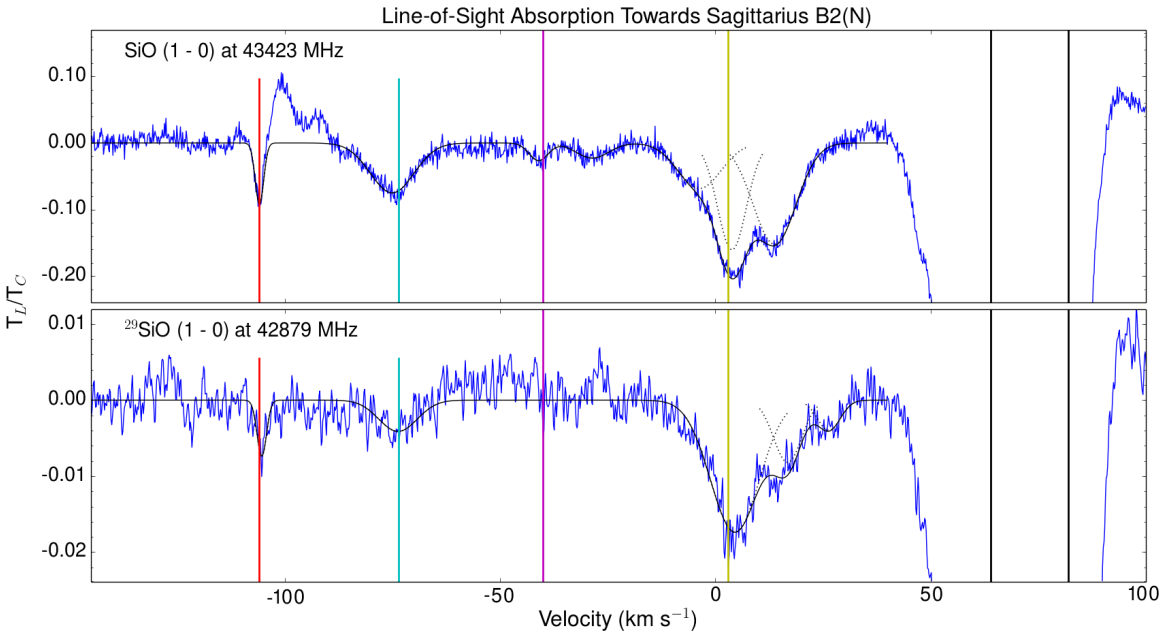

Fig. 5.4 – The absorption profiles of ^{28}SiO and ^{29}SiO are overlaid by the best fit Gaussian components (black dotted line) and the sum of best-fit Gaussians (black solid line). Black vertical lines indicate the velocities of line absorption by Sgr B2 at +64 and +82 km s^{-1}, and colored lines are located at -106, -73.5, -40, and +3 km s^{-1}.

sorption by the -40 and -73 km s^{-1} clouds. Thus, if the absorption at -57 and -48 km s^{-1} is from *l*-C_3H, then the -58 and -47 km s^{-1} clouds would have exceptionally high abundances of *l*-C_3H compared to other clouds. If the features are from *l*-C_3H, the (F = 1 - 0) hyperfine transitions should occur at -122 and -113 km s^{-1}, respectively, in the rest frame of the (F = 2 - 1) transition. Absorption features are present at both of these velocities, although the observed features are somewhat weaker than the hyperfine lines should be given the strength of the (F = 2 - 1) features. In the (*l* = e) transition at 32660 MHz, the velocity range of -60 to -20 km s^{-1} is obscured by blending with line absorption from *cis*-CH_2OHCHO in Sgr B2 at +64 and +82 km s^{-1}. Nonetheless, an absorption feature at -58 km s^{-1} is possibly detectable and somewhat resolved on the low-velocity edge of the +64 km s^{-1} component of *cis*-CH_2OHCHO. This profile is also not inconsistent with there being line absorption by *l*-C_3H at -47 km s^{-1}, although it is not possible to claim this feature is detected. However,

if absorption by the (F = 2 - 1 l = e) transition is present at -58 and -47 km s^{-1}, the (F = 1 - 0) hyperfine components would occur at -80 and -73 km s^{-1}, and would account for all absorption at these velocities. Because the -73 and -80 km s^{-1} components were detected in the (l = f) component, we are inclined to believe that the absorption at -80 and -73 km s^{-1} is from the -80 and -73 km s^{-1} clouds, and are not hyperfine features from the -58 and -47 km s^{-1} clouds. Therefore, we treat the features at -48 and -57 km s^{-1} in the (l = f) profile at 32627 MHz as unidentified lines but warn of the possibility that the absorption is from the line-of-sight clouds.

In the line profile of l-C_3H^+ (2 - 1), line absorption is clearly detected within the 0 km s^{-1} cloud, and absorption is also present in the -106, -73, and -47 km s^{-1} clouds. An unidentified emission line at 44994 MHz in the rest frame of Sgr B2 prevents characterization of the -40 km s^{-1} cloud. In the (1-0) transition of l-C_3H^+ (Appendix A), absorption is also clearly detected at $\sim$0 km s^{-1}, and the profile provides evidence supporting the detection of l-C_3H^+ in the -73 km s^{-1} cloud. The detection of l-C_3H^+ remains somewhat suspect, as it either contains substantial absorption from -120 to -110 km s^{-1} or is confused with a different line or with baseline effects. We note that the baseline is stable on either side of the velocity range of interest, so do not favor the latter explanation. However, as the -106 km s^{-1}component is too weak to be detected in the (1-0) transition, we treat l-C_3H^+ in the -106 km s^{-1} cloud tentatively, and recommend that it should be confirmed in an additional transition.

Figure 5.23 shows profiles of $^{12}CH_3OH$ and $^{13}CH_3OH$ with detected absorption by the diffuse and translucent clouds. Most notably, we observe emission at $\sim$3 km s^{-1} in the class I methanol maser line at 36.2 GHz, although the line has a Gaussian shape and therefore does not exhibit apparent line narrowing associated with strong masing. No maser emission is observed from the other diffuse and translucent clouds. We also observe promi-

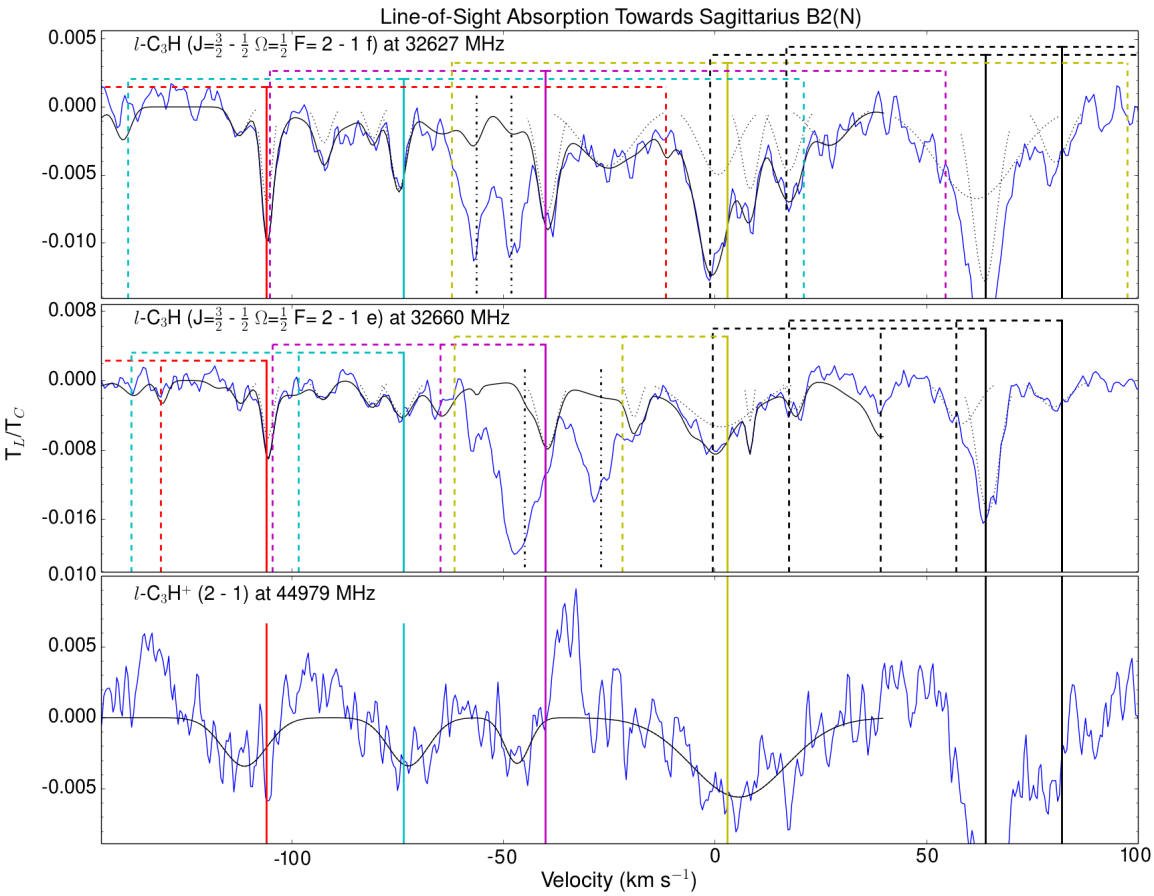

Fig. 5.5 – Absorption profiles of l-C_3H and l-C_3H^+ are overlaid by the best fit Gaussian components (black dotted line) and the sum of best-fit Gaussians (black solid line). Black vertical lines indicate the velocities of line absorption by Sgr B2 at +64 and +82 km s^{-1}, and colored lines are located at -106, -73.5, -40, and +3 km s^{-1}. Hyperfine structure for each of these velocity components is indicated by dotted vertical lines of the same color. The data are overlaid by Gaussian components fit to the main hyperfine component shown in blacked dotted lines, and by the total fit to the profile, which assumes that hyperfine or A/E components are present with the same line shape as the primary component, but with the height scaled by the ratio of the line strengths. In the profile of l-C_3H at 32627 MHz, the black dashed-dotted line marks unidentified transitions that are not consistent with the typical profile of diffuse cloud absorption in this line of sight. In the line profile of l-C_3H at 32660 MHz, the black dashed-dotted line marks a transition of *cis*-CH_2OHCHO at velocities of +64 and +82 km s^{-1} associated with Sgr B2.

nent absorption centered at $\sim$3 km s^{-1} in the ($2_{0,2}$-$3_{-1,3}$) transition at 12.2 GHz and in the ($2_{1,1}$-$3_{0,3}$) transition at 19.97 GHz. Absorption by the ($2_{0,2}$-$3_{-1,3}$) transition of $^{13}CH_3OH$ is also present at $\sim$3 km s^{-1}. All of the above transitions are associated with the E-state of methanol and are very likely affected by population inversions, which generate the maser emission at 36 GHz and enhanced absorption in cerain other transitions. Finally, we observe the ground state transition of the A-state of methanol at 48 372 MHz. Whereas absorption by the $\sim$0 km s^{-1} cloud is blended with the wing of the emission by Sgr B2 and with a line of CH_3NH_2, the profile includes clearly detected absorption at -106, -73, and -40 km s^{-1}. As these clouds do not show any sign of having a population inversion, we expect that the profile is reflective of the true methanol columns in these clouds.

Figure 5.7 includes the profiles of other complex organic species, including HC_3N, CH_3CN, CH_3CHO, and NH_2CHO. Hyperfine structure is handled as described above. The COMs are prominent in the -106, -73, -40, and 0 km s^{-1} clouds, and are typically strongest at -106 and $\sim$0 km s^{-1}. While CH_3OH absorption in the (1_{01}-0_{00}^{++}) transition is strongest at -106 km s^{-1}, weaker by a factor of two at -73 km s^{-1}, and weaker by another factor of two in the -40 km s^{-1} cloud (Figure 5.23), the molecules shown in Figure 5.7 have different relative line strengths within these clouds. For HC_3N and CH_3CHO, the -106 and $\sim$0 km s^{-1} clouds have similar peak line strengths, and are a factor of 2 to 3 stronger than in the -73 km s^{-1} cloud. CH_3CN is stronger in the -106 km s^{-1} cloud than in the $\sim$0 km s^{-1} cloud by a factor of $>$2, whereas absorption by NH_2CHO has a significantly greater peak line strength in the $\sim$0 km s^{-1} cloud than in the -106 km s^{-1} cloud, by a factor of $\sim$3. The -40 km s^{-1} cloud is in most cases the weakest of the four clouds marked by vertical lines. For CH_3CN and CH_3CHO, the peak line strength in the -40 km s^{-1} cloud is similar to that in the -73 km s^{-1} cloud. On the other hand, absorption by HC_3N and NH_2CHO are significantly weaker in this component than in the -73 km s^{-1} cloud.

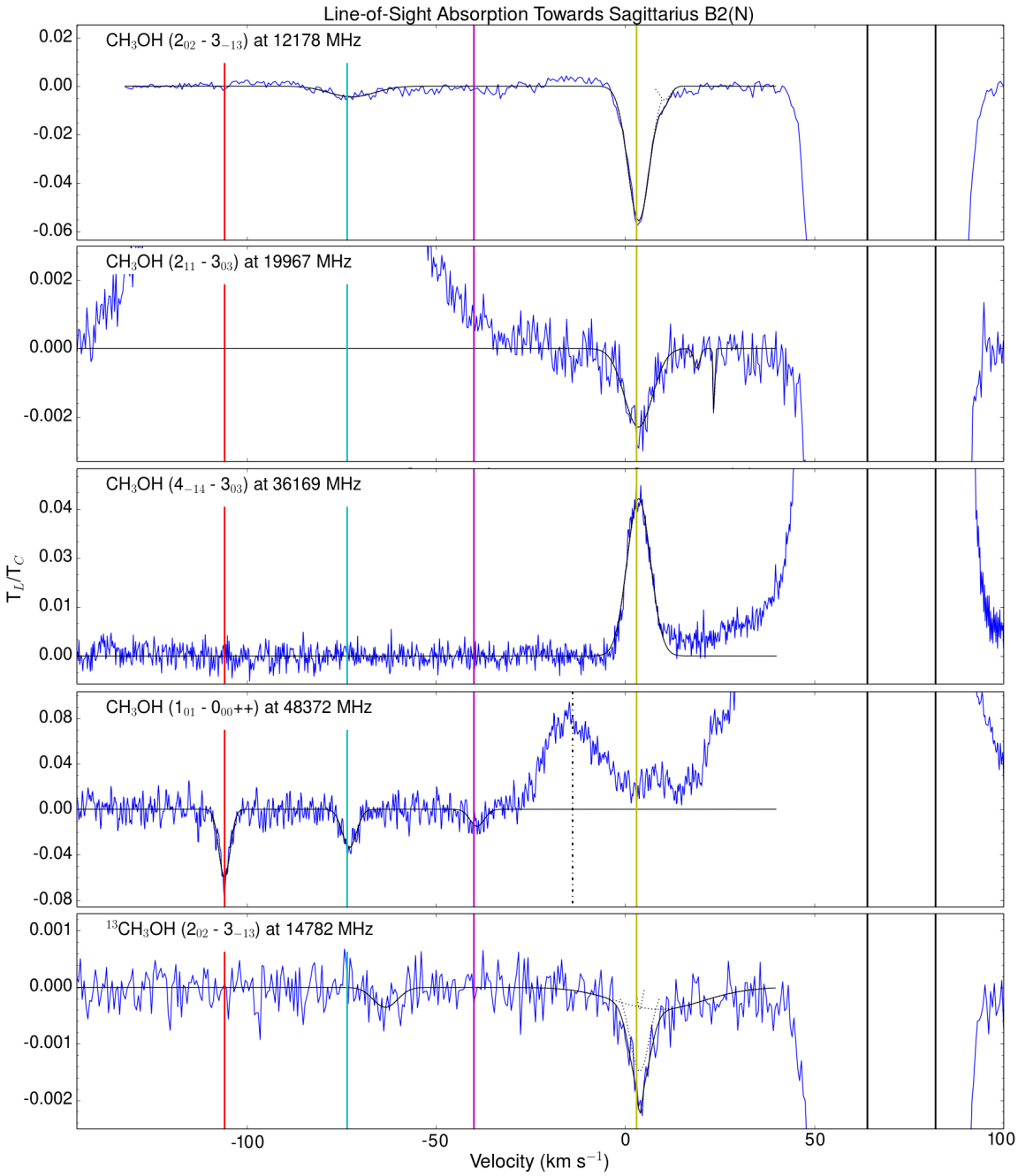

Fig. 5.6 – The absorption profiles of CH_3OH and $^{13}CH_3OH$ are overlaid by the best fit Gaussian components (black dotted lines) and the sum of best-fit Gaussians (black solid line). Black vertical lines indicate the velocities of line absorption by Sgr B2 at +64 and +82 km s^{-1}, and colored lines are located at -106, -73.5, -40, and +3 km s^{-1}. In the profile of CH_3OH at 48372 MHz, the black dashed-dotted line marks a transition of CH_3NH_2 at +64 km s^{-1} associated with Sgr B2.

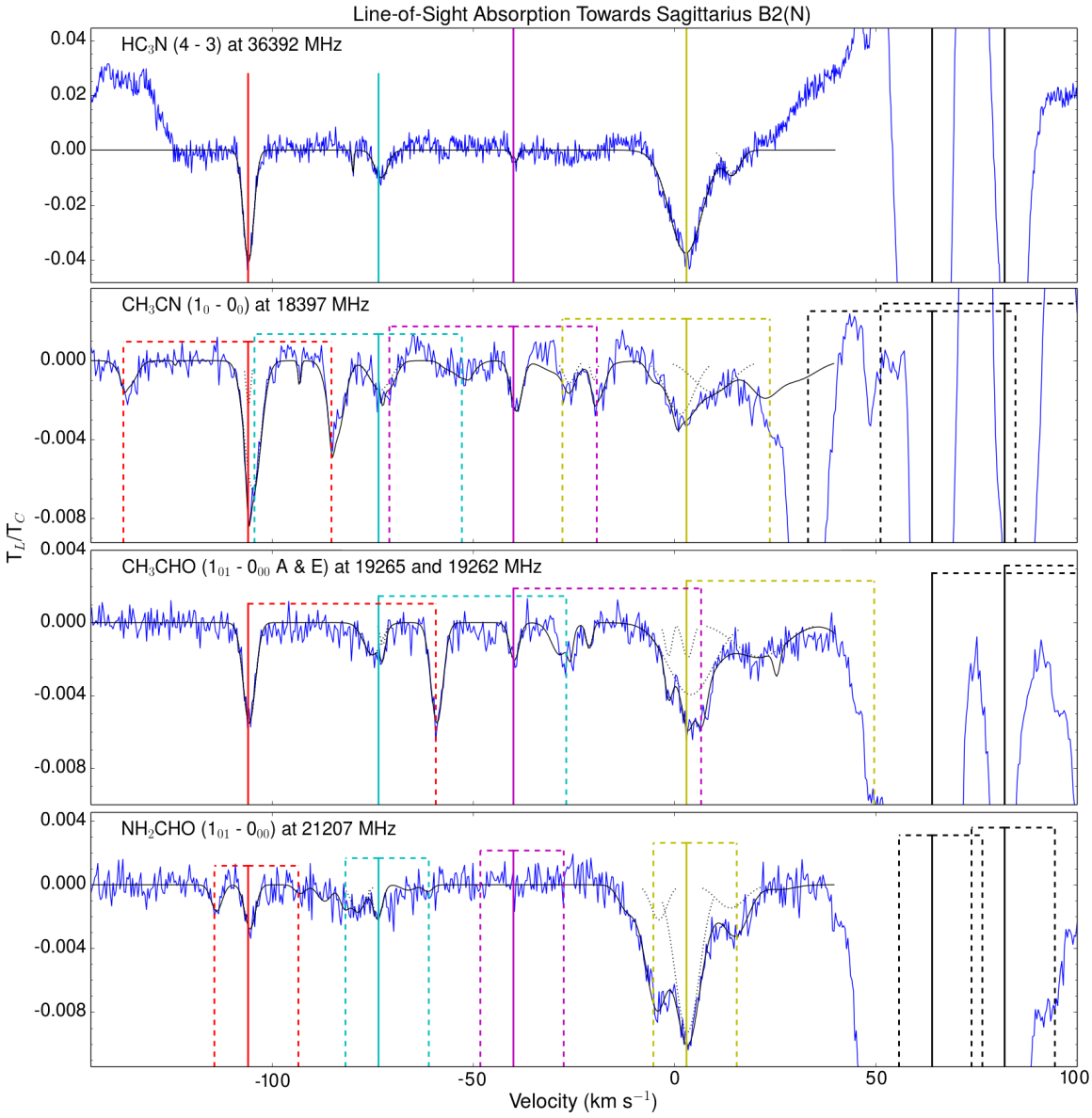

Fig. 5.7 – Absorption profiles of HC_3N, CH_3CN, CH_3CHO, and NH_2CHO are shown in blue. Black vertical lines indicate the velocities of line absorption by Sgr B2 at +64 and +82 $\mathrm{km\,s^{-1}}$, and colored lines are located at -106, -73.5, -40, and +3 $\mathrm{km\,s^{-1}}$. Hyperfine or A/E structure for each of these velocity components is indicated by dotted vertical lines of the same color. The data are overlaid by Gaussian components fit to the main hyperfine component shown in blacked dotted lines, and by the total fit to the profile, which assumes that hyperfine or A/E components are present with the same line shape as the primary component, but with the height scaled by the ratio of the line strengths.

5.2.2 Cloud Kinematics

Figure 5.8 shows the Gaussian fit parameters of center velocity and line width for all components fit to selected line profiles. In this figure, it is apparent that the -106 km s^{-1} component has particularly consistent and well defined parameters of line center and width, at $v \approx$ -105.7 km s^{-1} and $\Delta v \approx 3.1$ km s^{-1}. The standard deviations on these parameters, of 0.2 and 0.3, respectively, are consistent with the errors to individual measurements. While a few of the high signal-to-noise lines (like H_2CO (1_{10}-1_{11})) have broader components at or near -106 km s^{-1}, all transitions shown in Figure 5.8 have absorption at (v, Δv) $\approx$ (-105.7 km s^{-1}, 3 km s^{-1}), with the exception of CH_3CN, which requires a 2-component fit at -106 km s^{-1}. For some high signal-to-noise transitions, a narrow wing is present to the positive velocity side of the -106 km s^{-1} cloud, at approximately -102 km s^{-1}, and a moderately broad wing is present towards the negative velocity side, at $\sim$115 km s^{-1}.

The -92 km s^{-1} cloud is centered at -92.6 km s^{-1} and has mean width of Δv = 2.7 km s^{-1}. The line widths vary significantly more for the -92 km s^{-1} cloud than for the -106 km s^{-1} cloud, with measured values ranging from $\Delta v = 1$ to 5 km s^{-1}.

In the -80 km s^{-1} cloud, most line fits are tightly clustered around $v \approx 80.4$ km s^{-1} and $\Delta v \approx 3.5$ km s^{-1}. Absorption by the -73 km s^{-1} cloud typically has a larger line width, with a median value of 4.9 km s^{-1}. Whereas lines of SiO, and H_2CO have higher line widths, of 9-12 km s^{-1}, most other species have widths of $\sim$5 km s^{-1}, although significant scatter exists.

The -58 km s^{-1} cloud is centered at -57.6 km s^{-1}, and has a line width of $\sim$2.1 km s^{-1} with statistically significant scatter.

The -47 km s^{-1} cloud consists of two narrow velocity components, at -46.6 and -44 km s^{-1}, in addition to a broad component that is prominent in transitions of c-C_3H_2 and

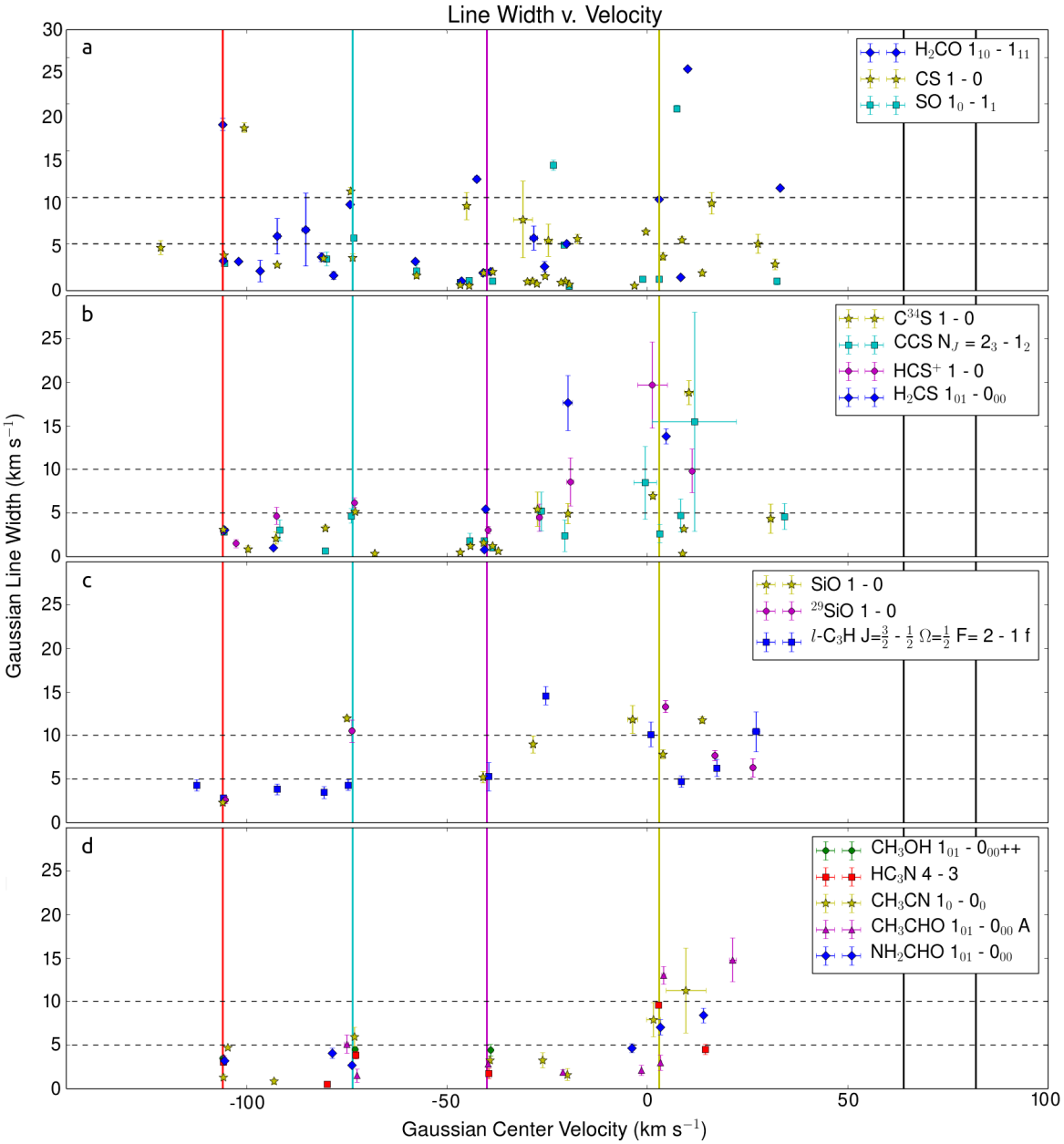

Fig. 5.8 – Gaussian fit parameters of center velocity and line width for individual Gaussian components fit to selected transitions of **a** H_2CO, CS, and SO, **b** CS-bearing molecules, **c** isotopologues of SiO and *l*-C_3H, and **d** complex organic molecules. In all panels, black vertical lines indicate the velocities of line absorption by Sgr B2 at +64 and +82 $\mathrm{km\,s^{-1}}$, and colored lines are located at -106, -73.5, -40, and +3 $\mathrm{km\,s^{-1}}$. Horizontal dashed lines indicate line widths of 10 $\mathrm{km\,s^{-1}}$ and 5 $\mathrm{km\,s^{-1}}$.

H_2CO. The narrow components have very consistent line center velocities, and typical widths of 0.7 and 1.0 $\mathrm{km\,s^{-1}}$ at -46.6 and -44 $\mathrm{km\,s^{-1}}$, respectively. Similarly, for small species with high signal-to-noise, the -40 $\mathrm{km\,s^{-1}}$ component consists of two narrow lines, at -40.8 and -38.7 $\mathrm{km\,s^{-1}}$, with widths of 1.9 and 1.5 $\mathrm{km\,s^{-1}}$, respectively. For lower signal-to-noise transitions, the two components are fit with a single Gaussian with a higher line width.

As observed in the highest signal-to-noise transitions, the -23 $\mathrm{km\,s^{-1}}$ cloud consists of many narrow features superposed on two moderately broad features which dominate the integrated flux. These two moderately broad features are at -27.1 and -20.1 $\mathrm{km\,s^{-1}}$, with widths of 4.8 and 4.6 $\mathrm{km\,s^{-1}}$, respectively, although significant scatter exists. The -23 $\mathrm{km\,s^{-1}}$ cloud was fit with a single Gaussian feature for some transitions with low signal-to-noise. Naturally, these fits therefore have higher line widths.

Finally, the $\sim$0 and +25 $\mathrm{km\,s^{-1}}$ clouds contain multiple superposed components, including broad profiles ($\Delta v > 10$ $\mathrm{km\,s^{-1}}$) with moderately broad ($3 < \Delta v < 10$ $\mathrm{km\,s^{-1}}$) and narrow ($\Delta v < 3$ $\mathrm{km\,s^{-1}}$) features superposed. Fits to this material typically include a feature at -1.8 $\mathrm{km\,s^{-1}}$, a strong component at +3.5 $\mathrm{km\,s^{-1}}$, a component at +9 $\mathrm{km\,s^{-1}}$, a broad component centered between $10 < v < 15$ $\mathrm{km\,s^{-1}}$, and a broad feature at +30 $\mathrm{km\,s^{-1}}$. The exact profiles vary significantly in different lines however, producing substantial scatter in Figure 5.8.

5.2.3 Column Density and Abundance Measurements

We determined column densities of every molecule in each distiguishable cloud component. To do so, we obtained the integrated line optical depths by

$$\int \tau dv = \int_{v_0}^{v_1} -ln\left(1 + \frac{T_L}{T_C - [f(3\text{ K}) - f(T_{\text{CMB}})]}\right); \qquad f(T) = \frac{h\nu/k}{e^{h\nu/kT} - 1} \leq T \tag{5.1}$$

(Nyman 1984; Greaves & Nyman 1996) with T_{CMB} = 2.73 K over the bounding velocities v_0 and v_1 provided in Table 5.2. We obtain column density values for clouds at -120, -106, -92, -80, -73, -58, -46, -40, -23, ∼0, and +20 km s^{-1}, and the bounding velocities for these clouds are provided in Table 5.2. We convert from integrated line optical depths to column densities by:

$$N = 8.0 \times 10^{12} \frac{Q}{S_{ij}\mu^2} \frac{\int \tau dv}{e^{-E_L/kT_{Ex}} - e^{-E_U/kT_{Ex}}} \text{ cm}^{-2} \tag{5.2}$$

by the conventions used in (Lucas & Liszt 1993; Greaves & Nyman 1996), where Q is the partition function, E_L and E_U are the upper and lower state energies, S_{ij} is the intrinsic line strength, and μ is the dipole moment in Debye. The calculation presumes that the absorbing gas extends homogenously over the continuum. This assumption is standard in studies of diffuse and translucent gas in line-of-sight absorption.

While the value of the partition function is typically estimated from equations like those provided in McDowell (1988, 1990), these equations diverge from the true values at low temperatures of T_{ex} <10 K. Due to the extremely low excitation temperatures in the line-of-sight clouds, we determined the partition functions directly by counting states with $Q = \Sigma g e^{-E/kT_{ex}}$. For this and for input line parameters required in Equation 5.2, line data from the Cologne Database of Molecular Spectroscopy (CDMS; Müller et al. 2005), the NASA Jet Propulsion Laboratory catalogue (JPL; Pickett et al. 1998) and the Spectral Line Atlas of

Interstellar Molecules (SLAIM; F. J. Lovas, private communication) were accessed through the ALMA Spectral Line Catalogue - Splatalogue[1]. In the data output from the CDMS and JPL catalogs, the value $S_{ij}\mu^2$ incorporates the degeneracy of the upper state g_U. The value of the degeneracy varies depending on how states are defined, i.e. whether hyperfine states and torsionally excited states are treated individually or collapsed. As a result, care must be taken to ensure consistency between the adopted or calculated value of the partition function and the line parameters used for the column density calculation. In our work, the partition functions were computed directly from the line data at T = 3 K using all states with energy $E < 100$ K (and up to 300 K for molecules with fewer transitions). We further verified that our calculated values of the partition function are in agreement with the values published by the catalogs at temperatures of 9, 19, and 38 K. We applied the method of direct summation for all species except for CH_3OH and $^{13}CH_3OH$, for which we used $Q = 1.2\ T^{3/2}$ and $Q = 1.26\ T^{3/2}$, respectively, as calculated from equations provided in Blake et al. (1987).

For molecules with only a single transition observed in line-of-sight absorption (i.e. SiO, SO, and CS isotopologues), it was then straightforward to determine the molecular column density. For molecules with multiple transitions, we determined the reported column density as the best fit to all measured transitions as determined by an error-weighted least-squares method. Within the velocity range, the error (ϵ) was determined by the errors on the heights and line widths of Gaussian fits added in quadrature, plus a 2 mK error over the Gaussian components contributed by baseline uncertainty. The baseline uncertainty refers to the baseline being slightly above or below the zero line in segments of the line profile, despite our best efforts of baseline subtraction.

We determine that a model with T_{ex} = 3 K does a good job of accounting for the line absorption for nearly all molecules in nearly all components. Initially, we allowed

[1]The ALMA Spectral Line Catalogue is available at www.splatalogue.net; (Remijan et al. 2007)

both T_{ex} and N_{molec} to vary and determined that values of 2.5 - 4 K produced the best fits in almost all cases. After determining that 3 K is appropriate, we set T_{ex} = 3 K before obtaining the best-fit values for the molecular column density. For illustration, Figure 5.9 shows the modeled and observed values of the integrated line optical depth obtained with T_{ex} = 3 K for seven observed transitions of CH_3CHO and three of c-C_3H_2. For all transitions, the best fit was within 1.5ϵ of the observed value. For most molecules, the values of N_{molec} obtained with different transitions are within a factor of 2 of each other. For H_2CO, c-C_3H_2, and l-C_3H, the values typically vary by $\lesssim$10%. We generally recommend 30% erros on the column density estimates, and somewhat lower errors of $\sim$15% on relative column densities between different components of a single molecule.

The only molecule for which the model with T_{ex} = 3 K does not work very well is CH_3CN. The CH_3CN (J_K = 2_0-1_0) and (2_1-1_1) transitions appear to have higher line strengths than expected given the strength of the J = 1-0 transition. This would suggest a higher excitation temperature and would therefore provide a lower limit to the molecular column. However, the (2-1) transition CH_3CN is very difficult to constrain due to the overlap of the hyperfine structure in the (J_K = 2_0-1_0) and (2_1-1_1) transitions and the presence of multiple velocity components; thus it is not entirely clear if the excitation of this species is higher. As 3 K works well for the remaining species, we expect that 3 K is also appropriate for CH_3CN.

In order to determine abundances relative to H_2, we estimated the hydrogen column in each component assuming that the abundance of c-C_3H_2 is constant and equal to X = $\frac{N_{c\text{-}C_3H_2}}{N_{H_2}}$ = 2.5 $\times 10^{-9}$. This assumption is based on the work of Liszt et al. (2012), which found that $X_{c\text{-}C_3H_2}$ = (2-3) $\times$ 10^{-9} with little variation in diffuse clouds in the Galactic disk. In §5.3.1 we argue that this is the best method for estimating the molecular hydrogen column in the PRIMOS data. The resulting hydrogen columns are provided in Table 5.3. For

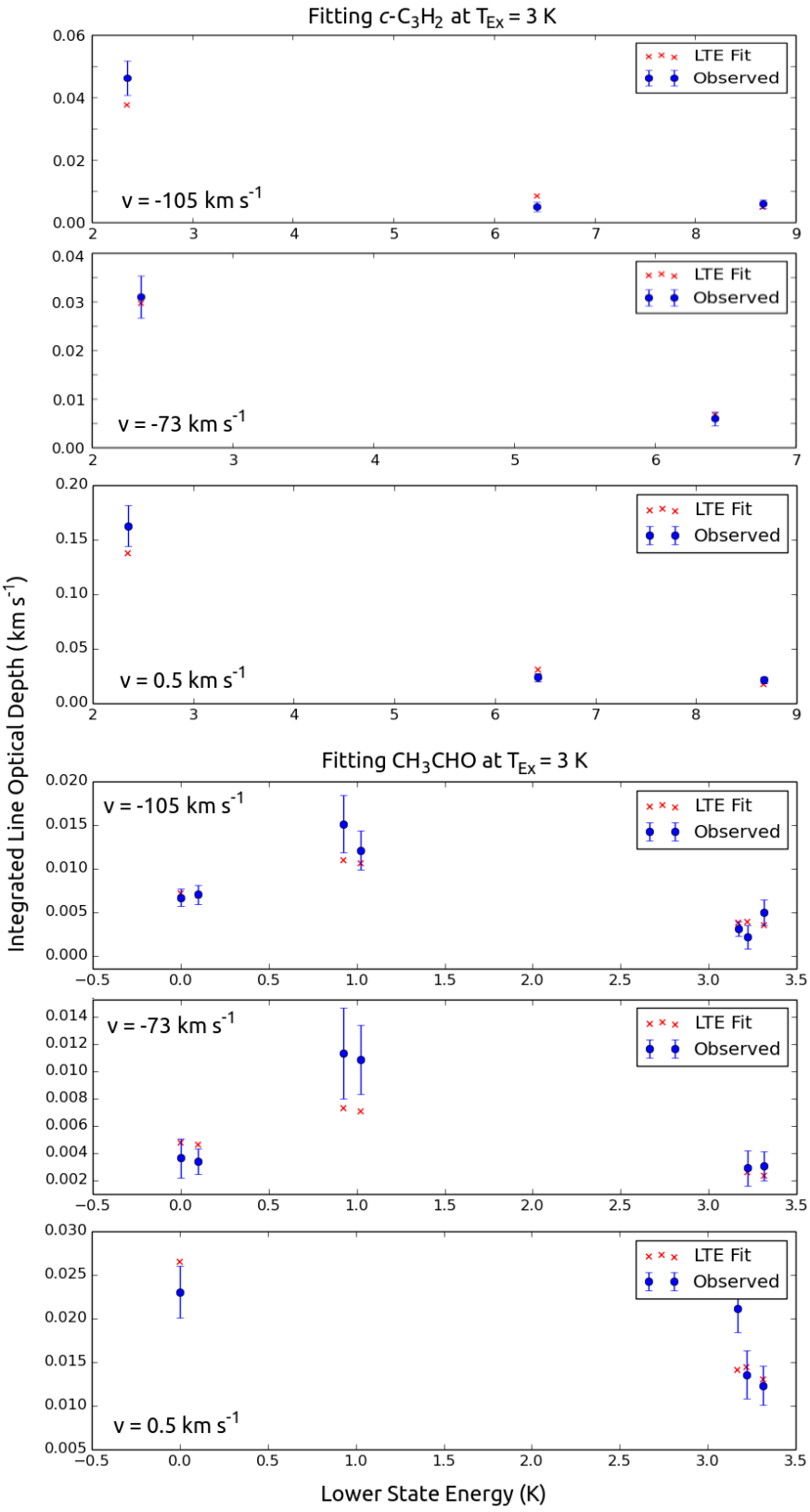

Fig. 5.9 – Observed integrated line optical depths of c-C_3H_2 and CH_3CHO and best fit models at T_{ex} = 3K. Error bars indicate 1σ errors.

the sake of comparison, we also include the hydrogen columns measured by previous authors towards Sgr B2(M), located 45 arcsec south of (N), by conversion from $H^{13}CO^+$ and ^{13}CO (Greaves & Nyman 1996; Irvine et al. 1987). Although clouds are present at mostly the same velocities in the two sightlines, the relative line strengths in the different kinematic components vary. As such, the two estimates of the molecular hydrogen column density are not expected to match perfectly. However, we do see approximate agreement for most of the clouds, providing one indication that our conversion from $N_{c\text{-}C_3H_2}$ to N_{H_2} is appropriate.

Additionally, Table 5.3 includes the neutral hydrogen column densities reported by (Indriolo et al. 2015) in the sightline to Sgr B2(N). These were measured by HI absorption in the 21-cm line observed with the Effelsberg 100-m telescope (Winkel et al. 2016). While (Indriolo et al. 2015) reported column densities over velocity ranges that include multiple distinct clouds as observed by c-C_3H_2, quite very strong trends are present in the molecular fractions measured. The molecular fraction in the -23 km s^{-1} cloud, located in the disk, is 0.4, consistent with values measured in other diffuse clouds that contain heavy molecules (Liszt et al. 2012). In the velocity range dominated by gas in the 3 kpc arm, 80 % of the hydrogen is in molecular form, and an even higher molecular fraction is measured in the velocity range dominated by Galactic Center gas, with $\gtrsim$90% of the hydrogen column in molecular form.

5.2.4 Abundance Patterns

Using the molecular hydrogen columns in the first row of Table 5.3, we convert molecular column densities to abundances with respect to H_2. The resulting abundances are provided in Table 5.4 and plotted against N_{H_2} in Figures 5.10, 5.11, and 5.12. The abundance results are summarized for each molecule below.

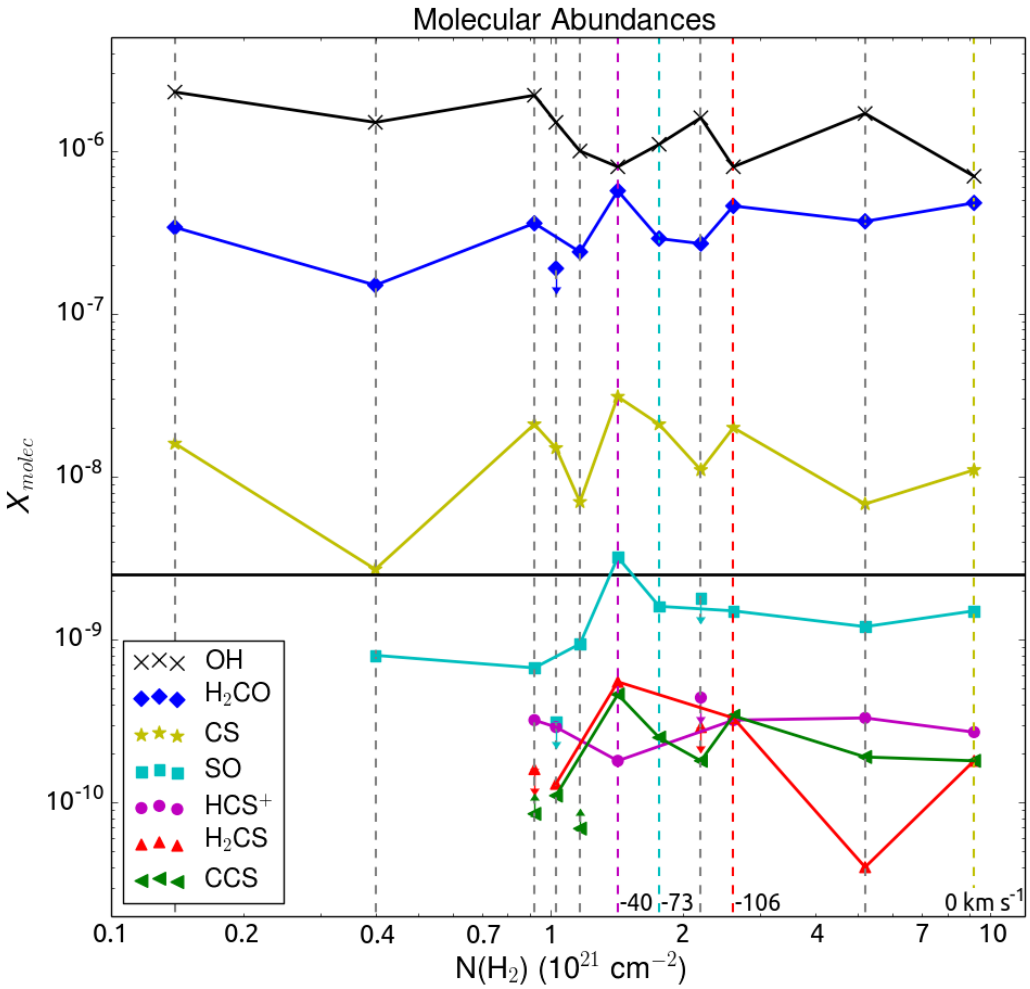

Fig. 5.10 – Molecular abundances of OH, H_2CO, SO, and CS-bearing species. The black solid line represents the assumed abundance of c-C_3H_2 used for the abundance determination. In order from lowest to highest hydrogen column, the -120, -58, -80, -92, -47, -40, -73, -23, -106, +25, and $\sim$0 km s^{-1} components are marked with vertical dashed lines. Colored vertical lines, as labeled, mark the -106, -73, -40, and 0 km s^{-1} clouds.

Table 5.3 – Molecular and neutral hydrogen column density estimates in units of 10^{21} cm^{-2}

Parameter	Position	Absorption Cloud Velocity (km s^{-1})										
		-120	-106	-92	-80	-73	-58	-47	-40	-23	0	+25
N(H_2)	(N)	0.14	2.6	1.03	0.92	1.8	0.40	1.2	1.4	2.2	9.2	5.2
N(H_2)[1]	(N)		3.8		2.7		0.40	2.6		2.2	14.4	
N(H_2)[2]	(M)		6		1.2		0.9	9		3	16	
N(H_2)[3]	(M)		5					9		4	14	
N(HI)[4]	(N)			1.0				1.5		4.0		
$f(H_2)$	(N)			0.9 - 0.95				0.8		0.4		
A_{Vo}[5] $\approx$	(M)	0.1	1.3	0.5	0.5	0.9	0.25	0.7	0.85	1.9	>4.2	>2.4

[1] Measurements are binned from previous row.
[2-4] Values from [2] Greaves & Nyman (1996) by conversion from $H^{13}CO^+$, [3] Irvine et al. (1987) by conversion from ^{13}CO, and [4] Indriolo et al. (2015) from 21 cm HI absorption.
[5] Central extinction of the cloud, estimated by $2A_{Vo} = A_V = (N_{HI} + 2N_{H_2})/(2.2 \times 10^{21}$ cm$^{-2})$, from (Güver & Özel 2009).

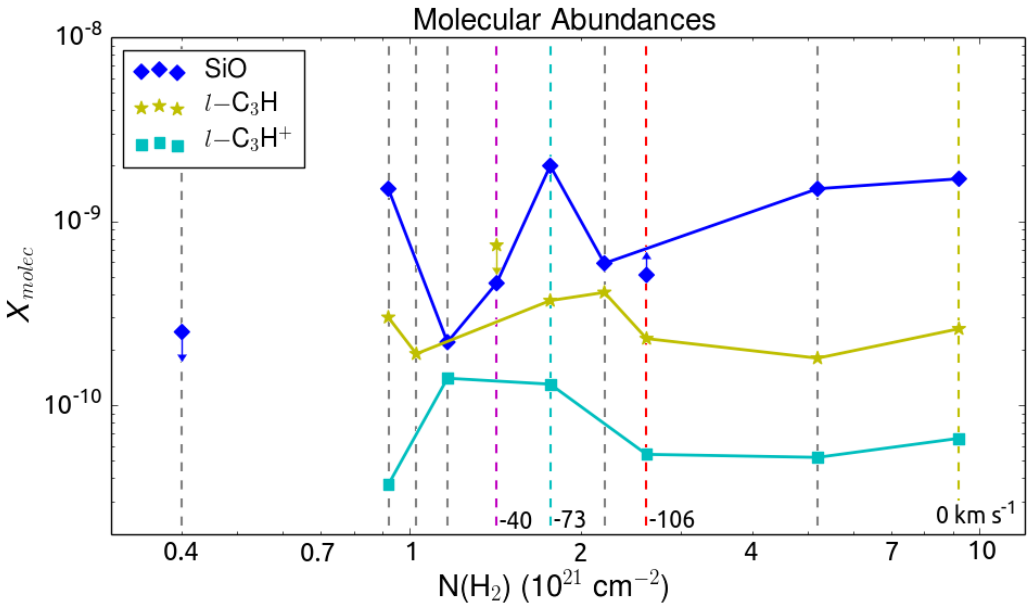

Fig. 5.11 – Molecular abundances of SiO, l-C_3H, and l-C_3H^+. In order from lowest to highest hydrogen column, the -58, -80, -92, -47, -40, -73, -23, -106, +20, and $\sim$0 km s^{-1} components are marked with vertical dashed lines. The abundances were calculated using two slightly different hydrogen columns for the -40 km s^{-1} cloud, as marked by magenta vertical lines.

Table 5.4 – Derived molecular abundances.

Molecule	Absorption Cloud Velocity ($km\,s^{-1}$)											Units
	-120	-106	-92	-80	-73	-58	-47	-40	-23	0	+25	
OH	2.3	0.8	1.5	2.2	1.1	1.5	1.0	0.8	1.6	0.7	1.7	10^{-6}
c-C_3H_2	2.5	2.5	2.5	2.5	2.5	2.5	2.5	2.5	2.5	2.5	2.5	10^{-9}
c-$H^{13}CCCH$		1.0	1.5		0.7			$<$0.3	0.3	1.0	1.2	10^{-10}
H_2CO	3.4	4.6	$<$1.9	3.6	2.9	1.5	2.4	5.7	2.7	4.8	3.7	10^{-7}
$H_2^{13}CO$		7.3		3.8	3.1		$\geq$1.6	8.8	5.9	9.7	$\geq$0.5	10^{-9}
SO		1.5	$<$0.3	0.7	1.6	0.8	0.9	3.2	$\lesssim$1.8	1.5	1.2	10^{-9}
CS	1.6	2.0*	1.5	2.1	2.1	0.3	0.7	3.1*	1.1	1.1*	$\geq$0.7	10^{-8}
$C^{34}S$		2.3	0.5	2.4	3.4	$<$1.3	0.7	4.5	1.2	2.0	1.1	10^{-9}
CCS		3.4	1.1	$\gtrsim$0.9	2.5		$\gtrsim$0.7	4.6	1.8	1.8	1.9	10^{-10}
HCS^+		3.2	2.9		3.2			1.8	$\lesssim$4.4	2.7	3.3	10^{-10}
H_2CS		3.3	1.3		$\leq$1.6			5.5	$\lesssim$2.9	1.8	0.4	10^{-10}
SiO		$\geq$0.5		1.5†	2.0	$<$0.3	0.2†	0.5	0.6	1.7	1.5	10^{-9}
^{29}SiO		4.2		4.6†	11					14	13	10^{-11}
^{30}SiO		2.7										10^{-11}
l-C_3H		2.3	1.9	3.0	3.7			$\lesssim$7.4	4.1	2.6	1.8	10^{-10}
l-C_3H^+		5.4		3.7	13		14			6.6	5.2	10^{-11}
CH_3OH		1.0			1.1			0.6		$\leq$430‡	$\leq$14‡	10^{-8}
$^{13}CH_3OH$										14	$\leq$6.8	10^{-8}
HC_3N		17		5.8	6.8			2.0	$\leq$2.3	14	9.1§	10^{-10}
CH_3CN		5.8	0.4		2.0			2.9	$\leq$0.6	3.7		10^{-10}
CH_3CHO		1.0		$<$1.1	1.1		$<$0.4	0.6	$<$0.4	1.0	0.7	10^{-9}
NH_2CHO		1.2		$\leq$2.0	2.2			0.4	$<$1.3	4.0	1.4	10^{-10}

* Peak optical depths are $>$0.7 in CS absorption.

† Appears to be a wing associated with the -73 or -40 $km\,s^{-1}$ gas instead of a separate component.

‡ Value is likely overestimated due to the presence of methanol maser emission at $\sim$3 $km\,s^{-1}$.

§ Due to the hyperfine wing of HC_3N, we used a velocity range of +11.5 to +20 $km\,s^{-1}$ for the measurement.

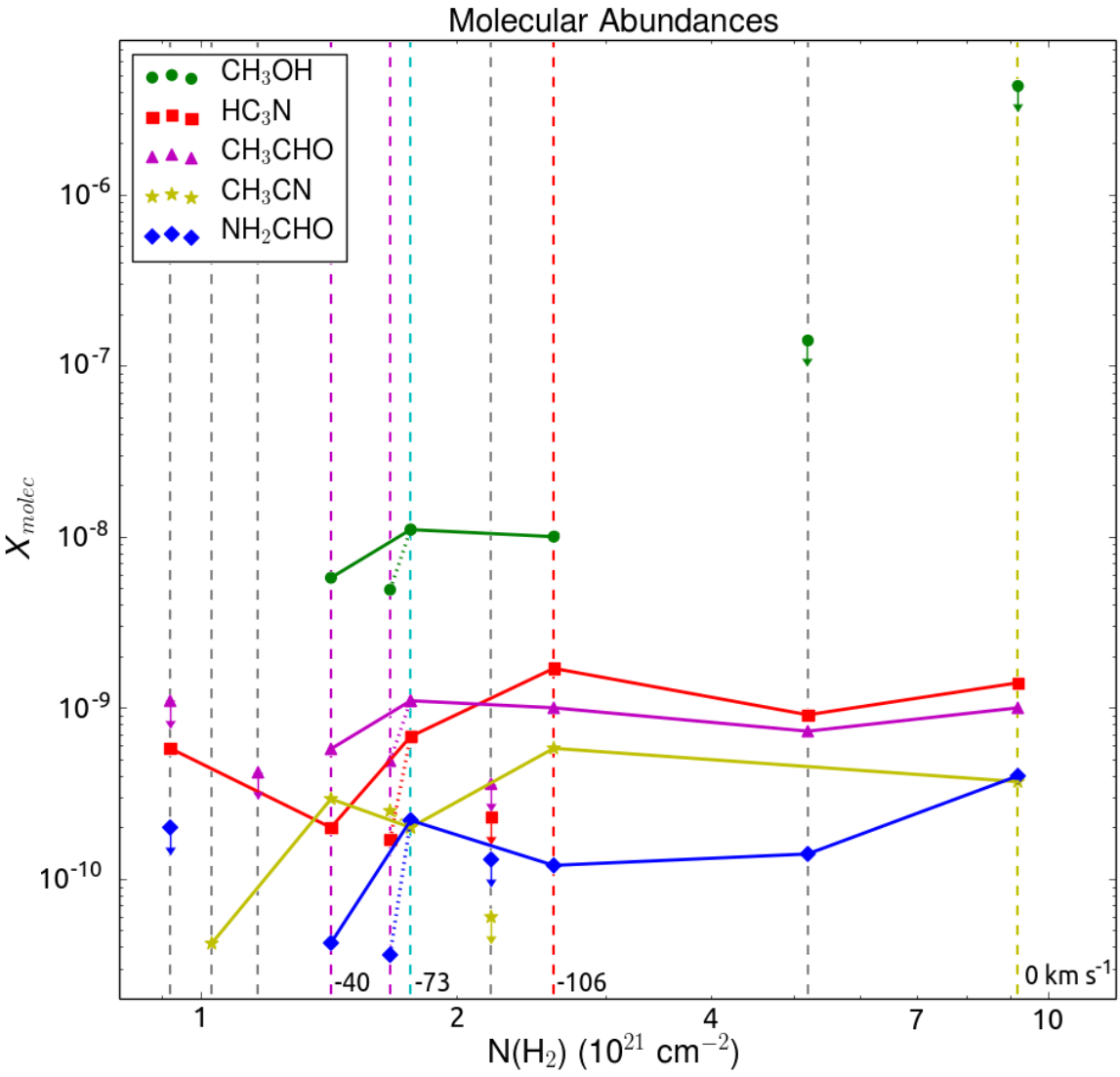

Fig. 5.12 – Molecular abundances of complex organic molecules. In order from lowest to highest hydrogen column, the -80, -92, -47, -40, -73, -23, -106, +25, and $\sim$0 km s^{-1} components are marked with vertical dashed lines. Colored vertical lines, as labeled, mark the -106, -73, -40, and 0 km s^{-1} clouds. The abundances were calculated using two slightly different hydrogen columns for the -40 km s^{-1} cloud, as marked by magenta vertical lines.

OH

The (J=$\frac{3}{2}$ Ω=$\frac{3}{2}$ F=1^+-1^-) and (J=$\frac{3}{2}$ Ω=$\frac{3}{2}$ F=2^+-2^-) transitions of OH at 1665 and 1667 MHz have extremely similar line profiles and very consistent values of N_{molec} are derived using the two lines, with measurements nearly always within 10% of one another. In Table 5.4, we report values obtained from a best fit to these two lines and obtain values of order 10^{-6}. The (J=$\frac{3}{2}$ Ω=$\frac{3}{2}$ F=1^+-2^-) line profile at 1612 MHz appears somewhat different however. Column density measurements made using the 1612 MHz transition are slightly higher, by a factor of 1.5 to 3, than the values reported in Table 5.4 for the clouds at -120, -58, -46, -40, -23, 0, and +25 $\mathrm{km\,s^{-1}}$ clouds. The abundance estimate is slightly lower (by a factor of 3) in the -92 $\mathrm{km\,s^{-1}}$ cloud, and an order of magnitude lower than the reported values at -80 and -73 $\mathrm{km\,s^{-1}}$. OH does not appear to occupy the same volume of gas as c-C_3H_2, as evidenced by the differences in the line profiles, so it is not appropriate to interpret the measurements as true abundances. We include the values as they likely have physical significance, however, as discussed in §5.5.2.

CS-bearing molecules, SO, and H_2CO

H_2CO, SO, and most of the CS-bearing species share similar abundance patterns. The CS abundance varies by an order of magnitude within the clouds, and no trend is evident with the cloud hydrogen column. While an abundance of $\sim 2 \times 10^{-8}$ is most commonly measured, we note anomolously lower values in some clouds, and a particularly high value of 3.1 $\times 10^{-8}$ in the -40 $\mathrm{km\,s^{-1}}$ cloud. In addition to CS, high abundances of H_2CO, SO, CCS, and H_2CS are measured in the -40 $\mathrm{km\,s^{-1}}$ cloud. Conversely, the abundance of HCS^+ is lower in the -40 $\mathrm{km\,s^{-1}}$ cloud than in other measured clouds. Whereas HCS^+ is consistently measured to have an abundance of $\sim 3 \times 10^{-10}$ in other clouds, it is nearly a factor of two lower in the -40 $\mathrm{km\,s^{-1}}$ cloud. Figure 5.13 shows the abundances of H_2CO,

SO, CCS, H_2CS, and HCS^+ plotted against the abundance of CS. The abundances of CCS and H_2CS positively correlate with the CS abundance, with a slope that is similar to the identity line, although scatter exists. On the other hand, the abundance of HCS^+ does not vary linearly with the CS abundance; instead it is low in the -40 $km\,s^{-1}$ cloud and nearly constant for all other clouds.

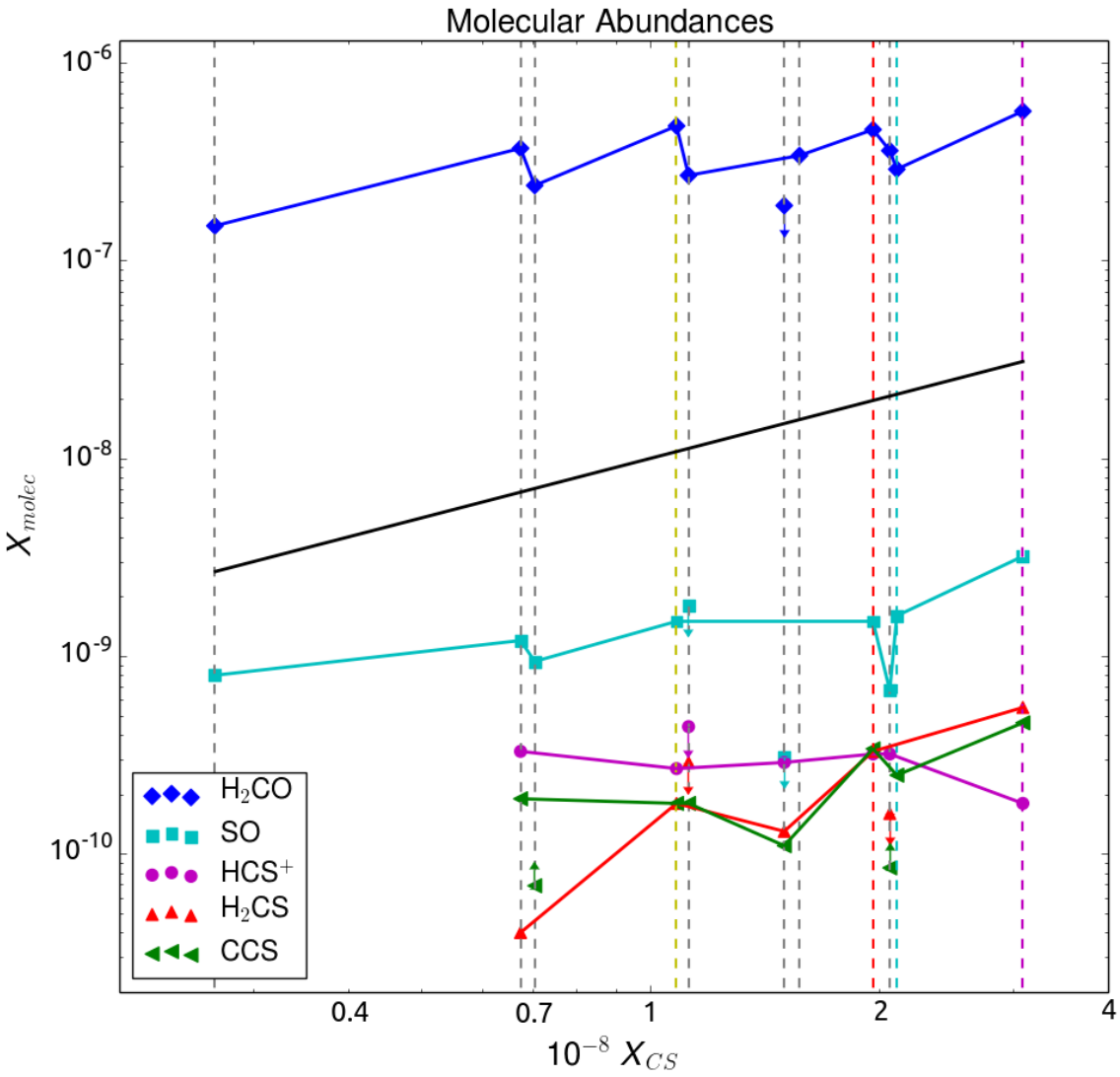

Fig. 5.13 – Molecular abundances of H_2CO, SO, and CS-bearing species plotted against the abundance of CS. The black solid line represents the identity line of the CS abundance. In order from lowest to highest CS abundance, the -58, +25, -46, 0, -23, -92, -120, -106, -80, -73, and -40 $km\,s^{-1}$ components are marked with vertical dashed lines.

The abundances of H_2CO and SO also positively correlate with that of CS. The observed trends in $log(X_{\rm SO})$ v. $log(X_{\rm CS})$ and $log(X_{\rm H_2CO})$ v. $log(X_{\rm CS})$ are shallower than the CS-identity line, however, with slopes of 0.25 and 0.5, respectively. Additionally, while these species show a clear correlation, significant scatter is present.

SiO

The abundance of SiO varies by an order of magnitude in different clouds. Furthermore, $X_{\rm SiO}$ does not correlate with $N_{\rm H_2}$or $X_{\rm CS}$. In the -73 km s^{-1}, $\sim$0 km s^{-1} , and +25 km s^{-1} clouds in the Galactic Center, the SiO abundance is 1.5 to 2 $\times 10^{-9}$. However, not all clouds believed to occur in the Galactic Bar or Galactic Center have high abundances of SiO; in the -58 km s^{-1} cloud, for example, SiO is at least an order of magnitude less abundant. In material located external to the Galactic Bar at -23 and -40 km s^{-1}, SiO abundances are of order 5 $\times 10^{-10}$.

***l*-C_3H and *l*-C_3H^+**

The abundances of *l*-C_3H range from $\sim$2 to 4 $\times 10^{-10}$, with a median value of 2.6 $\times 10^{-10}$, whereas the abundance of *l*-C_3H^+ varies more substantially, from 3.7 $\times 10^{-11}$ to 1.4 $\times 10^{-10}$. The *l*-C_3H and *l*-C_3H^+ abundances do not appear to correlate with $N_{\rm H_2}$ or with X_{CS}.

Complex Organic Molecules

CH_3OH: The relative abundances of the COMs show significant variation in different clouds. The abundance of CH_3OH is measured from absorption in the ground state transition of the A-state (1_{01}-0_{00}++) for the -106, -73, and -40 km s^{-1} clouds. While abundances of $\sim 10^{-8}$ are measured in the -106 and -73 km s^{-1} clouds, located in the Galactic Cen-

ter and deep within the Bar, a slightly lower value of $\sim 6 \times 10^{-9}$ is measured in the -40 km s^{-1} cloud.

In the material at 0 km s^{-1}, absorption by the E-state ($2_{0,2}$-$3_{-1,3}$) transition at 12.2 GHz and the ($2_{1,1}$-$3_{0,3}$) transition at 19.97 GHz indicate an exceptionally high abundance of 4.3 $\times 10^{-6}$. The values estimated by the two lines differ by about 15%, thereby exhibiting good agreement. However, it is likely that the line absorption in these two lines is affected by the population inversion responsible for the emission feature in the 36 GHz class I methanol maser (Figure 5.23). It is well established that in many class I methanol maser sources, the class II maser transition at 12.2 GHz displays enhanced absorption relative to LTE (Val'tts et al. 2010; Menten 1991). This would cause the methanol column density to be overestimated based on this line. The mechanism for creating the enhanced absorption is quite obvious for the 12.2 GHz line; for the E-state, the population inversion of the class I masers act to overpopulate the $k = -1$ states. As the lower energy state in the 12.2 GHz line is a $k = -1$ state, we should see significantly enhanced absorption. While the 19.97 GHz line is also a class II maser line (see e.g. Val'tts et al. 2010), although less common and typically weaker than the 12.2 GHz line, the mechanism for creating the enhanced absorption is less obvious, and this line has not been discussed as exhibiting enhanced absorption towards class I maser sources to the best of our knowledge. Nonetheless, enhanced absorption may be the most likely reason for the severely high abundance measured, and we interpret the value measured in the 0 km s^{-1} cloud as an upper limit that may be a severe overestimate. A precise treatment of the radiative transfer is warrented for methanol at 0 km s^{-1}.

HC_3N, CH_3CN, CH_3CHO, NH_2CHO: The abundance of HC_3N varies by nearly an order of magnitude, from $\sim 2 \times 10^{-10}$ in the -40 and -23 km s^{-1} clouds, located at the outer edge of the Bar and in the disk, respectively, to 1.7 and 1.4 $\times 10^{-9}$ in the -106 and $\sim$0 km s^{-1} clouds located in to the Galactic Center. The -73 and -80 km s^{-1} clouds,

believed to be located deep within the the Galactic Bar, have intermediate values of ~ 6 to 7×10^{-10}. Therefore, the abundance of HC_3N appears to be higher in clouds within the Galactic Center than in clouds external to the Galactic Bar.

The median abundance of CH_3CN is 2.5×10^{-10}, and the measured abundances span an order of magnitude. In the Galactic Center clouds at -106 and $\sim$0 km s^{-1}, CH_3CN has a high abundance of 5.8 and 3.7 $\times 10^{-10}$. In the -92 km s^{-1} cloud, also believed to be located in the Galactic Center, the abundance is significantly lower, at 4.2 $\times 10^{-11}$. The -40 km s^{-1} cloud also contains a fairly high abundance of CH_3CN, of 2.9 $\times 10^{-10}$, which is slightly greater than the measured value in the -73 km s^{-1} cloud located internal to the Galactic Center. The -23 km s^{-1} cloud contains a lower abundance of CH_3CN, with an upper limit of 6×10^{-11}. Thus, the abundance of CH_3CN appears to vary substantially in the diffuse and translucent clouds, but there is no clear distinction between Galactic disk and Galactic Center clouds.

CH_3CHO has an abundance of $\sim$1 $\times 10^{-9}$ in the Galactic Center clouds at -106 and $\sim$0 km s^{-1}, and in the Galactic Bar material at -73 km s^{-1}. In the -40 km s^{-1} cloud located at the outer edge of the Galactic Bar, the abundance is lower, at $\sim$6 $\times 10^{-10}$, and in the Galactic disk cloud at -23 km s^{-1}, it is even less abundant, with an upper limit of $\sim$4 $\times 10^{-10}$. Thus, from the clouds sampled in this line of sight, CH_3CHO appears to be more abundant in diffuse clouds internal to the Galactic Bar than in the Galactic disk.

Finally, the abundance of NH_2CHO also varies by an order of magnitude. NH_2CHO is most abundant in the $\sim$0 km s^{-1} cloud, at 4×10^{-10}, moderately abundant at $\sim$1 to 2×10^{-10} in the -106 and -73 km s^{-1} clouds located in the Galactic Center and Bar, respectively, and significantly less abundant in the -40 km s^{-1} cloud, at 4×10^{-11}. This suggests that the abundance of NH_2CHO is systematically higher in translucent clouds located closer to the Galactic Center.

Isotopologue Ratios

The abundance ratios (or equivalently, integrated column density ratios) between isotopologues show significant variation within different clouds (Table 5.5 and Figure 5.14). The $^{12}C/^{13}C$ ratio is probed by H_2CO, c-C_3H_2, and CH_3OH. Values of $H_2CO/H_2^{13}CO$ of 45 to 65 are obtained for the -106, -40, -23, and $\sim$0 km s^{-1} gas, while higher values of $\sim$95 are found in the material at -73 and -80 km s^{-1}. Thus, the ratios of $H_2CO/H_2^{13}CO$ do not show any systematic change with respect to Galactocentric distance. Values of c-C_3H_2/c-$H^{13}CCCH$ are $\sim$20 in the Galactic Center clouds at -106, -92, $\sim$0 , and +25 km s^{-1}, slightly higher at $\sim$35 in the -73 km s^{-1} cloud located deep within the Galactic Bar, and significantly higher, at $\geq$74 and $\sim$100 in material in the Galactic disk at -40 and -23 km s^{-1}, respectively. The ratio of $CH_3OH/^{13}CH_3OH$ is measured to be 33 in the $\sim$0 km s^{-1} material assuming similar excitation of $^{12}CH_3OH$ and $^{13}CH_3OH$, and this value is intermediate between the $^{12}C/^{13}C$ ratios for H_2CO and c-C_3H_2 in this cloud.

Table 5.5 – Isotopologue abundance ratios. Components marked with a '*' are optically thick in absorption by CS.

Molecules	Absorption Cloud Velocity (km s^{-1})									
	-106	-92	-80	-73	-58	-47	-40	-23	0	+25
$X(c\text{-}C_3H_2)/X(c\text{-}H^{13}CCCH)$	24	17		35			$\geq$74	100	25	21
$X(H_2CO)/X(H_2^{13}CO)$	63		94	96		$\leq$152	64	46	49	$\leq$791
$X(CS)/X(C^{34}S)$	8.5*	30	8.5	6.3*		9.6	6.8*	9.7	5.4*	6.2
$X(SiO)/X(^{29}SiO)$	$\gtrsim$13			22[1]				12	12	
$X(SiO)/X(^{30}SiO)$	$\gtrsim$19									
$X(^{29}SiO)/X(^{30}SiO)$	1.6									
$X(CH_3OH)/X(^{13}CH_3OH)$									32	

[1] Absorption in the velocity range of -85 to -67 km s^{-1} was included in this measurement.

Isotope ratios of silicon are probed by measurements of ^{28}Si, ^{29}Si, and ^{30}Si. In the $\sim$0 and +25 km s^{-1} material, we obtain $^{28}SiO/^{29}SiO$ = 12, and at -73, we obtain a higher value of 22. The $^{29}Si/^{30}Si$ ratio is measured to be 1.6 in the -106 km s^{-1} cloud.

The $^{32}S/^{34}S$ ratio is probed by $CS/C^{34}S$. For all clouds except for the -92 km s^{-1} cloud,

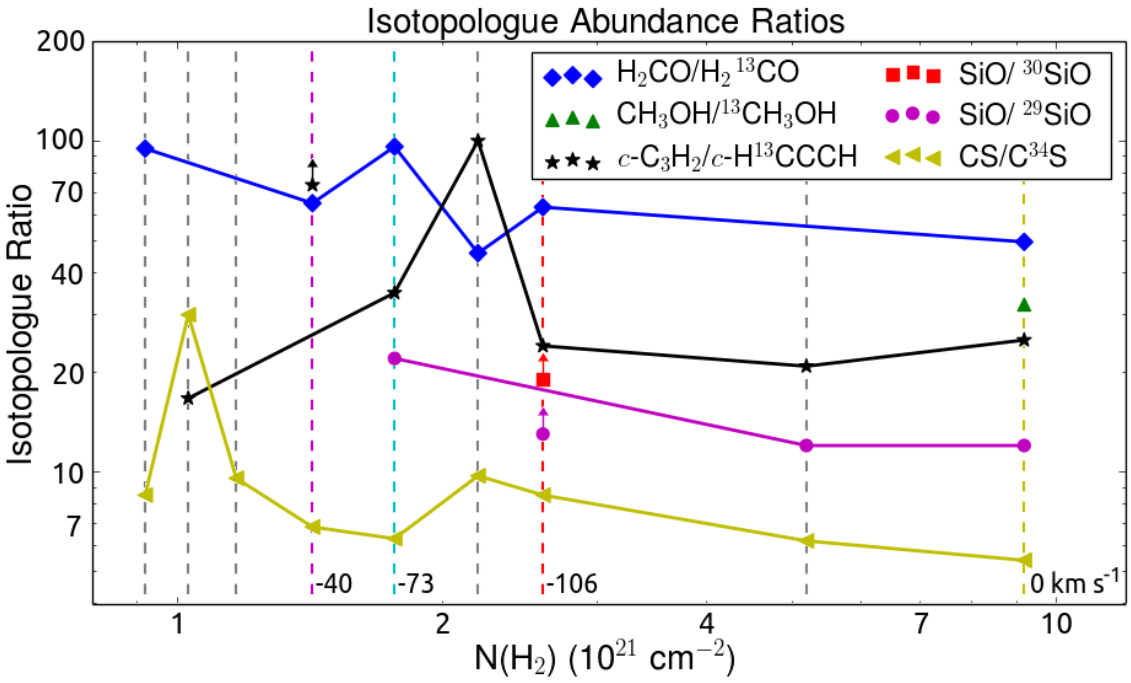

Fig. 5.14 – Isotopologue abundance ratios. In order from lowest to highest hydrogen column, the -80, -92, -47, -40, -73, -23, -106, +20, and $\sim$0 km s^{-1} components are marked with vertical dashed lines.

the measured isotopologue ratio ranges from 5 to 10. No trend is evident with hydrogen column or with Galactocentric distance. Within the components with optically thick CS absorption (with peak $\tau > 0.7$), in which the measured isotopologue ratio may be depressed from the true value, we obtain measurements ranging from 5.4 to 8.5. In components with lower optical depths (of τ <0.5) in the CS (1-0) line, values of $\lesssim$10 are observed. In the -92 km s^{-1} component, we obtain CS/C^{34}S = 30, and it is unclear why this component is anomolous.

5.3 Cloud Hydrogen Columns: Considerations for Interpreting Abundances

We have obtained new measurements on the hydrogen columns within each cloud in the line-of-sight to Sgr B2, and on abundances of more than a dozen molecules and their isotopologues. Before discussing the molecular abundances, we explore the validity of using c-C_3H_2 as a proxy for H_2 and other preliminaries required for intrepreting the abundance measurements.

5.3.1 Molecular Hydrogen Columns by Conversion from c-C_3H_2

The hydrogen columns estimated by conversion from c-C_3H_2 column densities are, for most clouds, similar to previous estimates made in the line-of-sight towards Sgr B2(M) (Table 5.3). To the best of our knowledge, molecular hydrogen columns within diffuse and translucent clouds have not previously been estimated by conversion from $N_{c\text{-}C_3H_2}$. We propose that this is a more direct and accurate method of estimating the hydrogen column, and discuss the possible limitations of this method. In previous studies of diffuse and translucent clouds, hydrogen column estimates have been made assuming a constant

abundance of either CO or HCO^+ (Greaves & Nyman 1996; Irvine et al. 1987). However, due to the high optical depths of transitions of CO and HCO^+, the column densities of the ^{12}C isotopologues are estimated by conversion from ^{13}CO or $H^{13}CO^+$. Previous authors have assumed differing ratios of $^{12}C/^{13}C$ isotopologues internal to the Galactic Center, Bar and disk. This is dangerous for numerous reasons, including that some of the clouds have poorly constrained Galactocentric distances. These methods require two assumed conversion factors, and each conversion introduces substantial error. As is clear from our observations of isotopologues (Figure 5.14), significant variation occurs in the isotopologue ratios in different clouds, and for many molecules, these cannot be accounted for by the Galactocentric distances presumed. Furthermore, it is known that isotope fractionation occurs, creating discrepancies between the true isotope ratios (i.e. $^{12}C/^{13}C$) and the isotopologue ratios (i.e. $^{12}CO/^{13}CO$ and $H^{12}CO^+/H^{13}CO^+$). Also, while it may be safe to assume a constant abundance of HCO^+ with respect to H_2, the assumption of a constant CO abundance is easily contested in diffuse and translucent gas, given a growing body of evidence suggesting the presence of CO-dark molecular gas in UV-irradiated environments (see e.g. Wolfire et al. 2010), and evidence that N_{CO}/N_{H_2} varies by a factor of $>$100 in diffuse and translucent clouds (Sonnentrucker et al. 2007). Thus, the assumptions required for estimating the molecular hydrogen column by conversion from CO and/or HCO^+ are not supported by observations.

Conversion from c-C_3H_2 is more direct, as it utilizes optically thin transitions of a molecule that has been systematically explored in diffuse and translucent clouds (e.g. Liszt et al. 2012) and does not require an isotope ratio conversion. In addition to having a stable abundance in diffuse and translucent clouds, c-C_3H_2 is observed to have precisely the same abundance with respect to molecular hydrogen in the dense ($n \sim 10^5$ cm^{-3}) Horsehead PDR (Pety et al. 2005), indicating that the value of N(c-C_3H_2)/N(H_2) may be highly

stable in UV-irradiated gas over a wide range of temperatures and densities. The primary limitation to this method of conversion results from the fact that the constant abundance of c-C_3H_2 was established in diffuse gas in the Galactic spiral arms and has not been sufficiently tested in the Galactic Bar or Center where CR-ionization rates and X-ray flux are elevated. Nonetheless, this appears to be the best means of determining the hydrogen column at our disposal, and we recommend further exploration of abundance patterns of c-C_3H_2 via observations and modeling.

5.3.2 Defining Cloud Borders

We also point out differences in how we distinguish between clouds. In the previous studies, authors have combined multiple cloud components for hydrogen column and molecular abundance estimates. For example, the clouds at -47 and -40 $\mathrm{km\,s^{-1}}$ were treated as a single cloud in analyses by previous authors (Irvine et al. 1987; Greaves & Nyman 1996; Wirström et al. 2010). As the -47 and -40 $\mathrm{km\,s^{-1}}$ clouds have demonstrable differences in molecular abundances, for example in the abundance of CS, we treat these systems as distinct. For the purpose of follow-up studies of the chemistry within these environments, we consider it prudent to treat the clouds as specifically as is possible rather than present average abundance values which may not be representative of any environment in the cloud. In this vein, we might consider dividing the clouds further. For example, the -40 $\mathrm{km\,s^{-1}}$ cloud contains two narrow velocity components that are clearly resolvable in CS absorption. However, for many of the lower signal-to-noise transitions, particularly of the COMs and low-abundance CS-bearing species, we do not have the signal-to-noise required to distinguish the two components. Thus, we have maximized the specificity with which we may treat individual clouds.

Finally, it is standard to interpret a hydrogen column as an extinction value, with A_V=

1 corresponding to

$$N_{HI} + 2\,N_{H2} = 2.2 \times 10^{21}\ \mathrm{cm}^{-2}$$

(Güver & Özel 2009). Obviously, the implied extinction values will vary depending on where the clouds are distinguished. For example, if the -47 and -40 $\mathrm{km\,s^{-1}}$ clouds are adjacent and do not contain UV-radiation sources located between the two clouds, then it is, indeed, physically appropriate to treat the two clouds as a combined system with a higher extinction. However, we know little about the three-dimensional geometry of the clouds and incident radiative fields. In fact, substantial differences may occur in the incident UV radiation field depending on the Galactocentric distance and on the precise local environment of the cloud, so that two clouds with similar hydrogen columns may experience very different radiative fields at their centers. Secondly, cosmic rays, known to be multiple orders of magnitude more prevalent in diffuse clouds the Galactic Center (Le Petit et al. 2016), may induce local UV-radiation fields very deep within the cloud, and X-rays which are particularly prevalent in the Galactic Center can penetrate the diffuse and translucent clouds (Amo-Baladrón et al. 2009). Finally, the geometry and structure of the diffuse and translucent ISM can significantly affect the radiative field experienced within the cloud. Thus, we do not put much emphasis on the total hydrogen column as a determinant of the chemistry observed within the clouds, and indeed we do not observe significant trends with total hydrogen column in Figures 5.10 - 5.12. Instead, we point out differences between clouds located internal and external to the Galactic Center and Galactic Bar, and look for clues to the structure of different clouds.

Translucent clouds are typically defined as systems with central extinction values of $1 < A_V < 2.5$. Most of the clouds, as divided in this work, do not meet this definition, having central extinction values of 0.5 to 1.0 (Table 5.3). This clearly depends on how the clouds are binned, however we point out that most of the clouds considered here are intermediate

between diffuse clouds and translucent clouds as defined by this extinction threshold, and are likely transitional regions.

5.4 Discussion of Isotopologue Ratios and Fractionation

The observed isotopologue ratios of H_2CO and c-C_3H_2 suggest systematic differences between the two. Therefore, it is clear that isotope fractionation is present for at least one of the species. While isotope ratios of c-C_3H_2 have not been studied closely, models by Langer et al. (1984) indicate fractionation occurs for the $H_2CO/H_2^{13}CO$ ratio, such that this provides an upper limit to $^{12}C/^{13}C$, while the $^{12}CO/^{13}CO$ ratio provides a lower limit. Extensive studies of the $^{12}C/^{13}C$ ratio have been published using isotopologues of CO, H_2CO, CN, and CH^+ (Wilson 1999; Wilson & Rood 1994; Stahl et al. 2008; Milam et al. 2005). While the studies show definitive evidence for variation in different sources of the same galactocentric distance, a general trend of increasing $^{12}C/^{13}C$ ratios with increasing Galactocentric distance D_{GC} is well established, with typical values of $\sim$20 in the Galactic Center, $\sim$50 at a Galactocentric distance of 4 kpc, and $\sim$70 at the solar Galactocentric distance. The ratios measured by $H_2CO/H_2^{13}CO$ in this data are significantly larger than these values and do not show any trend with Galactocentric distance, but do show substantial variation. The ratios measured by c-C_3H_2/c-$H^{13}CCCH$, namely $\sim$20 in the Galactic Center, 35 at $\lesssim$1 kpc, 75 at 3 kpc, and 100 at 4 kpc, show a very clear trend with Galactocentric distance, and are mostly similar to the previous measurements of $^{12}C/^{13}C$ ratios.

The isotope ratio of $^{32}S/^{34}S$ has been investigated (Frerking et al. 1980; Chin et al. 1996; Mauersberger et al. 1996) as well, but is not as thoroughly researched as the carbon isotope ratio, and disagreement persists over what trends are present with Galactocentric distance. These authors obtained values of 24.4 ± 5, whereas we observe substantially lower values of $5 < CS/C^{34}S < 10$ for all clouds with the exception of the -92 $km\,s^{-1}$ cloud, which

has a higher value of 30. Generally, chemical fractionation is not believed to affect sulfur chemistry substantially, as the zero point energies of ^{32}S and ^{34}S are quite similar.

Finally, the ratios of ^{28}Si/^{29}Si and ^{29}Si/^{30}Si have not been systematically investigated in the Galaxy. In the $\sim$0 and +25 km s^{-1} material, we obtain ^{28}SiO/^{29}SiO = 12, and at -73, we obtain a higher value of 22. Additionally, we measure ^{29}SiO/^{30}SiO = 1.6. Within the solar system, a value of ^{28}Si/^{29}Si= 19.7 is observed (Wilson 1999; Penzias 1981). Assuming that chemical fractionation does not significantly affect the SiO isotopoluges, our data indicates that the ^{28}Si/^{29}Si in the -73 km s^{-1} cloud is consistent with the local value, while ^{29}Si is enhanced relative to the main isotope in the $\sim$0 and +25 km s^{-1} material located in the Galactic Center. Additionally, early investigations of ^{29}Si/^{30}Si have determined values of 1.5 without a gradient with galactocentric distance (Penzias 1981; Huettemeister et al. 1998). The measured value of ^{29}Si/^{30}Si in the -106 km s^{-1} gas is consistent with this, supporting the supposition that the value of ^{29}Si/^{30}Si does not systematically vary with Galactocentric distance.

Given these observations, a few trends can be pointed out. First, $H_2CO/H_2^{13}CO$ is not a good probe of the ^{12}C/^{13}C ratio, and includes significant fractionation. If the fractionation can be understood, this may be interesting from a chemistry perspective. Secondly, ^{34}S is substantially enhanced in the clouds measured here compared to previous measurements in other clouds, assuming that CS/C^{34}S does not undergo fractionation. Finally, we notice that the -73 km s^{-1} material has values of c-C_3H_2/c-H^{13}CCCH and ^{28}Si/^{29}Si that are intermediate between those observed in Galactic Center clouds and those of clouds located external to the Galactic disk. This is consistent with the -73 km s^{-1} material being located external to the Galactic Center and in the Bar.

5.5 Discussion of Molecular Abundances and Implications for Cloud Structure

5.5.1 Sulfur-bearing Chemistry: CS, SO, HCS^+, CCS, and H_2CS

Clearly, diverse sulfur-bearing chemistry is observed within the diffuse and translucent clouds. The abundances of a few of the sulfur-bearing molecules detected here have been investigated in previous studies of diffuse and translucent clouds, most recenty by Lucas & Liszt (2002) and Neufeld et al. (2015). Lucas & Liszt (2002) measured the abundances of CS, SO, and HCS^+ in diffuse clouds absorbing against extragalactic point sources at high Galactic latitude, while Neufeld et al. (2015) measured the abundances of CS and SO in diffuse and translucent clouds in the Galactic plane. In this section, we discuss our observational results in frequent reference to these two papers. Additionally, Drdla et al. (1989) reported abundance measurements of CS and HCS^+ in diffuse and/or translucent clouds at high Galactic latitude, and contributed the most comprehensive theoretical model predictions for sulfur-bearing molecule abundances in diffuse clouds published to date.

In the following discussion, we come to the following main conclusions on sulfur-bearing chemistry based on the data shown here and in the context of these papers. First, in clouds in the Galactic disk, we find that CS, and likely SO to a lesser degree, preferentially inhabit the highest density regions of the diffuse and translucent clouds, with true abundance enhancements in high density material. Secondly, whereas the abundances of CS and HCS^+ are predicted to be closesly coupled (Drdla et al. 1989; Lucas & Liszt 2002), we do not observe this and our abundance ratios of CS:HCS^+ disagree with the observations of Lucas & Liszt (2002) and Neufeld et al. (2015). Third, SO and H_2CS are severely overabundant as compared to model predictions (Drdla et al. 1989), and model predictions for CCS in diffuse and translucent clouds have not been published. With the wealth of data

published, and with recent advances in chemical models, we suggest the sulfur-bearing chemistry in diffuse clouds should be revisited.

CS: Abundances and Implications for Cloud Structure

Our reported CS abundances vary by more than an order of magnitude, with a median of 1.6×10^{-8}. Thus, CS has a high abundance in this material as compared to most interstellar environments; the median value is similar to the abundances observed in the hot core in Sgr B2(N) and in the Orion Molecular Ridge (Neill et al. 2014; Crockett et al. 2014) and a factor of two to three times higher than in the dense Horsehead PDR (Goicoechea et al. 2006) and the dark cloud TMC-1 (Ohishi et al. 1992). While the measurements presented here are in excellent agreement with values reported by Greaves & Nyman (1996) in the line-of-sight to Sgr B2(M), the CS abundances in the sightlines to Sgr B2(N) and (M) are significantly larger than those reported in other sightlines by Lucas & Liszt (2002) and Neufeld et al. (2015). In both latter papers, the authors derived abundances that typically ranged from 1 to 5 $\times 10^{-9}$, although one of the ten clouds measured by Neufeld et al. (2015) was larger, at 10^{-8}. While Lucas & Liszt (2002) obtained significantly lower values than we measure, they noted that the CS abundance appears sporadic in the diffuse clouds; in some clouds with significant column densities of HCO^+, and presumably therefore of H_2, CS was undetected, whereas it was clearly detected in other clouds with lower HCO^+ columns. In the data presented here, by Lucas & Liszt (2002), and by Neufeld et al. (2015), the abundance of CS does not appear to scale with the total molecular or neutral hydrogen column. Additionally, we do not observe systematically higher or lower abundances in the Galactic Center/Bar clouds compared to disk clouds.

While there is no clear differentiation between Galactic Center/Bar clouds and disk clouds based on the CS abundance values observed, there is an apparent distinction be-

tween the shapes of the CS profiles in Galactic Center clouds compared to disk clouds. As described in Section 5.2.1 the CS absorption in Galactic Centar/Bar clouds, for example at -106, -73, and 0 $\mathrm{km\,s^{-1}}$, includes absorption over the same moderately broad velocity ranges as do c-C_3H_2 and H_2CO. On the other hand, the profile of CS contains very sharp, narrow peaks in the clouds located external to the Galactic Bar, namely in the -47 and -40 $\mathrm{km\,s^{-1}}$ clouds believed to be located in the 3-kpc arm at the outer edge of the Bar and in the -23 $\mathrm{km\,s^{-1}}$ cloud. This suggests that CS is highly sensitive to the physical conditions within the clouds, and may indicate a systematic difference in the structure of clouds that are located in the Galactic Center compared to those present in the disk.

In the Galactic disk clouds, where CS contains narrow peaks with little broad component absorption as compared to c-C_3H_2 and H_2CO, we suggest that CS is significantly more abundant in the highest density regions of the cloud. While chemical models notoriously underpredict abundances of sulfur-bearing species in the diffuse ISM, the known reactions can achieve higher CS abundances at higher physical densities and/or higher visual extinctions (see e.g. Lucas & Liszt 2002; Neufeld et al. 2015, and references therein). However, as the total hydrogen column has been shown to be a poor predictor of the CS column density and abundance in the data presented here, in Lucas & Liszt (2002), and in Neufeld et al. (2015), it appears that the CS abundance is more sensitive to density conditions than to extinction in the diffuse and translucent medium. This claim is also supported by previous observations; the work of Greaves et al. (1992) suggests that CS resides in material that is significantly more dense than average in the line-of-sight to Sgr B2(M). While the mean densities in the clouds appear to be $n \sim 300$ to 500 $\mathrm{cm^{-3}}$, CS resides in material with densities of $4000 \lesssim n \lesssim 15\,000$ $\mathrm{cm^{-3}}$ as estimated by a Large Velocity Gradient (LVG) analysis of CS (1-0) and (2-1).

This result suggests that the diffuse and translucent clouds contain a significant amount

of structure. The CS observations cannot be accounted for by a gradual density enhancement with A_V, indicating a greater degree of clumping than previously assumed.

SO

The absorption profile of SO suggests that it too has an enhanced abundance in the highest density regions in the -47, -40, and -23 $\mathrm{km\,s^{-1}}$ clouds, with narrow peaks dominating the absorption in the -47 and -40 $\mathrm{km\,s^{-1}}$ clouds especially. The abundance of SO shows a positive linear correlation with the CS abundance but does not vary as much as CS does (Figure 5.13). Therefore the SO abundance may be enhanced, but by a lower factor than CS, in the highest density regions. Lucas & Liszt (2002) also found a positive but loose correlation between SO and CS in diffuse gas.

The SO abundances, with a median value of 1.4×10^{-9}, are similar to those measured by Lucas & Liszt (2002) and Neufeld et al. (2015). Lucas & Liszt (2002) notes that gas phase models of sulfur-bearing chemistry underpredict this value by multiple orders of magnitude. Even upon considering shocks and turbulence dissipation, models underpredict the SO abundance by an order of magnitude (Neufeld et al. 2015). Because the abundances of CS are significantly higher in clouds along the sightline to Sgr B2(N), we obtain significantly larger values of the ratio N_{CS}/N_{SO} than do Lucas & Liszt (2002) and Neufeld et al. (2015). In most clouds, these authors had found that $N_{CS}/N_{SO} = 2$, although a higher value of 5.8 was present in the cloud with the anomolously high CS abundance, mentioned above, in Neufeld et al. (2015). We obtain values of N_{CS}/N_{SO} ranging from 3 to $\sim$50, with a median value of 7. Ratios of N_{CS}/N_{SO} have been observed to vary significantly in different clouds; even in clouds in similar evolutionary states and with apparently similar conditions, very different values may be observed (e.g. Gerin et al. 1997).

HCS^+, CCS, and H_2CS

Among the lower abundance CS-bearing species the results demonstrate a positive linear correlation between the abundances of CCS and H_2CS with CS (Figure 5.13), although scatter exists, due in part to baseline instability and line confusion in the lower signal transitions. On the other hand, HCS^+ displays a different abundance pattern, with a consistent abundance in all clouds except for the -40 $km\,s^{-1}$ cloud. While observation of additional transitions of HCS^+ should be conducted to confirm this trend, the depressed abundance of HCS^+ in the -40 $km\,s^{-1}$ cloud is notable because all other sulfur-bearing species have higher abundances in this cloud than in any other. If a larger fraction of the -40 $km\,s^{-1}$ cloud consists of higher density material, it may be that the HCS^+ abundance is lower in the highest density regions of diffuse and translucent clouds. The abundance patterns thus suggest that the ratios of N_{HCS^+}/N_{CS}, N_{HCS^+}/N_{CCS}, and N_{HCS^+}/N_{H_2CS} appear to be sensitive to cloud conditions within diffuse and translucent clouds, making these ratios potentially useful probes of physical conditions. Although in a distinct environment, Corby et al. (2015) observed that CS, CCS, and H_2CS have indistinguishable spatial distributions in Sgr B2, while HCS^+ has a distinct spatial distribution, further supporting the trend that CS, CCS, and H_2CS track each other, and that the ratios of HCS^+ to other CS-bearing species are sensitive to physical conditions.

According to chemical models, the molecules HCS^+ and CS are among the most closely related species present in the ISM, as they participate in a direct exchange in both the formation and destruction of CS (Drdla et al. 1989; Lucas & Liszt 2002). In the reaction network considered by Drdla et al. (1989) and Lucas & Liszt (2002), CS is believed to be formed primarily from the dissociative recombination reaction of

$$HCS^+ + e^- \rightarrow CS + H, \tag{5.3}$$

where HCS^+ is first formed by reactions beginning with S^+. Three mechanisms dominate the destruction of CS in these networks. In the first two, photoionization and ion-exchange reactions destroy CS to form CS^+, by

$$CS + \gamma \rightarrow CS^+ \tag{5.4}$$

and

$$CS + X^+ \rightarrow CS^+ + X, \tag{5.5}$$

where X^+ is a cationic species and X is the corresponding neutral species. CS^+ then quickly reacts to form HCS^+:

$$CS^+ + H_2 \rightarrow HCS^+ + H \tag{5.6}$$

In the third destruction route, CS reacts with H_3^+ to form HCS^+ directly:

$$CS + H_3^+ \rightarrow HCS^+ + H_2. \tag{5.7}$$

As CS is formed by a reaction of HCS^+ and all dominant destruction pathways for CS form HCS^+, we would expect the abundances of CS and HCS^+ to be delicately balanced, and for the two abundances to track each other. While chemical models of sulfur-bearing chemistry in diffuse clouds underpredict the abundance of HCS^+ by multiple orders of magnitude, Lucas & Liszt (2002) determined that if the observed abundance of HCS^+ is injected into a diffuse cloud, it is possible to account for the CS abundances observed in their sample, further emphasizing the theoretical importance of N_{CS}/N_{HCS^+}. In clouds in the Galactic Center, where H_3^+ is $\gtrsim 10$ times more abundant compared to diffuse clouds in the disk (Oka et al. 2005), we might expect an offset in the ratio, tending towards a higher

relative abundance of HCS^+.

In stark contrast to this, the abundance of HCS^+ appears to be uncorrelated with that of CS. HCS^+ exhibits an exceptionally consistent abundance of 3×10^{-10} in this study, and this value perfectly matches the measurements made in the diffuse clouds sampled by Lucas & Liszt (2002). On the other hand, we observe very large variations in CS abundances, by a factor of $\gtrsim 10$ in our study and $\gtrsim 30$ if we also consider the measurements made by Lucas & Liszt (2002) and Neufeld et al. (2015). Furthermore, instead of observing more HCS^+ relative to CS in the Galactic Center clouds due to the higher abundance of H_3^+, we see the opposite. Whereas Lucas & Liszt (2002) measured N_{CS}/N_{HCS^+} = 13.3 $\pm$ 1.0 in diffuse clouds in the Galactic disk, we find much higher values (and therefore lower HCS^+ abundances relative to CS) ranging from 50 to 65 in most Galactic Center/Bar clouds. The constancy of the HCS^+ abundance in clouds measured in this study and in Lucas & Liszt (2002) indicates that the HCS^+ abundance is (1) consistent over a wide range of densities and extinction values, (2) independent of the CS abundance, and (3) independent of the Galactocentric distance. As the same values are measured in absorbing clouds in the Galactic disk as in the Galactic Center and Bar, it appears that the HCS^+ abundance is not highly sensitive to the CR-ionization rate or X-ray fluxes in diffuse gas.

CCS and H_2CS have similar abundances to HCS^+, of (1-3) $\times 10^{-10}$, and like HCS^+, these are also significantly more abundant than predicted by models appropriate in diffuse, translucent, and/or any other UV-irradiated material (e.g. Drdla et al. 1989; Goicoechea et al. 2006). In fact, the observed enhancement of H_2CS is five orders of magnitude larger than predicted by Drdla et al. (1989), and no prediction was published for CCS. With the recent observational constraints on sulfur-bearing chemistry in diffuse and translucent clouds provided here, in Lucas & Liszt (2002), and Neufeld et al. (2015), and in dense PDRs (Goicoechea et al. 2006), a revised theoretical treatment of sulfur-bearing chemistry,

and particularly of CS-bearing chemistry, is warrented. Certainly, advances in the theory of turbulence chemistry, PDR chemistry, and gas phase and grain surface reaction networks could prove effective for reproducing the observed chemistry. More importantly, a thorough theoretical treatment of the sulfur-bearing chemistry may illuminate the patterns embedded in the varying abundance ratios, producing a more nuanced understanding of what the chemistry tells us about the physical and radiative structure of the diffuse and translucent ISM. For example, the ratio of $N_{\rm CS}$ to $N_{\rm HCS^+}$ may prove an excellent probe of physical conditions, however a solid theoretical understanding of the reaction networks is requisite for interpreting the ratios.

5.5.2 Oxygen-bearing Chemistry: OH, H_2CO, and SiO

Interpreting OH Absorption

OH has four hyperfine transitions in the ($^2\Pi_{3/2}$ $J = \frac{3}{2}$) state, at 1612, 1665, 1667, and 1720 MHz. All four transitions can exhibit masing, typically in very high density ($10^6 \leq n \lesssim 10^9$ cm^{-3}) environments (Gray et al. 1991; Elitzur 1992) associated with star formation, shocks, and AGB winds. Under lower density conditions in which strong masing is not produced, thermal absorption or emission line profiles are observed. However, to the best of our knowledge, there have been no reported observations in which the four hyperfine transitions are in LTE. Instead, recent work by Ebisawa et al. (2015) has demonstrated that non-LTE excitation of the ground state hyperfine transitions of OH are ubiquitous in clouds that do not host strong masing, including a translucent cloud, a cold dark cloud, and a PDR, and additional reports of similar behaviors have been reported commonly (see references in Ebisawa et al. 2015), although the reported instances tend to involve emission line sources. Whereas the 1665 and 1667 MHz transitions produce emission that is more consistent with LTE conditions over a wider range of physical con-

ditions, the 1612 MHz component appears in absorption against the CMB background and enhanced emission is present in the 1720 MHz linet (Ebisawa et al. 2015). The divergence from LTE occurs by a collisional excitation mechanism, even at very low physical densities of $\sim$10 cm^{-3} (Elitzur 1992).

In §5.2.4, we described that the 1665 MHz and 1667 MHz transitions have very consistent absorption profiles, with primarily broad (Δv $\geq$ 10 km s^{-1}) absorption components, resulting in statistically identical OH column density measurements. However, the profile of the 1612 MHz transition is clearly different, as are the column density values measured using the 1612 MHz transition. The discrepancy between the measured values indicates that a non-LTE excitation effect is present for OH in diffuse clouds. The 1665 and 1667 MHz transitions should better represent the true kinematic distribution and column density of OH, and we thus exclude the 1612 MHz profile from further discussion.

OH is the only molecule observed in the PRIMOS data that is more typically present in the most diffuse gas of the CNM and in the WNM than in the higher density regions. It is formed through warm temperature chemistry which can occur efficiently under conditions of shocks and turbulence dissipation (see e.g. Godard et al. 2009, 2014, and references therein). Turbulence dissipation in particular is believed to significantly impact the chemistry observed in the CNM, with periodic episodes of turbulence dissipation injecting significant amounts of high-temperature molecules into the CNM (Godard et al. 2009). Under the denser, darker, cooler, and less turbulent conditions of the embedded translucent cloud material, OH should not be formed efficiently, and the reactive radical species should be destroyed efficiently.

As expected from this, the OH absorption profiles at 1665 and 1667 MHz are more similar to those of small hydride molecules observed with Herschel (e.g. Godard et al. 2012; Indriolo et al. 2015) than to other absorption profiles observed in the PRIMOS data.

Comparing the profiles of OH and c-C_3H_2 (Figure 1), it is apparent that OH is present in more diffuse material than c-C_3H_2. If c-C_3H_2 indeed traces H_2 even at very low extinction (Liszt et al. 2012), this implies that OH is present in material in which there is not sufficient H_2 self-shielding to yield a high molecular hydrogen fraction. Furthermore, the OH absorption profiles indicate that OH is less abundant in the regions of enhanced density. This is evident as the profiles do contain significant optical depths within the narrow peaks corresponding to the enhanced c-C_3H_2 absorption.

Finally, we comment on the values of N_{OH}/N_{H_2} derived. We determine a median value of N_{OH}/N_{H_2} = 1.5 $\times 10^{-6}$. In the line of sight to Sgr A, Karlsson et al. (2013) found similar but slightly higher values of 1.8 to 5.8 $\times 10^{-6}$ in line-of-sight clouds associated with the same structures that we observe, namely in the EMR (at -130 to -95 km s^{-1} in our data), the 3-kpc arm (at $\sim$40 km s^{-1} towards Sgr B2), and in the 0 km s^{-1} gas. The values reported here and by Karlsson et al. (2013) are significantly larger than those observed in diffuse and translucent gas towards other sightlines however, with values ranging from 5×10^{-8} to 2×10^{-7} observed towards W51 and W49N (Neufeld et al. 2002; Wiesemeyer et al. 2003). If we consider the abundance with respect to the total hydrogen column by $N_H = N_{HI} + 2\,N_{H_2}$, adopting the HI column densities published in Indriolo et al. (2015), we obtain typical values of 4 to 6 $\times 10^{-7}$.

While it is not appropriate to adopt the values of N_{OH}/N_{H_2} in Table 5.4 as true abundances, as OH primarily occupies a different phase of the ISM than the c-C_3H_2 from which N_{H_2} was estimated, we include the values as they likely have physical significance. Lower than average values may indicate that a cloud is more dominated by translucent material as opposed to diffuse material. Notably, lower than average values are observed in the -106, -73, -40, and 0 km s^{-1} , where translucent clouds are particularly prominent and complex organic species are present.

H_2CO

Excluding OH, formaldehyde is the most abundant species measured in this work, at typical levels of a few $\times$ 10^{-7}. This is significantly higher, by nearly two orders of magnitude, compared to measurements in high latitude cirrus clouds and diffuse clouds (Turner 1993; Liszt et al. 2006). With respect to different interstellar environments, these abundances are very high, comparable to those observed in the Orion hot core and molecular ridge (Neill et al. 2014), and two and four orders of magnitude, respectively, larger than what is observed in the dark clouds TMC-1 and in the Horsehead PDR (Ohishi & Kaifu 1998; Guzmán et al. 2014).

The abundance of H_2CO varies by a factor of $\sim$4 within the observed clouds. The abundance does not exhibit an apparent correlation with $N_{c\text{-}C_3H_2}$, however H_2CO exhibits a positive linear correlation with the observed abundance of CS (Figure 5.13). Liszt et al. (2006) has demonstrated that the abundances of H_2CO and CS are tightly correlated, while H_2CO is not correlated with hydrocarbons like c-C_3H_2. Once again, the abundance ratios that we observe in the line-of-sight clouds to Sgr B2 are different than what has been reported in other sightlines; whereas N_{H_2CO}/N_{CS} was measured to be approximately 2-3 by Liszt et al. (2006), we obtain higher values of $\sim$20. From comparing the profiles of H_2CO and CS, it is unclear why the two species should correlate well. Whereas CS appears to prefer higher density regions of the diffuse clouds, the absorption profile of H_2CO includes moderately broad absorption components indicating that H_2CO is likely abundant in a larger fraction of the cloud volume. Additionally, it is entirely unclear from a chemistry viewpoint; whereas CS is believed to form in the gas phase, H_2CO is typically believed to form on grain surfaces, and grain surface processes have not typically been implicated in diffuse cloud chemistry, as ice mantles should not form under the low extinction, low density, and warm temperature conditions present. Furthermore, H_2CO is not predicted to

be nearly as abundant as observed under low extinction conditions due to photodissociation (Liszt et al. 2006).

SiO

Abundances of SiO in the line-of-sight to Sgr B2(M) have been measured by Greaves & Nyman (1996), and abundance patterns in the sightlines to Sgr B2(M) and W49 N were discussed by Greaves et al. (1996). In the line-of-sight towards Sgr B2(M), values measured by Greaves & Nyman (1996) varied by an order of magnitude, from 3×10^{-10} in the -40 km s^{-1} cloud, to 2 and 3×10^{-9} in the -106 and -75 km s^{-1} clouds, respectively. In our data, we observe values in a similar range, of $<2.5 \times 10^{-10}$ to 2.0×10^{-9}. We observe lower values in clouds located closer to the Galactic disk, namely 4 to 6 $\times 10^{-10}$ in the -40 and -23 km s^{-1} clouds, and higher values of 1.5 to 2 $\times 10^{-9}$ in the -73, 0, and +25 km s^{-1} clouds located in the Galactic Bar and Center. We observe a very low value in the -58 km s^{-1} cloud, which is surprising because this is believed to be located internal to the Galactic Bar or Center.

The profile of SiO may also hold clues to the nature of the gas in which SiO is most abundant. The absorbing components at -73, -40, and -23 km s^{-1} in particular appear to be broader and more smoothly varying than in profiles of most other molecules. The profile does not contain the narrow absorption features present in the profiles of most other species observed in this study, and particularly of CS and SO. Therefore, it does not appear that SiO is enhanced in the densest material. The components of SiO may be shock broadened and SiO may be abundant only in recently shocked material. In this scenario, SiO could be confined to a small spatial region on a shock front, or could be spatially extended perhaps occupying gas with more recent episodes of turbulence, which is believed to be important in the diffuse ISM (Godard et al. 2009). Alternatively, the SiO abundance could be governed

more directly by the X-ray or CR flux in the medium, and the species may inhabit more diffuse conditions than most molecules observed in this study.

A deeper investigation of the formation and destruction of SiO in diffuse clouds could help elucidate the structure of the diffuse clouds. For instance, if the SiO abundance is most directly governed by shocks in these environments, then this data may indicate that the high density clumps in which CS and SO are abundant are not subjected to the shocks associated with turbulence dissipation, and tend to be undisrupted within a turbulent medium. This would put a limit on the size scales of the clumps and could advance our understanding of the turbulence.

5.5.3 Linear Hydrocarbons: *l*-C_3H and *l*-C_3H^+

The linear hydrocarbon species *l*-C_3H has been a known interstellar molecule for three decades, and is present in multiple distinct environments including evolved stars (Thaddeus et al. 1985; Pardo & Cernicharo 2007), dark clouds (Thaddeus et al. 1985), and PDRs (Pety et al. 2012). The cation of this species, *l*-C_3H^+, was first detected much more recently, by Pety et al. (2012) in the Horsehead PDR. Whereas most molecules observed in the PDR, including *l*-C_3H (Pety et al. 2012), are also detected in a dense, UV-shielded core in the Horsehead nebula (e.g. Guzmán et al. 2014), *l*-C_3H^+ was not observed towards the core, providing the first indication that it is abundant only in the presence of far-UV radiation. Since the initial detection, *l*-C_3H^+ has also been detected in the Orion Bar PDR (McGuire et al. 2014b) and in material in Sgr B2 (McGuire et al. 2013) that likely contains a high UV and X-ray flux (Corby et al. 2015; Goicoechea et al. 2003). Additionally, *l*-C_3H^+ has been rigorously detected in three other PDR sources, and it is tentatively detected in two additional PDRs (B. McGuire 2015, private communication). Despite a search for *l*-C_3H^+ towards 35 additional sources including hot cores, hot corinos, and evolved stars,

the species was not detected (McGuire et al. 2014a,b). Thus, l-C_3H^+ appears to be an excellent indicator of a PDR environment.

Although the profile of l-C_3H is difficult to interpret due to the presence of hyperfine structure, line confusion, and weak signal, we determine reasonably consistent l-C_3H abundances of 2 to 4 $\times 10^{-10}$. These values are slightly higher than the observed values in the Horsehead PDR of $(1.4 \pm 0.7) \times 10^{-10}$. Adopting the l-C_3H column derived in Sgr B2(N) (McGuire et al. 2013) and the molecular hydrogen column derived in Appendix A of Quan et al. (2016), a similar value of (1-2) $\times 10^{-10}$ is present in the PDR/XDR material in Sgr B2(N).

Measured l-C_3H^+ abundances in this work range from 4 to 14 $\times 10^{-11}$, although they have considerable uncertainties of about a factor of 2 given the weak signal and the presence of line blending. These values are slightly higher than in the Horsehead PDR (3×10^{-11}) and in Sgr B2 (2 to 3×10^{-11}). For most clouds with measured abundances of both l-C_3H and l-C_3H^+ in this survey, the ratio of l-C_3H/l-C_3H^+ ranges from $\sim$3 to 4. The ratios are therefore quite similar to the value of $\sim$4 observed in the Horsehead PDR, and slightly lower than the value of $\sim$6 observed in the PDR/XDR gas in Sgr B2. We also note that the absorbing components of l-C_3H^+ are, like in the profile of SiO, broader than observed in the profiles of most other species in this study. While the weak signal may contribute to this effect, it may be that l-C_3H^+ is more spatially extended than most species observed here, preferentially populating the more diffuse material rather than the embedded clumps. This would be expected if l-C_3H^+ is formed only in the presence of a strong far-UV field.

While PDR chemistry does a poor job of accounting for the abundances of most molecules observed in the diffuse ISM (e.g. Godard et al. 2009, 2014), it will be interesting to determine whether PDR conditions can account for the observed abundances of these two linear hydrocarbon species, and to explore the effect of turbulence on the molecules. Pety et al.

(2012) was able to reproduce the observed abundances of both species in the Horsehead PDR using a PDR model with conditions appropriate in that environment. While the mean densities are much lower in the diffuse and translucent clouds considered here, it is plausible that the observed abundances of *l*-C_3H and *l*-C_3H^+ may also be consistent with PDR model predictions. A more recent study of the molecules suggests that they are formed from the photo-destruction of PAHs, with *l*-C_3H^+ being an intermediate to the formation of *l*-C_3H (Guzmán et al. 2015). As it is well established that PAHs are prevalent in the diffuse ISM, the abundances of *l*-C_3H and *l*-C_3H^+ should not be sensitive to the gas density, and rather should be sensitive to PAH abundances and the UV field within the cloud.

5.6 Complex Organic Molecule Abundances and Implications for Cloud Structure

5.6.1 CH_3OH

First, it is surprising to see emission in the 36 GHz class I maser line by material at $\sim$3 km s^{-1}. Maser emission has never been associated with diffuse or translucent cloud material. In most molecular lines, the material near 0 km s^{-1} behaves in a way that is consistent with a diffuse or translucent cloud. In particular, for molecules with multiple observed transitions, relative line strengths are reasonably consistent with excitation to the CMB temperature in this material, requiring that the gas has a low to moderate density. The population inversion generating 36 GHz masing can be excited over a wide range of densities, including $n \sim 10^3$ to 10^4 cm^{-3} (Cragg et al. 1992), appropriate in the highest density material in these clouds. However, masing is not observed in all gas in this density range, and the 0 km s^{-1} cloud is unique amongst the line-of-sight clouds treated here. The $\sim$0 km s^{-1} cloud therefore is set apart from the other systems by this feature.

Although masing by the 36 GHz line is observed in various environments, it is commonly associated with colliding systems, including bipolar outflows and HII regions expanding into a medium (Flower et al. 2010; Val'tts et al. 2010). It has been suggested that the $\sim$0 km s^{-1} cloud consists of ejecta from the cores of Sgr B2 (Gardner et al. 1988; Wirström et al. 2010). If this is the case, the masing might be due to a collision of the ejecta with ambient gas. However, the cause remains uncertain, particularly because there is insufficient evidence to conclude that the material is the Sgr B2 ejecta, as absorption at $\sim$0 km s^{-1} is pervasive across the Galactic Center (Royster & Yusef-Zadeh 2014; Jones et al. 2012; Neufeld et al. 2003) rather than local to the vicinity of Sgr B2. It will be interesting to determine whether masing occurs at a similar velocity in additional positions across the Galactic Center.

We interpret the abundances at -106, -73, and -40 km s^{-1}, determined from the ground state transition of A-CH_3OH as true abundances of $\sim$1 $\times 10^{-8}$ in the -106 and -73 km s^{-1} clouds, located in and near the Galactic Center, respectively, and slightly lower at $\sim$6 $\times 10^{-9}$ in the -40 km s^{-1} cloud, located at the outer edge of the Galactic Bar. Additionally, while our upper limits to the abundance in other clouds are not severely restrictive, we can definitively say that CH_3OH has a lower abundance within a few of the clouds in the Galactic Center. Therefore, CH_3OH is not equally abundant in all of the Galactic Center clouds observed in this line of sight, however, in the very limited sample of three clouds with measured abundances, CH_3OH is more abundant near the Galactic Center.

The measured CH_3OH abundances can be compared to values reported by Turner (1998) in a sample of high latitude cirrus clouds and Clemens-Barvainis cores, and to upper limits established by Liszt et al. (2008) in high latitude diffuse clouds. While a few of the clouds measured by Turner (1998) had much higher values (of up to nearly 10^{-7}) and nearly half had non-detections, a value of $\sim$3 $\times 10^{-9}$ was representative of most of

the clouds with detected methanol. We note that the majority of the clouds with detected methanol had higher hydrogen columns than most of the clouds measured here, implying central extinctions of $1.6 < A_{\mathrm{V}o} < 2.0$. Turner (1998) estimated the methanol abundances upon adopting assumptions about the cloud geometry and density structure and assuming that methanol was confined to a small filling factor of $\sim$25%. On the other hand, our measurements are made as average values over the velocity range specified, and we would obtain even higher values under the same assumptions. As a result, the lower limits for clouds with non-detections in the line-of-sight to Sgr B2 are in the range of measurements in the sources observed by Turner (1998). The abundances measured in the -106 km s^{-1} and -73 km s^{-1} cloud are greater than in most clouds observed by Turner (1998), and if we adjusted the abundances based on the assumptions applied by Turner (1998), they would be substantially more so. Finally, in their sample of high latitude diffuse clouds, Liszt et al. (2008) did not detect methanol and obtained upper limits to the abundance of 2 to 7 $\times 10^{-10}$, significantly lower than values observed in the -106, -73, and -40 km s^{-1} clouds.

The detection of CH_3OH in these sources is interpreted to indicate that dust surface chemistry plays a significant role in the clouds in which methanol is detected, as asserted by Turner (1998) and Liszt et al. (2008). Although some models of diffuse gas indicate that grain surface chemistry may play an important role in diffuse and translucent clouds (Viti et al. 2000; Price et al. 2003; Hocuk et al. 2016), grain surface chemistry has been ignored in most models due to the difficulty of forming ices on grain surfaces under the UV fields present in these low-extinction environments (e.g. Drdla et al. 1989; Turner et al. 1999; Godard et al. 2014). By our current understanding, ice mantles can form only when the extinction experienced by the grain is $A_{\mathrm{V}} \gtrsim 2$ under the standard interstellar radiation field with G_o = 1 (Tielens & Allamandola 1987). Given the hydrogen columns measured (Table 5.3) in the -106, -73, and -40 km s^{-1} clouds, we would not expect ice mantles to form

under standard assumptions of the cloud structure, and this is especially true in the -106 and -73 $\mathrm{km\,s^{-1}}$ clouds located in or near the Galactic Center, due to the stronger X-ray and CR irradiation present.

5.6.2 HC_3N, CH_3CN, CH_3CHO, and NH_2CHO

The observation of COMs in this material is somewhat surprising. While some of the COMs were detected in clouds with much lower hydrogen columns (e.g. CH_3CN at -92 $\mathrm{km\,s^{-1}}$), five clouds are observed to contain the most prominent absorption by COMs. These clouds include the highest molecular hydrogen column clouds, with $N_{\mathrm{H_2}} \geq 2.5 \times 10^{21}$ $\mathrm{cm^{-2}}$, but in this small sample, we do not observe trends of increased abundance with hydrogen column. Of the five prominent clouds, three are located in the Galactic Center (at -106, $\sim$0 and +25 $\mathrm{km\,s^{-1}}$), one is located deep within the Galactic Bar (at -73 $\mathrm{km\,s^{-1}}$), and one is located on the external edge of the Galactic Bar in the 3-kpc arm (at -40 $\mathrm{km\,s^{-1}}$). Additionally, we consider the upper limits to abundances in material in the disk at -23 $\mathrm{km\,s^{-1}}$. For comparison, we note that clouds at -73, -40, and -23 $\mathrm{km\,s^{-1}}$ have similar molecular hydrogen columns in our measurements, and the total hydrogen columns ($N_{\mathrm{H}} = 2N_{\mathrm{H_2}} + N_{\mathrm{HI}}$) are larger in the -40 and -23 $\mathrm{km\,s^{-1}}$ clouds than in the -73 $\mathrm{km\,s^{-1}}$ clouds. The -106 $\mathrm{km\,s^{-1}}$ cloud has a 30 to 40% higher molecular hydrogen column, whereas the $\sim$0 and +25 $\mathrm{km\,s^{-1}}$ clouds have significantly higher molecular hydrogen columns under the current cloud divisions employed.

Based on the very limited sample of measured abundances, HC_3N appears to have systematically higher abundances within clouds located in the Galactic Center compared to the disk, and intermediate values in the Bar. Comparing the -73, -40, and -23 $\mathrm{km\,s^{-1}}$ clouds which have similar total hydrogen columns, and the -80 $\mathrm{km\,s^{-1}}$ cloud with a lower hydrogen column, we observe significantly higher abundances by a factor of $\gtrsim$3 in the Galactic

Bar clouds at -80 and -73 $\mathrm{km\,s^{-1}}$ compared to the -40 and -23 $\mathrm{km\,s^{-1}}$ clouds in the disk. The Galactic Center clouds at -106 and $\sim$0 $\mathrm{km\,s^{-1}}$ have even higher abundances by a factor of 2 to 2.5. HC_3N is also abundant in energetic and highly irradiated environments in the central regions of external galaxies, including Ultra-Lumininous Infrared Galaxies (ULIRGs) (Lindberg et al. 2011). HC_3N has further been detected in the Horsehead PDR with an abundance of $\sim10^{-11}$ (Gratier et al. 2013), an order of magnitude less abundant than the disk translucent clouds and two orders of magnitude lower than the Galactic Center translucent clouds measured here. The work by Gratier et al. (2013) shows that the abundance of HC_3N is sustained in a UV-irradiated environment, however, it does not demonstrate an increased abundance in the PDR compared to a UV-shielded core. Thus, UV-irradiation alone does not appear to drive the HC_3N enhancement. The observational results presented here, and the extragalactic observations of HC_3N suggest that it may form efficiently in the presence of strong UV, X-ray, and/or CR irradiation; yet models predict reduced abundances of HC_3N in the presence of radiative and CR fluxes in excess of Galactic disk values (D. Maffucci 2016, private communication).

The abundance of CH_3CN appears to vary in the diffuse and translucent clouds, but there is no clear distinction between Galactic disk and Galactic Center clouds. On the other hand, CH_3CHO appears to be more abundant in diffuse clouds internal to the Galactic Bar than in the Galactic disk, with a factor of two lower abundance in the -40 $\mathrm{km\,s^{-1}}$ cloud and a factor of $>$3 in the -23 $\mathrm{km\,s^{-1}}$ cloud as compared to material in the Galactic Center and Bar. Perhaps CH_3CHO, like HC_3N, is enhanced in the presence of high X-ray or CR-irradiation.

The detection of NH_2CHO is notable because there is presently no known gas phase formation route for NH_2CHO capable of producing observed abundances, and ice surface chemistry is observed to occur efficiently in the laboratory (Kaňuchová et al. 2016), and

is believed to be essential for forming NH_2CHO. In the five clouds in which it is firmly detected, NH_2CHO has a much greater abundance in material in the Galactic Center and Bar compared to the -40 $\mathrm{km\,s^{-1}}$ cloud in the disk, with abundance ratios ranging from 3 to 10. The abundance of NH_2CHO is most elevated in the $\sim$0 $\mathrm{km\,s^{-1}}$ cloud, which has the highest hydrogen column density, and is also quite high in the -73 $\mathrm{km\,s^{-1}}$ cloud. Notably, these two clouds have the highest SiO abundances, suggesting a possible association with shocks. While we do not favor interpreting the column density directly as extinction due to the multitude of uncertainties in physical conditions and spatial structure (§5.3.2), it is notable that the 0 $\mathrm{km\,s^{-1}}$ cloud has a sufficient hydrogen column that ice chemistry should occur on the dust grains, and NH_2CHO may be liberated by passing shocks. However, under the assumption of a homogeneous dust distribution, the -73, -106, and -40 $\mathrm{km\,s^{-1}}$ clouds would not be expected to form ice mantles at extinction levels of $A_{\mathrm{V}o} \lesssim 1$. Nonetheless, we observe considerable abundances of NH_2CHO within these clouds, and particularly within the -73 $\mathrm{km\,s^{-1}}$ cloud.

Clearly, the results warrent further investigation by chemical modeling, including closer consideration of the impact that Galactic Center conditions, with higher densities, temperatures, shocks, and X-ray and CR-ray fluxes, may have on the chemistry of the COMs. The detection of the diverse range of COMs may indicate that ice grain mantles are able to form within these systems despite the harsh conditions in these low extinction translucent clouds. The results may further indicate that this process of ice accummulation occurs more readily in the Galactic Center than in the disk, requiring substantial differences in the cloud structure. This may be related to the differences in the kinematic signatures in CS absorption by clouds located internal and external to the Galactic Bar.

5.7 Conclusions

We have compiled the line profiles of ∼40 molecular lines with line-of-sight absorption by diffuse and translucent clouds observed towards Sgr B2(N) with the GBT PRIMOS data. The data reveal the presence of ∼10 kinematically separate clouds. In each cloud, we determined the column densities of observed molecules and estimated the molecular hydrogen column density by assuming a constant abundance of c-C_3H_2. Conversion from the c-C_3H_2 column density provides a new method for measuring the hydrogen column, which is, for numerous reasons, preferable to conversion from isotopologues of more abundant molecules like CO and HCO^+. We then converted the molecular column densities to abundances and considered the abundance patterns. We summarize new results below, including systematic trends with Galactocentric distance.

The CS profiles indicate that CS may be a good diagnostic for physical conditions. Whereas c-C_3H_2 has been shown to have a constant abundance in diffuse and translucent clouds (Liszt et al. 2012), the abundance of CS varies quite significantly in different clouds. No systematic offset is apparent in the abundances within clouds located in the Galactic Center/Bar compared to the disk, and we do not observe a trend with N_{H_2}. In the clouds located in the disk, CS appears to preferentially occupy the highest density material, and the kinematic profile suggests a difference in the cloud structure between diffuse and translucent clouds in the Galactic Center and the disk. Namely, the translucent clouds in the disk contain embedded sources with narrow line widths (of $\Delta v \approx 1$) and high CS abundances; clouds in the Bar and Center instead contain CS ubiquitously over the same velocity range as c-C_3H_2 and H_2CO are observed. Abundances of H_2CO and SO are positively correlated with the CS abundance, confirming the correlation between H_2CO and CS observed by (Liszt et al. 2006). Finally, CS-bearing molecules may prove excellent diagnostics for the cloud physical conditions, however significant advancement in chemical models is needed

first.

The abundance of SiO varies significantly in the clouds, and the broad profiles of SiO may suggest that it is more spatially extended than most of the molecules and does not reside in higher density embedded clumps. If SiO indicates shocks in these environments, then it is apparent that the -106, -73, and $\sim$0 km s^{-1} material is highly shocked, with the highest SiO abundance in the -73 km s^{-1} cloud, and that the -40 km s^{-1} material has recently experienced shocks. These clouds also contain high abundances of the complex organic molecules, so that shocks may be implicated in their formation or observed gas phase abundances. If shocks enhance the COM abundances by liberating ice mantle species from the dust grains, this would imply that ice grain chemistry is effective in environments where ice mantles are not classically expected to form (Tielens & Allamandola 1987). If the gas structure is highly inhomogeneous, however, ice mantle formation may be effective.

Finally, the COMs CH_3OH, HC_3N, CH_3CN, CH_3CHO, and NH_2CHO are prevalent in the observed material, and their formation is not understood in these environments. Particularly CH_3OH and NH_2CHO are believed to form on ice mantles, and efficient gas phase synthesis routes are not known. While ice mantle chemistry could occur in the $\sim$0 and +25 km s^{-1} clouds, it is not expected in the other material. This can potentially be accounted for if the structure of the material is highly inhomogeneous, as explored in Chapter 6. Additionally, HC_3N and CH_3CHO appear to be systematically more abundant in the translucent clouds in the Galactic Center compared to the disk, and may be associated with CR or X-ray irradiation.

5.8 Appendix: All Spectral Line Profiles

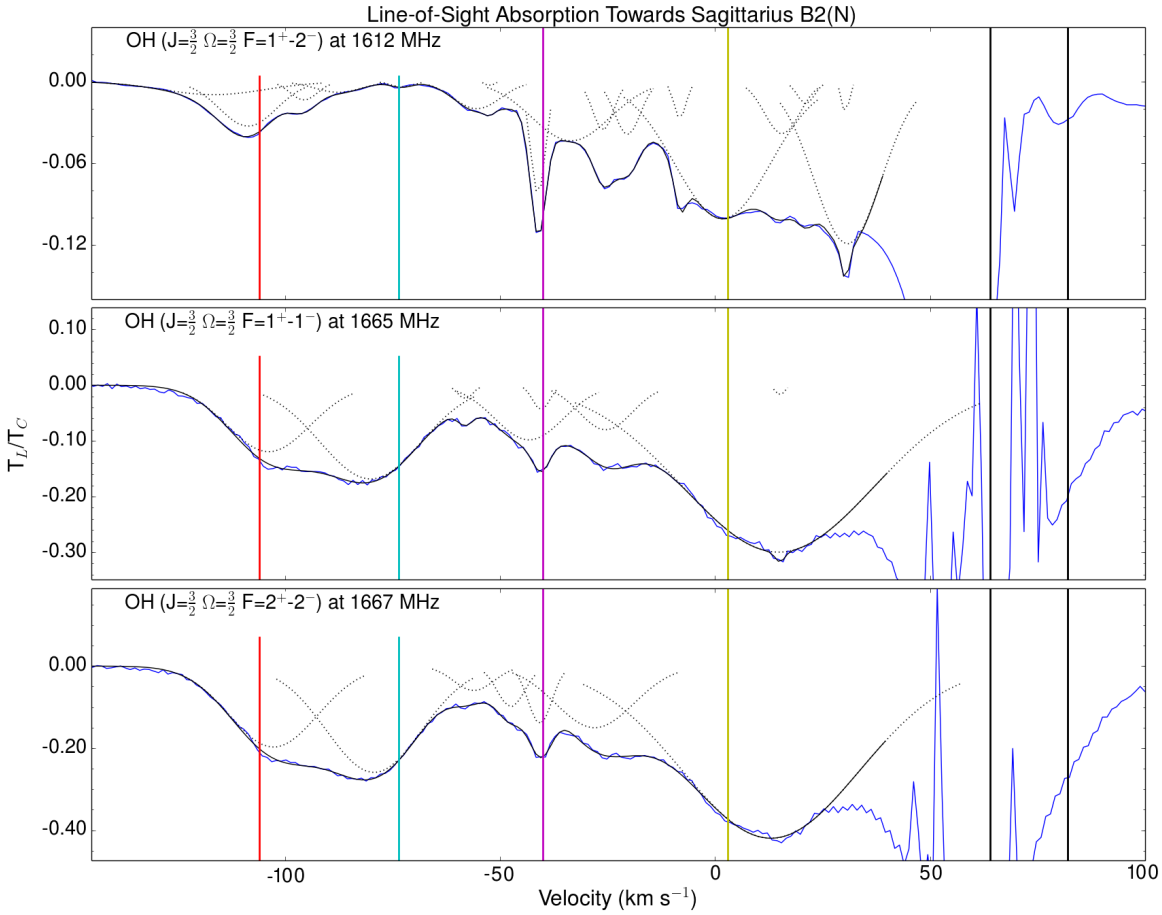

Fig. 5.15 – Absorption profiles of OH are shown in blue. Black vertical lines indicate the velocities of line absorption by Sgr B2 at +64 and +82 $\mathrm{km\,s^{-1}}$, and colored lines are located at -106, -73.5, -40, and +3 $\mathrm{km\,s^{-1}}$. Hyperfine or A/E structure for each of these velocity components is indicated by dotted vertical lines of the same color. The data are overlaid by individual Gaussian components fit (blacked dotted lines), and by the total fit to the profile (black solid line).

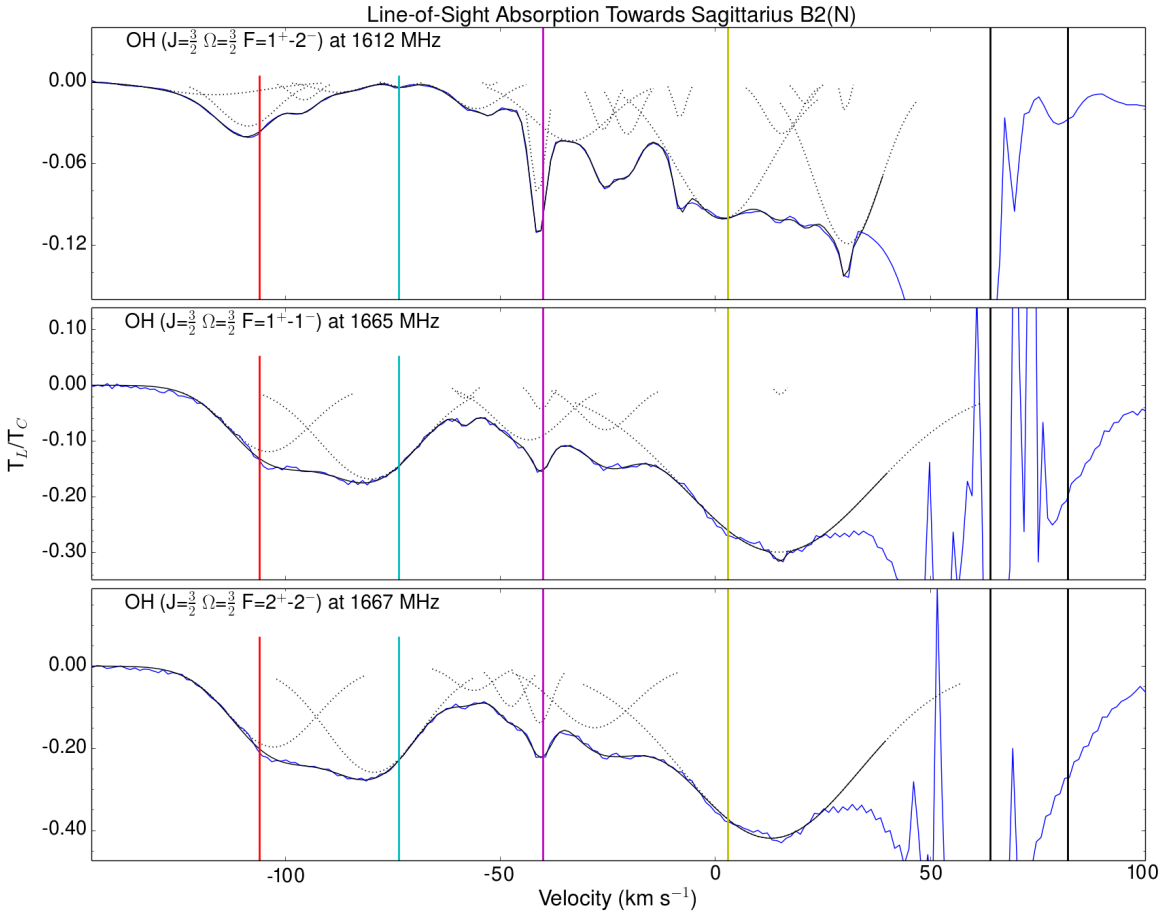

Fig. 5.16 – Absorption profiles of OH are shown in blue. Black vertical lines indicate the velocities of line absorption by Sgr B2 at +64 and +82 $\mathrm{km\,s^{-1}}$, and colored lines are located at -106, -73.5, -40, and +3 $\mathrm{km\,s^{-1}}$. The data are overlaid by individual Gaussian components fit (blacked dotted lines), and by the total fit to the profile (black solid line).

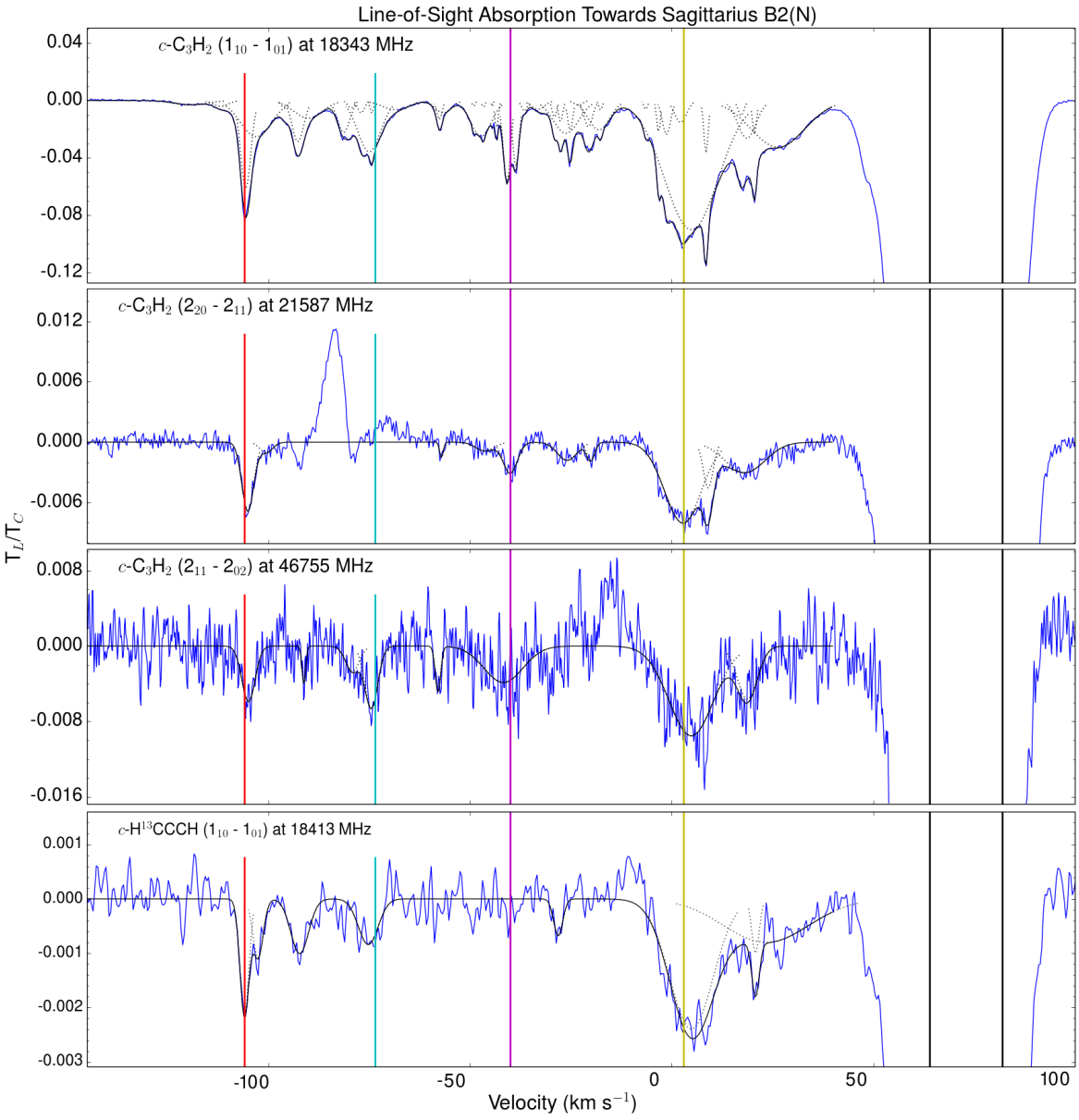

Fig. 5.17 – Absorption profiles of c-C_3H_2 and c-$H^{13}CCCH$ are shown in blue. Black vertical lines indicate the velocities of line absorption by Sgr B2 at +64 and +82 km s^{-1}, and colored lines are located at -106, -73.5, -40, and +3 km s^{-1}. The data are overlaid by individual Gaussian components fit (blacked dotted lines), and by the total fit to the profile (black solid line).

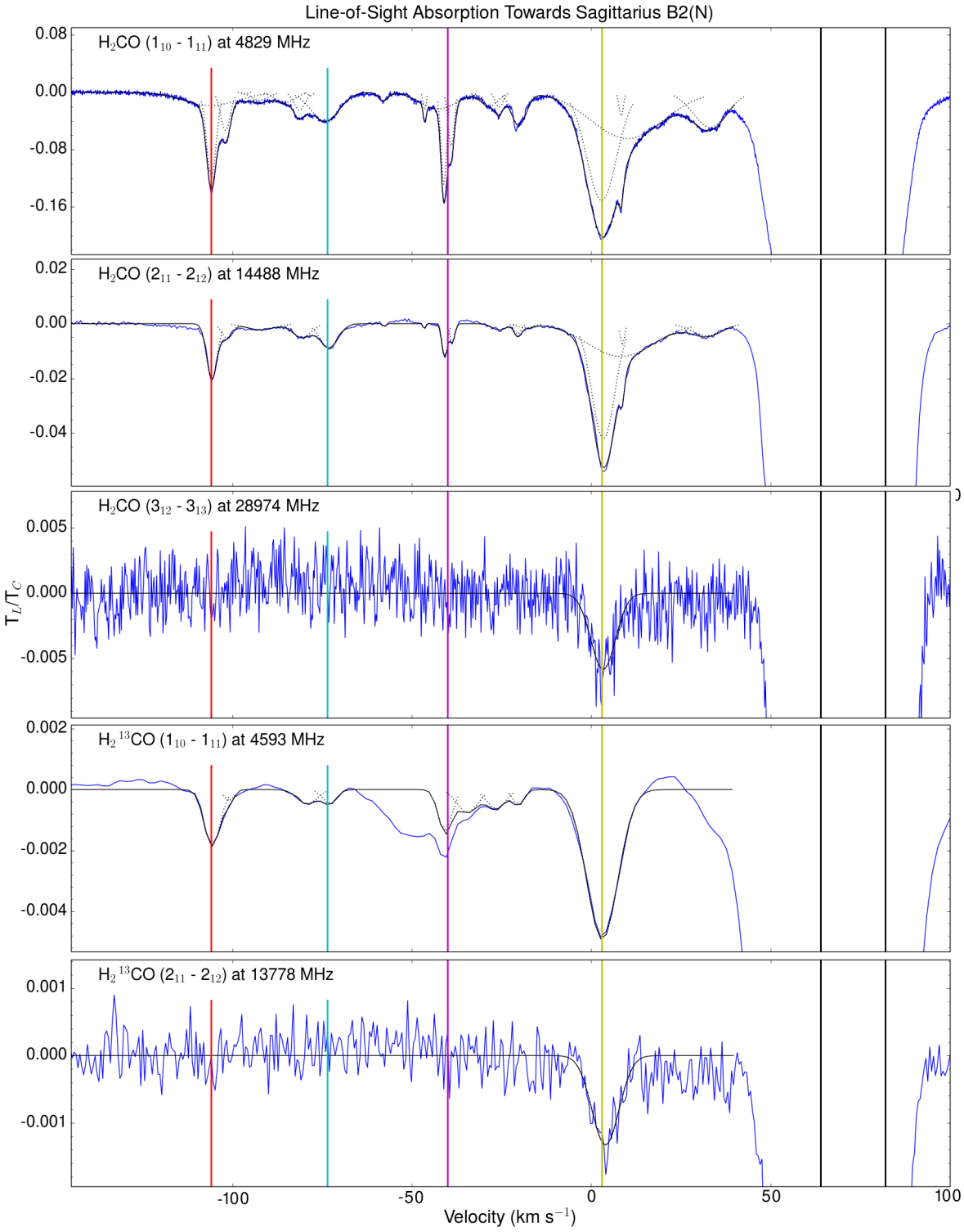

Fig. 5.18 – Absorption profiles of H_2CO and $H_2^{13}CO$ are shown in blue. Black vertical lines indicate the velocities of line absorption by Sgr B2 at +64 and +82 $\mathrm{km\,s^{-1}}$, and colored lines are located at -106, -73.5, -40, and +3 $\mathrm{km\,s^{-1}}$. The data are overlaid by individual Gaussian components fit (blacked dotted lines), and by the total fit to the profile (black solid line).

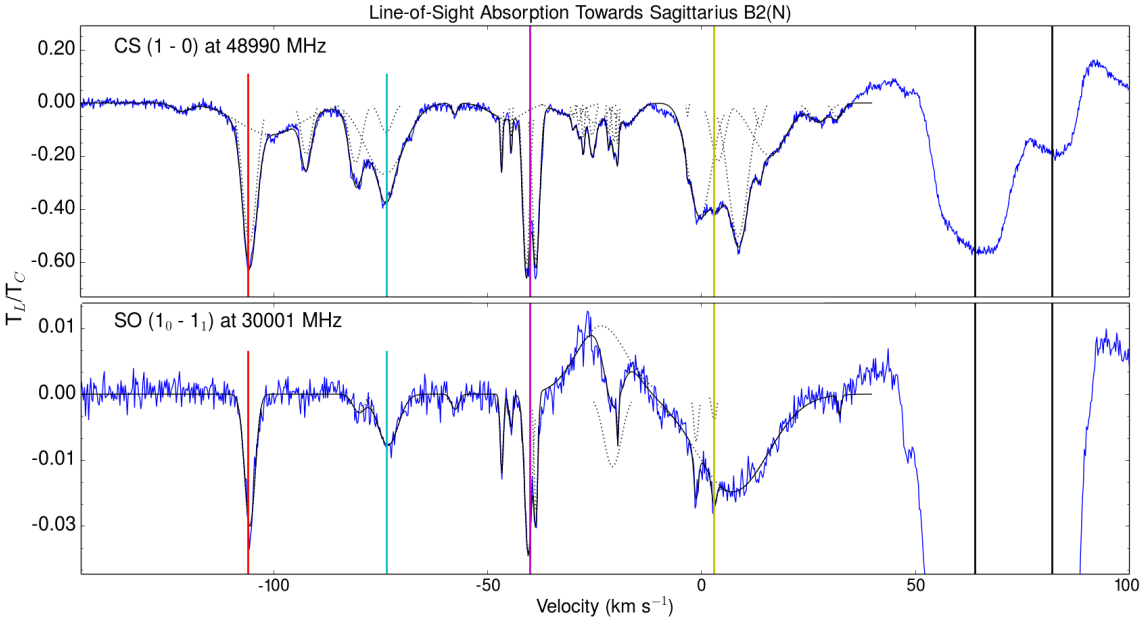

Fig. 5.19 – Absorption profiles of SO and CS are shown in blue. Black vertical lines indicate the velocities of line absorption by Sgr B2 at +64 and +82 km s^{-1}, and colored lines are located at -106, -73.5, -40, and +3 km s^{-1}. The data are overlaid by individual Gaussian components fit (blacked dotted lines), and by the total fit to the profile (black solid line).

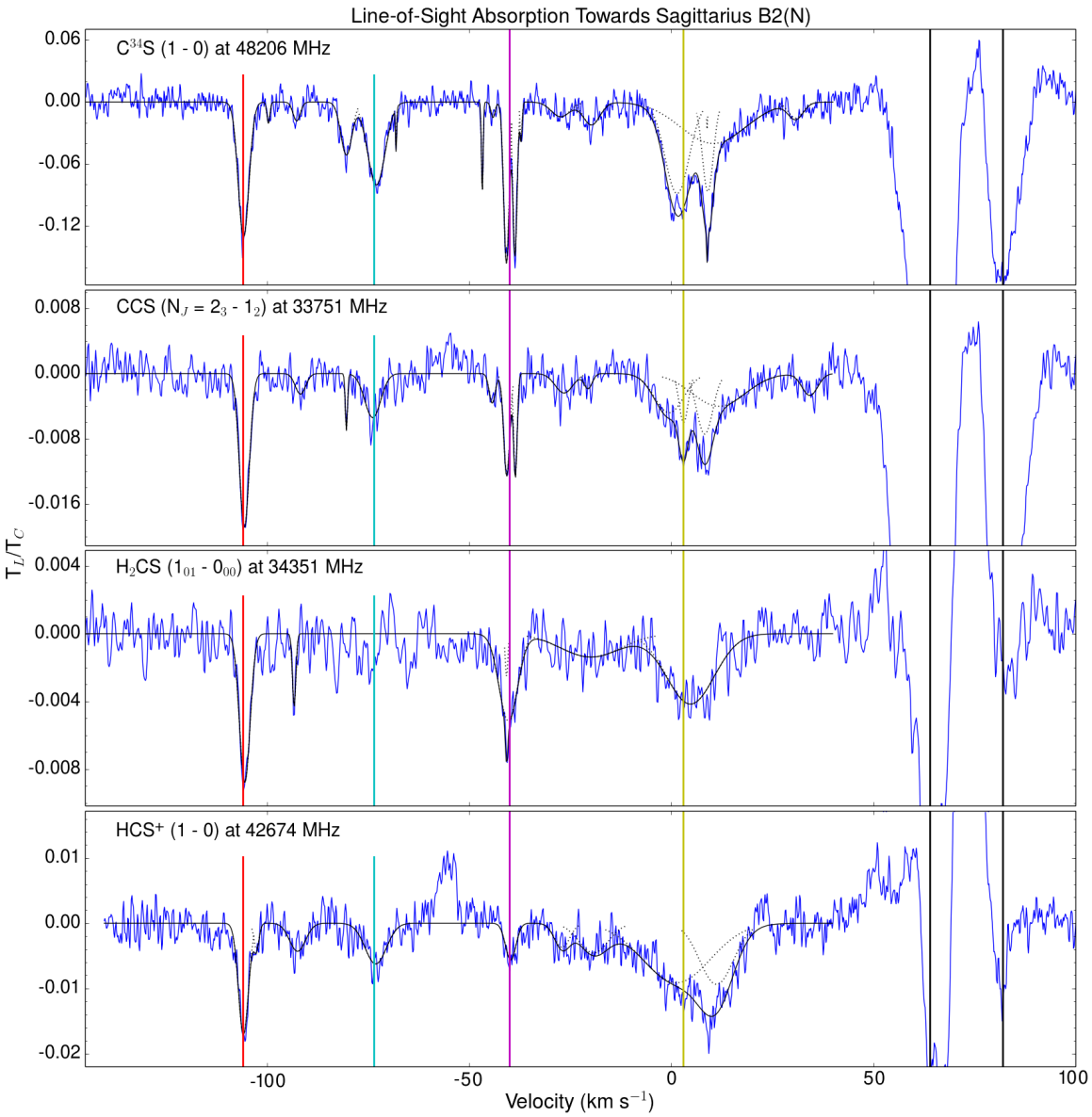

Fig. 5.20 – The absorption profiles of CS-bearing species are overlaid by the best fit Gaussian components (black dotted line) and the sum of best-fit Gaussians (black solid line). Black vertical lines indicate the velocities of line absorption by Sgr B2 at +64 and +82 km s^{-1}, and colored lines are located at -106, -73.5, -40, and +3 km s^{-1}.

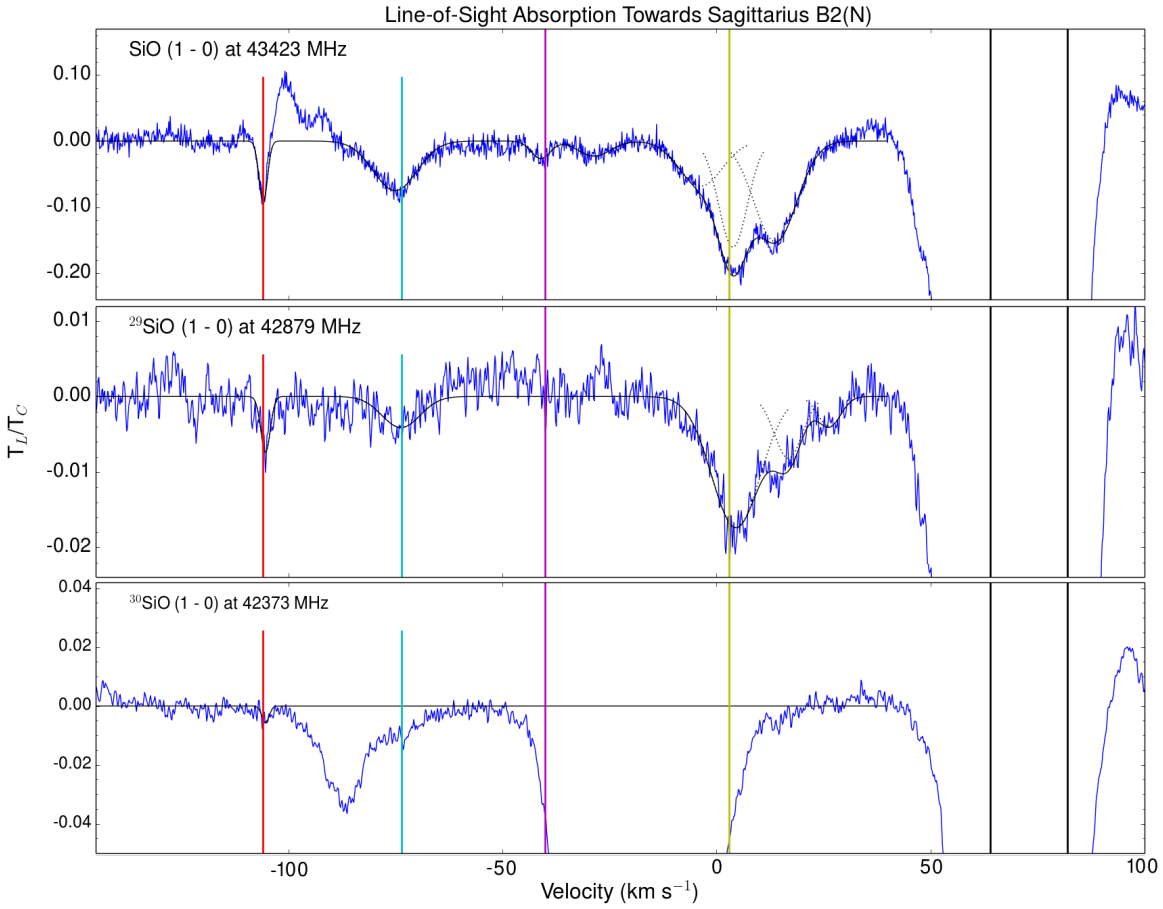

Fig. 5.21 – The absorption profiles of SiO isotopologues are overlaid by the best fit Gaussian components (black dotted line) and the sum of best-fit Gaussians (black solid line). Black vertical lines indicate the velocities of line absorption by Sgr B2 at +64 and +82 km s^{-1}, and colored lines are located at -106, -73.5, -40, and +3 km s^{-1}. The profile of ^{30}SiO includes a single detected component, as much of the profile is blended with the line-of-sight absorption profile of NH_2CHO.

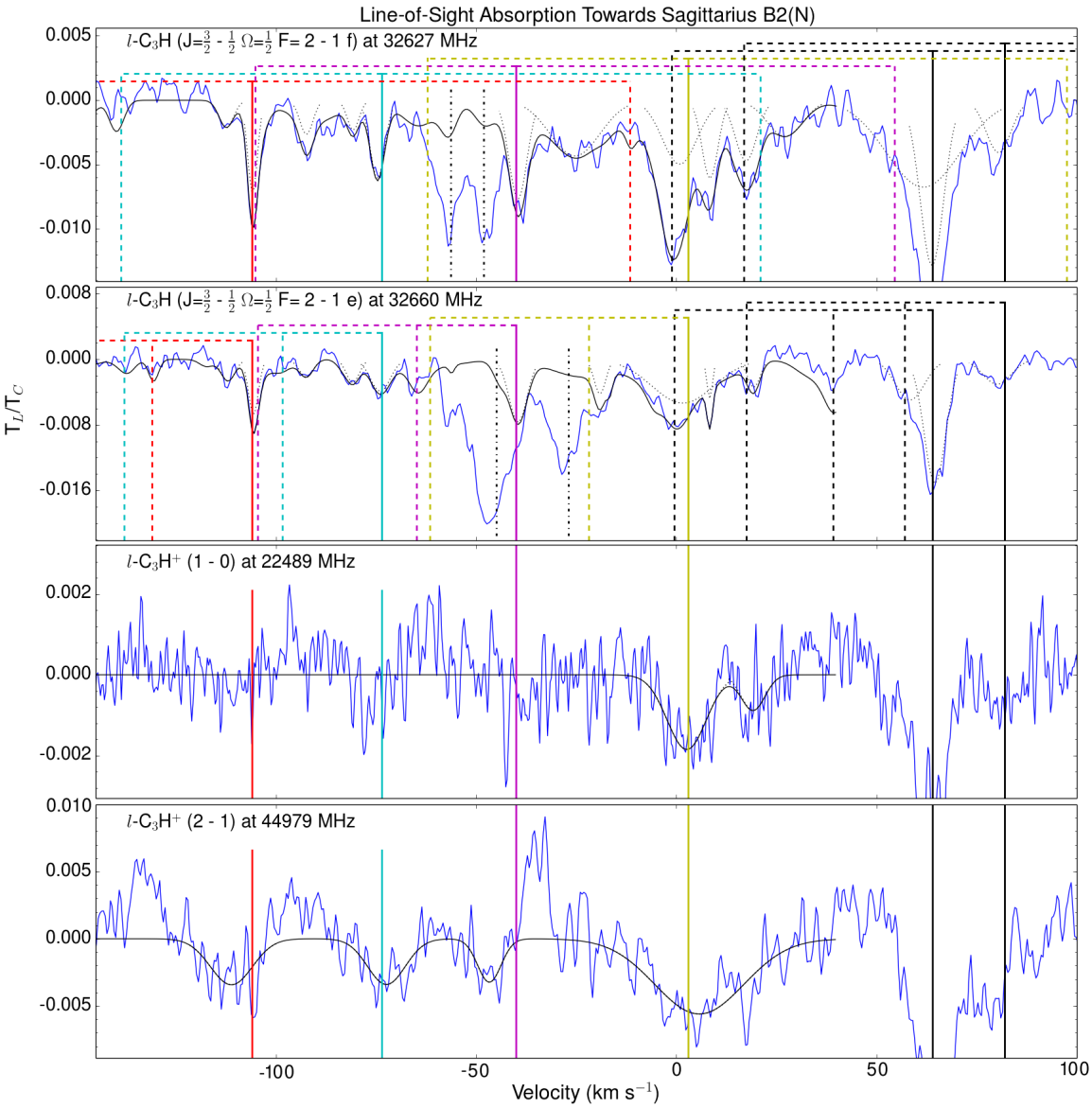

Fig. 5.22 – Absorption profiles of *l*-C_3H and *l*-C_3H^+ are overlaid by the best fit Gaussian components (black dotted line) and the sum of best-fit Gaussians (black solid line). Black vertical lines indicate the velocities of line absorption by Sgr B2 at +64 and +82 km s^{-1}, and colored lines are located at -106, -73.5, -40, and +3 km s^{-1}. Hyperfine structure for each of these velocity components is indicated by dotted vertical lines of the same color. The data are overlaid by Gaussian components fit to the main hyperfine component shown in blacked dotted lines, and by the total fit to the profile, which assumes that hyperfine or A/E components are present with the same line shape as the primary component, but with the height scaled by the ratio of the line strengths. In the profile of *l*-C_3H at 32627 MHz, the black dashed-dotted line marks unidentified transitions that are not consistent with the typical profile of diffuse cloud absorption in this line of sight. In the line profile of *l*-C_3H at 32660 MHz, the black dashed-dotted line marks a transition of *cis*-CH_2OHCHO at velocities of +64 and +82 km s^{-1} associated with Sgr B2.

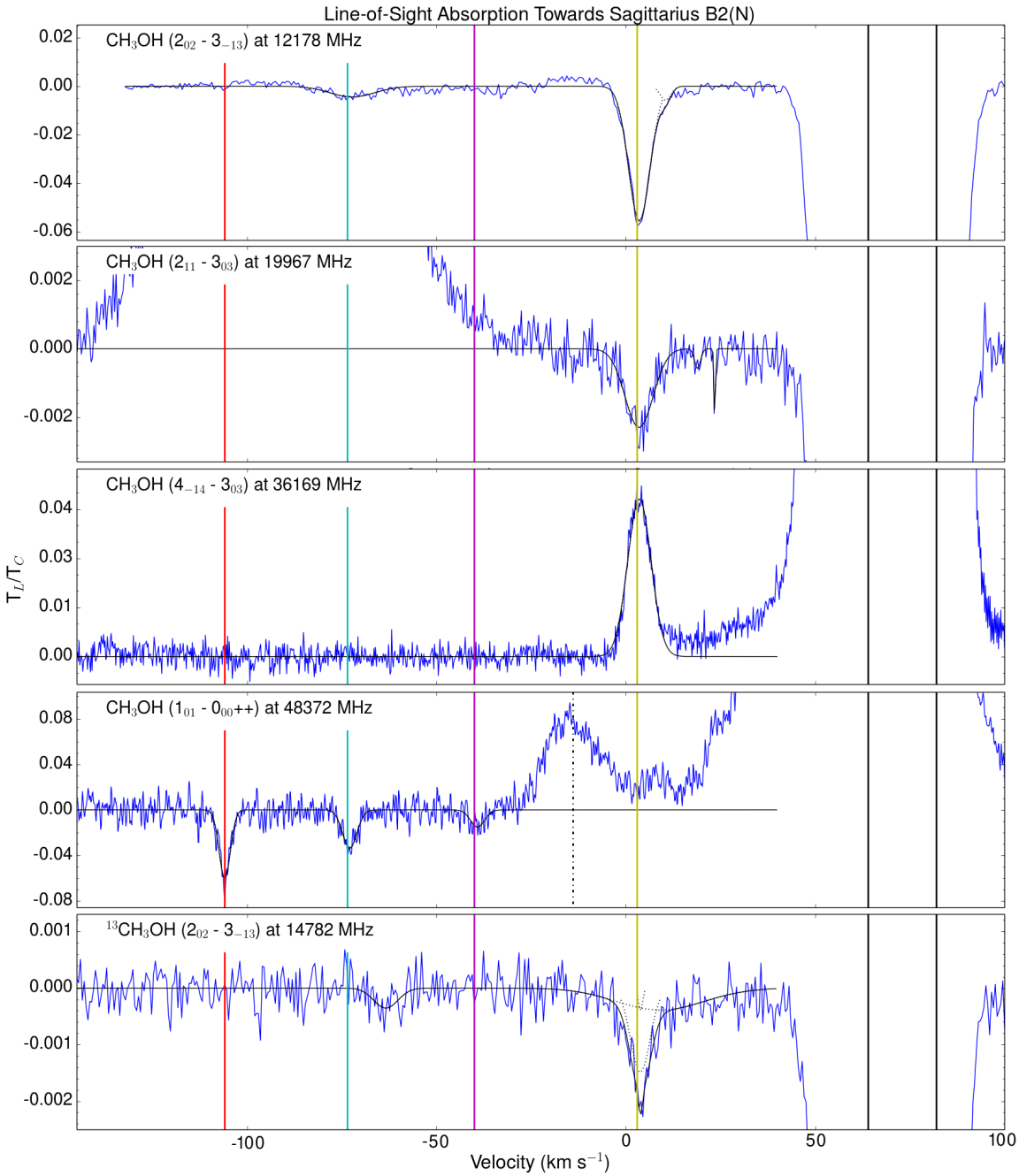

Fig. 5.23 – The absorption profiles of CH_3OH and $^{13}CH_3OH$ are overlaid by the best fit Gaussian components (black dotted lines) and the sum of best-fit Gaussians (black solid line). Black vertical lines indicate the velocities of line absorption by Sgr B2 at +64 and +82 km s^{-1}, and colored lines are located at -106, -73.5, -40, and +3 km s^{-1}. In the profile of CH_3OH at 48372 MHz, the black dashed-dotted line marks a transition of CH_3NH_2 at +64 km s^{-1} associated with Sgr B2.

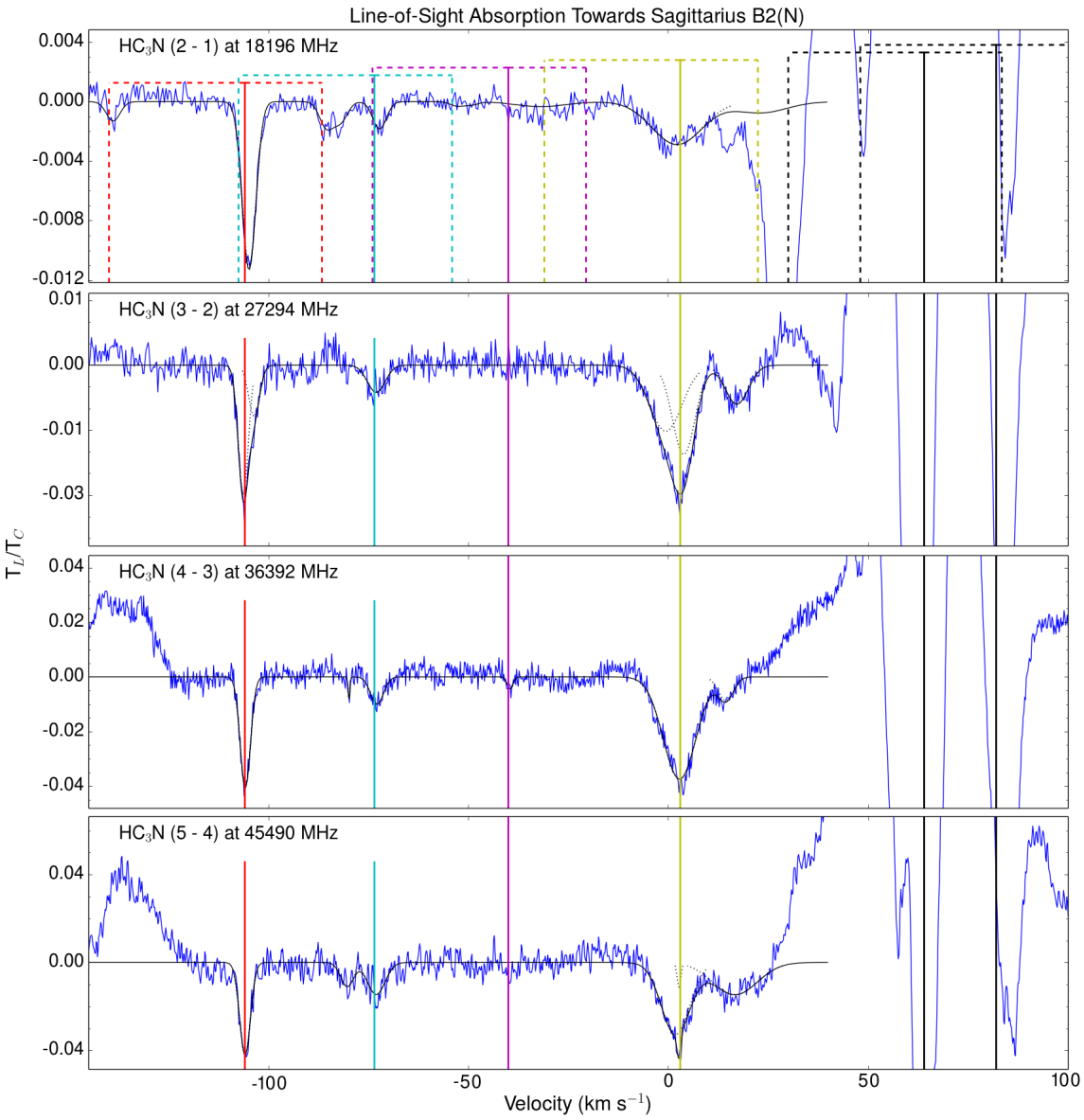

Fig. 5.24 – Absorption profiles of HC_3N are overlaid by the best fit Gaussian components (black dotted line) and the sum of best-fit Gaussians (black solid line). Black vertical lines indicate the velocities of line absorption by Sgr B2 at +64 and +82 $\mathrm{km\,s^{-1}}$, and colored lines are located at -106, -73.5, -40, and +3 $\mathrm{km\,s^{-1}}$. Hyperfine structure for each of these velocity components is indicated by dotted vertical lines of the same color. The data are overlaid by Gaussian components fit to the main hyperfine component shown in blacked dotted lines, and by the total fit to the profile, which assumes that hyperfine or A/E components are present with the same line shape as the primary component, but with the height scaled by the ratio of the line strengths.

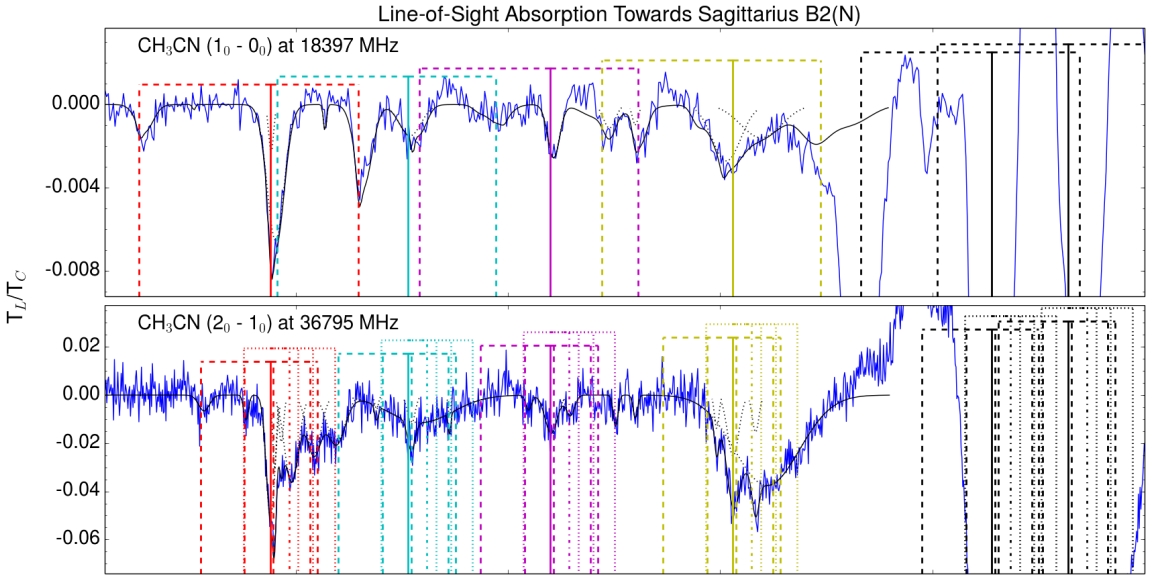

Fig. 5.25 – Absorption profiles of CH_3CN are overlaid by the best fit Gaussian components (black dotted line) and the sum of best-fit Gaussians (black solid line). Black vertical lines indicate the velocities of line absorption by Sgr B2 at +64 and +82 $\mathrm{km\,s^{-1}}$, and colored lines are located at -106, -73.5, -40, and +3 $\mathrm{km\,s^{-1}}$. Hyperfine structure for each of these velocity components is indicated by dotted vertical lines of the same color. The data are overlaid by Gaussian components fit to the main hyperfine component shown in blacked dotted lines, and by the total fit to the profile, which assumes that hyperfine or A/E components are present with the same line shape as the primary component, but with the height scaled by the ratio of the line strengths.

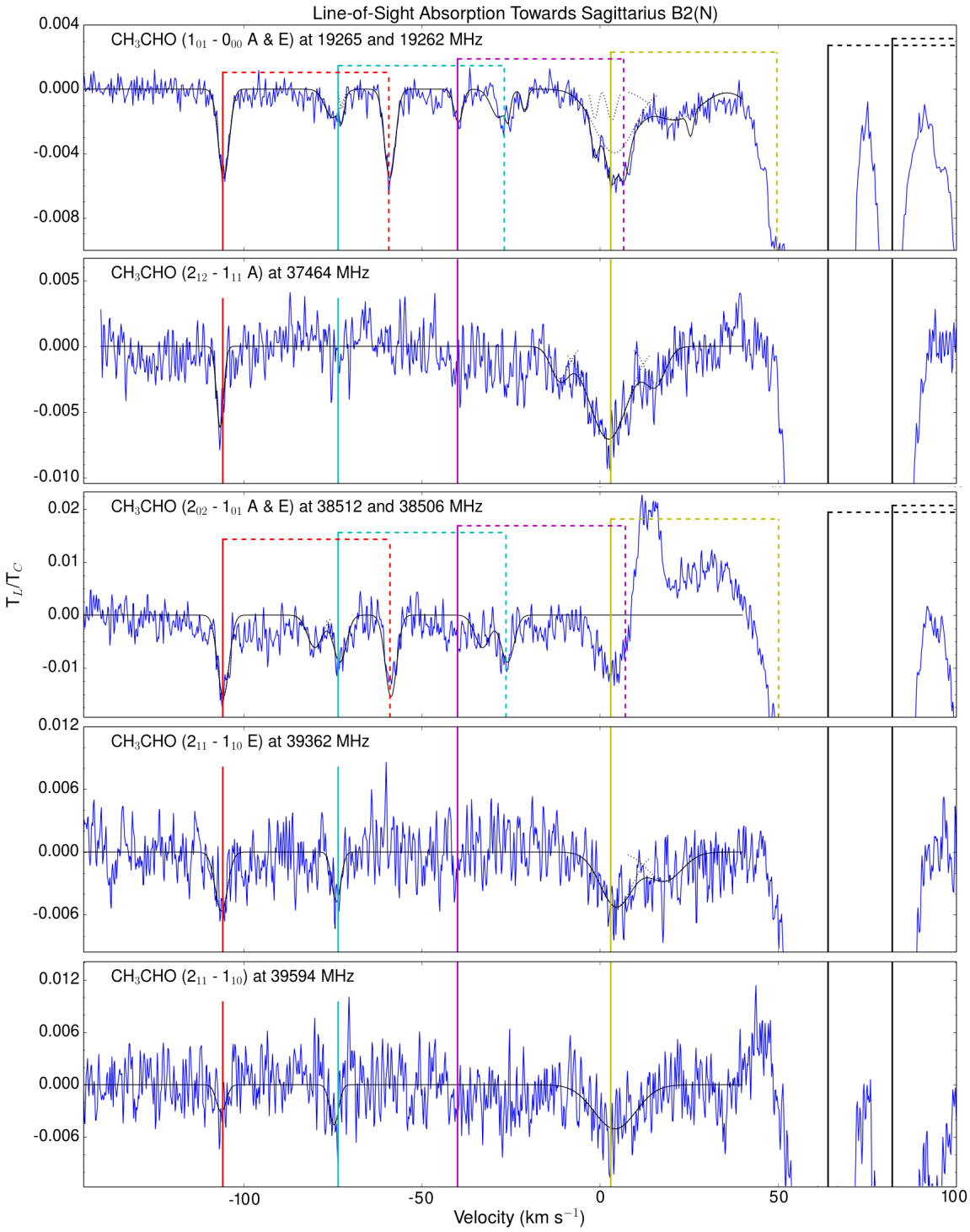

Fig. 5.26 – Absorption profiles of CH_3CHO. For the (2_{02}-1_{01}) and (1_{01}-0_{00}) transitions, the solid vertical lines represent absorption by the A-state transition and the dashed vertical lines by the E-state transition. Black vertical lines indicate the velocities of line absorption by Sgr B2 at +64 and +82 $\mathrm{km\,s^{-1}}$, and colored lines are located at -106, -73.5, -40, and +3 $\mathrm{km\,s^{-1}}$. The data are overlaid by Gaussian components fit to the main hyperfine component shown in blacked dotted lines, and by the total fit to the profile, which assumes that A-state line strengths and widths are equivalent to the E-state strength for the (2_{02}-1_{01}) and (1_{01}-0_{00}) transitions.

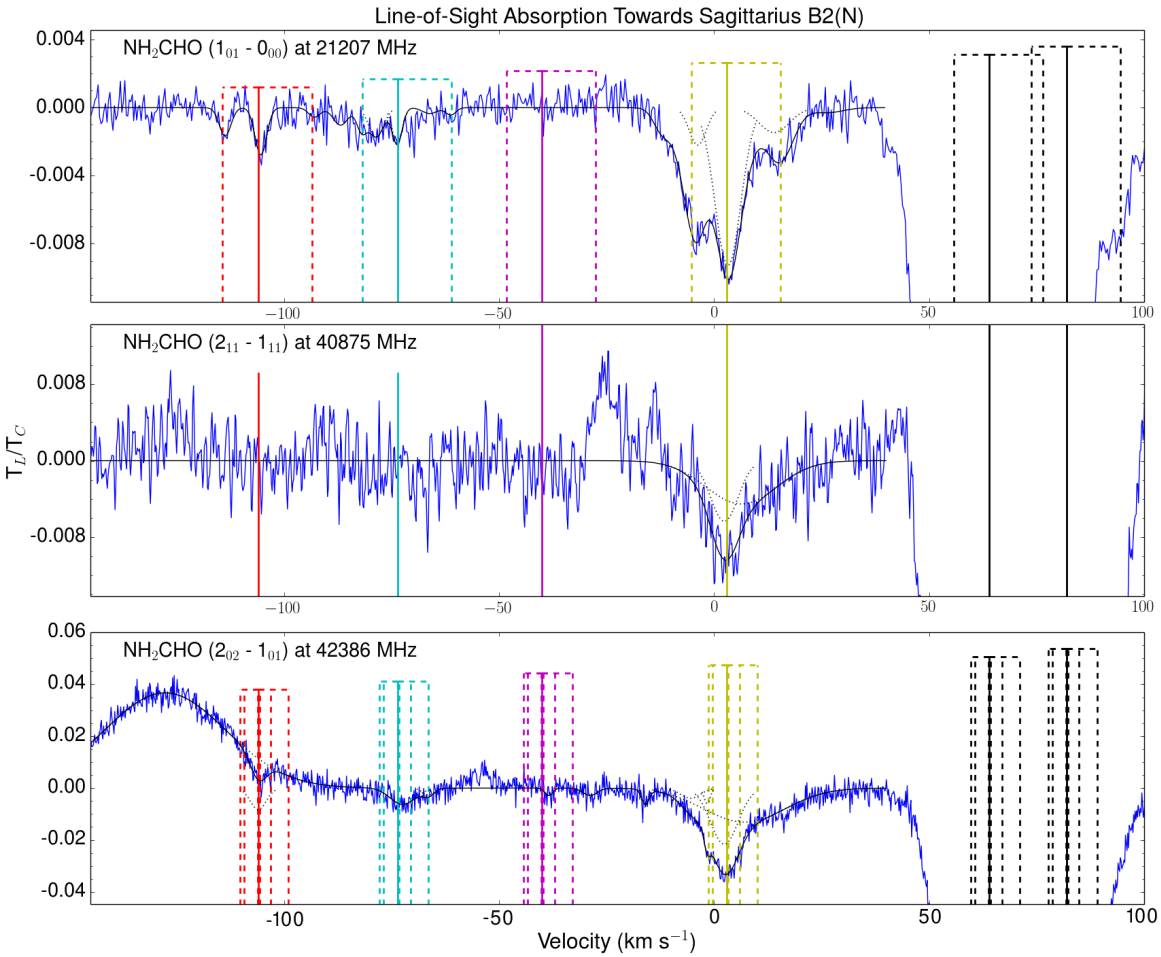

Fig. 5.27 – Absorption profiles of NH_2CHO are overlaid by the best fit Gaussian components (black dotted line) and the sum of best-fit Gaussians (black solid line). Black vertical lines indicate the velocities of line absorption by Sgr B2 at +64 and +82 $km\,s^{-1}$, and colored lines are located at -106, -73.5, -40, and +3 $km\,s^{-1}$. Hyperfine structure for each of these velocity components is indicated by dotted vertical lines of the same color. The data are overlaid by Gaussian components fit to the main hyperfine component shown in blacked dotted lines, and by the total fit to the profile, which assumes that hyperfine or A/E components are present with the same line shape as the primary component, but with the height scaled by the ratio of the line strengths.

Chapter 6

The Inhomogeneous Structure of Translucent Clouds Observed by Radio Interferometry

Abstract

In this final scientific chapter, we present exploratory work on the spatial structure of diffuse and translucent clouds. The work highlights a recent serendipitous discovery within broadband data obtained for an alternate scientific purpose. The data include direct observations of the inhomogeneous structure of the diffuse and translucent ISM on spatial scales of 6000 AU to 0.1 pc. In this chapter, we present the observational results, discuss the implications for the structure of this material, and discuss the capabilities that broadband observations offer for extending our understanding of the coupled physics and chemistry occuring. We discuss the results in the context of recent theoretical predictions for the distribution of dust in the diffuse ISM, in which hypercompact condensates of dust form the seeds of cool, dense gas clumps embedded in the diffuse ISM.

6.1 The Spatial Structure of Diffuse and Translucent Clouds

Diffuse and translucent clouds are observed in the foreground of either extragalactic point sources or Galactic HII regions spanning a few tens of arcseconds. To date, observational analyses have assumed that diffuse and translucent clouds are homogeneously extended over the continuum source. It has been conjectured that translucent clouds are moderately extended, spanning spatial scales of a few parsecs (Greaves & Nyman 1996; Greaves & Williams 1994), significantly larger than the background continuum sources they are observed against, and that diffuse clouds are even more extended and homogeneous (e.g. Qin et al. 2010).

The molecular chemistry has been treated under the assumption of homogeneity in spite of observations indicating substantial inhomogeneities in the HI distribution. So-called "tiny HI clouds", or alternatively tiny scale atomic structure (TSAS), have been observed

in the Galactic disk (e.g. Heiles 1997; Dutta et al. 2014). These systems are observed to occupy size scales of tens to hundreds of AU in the Galactic disk (Rollinde et al. 2003; Heiles & Stinebring 2007), and may contain neutral hydrogen column density enhancements of $\sim$30 to 50% compared to sightlines that do not intersect the tiny clouds. While there have been a few reports of time variability for molecular lines revealing tiny scale molecular structure (TSMS) (Rollinde et al. 2003; Heiles & Stinebring 2007), there has been little investigation of how the distributions of molecules couple with the HI distributions.

Furthermore, a few structures have been reported with inhomogeneities of somewhat larger size scales, of a few thousand AU, which are still very small compared to the size scales of typical molecular clouds. In their review of the 2006 meeting entitled *Small Ionized and Neutral Structures in the Diffuse ISM*, Heiles & Stinebring (2007) remarks that "There's a large range of unstudied scale sizes lying between tiny and typical parsec-scale structures."

The literature contains a few chemical modeling studies of diffuse clouds with microstructure under low extinctions of A_V<0.5. The authors assume that the embedded hyperdensities are overpressured and therefore transient systems; models have included embedded hyperdensities of 10 by 100 pc size scales under a range of densities from 3×10^2 cm^{-3} to 10^5 cm^{-3} and lifespans of 1 to 1000 yr (Bell et al. 2005; Cecchi-Pestellini et al. 2009). The models demonstrate that the embedded systems can significantly affect the observed chemistry in the entire system (Cecchi-Pestellini et al. 2009), even with transient knot lifespans of 100 yr (Bell et al. 2005). These models have assumed that the hyperdensities have high temperatures, even larger than the diffuse clouds in which they are embedded, and are byproducts of turbulent wave energy dissipation. The model presented in Cecchi-Pestellini et al. (2009) predicted that H_2O^+ and SH^+ should be present in detectable abundances, and indeed, these species were observed soon thereafter (Ossenkopf

et al. 2010; Menten et al. 2011), making this a rare case where a chemical model prediction was clearly validated by observations.

However, observational papers have expressed consternation as to the source of the inhomogeneities (Heiles & Stinebring 2007), and chemical models have included "a population of transient density enhancements maintained by some external and unspecified sources" (Cecchi-Pestellini et al. 2009). Both observational and theoretical researchers have assumed that the lifetimes of the hyperdensities must be short, as they should be extremely overpressured (Heiles & Stinebring 2007, and references therein). However, recent theoretical work on an electric effect of charged dust in the diffuse ISM (Tsytovich et al. 2014) may provide an explanation for these systems. The models of Tsytovich et al. (2014) predict that dust in the diffuse and translucent ISM should not be homogeneously distributed, but instead should congregate into tiny cloudlets of dust with very high dust densities. These cool very efficiently, so that a cool gas halo can form surrounding the tiny cloudlet, possibly explaining the TSAS. The models provide the first theoretical explanation for the TSAS, and they predict that the hyperdensities are cool, whereas previous treatments of the systems assumed that they should be hot. The systems are thereby stabilized, enabling them to be more long-lived, although they could be periodically disrupted by turbulence.

In this chapter, we discuss observations of inhomogeneities in translucent clouds on spatial scales of 6000 AU to 0.1 pc, intermediate between the size scales of previously observed TSAS and the supposed spatial scales of the translucent clouds. We additionally explore the possible connection between the observed chemistry and spatial structure with the model predictions by Tsytovich et al. (2014).

6.2 Novel Observations of Translucent Cloud Inhomogeneities

VLA data of 18 GHz transitions of HC_3N and CH_3CN show that, at least for organic species in translucent clouds located in the Galactic Center, the assumption of homogeneity is incorrect. While the HC_3N and CH_3CN transitions were targeted for a different scientific purpose, the large bandwidths provided by the upgraded VLA enabled this discovery.

If the translucent clouds have homogeneous distributions over the background source continuum structure as typically assumed, a high resolution image of an absorption line observed against a background HII region should show a constant line optical depth. Because molecular excitation temperatures in diffuse and translucent gas are equivalent to $T_{\rm CMB}$, the optical depth of an absorption line is entirely characterized by the ratio of T_L/T_C (e.g. Liszt et al. 2012). Thus, if the foreground material is extended and homogeneous, the value of T_L/T_C should be constant in all pixels in which a measurement can be made (i.e. in pixels with a sufficient background continuum strength).

Towards Sgr B2(N), an optical depth measurement can be made over a $\sim$20 arcsec field, as defined by the spatial extent of the shell-shaped HII regions and adjacent compact HII regions (Gaume et al. 1995). When imaged by the VLA with 1 arcsec resolution, clumps containing high column densities of HC_3N and CH_3CN are clearly detected at the velocities associated with translucent clouds in the line-of-sight. Figure 6.1 shows the integrated line strength in the specified velocity component, showing that each detected velocity component consists of a clump at a different spatial position. The $\sim$0 km s^{-1} component consistently appears at a position to the NW of the shells, whereas the -106 km s^{-1} component appears at a position to the E of the center of the shells, and the -73 km s^{-1} component has an enhanced line strength towards a position to the SW of the center. The spectrum extracted from the position of each clump is shown below each panel. The spectra further demonstrate the optical depth differences. For instance, towards the strong continuum

source (known as K4) against which the $\sim$0 km s^{-1} component is observed, a clear absorption feature is observed at +3 km s^{-1}, but no absorption features are detected at the velocities of other line-of-sight features at -40, -73, or -106 km s^{-1}. At the position of the -106 km s^{-1} clump, little to no absorption is observed associated with other line-of-sight clouds at $\sim$0, -40, or -73 km s^{-1}, and the corollary can be said at the position of the -73 km s^{-1} clump. Figure 6.2 shows the integrated line optical depth images for each velocity component; at the positions of the clumps, the line optical depth is enhanced by a factor of $\gtrsim$5 over most positions on the field. Given the signal-to-noise of the measurement, the clumps have column densities that are at least a factor of 20 higher than some positions on the field. The clumps have spatial scales with an upper limit of the beam size of 1 arcsec. The 1 arcsec size scale corresponds to 8000 AU at an 8.5 kpc distance (likely appropriate for the -106 and $\sim$0 km s^{-1} clouds) and 7000 AU at a distance of 7.5 kpc (likely appropriate for the -73 km s^{-1} cloud at a Galactocentric distance of 1 kpc). We note that clumping is also present towards Sgr B2(M), located 45 arcsec south of Sgr B2(N), indicating that multiple clumps containing strong absorption by the COMs are embedded in more extended systems.

This result is further corroborated by ATCA data at 30 to 44 GHz towards Sgr B2 with $\sim$5 arcsec resolution, in which clumps are found at positions that are consistent with those observed with the VLA. Figure 6.3 shows the integrated optical depth in gas at $\sim$0 and $\sim$10 km s^{-1} in 36 to 40 GHz lines of CH_3CN, HC_3N, and NH_2CHO. Nearly all of the detected absorption by the $\sim$0 km s^{-1} material is observed towards precisely the same position as in the VLA data, showing an optical depth enhancement by at least a factor of 6 over most positions on the field. This figure also shows that the material at $\sim$10 km s^{-1} has a somewhat different spatial distribution than absorption at $\sim$0 km s^{-1}. Although the $\sim$10 km s^{-1} material, like the $\sim$0 km s^{-1} material, has the strongest absorption at the position

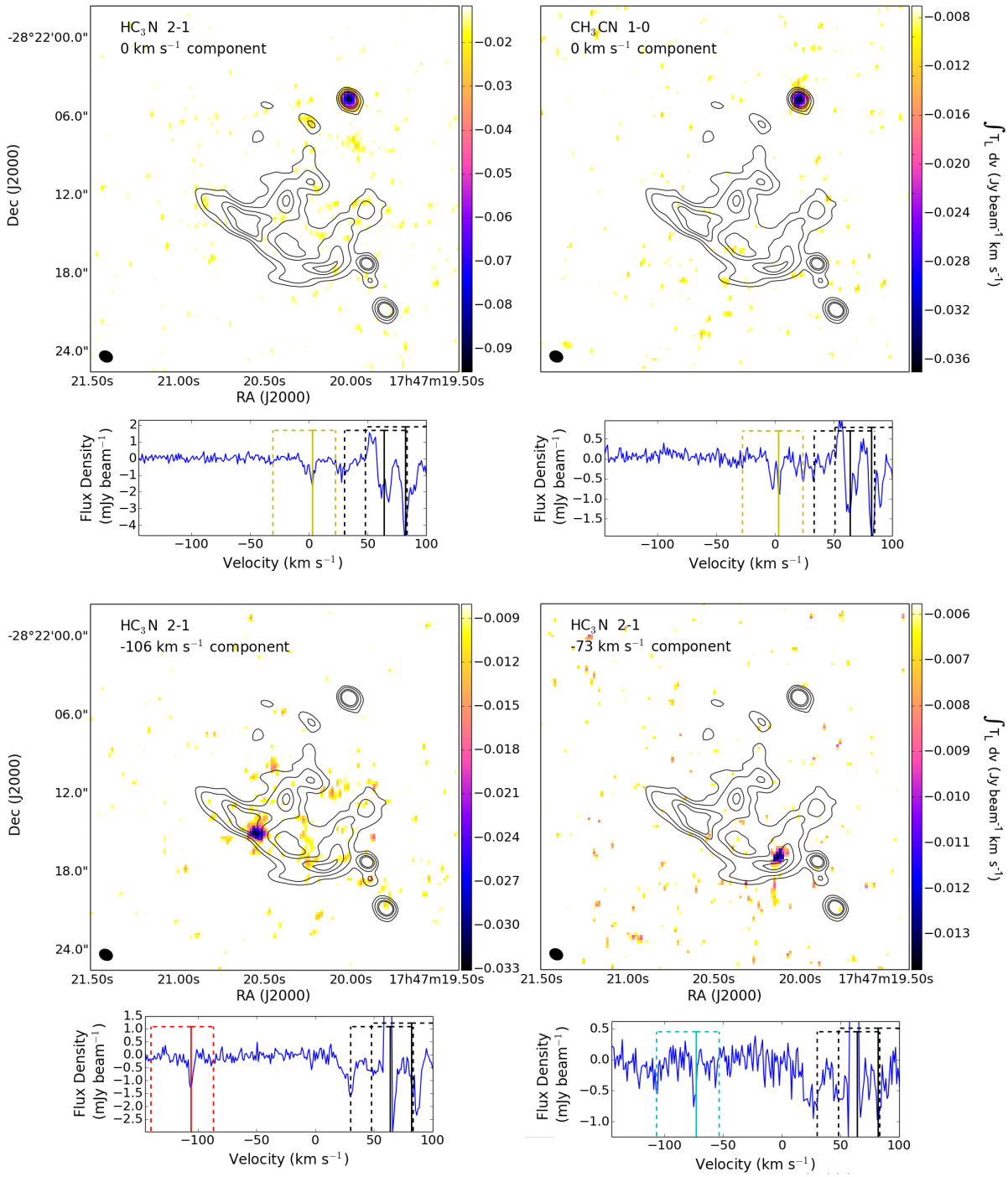

Fig. 6.1 – Line intensities integrated over the specified velocity component are shown in color scale, with continuum contours overlaid. Below each image panel is a spectrum extracted at the pixel with the highest line strength, showing clear absorption at specified velocity. Black vertical lines indicate the velocities associated with Sgr B2, and colored lines indicate the specified velocity component. Dashed lines indicate hyperfine structure.

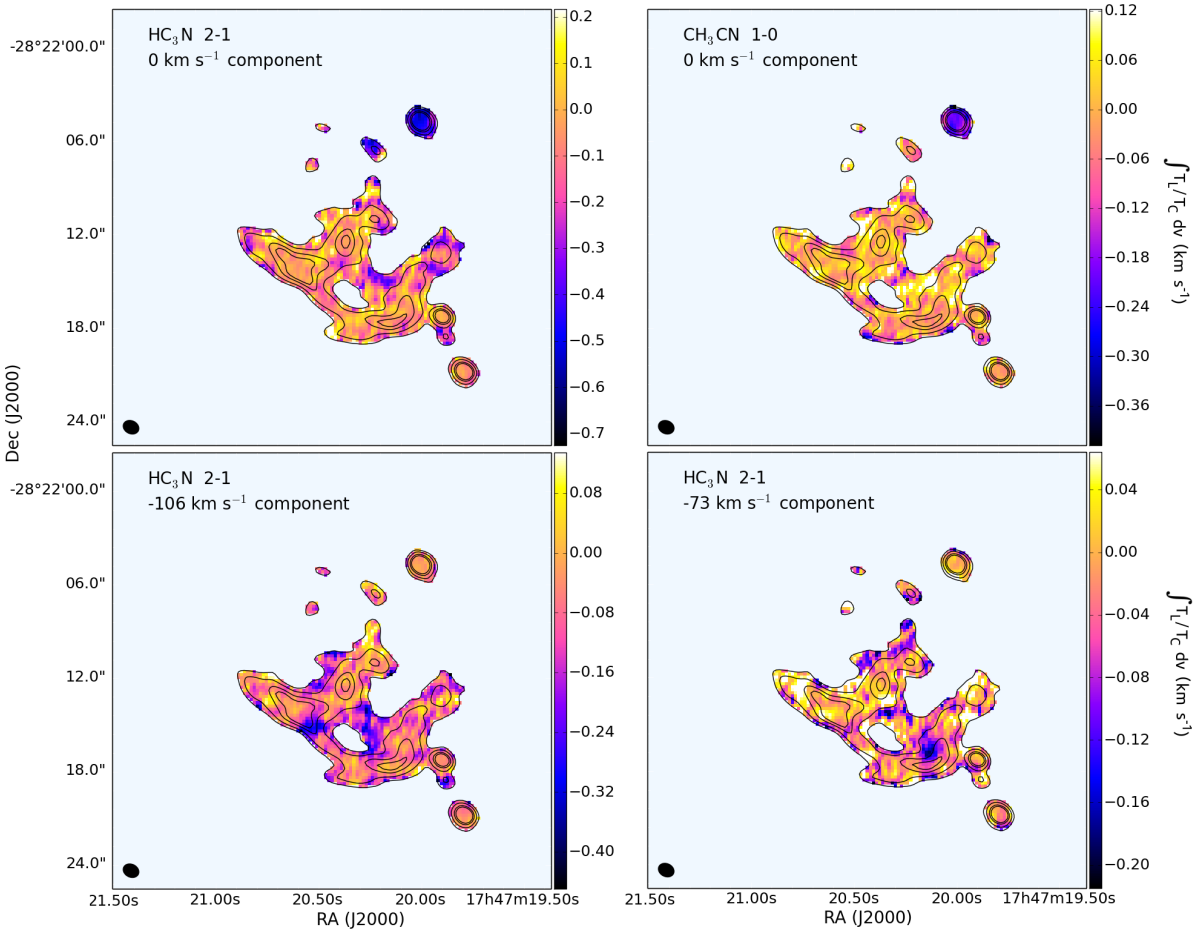

Fig. 6.2 – Line-to-continuum ratio images integrated over the specified velocity component are shown in color scale, with continuum contours overlaid. Measurements are only made inside the first continuum contour. Enhancement by a factor of >5 is observed at the positions of the clumps as compared to the majority of the field.

of the NW continuum source (namely K4), the $\sim$10 km s^{-1} material is more widespread. The ATCA data also contains line-of-sight absorption profiles by smaller molecules, and Figure 6.4 shows the absorption by the $\sim$0 and $\sim$10 km s^{-1} clouds by CCS, SO, and SiO. The figure shows the same general trends, although the distributions of CCS and SO in particular are more widespread both at 0 and 10 km s^{-1}, thereby demonstrating a lesser degree of enhancement in the clumps. From this, it is evident that the COMs preferentially reside within the clumps to a greater degree than the smaller species.

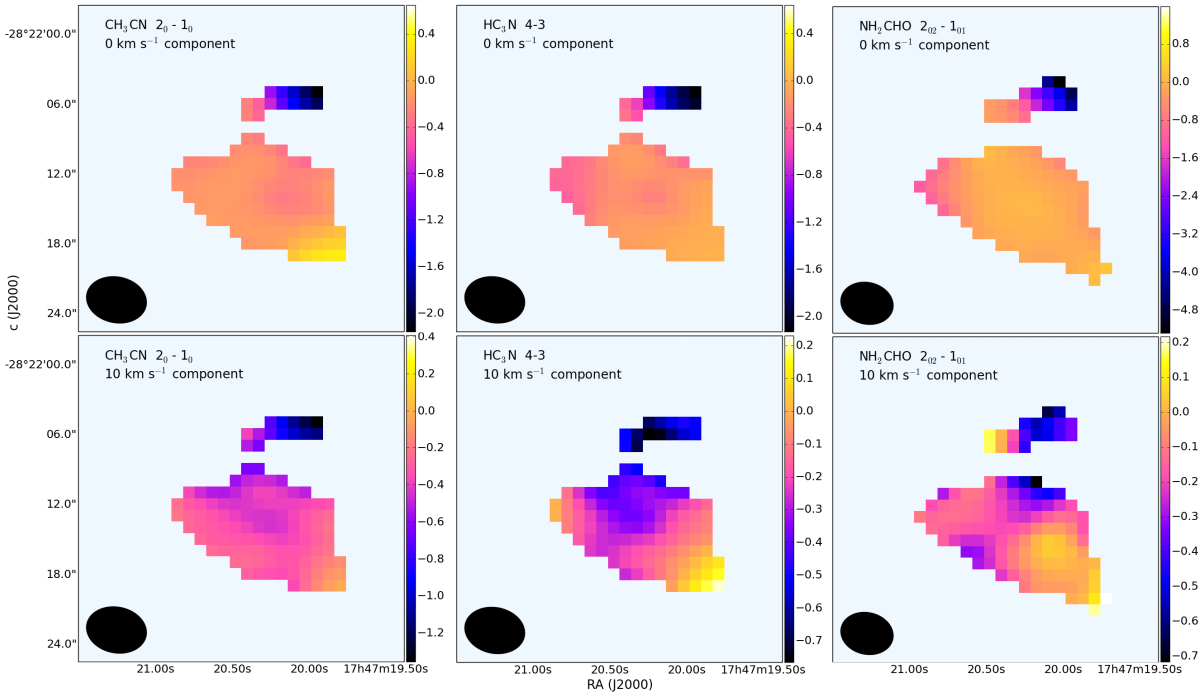

Fig. 6.3 – Line-to-continuum ratio images integrated over the 0 and +10 km s^{-1} velocity components for COMs in ATCA data. Pixels with continuum strengths $<$300 mJy beam^{-1} are zeroed out.

Figures 6.5 shows the integrated line optical depths of COMs in the -106, -73, and -40 km s^{-1} clouds. Again, inhomogeneities are apparent, with a factor of $\sim$5 enhancement towards positions that generally agree with the positions at which the clumps were observed with the VLA. Figure 6.6 shows the spatial distributions of smaller species in the -106, -73, and -40 km s^{-1} clouds. In general, these appear to be more widespread than the COMs,

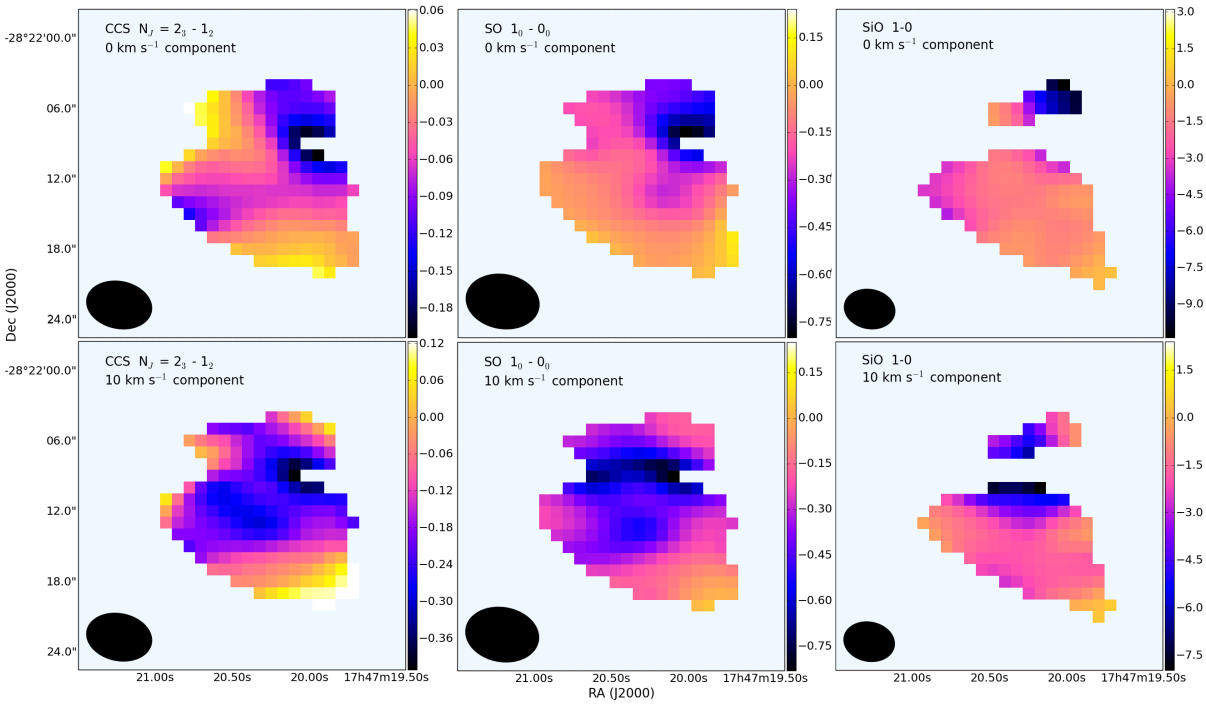

Fig. 6.4 – Line-to-continuum ratio images integrated over the 0 and +10 km s^{-1} velocity components for smaller species in ATCA data. Pixels with continuum strengths $<$300 mJy beam^{-1} are zeroed out.

and show somewhat different spatial patterns. ALMA data at 3-mm further indicate that many smaller translucent cloud species exhibit a clumpy distribution in translucent clouds in the Galactic Bar, Center, and disk, on spatial scales probed with a 3 arcsec beam (A. Belloche 2015, private communication).

The independent observations of different transitions provide significant evidence that spatial inhomoegeity is substantial; in some cases, nearly all of the absorption arises from a single position with an upper limit to the size scale set by the beam size. Given these independent confirmations, it is evident that interferometric observations towards this pointing position enable us to directly observe the clumpy substructure of translucent clouds.

6.3 An Emerging Theory of Diffuse Cloud Substructure

As briefly mentioned above, recent theoretical results predict the presence of significant clustering in the distribution of dust, and the predicted systems may be related to the observed inhomogeneities. In the work of Tsytovich et al. (2014), models of interstellar dust in the diffuse ISM predict the formation of compact, optically thin cloudlets of dust in which the dust density is enhanced by a factor of $\sim 10^7$ compared to a homogeneous distribution. In conditions appropriate for the Galactic disk, the dust cloudlets should occupy size scales of 1 to 10 AU. In the models, irrespective of the dust size and composition, nearly all interstellar dust condenses into these systems; while the clouds may be periodically disrupted by turbulence, they reform on very fast time scales, so that most interstellar dust should be within them rather than dispersed in the ISM at any given time. The precise size scale of the dust cloudlets is determined by how highly charged the dust is. Cloudlets forming in a medium with substantial UV or CR irradiation (like in the Galactic Center) may be an order of magnitude larger, spanning perhaps 50 to 100 AU (A. Ivlev 2016, private communication).

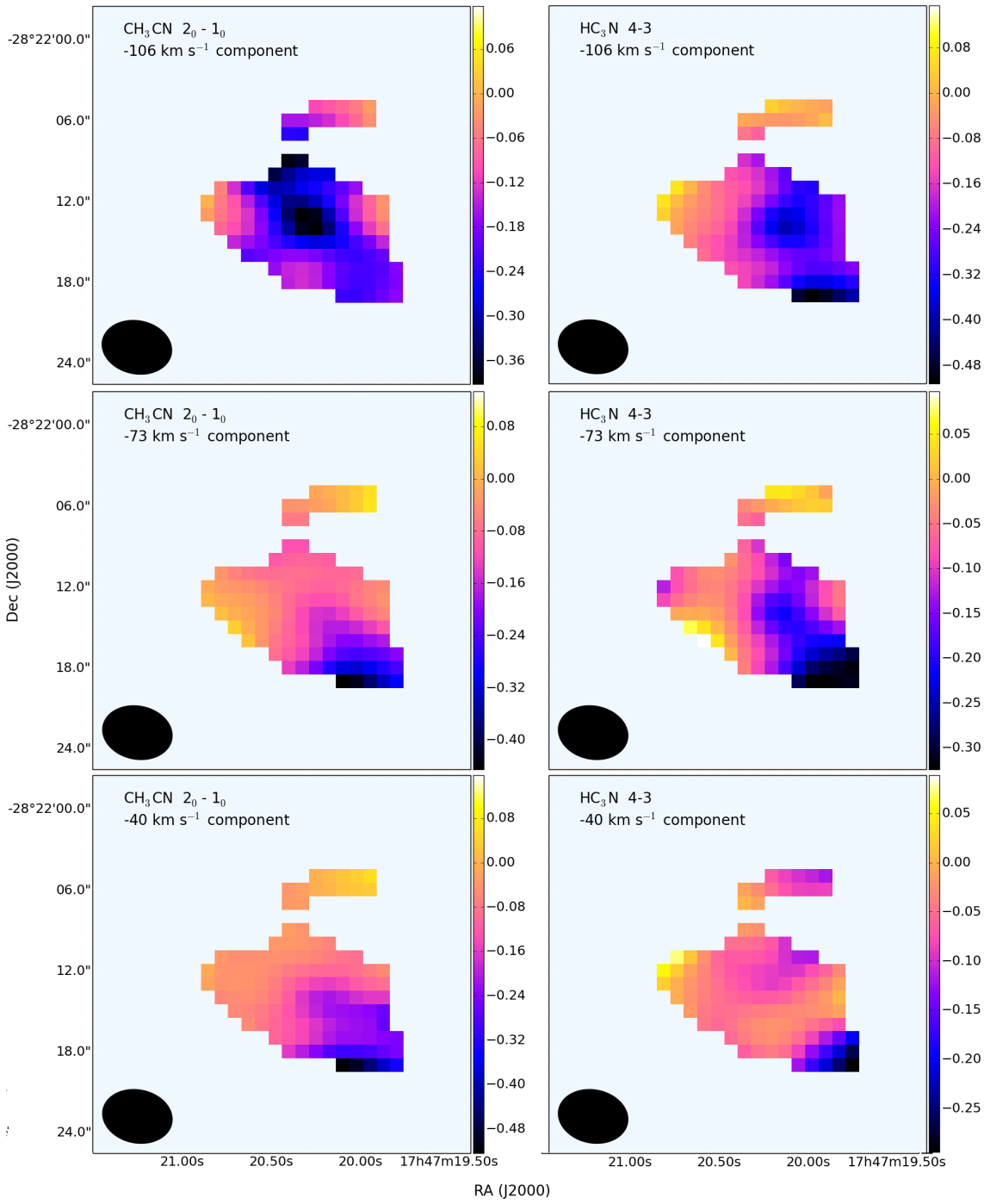

Fig. 6.5 – Line-to-continuum ratio images of HC_3N and CH_3CN integrated over the -106, -73, and -40 $\mathrm{km\,s^{-1}}$ velocity components in ATCA data. Pixels with continuum strengths $<$300 mJy $\mathrm{beam^{-1}}$ are zeroed out.

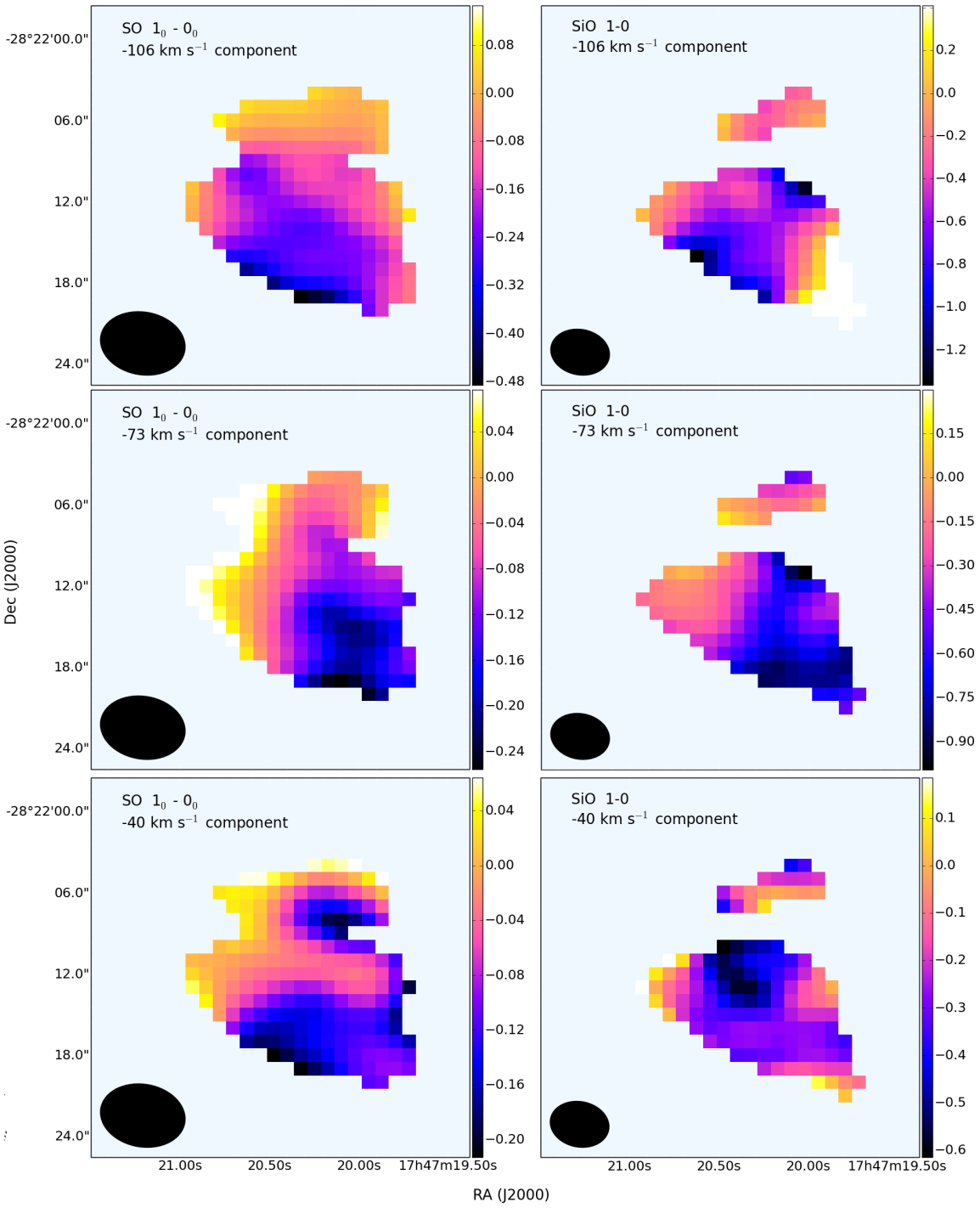

Fig. 6.6 – Line-to-continuum ratio images of SO and SiO integrated over the -106, -73, and -40 km s^{-1} velocity components in ATCA data. Pixels with continuum strengths $<$300 mJy beam^{-1} are zeroed out.

The dust cloudlets affect the surrounding gas in a few important capacities. First, they provide efficient coolants to gas, enabling gas to condense and form gas halos surrounding the dust cloudlets. According to the model, the halos should be 1 to 2 orders of magnitude larger in spatial extent than the dust cloudlets (Tsytovich et al. 2014). Thus, in the Galactic Center, these halos may occupy size scales of 500 to 5000 AU. Compared to the surrounding diffuse material, the gas density in the halo is enhanced by a factor of T_0/T_{dust}, where T_0 is the temperature in the initial diffuse medium. From observations in Galactic disk diffuse clouds, this factor is typically 10 to 20; in Galactic Bar and Center clouds, this factor may be more like 20 to 30. We note that this factor is similar to the observed density margin between translucent clouds and diffuse clouds.

The dust cloudlet/gas halo substructure also enhances grain surface chemistry on the cold dust grains (Ivlev et al. in prep). Ongoing investigations indicate that the molecular hydrogen fraction $f(H_2)$ in the entire body of diffuse gas can be significantly enhanced with this structure compared to a homogeneous dust structure, providing better consistency with observations (A. Ivlev 2016, private communication; Ivlev et al. in prep). The substructure should also enhance the production of ice mantle species including H_2CO, CH_3OH, and NH_2CHO. In fact, similar physical structures have been implicated in chemical models attempting to account for the chemistry observed in other Galactic environments due to the improved efficiency of chemical reactions in conditions of high dust densities (A. Vasyunin, private communication).

6.4 Implications for Diffuse and Translucent Cloud Structure and Chemistry

While translucent clouds have typically been treated as cohesive systems, interferometric data shows that they contain a clumpy structure as traced by complex organic molecules. From the VLA data, we have an upper limit to the clump size corresponding to 8000 AU; this is slightly larger than the size scales of the gas halos predicted by the models, of up to a few thousand AU. Additionally, as the translucent clouds in the line-of-sight to Sgr B2 are measured to have higher gas densities than the diffuse clouds by a factor of 20 to 30 times, it is quite plausible that the clumps composing the translucent clouds are the predicted gas halos. This could explain the complex molecular chemistry observed within them, as the organic species may be produced due to the presence of the dust cloudlets.

The dust and gas distribution may resolve several issues pertaining to the chemistry and physics of the diffuse ISM. First, recent results from Herschel data indicate that the gas and dust temperatures are entirely decoupled in the Central Molecular Zone, with very warm gas temperatures of $>$50 K in dense gas (Morris & Serabyn 1996) to over 300 K in more diffuse material (Oka et al. 2005), but with cold dust temperatures of 15 to 20 K throughout (Ginsburg et al. 2016). The predicted dust distribution accounts for the observed discrepancy.

Secondly, the structure can enhance the predicted abundances of molecules in the diffuse ISM. For numerous molecules, models underpredict the observed abundances by multiple orders of magnitude (Neufeld et al. 2015). The dense, cold dust enables the formation of ice mantles needed for forming NH_2CHO, for instance. Through mechanical exchange between the gas halo and the ambient diffuse media, the structure may also populate the diffuse ISM with smaller grain surface species like H_2CO that are not as easily destroyed.

Third, the theory predicts a distinct structure in the highly X-ray and CR irradiated material in the Galactic Center than in the disk. The predicted size scales for the dust cloudlets and gas halos are one to two orders of magnitude larger. The larger cloudlets in the Galactic Center may be more effective at enhancing the grain surface molecules than the smaller systems in the disk diffuse clouds. This is consistent with the results of the previous chapters, in which many molecules, and particularly complex organic molecules were observed to be more abundant in the Galactic Center clouds. Additionally, in the previous chapter, the kinematic profile of CS suggests a different structure in the Galactic Center diffuse and translucent clouds than in the disk clouds. Whereas the diffuse clouds in the disk contain many distinct embedded clumps of lower individual optical depths, the higher density clouds in the Galactic Center have more consistent and well-defined borders, with higher integrated optical depths. This too is consistent with the predicted differences in the structures in the Galactic Center and disk.

6.5 Future Prospects

The direct observations of the cloud substructure and the theoretical predictions suggest a very different structure for diffuse and translucent clouds. The proposed dust structure solves numerous questions raise by observations, and furthermore, it provides testable predictions. The interferometric data indicates that it is possible to directly observe the substructure in different molecules. In fact, the COM transitions are among the weakest lines detected in the line-of-sightmaterial by the PRIMOS data, so that it will be easier to observe the spatial structure of most other molecules. Therefore, we have access to the physical and chemical structure of the diffuse and translucent ISM. Utilizing this will involve observing spectral lines of multiple molecules at matched resolution to determine whether some species exhibit a greater deal of clumping than others. It is quite plausible that the COMs

will preferentially populate the densest or most UV-shielded material, whereas H_2CO may exhibit a lesser degree of enhancement in the clumps. These can be compared with HI distributions as measured by 21 cm line absorption and the H_2 distribution probed by c-C_3H_2.

In this way, we can directly observe the distributions of HI, H_2, and various molecules, combining multiple spatial resolutions as allowed by the source geometry and the signal strength. These measurements enable accurate constraints on the layered physical and chemical structure of the diffuse and translucent ISM, providing localized conditions that can be directly compared with model predictions. Iteratively through measurements and models, this material may provide an excellent opportunity to compile and demonstrate a working understanding of the physics and chemistry of the diffuse ISM.

Chapter 7

Concluding Remarks

7.1 Summary and Future Studies

This dissertation has highlighted the rich spectral line data that is now easily attainable with new-generation radio telescopes. We have explored a few of the many facets of these data sets, including:

- the increased potential for serendipity in broadband data sets compared to last-generation data sets, and the capacity to complete many different projects with a single observation requiring limited telescope time (Chapter 6).

- the need for a comprehensive, full-view perspective of interstellar molecular chemistry in order to advance astrochemistry toward being a predictive science (§1.2).

- the need for automated data handling to interpret data and to achieve this full-view perspective (Chapter 3).

- an integrative approach incorporating the kinematics and chemical abundances of tens of molecules to constrain the physical conditions of molecular-rich material in highly complex regions (Chapters 4 and 5).

In this work I presented scripts designed to fully fit broadband spectra and perform line identification (Chapter 3). I demonstrated the performance on data over the full span of centimeter wavelengths toward Sgr B2, the most line-dense object in the Galaxy. The scripts operate in an empirical rather than model-based way and provide output that characterizes the kinematics of the source.

Full spectral characterization is essential for inspecting the spatial distributions and analyzing data cubes for all but the strongest transitions. The utility of the code will increase dramatically if it is interfaced with the image domain, and even further when it is interfaced with a model for molecular line radiation. The method presented here is distinct

from that used in alternative efforts for broadband data analyses (Teuben et al. 2013; Möller et al. 2015), and provides advantages particularly for sources with very complex kinematic structures. Regardless of whether this or a different code becomes the foundation of a more widely adopted software for automated data handling, it is located in the context of exploring the best approach to the new challenges and possibilities introduced by the new generation broadband radio instruments.

We utilized the output of the code, coupled with inspection of the cubes, to characterize the chemistry present in rather exotic material in Sgr B2(N) (Chapter 4). The data suggests that the material is a PDR/XDR, and a great diversity of chemistry is present, including many complex O-bearing molecules like aldehydes, small S-bearing species, and N-bearing molecules including nitriles (with –C≡N) and imines (with –C=NH); imines in particular are believed to be biologically relevant. The detected molecules may be interesting targets to search for in other PDRs. The analysis of the code output additionally suggests that the molecular gas of interest is located near the star forming cores of Sgr B2, rather than in the envelope as previously proposed, and is affected by localized conditions in the core.

Additionally, we characterized the molecular content and structure of diffuse and translucent clouds located in the Galactic disk, Bar, and Center in the line-of-sight to Sgr B2. Data collected with the GBT reveal a greater deal of molecular complexity than previously known in this material, and complex organic molecules are observed in considerably high abundances. The observations introduce new puzzles to be addressed by chemical modeling efforts, particularly related to (1) the observed S-bearing molecule abundances and (2) the formation of COMs in material that would not be classically expected to form ice mantles. Interferometric observations indicate that the systems may be more complex than previously known, containing significant spatial structure in transitions of COMs. The observations of spatial structure enable direct tests of the coupled physics and chemistry

in this material, and direct constraints on the layered chemical abundances present. This provides a novel opportunity to compare chemical models to accurate and comprehensive measurements of localized chemistry and to utilize precise constraints on physical conditions.

Looking to the future, I anticipate dramatic advances in our understanding of the chemistry and physics of the ISM. These are made possible largely by the onset of the broadband radio astronomy era, but also by new laboratory setups designed to directly test chemistry in conditions analogous to those present in the ISM. The different projects presented here should be taken in the context of the larger challenge of understanding the chemistry of the Universe. Each project explores a different parameter space opened up by the arrival of broadband instruments. Each presented project enables us to peek behind a different curtain, to report that which is most obvious, but moreover to prepare for both the challenges and the bounty that lie ahead.

References

Aannestad, P. A. 1973, ApJS, 25

Allodi, M. A., Baragiola, R. A., Baratta, G. A., Barucci, M. A., Blake, G. A., Boduch, P., Brucato, J. R., Contreras, C., Cuylle, S. H., Fulvio, D., Gudipati, M. S., Ioppolo, S., Kaňuchová, Z., Lignell, A., Linnartz, H., Palumbo, M. E., Raut, U., Rothard, H., Salama, F., Savchenko, E. V., Sciamma-O'Brien, E., & Strazzulla, G. 2013, Space Sci. Rev., 180, 101

Amo-Baladrón, M. A., Martín-Pintado, J., Morris, M. R., Muno, M. P., & Rodríguez-Fernández, N. J. 2009, ApJ, 694, 943

Ao, Y., Henkel, C., Menten, K. M., Requena-Torres, M. A., Stanke, T., Mauersberger, R., Aalto, S., Mühle, S., & Mangum, J. 2013, A&A, 550, A135

Bell, T. A., Viti, S., Williams, D. A., Crawford, I. A., & Price, R. J. 2005, MNRAS, 357, 961

Belloche, A., Garrod, R. T., Müller, H. S. P., & Menten, K. M. 2014, Science, 345, 1584

Belloche, A., Menten, K. M., Comito, C., Müller, H. S. P., Schilke, P., Ott, J., Thorwirth, S., & Hieret, C. 2008, A&A, 482, 179

Belloche, A., Müller, H. S. P., Menten, K. M., Schilke, P., & Comito, C. 2013, A&A, 559, A47

Blake, G. A., Sutton, E. C., Masson, C. R., & Phillips, T. G. 1987, ApJ, 315, 621

Blank, M., Morris, M. R., Frank, A., Carroll-Nellenback, J. J., & Duschl, W. J. 2016, MNRAS

Boger, G. I. & Sternberg, A. 2005, ApJ, 632, 302

Caselli, P., Hartquist, T. W., & Havnes, O. 1997, A&A, 322, 296

Cecchi-Pestellini, C., Williams, D. A., Viti, S., & Casu, S. 2009, ApJ, 706, 1429

Cheung, A. C., Rank, D. M., Townes, C. H., Thornton, D. D., & Welch, W. J. 1968, Physical Review Letters, 21, 1701

Chin, Y.-N., Henkel, C., Whiteoak, J. B., Langer, N., & Churchwell, E. B. 1996, A&A, 305, 960

Contreras, Y., Garay, G., Rathborne, J. M., & Sanhueza, P. 2016, MNRAS, 456, 2041

Corby, J. F., Jones, P. A., Cunningham, M. R., Menten, K. M., Belloche, A., Schwab, F. R., Walsh, A. J., Balnozan, E., Bronfman, L., Lo, N., & Remijan, A. J. 2015, MNRAS, 452, 3969

Cragg, D. M., Johns, K. P., Godfrey, P. D., & Brown, R. D. 1992, MNRAS, 259, 203

Crockett, N. R., Bergin, E. A., Neill, J. L., Favre, C., Schilke, P., Lis, D. C., Bell, T. A., Blake, G., Cernicharo, J., Emprechtinger, M., Esplugues, G. B., Gupta, H., Kleshcheva, M., Lord, S., Marcelino, N., McGuire, B. A., Pearson, J., Phillips, T. G., Plume, R., van der Tak, F., Tercero, B., & Yu, S. 2014, ApJ, 787, 112

Crutcher, R. M., Roberts, D. A., Mehringer, D. M., & Troland, T. H. 1996, ApJ, 462, L79

Danks, A. C., Federman, S. R., & Lambert, D. L. 1984, A&A, 130, 62

De Pree, C. G., Gaume, R. A., Goss, W. M., & Claussen, M. J. 1995, ApJ, 451, 284

De Pree, C. G., Peters, T., Mac Low, M. M., Wilner, D. J., Goss, W. M., Galván-Madrid, R., Keto, E. R., Klessen, R. S., & Monsrud, A. 2015, ApJ, 815, 123

de Vicente, P., Martin-Pintado, J., & Wilson, T. L. 1997, A&A, 320, 957

Douglas, A. E. & Herzberg, G. 1941, ApJ, 94, 381

Drdla, K., Knapp, G. R., & van Dishoeck, E. F. 1989, ApJ, 345, 815

Dutta, P., Chengalur, J. N., Roy, N., Goss, W. M., Arjunwadkar, M., Minter, A. H., Brogan, C. L., & Lazio, T. J. W. 2014, MNRAS, 442, 647

Ebisawa, Y., Inokuma, H., Sakai, N., Menten, K. M., Maezawa, H., & Yamamoto, S. 2015, ApJ, 815, 13

Elitzur, M. 1992, ARA&A, 30, 75

Faure, A., Remijan, A. J., Szalewicz, K., & Wiesenfeld, L. 2014, ApJ, 783, 72

Fernández-López, M., Arce, H. G., Looney, L., Mundy, L. G., Storm, S., Teuben, P. J., Lee, K., Segura-Cox, D., Isella, A., Tobin, J. J., Rosolowsky, E., Plunkett, A., Kwon, W., Kauffmann, J., Ostriker, E., Tassis, K., Shirley, Y. L., & Pound, M. 2014, ApJ, 790, L19

Ferrière, K. M. 2001, Reviews of Modern Physics, 73, 1031

Flower, D. R., Pineau Des Forêts, G., & Rabli, D. 2010, MNRAS, 409, 29

Flower, D. R., Pineau des Forets, G., & Walmsley, C. M. 1995, A&A, 294, 815

Frerking, M. A., Wilson, R. W., Linke, R. A., & Wannier, P. G. 1980, ApJ, 240, 65

Furuya, R. S., Walmsley, C. M., Nakanishi, K., Schilke, P., & Bachiller, R. 2003, A&A, 409, L21

Gardner, F. F., Boes, F., & Winnewisser, G. 1988, A&A, 196, 207

Garozzo, M., Fulvio, D., Kanuchova, Z., Palumbo, M. E., & Strazzulla, G. 2010, A&A, 509, A67

Garrod, R. T. 2013, ApJ, 765, 60

Garrod, R. T., Widicus Weaver, S. L., & Herbst, E. 2008, ApJ, 682, 283

Gaume, R. A., Claussen, M. J., de Pree, C. G., Goss, W. M., & Mehringer, D. M. 1995, ApJ, 449, 663

Genova, F., Egret, D., Bienaymé, O., Bonnarel, F., Dubois, P., Fernique, P., Jasniewicz, G., Lesteven, S., Monier, R., Ochsenbein, F., & Wenger, M. 2000, A&AS, 143, 1

Gerin, M., de Luca, M., Black, J., Goicoechea, J. R., Herbst, E., Neufeld, D. A., Falgarone, E., Godard, B., Pearson, J. C., Lis, D. C., Phillips, T. G., Bell, T. A., Sonnentrucker, P., Boulanger, F., Cernicharo, J., Coutens, A., Dartois, E., Encrenaz, P., Giesen, T., Goldsmith, P. F., Gupta, H., Gry, C., Hennebelle, P., Hily-Blant, P., Joblin, C., Kazmierczak, M., Kolos, R., Krelowski, J., Martin-Pintado, J., Monje, R., Mookerjea, B., Perault, M., Persson, C., Plume, R., Rimmer, P. B., Salez, M., Schmidt, M., Stutzki, J., Teyssier, D., Vastel, C., Yu, S., Contursi, A., Menten, K., Geballe, T., Schlemmer, S., Shipman, R., Tielens, A. G. G. M., Philipp-May, S., Cros, A., Zmuidzinas, J., Samoska, L. A., Klein, K., & Lorenzani, A. 2010, A&A, 518, L110

Gerin, M., Falgarone, E., Joulain, K., Kopp, M., Le Bourlot, J., Pineau des Forets, G., Roueff, E., & Schilke, P. 1997, A&A, 318, 579

Gibb, E. L., Whittet, D. C. B., Boogert, A. C. A., & Tielens, A. G. G. M. 2004, ApJS, 151, 35

Ginsburg, A., Henkel, C., Ao, Y., Riquelme, D., Kauffman, J., Pillai, T., Mills, E., Requena-Torres, M., Immer, K., Testi, L., Ott, J., Bally, J., Battersby, C., Darling, J., Aalto, S., Stanke, T., Kendrew, S., Kruijssed, J., Longmore, S., Dale, J., Guesten, R., & Menten, K. 2016, in Proceedings of the 6th Zermatt ISM Symposium: Conditions and Impact of Star Formation From Lab to Space, European Astronomical Society Publications

Godard, B., Falgarone, E., Gerin, M., Lis, D. C., De Luca, M., Black, J. H., Goicoechea, J. R., Cernicharo, J., Neufeld, D. A., Menten, K. M., & Emprechtinger, M. 2012, A&A, 540, A87

Godard, B., Falgarone, E., & Pineau Des Forêts, G. 2009, A&A, 495, 847

Godard, B., Falgarone, E., & Pineau des Forêts, G. 2014, A&A, 570, A27

Godfrey, P. D., Brown, R. D., Robinson, B. J., & Sinclair, M. W. 1973, Astrophys. Lett., 13, 119

Goicoechea, J. R., Pety, J., Gerin, M., Teyssier, D., Roueff, E., Hily-Blant, P., & Baek, S. 2006, A&A, 456, 565

Goicoechea, J. R., Rodríguez-Fernández, N. J., & Cernicharo, J. 2003, Astronomische Nachrichten Supplement, 324, 139

Gratier, P., Pety, J., Guzmán, V., Gerin, M., Goicoechea, J. R., Roueff, E., & Faure, A. 2013, A&A, 557, A101

Gray, M. D., Doel, R. C., & Field, D. 1991, MNRAS, 252, 30

Greaves, J. S. & Nyman, L.-A. 1996, A&A, 305, 950

Greaves, J. S., Ohishi, M., & Nyman, L.-A. 1996, A&A, 307, 898

Greaves, J. S., White, G. J., Ohishi, M., Hasegawa, T., & Sunada, K. 1992, A&A, 260, 381

Greaves, J. S. & Williams, P. G. 1994, A&A, 290

Guélin, M., Brouillet, N., Cernicharo, J., Combes, F., & Wootten, A. 2008, Ap&SS, 313, 45

Güver, T. & Özel, F. 2009, MNRAS, 400, 2050

Guzmán, V. V., Pety, J., Goicoechea, J. R., Gerin, M., Roueff, E., Gratier, P., & Öberg, K. I. 2015, ApJ, 800, L33

Guzmán, V. V., Pety, J., Gratier, P., Goicoechea, J. R., Gerin, M., Roueff, E., Le Petit, F., & Le Bourlot, J. 2014, Faraday Discussions, 168, 103

Hasegawa, T., Sato, F., Whiteoak, J. B., & Miyawaki, R. 1994, ApJ, 429, L77

Hasegawa, T. I. & Herbst, E. 1993, MNRAS, 263, 589

Hasegawa, T. I., Herbst, E., & Leung, C. M. 1992, ApJS, 82, 167

Hatchell, J., Fuller, G. A., & Millar, T. J. 2001, A&A, 372, 281

Heiles, C. 1997, ApJ, 481, 193

Heiles, C. & Stinebring, D. 2007, in Astronomical Society of the Pacific Conference Series, Vol. 365, SINS - Small Ionized and Neutral Structures in the Diffuse Interstellar Medium, ed. M. Haverkorn & W. M. Goss, 331

Herbst, E. & Klemperer, W. 1973, ApJ, 185, 505

Hewish, A., Bell, S. J., Pilkington, J. D. H., Scott, P. F., & Collins, R. A. 1968, Nature, 217, 709

Ho, P. T. P. & Townes, C. H. 1983, ARA&A, 21, 239

Hocuk, S., Cazaux, S., Spaans, M., & Caselli, P. 2016, MNRAS, 456, 2586

Hodrick, R. J. & Prescott, E. C. 1997, Journal of Money, Credit and Banking, 29, 1

Hollenbach, D. J. & Tielens, A. G. G. M. 1997, ARA&A, 35, 179

Hollis, J. M. 2005, in IAU Symposium, Vol. 231, Astrochemistry: Recent Successes and Current Challenges, ed. D. C. Lis, G. A. Blake, & E. Herbst, 227–236

Hollis, J. M., Lovas, F. J., & Jewell, P. R. 2000, ApJ, 540, L107

Hollis, J. M., Pedelty, J. A., Boboltz, D. A., Liu, S.-Y., Snyder, L. E., Palmer, P., Lovas, F. J., & Jewell, P. R. 2003, ApJ, 596, L235

Hubble, E. P. 1926, ApJ, 64

Huettemeister, S., Dahmen, G., Mauersberger, R., Henkel, C., Wilson, T. L., & Martin-Pintado, J. 1998, A&A, 334, 646

Huettemeister, S., Wilson, T. L., Mauersberger, R., Lemme, C., Dahmen, G., & Henkel, C. 1995, A&A, 294, 667

Indriolo, N., Neufeld, D. A., Gerin, M., Schilke, P., Benz, A. O., Winkel, B., Menten, K. M., Chambers, E. T., Black, J. H., Bruderer, S., Falgarone, E., Godard, B., Goicoechea, J. R., Gupta, H., Lis, D. C., Ossenkopf, V., Persson, C. M., Sonnentrucker, P., van der Tak, F. F. S., van Dishoeck, E. F., Wolfire, M. G., & Wyrowski, F. 2015, ApJ, 800, 40

Ioppolo, S., Fedoseev, G., Lamberts, T., Romanzin, C., & Linnartz, H. 2013, Rev. Sci. Instrum., 84, 073112

Irvine, W. M., Goldsmith, P. F., & Hjalmarson, A. 1987, in Astrophysics and Space Science Library, Vol. 134, Interstellar Processes, ed. D. J. Hollenbach & H. A. Thronson, Jr., 561–609

Jones, P. A., Burton, M. G., Cunningham, M. R., Menten, K. M., Schilke, P., Belloche, A., Leurini, S., Ott, J., & Walsh, A. J. 2008, MNRAS, 386, 117

Jones, P. A., Burton, M. G., Cunningham, M. R., Requena-Torres, M. A., Menten, K. M., Schilke, P., Belloche, A., Leurini, S., Martín-Pintado, J., Ott, J., & Walsh, A. J. 2012, MNRAS, 419, 2961

Jones, P. A., Burton, M. G., Tothill, N. F. H., & Cunningham, M. R. 2011, MNRAS, 411, 2293

Karlsson, R., Sandqvist, Å., Hjalmarson, Å., Winnberg, A., Fathi, K., Frisk, U., & Olberg, M. 2013, A&A, 554, A141

Kaňuchová, Z., Urso, R. G., Baratta, G. A., Brucato, J. R., Palumbo, M. E., & Strazzulla, G. 2016, A&A, 585, A155

Lang, C. C., Morris, M., & Echevarria, L. 1999, ApJ, 526, 727

Langer, W. D., Graedel, T. E., Frerking, M. A., & Armentrout, P. B. 1984, ApJ, 277, 581

Le Petit, F., Ruaud, M., Bron, E., Godard, B., Roueff, E., Languignon, D., & Le Bourlot, J. 2016, A&A, 585, A105

Lindberg, J. E., Aalto, S., Costagliola, F., Pérez-Beaupuits, J.-P., Monje, R., & Muller, S. 2011, A&A, 527, A150

Linke, R. A., Stark, A. A., & Frerking, M. A. 1981, ApJ, 243, 147

Lis, D. C., Schilke, P., Bergin, E. A., & Emprechtinger, M. 2012, Philosophical Transactions of the Royal Society of London Series A, 370, 5162

Liszt, H., Sonnentrucker, P., Cordiner, M., & Gerin, M. 2012, ApJ, 753, L28

Liszt, H. S., Lucas, R., & Pety, J. 2006, A&A, 448, 253

Liszt, H. S., Pety, J., & Lucas, R. 2008, A&A, 486, 493

Liu, S.-Y. & Snyder, L. E. 1999, ApJ, 523, 683

Loeffler, M. J., Dukes, C. A., Christoffersen, R., & Baragiola, R. A. 2016, Meteoritics and Planetary Science, 51, 261

Loomis, R. A., Zaleski, D. P., Steber, A. L., Neill, J. L., Muckle, M. T., Harris, B. J., Hollis, J. M., Jewell, P. R., Lattanzi, V., Lovas, F. J., Martinez, Jr., O., McCarthy, M. C., Remijan, A. J., Pate, B. H., & Corby, J. F. 2013, ApJ, 765, L9

Lovas, F. J. & Dragoset, R. A. 2004, Journal of Physical Chemistry Reference Data, 33, 177

Lovas, F. J., Hollis, J. M., Remijan, A. J., & Jewell, P. R. 2006, ApJ, 645, L137

Lucas, R. & Liszt, H. S. 1993, A&A, 276, L33

—. 2002, A&A, 384, 1054

Martín, S., Requena-Torres, M. A., Martín-Pintado, J., & Mauersberger, R. 2008, ApJ, 678, 245

Martín-Pintado, J., de Vicente, P., Rodríguez-Fernández, N. J., Fuente, A., & Planesas, P. 2000, A&A, 356, L5

Martín-Pintado, J., Rizzo, J. R., de Vicente, P., Rodríguez-Fernández, N. J., & Fuente, A. 2001, ApJ, 548, L65

Mauersberger, R., Henkel, C., Langer, N., & Chin, Y.-N. 1996, A&A, 313, L1

McDowell, R. S. 1988, Journal of Chemical Physics, 88, 356

—. 1990, Journal of Chemical Physics, 93, 2801

McGuire, B. A., Carroll, P. B., Dollhopf, N. M., Crockett, N. R., Corby, J. F., Loomis, R. A., Burkhardt, A. M., Shingledecker, C., Blake, G. A., & Remijan, A. J. 2015, ApJ, 812, 76

McGuire, B. A., Carroll, P. B., Gratier, P., Guzmán, V., Pety, J., Roueff, E., Gerin, M., Blake, G. A., & Remijan, A. J. 2014a, ApJ, 783, 36

McGuire, B. A., Carroll, P. B., Loomis, R. A., Blake, G. A., Hollis, J. M., Lovas, F. J., Jewell, P. R., & Remijan, A. J. 2013, ApJ, 774, 56

McGuire, B. A., Carroll, P. B., Sanders, J. L., Weaver, S. L. W., Blake, G. A., & Remijan, A. J. 2014b, MNRAS, 442, 2901

McGuire, B. A., Loomis, R. A., Charness, C. M., Corby, J. F., Blake, G. A., Hollis, J. M., Lovas, F. J., Jewell, P. R., & Remijan, A. J. 2012, ApJ, 758, L33

McKellar, A. 1940, PASP, 52, 187

Mehringer, D. M. & Menten, K. M. 1997, ApJ, 474, 346

Meijerink, R., Spaans, M., & Israel, F. P. 2007, A&A, 461, 793

Menten, K. 1991, in Astronomical Society of the Pacific Conference Series, Vol. 16, Atoms, Ions and Molecules: New Results in Spectral Line Astrophysics, ed. A. D. Haschick & P. T. P. Ho, 119

Menten, K. M. 2004, in The Dense Interstellar Medium in Galaxies, ed. S. Pfalzner, C. Kramer, C. Staubmeier, & A. Heithausen, Vol. 91, 69

Menten, K. M. & van der Tak, F. F. S. 2004, A&A, 414, 289

Menten, K. M., Wyrowski, F., Belloche, A., Güsten, R., Dedes, L., & Müller, H. S. P. 2011, A&A, 525, A77

Miao, Y., Mehringer, D. M., Kuan, Y.-J., & Snyder, L. E. 1995, ApJ, 445, L59

Milam, S. N., Savage, C., Brewster, M. A., Ziurys, L. M., & Wyckoff, S. 2005, ApJ, 634, 1126

Minh, Y. C. & Irvine, W. M. 2006, New Astronomy, 11, 594

Molinari, S., Bally, J., Noriega-Crespo, A., Compiègne, M., Bernard, J. P., Paradis, D., Martin, P., Testi, L., Barlow, M., Moore, T., Plume, R., Swinyard, B., Zavagno, A., Calzoletti, L., Di Giorgio, A. M., Elia, D., Faustini, F., Natoli, P., Pestalozzi, M., Pezzuto, S., Piacentini, F., Polenta, G., Polychroni, D., Schisano, E., Traficante, A., Veneziani, M., Battersby, C., Burton, M., Carey, S., Fukui, Y., Li, J. Z., Lord, S. D., Morgan, L., Motte, F., Schuller, F., Stringfellow, G. S., Tan, J. C., Thompson, M. A., Ward-Thompson, D., White, G., & Umana, G. 2011, ApJ, 735, L33

Möller, T., Endres, C., & Schilke, P. 2015, ArXiv e-prints

Morris, M. & Serabyn, E. 1996, ARA&A, 34, 645

Müller, H. S. P., Schlöder, F., Stutzki, J., & Winnewisser, G. 2005, Journal of Molecular Structure, 742, 215

Neill, J. L., Bergin, E. A., Lis, D. C., Schilke, P., Crockett, N. R., Favre, C., Emprechtinger, M., Comito, C., Qin, S.-L., Anderson, D. E., Burkhardt, A. M., Chen, J.-H., Harris, B. J., Lord, S. D., McGuire, B. A., McNeill, T. D., Monje, R. R., Phillips, T. G., Steber, A. L., Vasyunina, T., & Yu, S. 2014, ApJ, 789, 8

Neill, J. L., Muckle, M. T., Zaleski, D. P., Steber, A. L., Pate, B. H., Lattanzi, V., Spezzano, S., McCarthy, M. C., & Remijan, A. J. 2012, ApJ, 755, 153

Neufeld, D. A., Bergin, E. A., Melnick, G. J., & Goldsmith, P. F. 2003, ApJ, 590, 882

Neufeld, D. A., Godard, B., Gerin, M., Pineau des Forêts, G., Bernier, C., Falgarone, E., Graf, U. U., Güsten, R., Herbst, E., Lesaffre, P., Schilke, P., Sonnentrucker, P., & Wiesemeyer, H. 2015, A&A, 577, A49

Neufeld, D. A., Kaufman, M. J., Goldsmith, P. F., Hollenbach, D. J., & Plume, R. 2002, ApJ, 580, 278

Nummelin, A., Bergman, P., Hjalmarson, Å., Friberg, P., Irvine, W. M., Millar, T. J., Ohishi, M., & Saito, S. 1998, ApJS, 117, 427

Nyman, L.-A. 1984, A&A, 141, 323

Ohishi, M., Irvine, W. M., & Kaifu, N. 1992, in IAU Symposium, Vol. 150, Astrochemistry of Cosmic Phenomena, ed. P. D. Singh, 171

Ohishi, M. & Kaifu, N. 1998, Faraday Discussions, 109, 205

Oka, T., Geballe, T. R., Goto, M., Usuda, T., & McCall, B. J. 2005, ApJ, 632, 882

Ossenkopf, V., Müller, H. S. P., Lis, D. C., Schilke, P., Bell, T. A., Bruderer, S., Bergin, E., Ceccarelli, C., Comito, C., Stutzki, J., Bacman, A., Baudry, A., Benz, A. O., Benedettini, M., Berne, O., Blake, G., Boogert, A., Bottinelli, S., Boulanger, F., Cabrit, S., Caselli, P., Caux, E., Cernicharo, J., Codella, C., Coutens, A., Crimier, N., Crockett, N. R., Daniel, F., Demyk, K., Dieleman, P., Dominik, C., Dubernet, M. L., Emprechtinger, M., Encrenaz, P., Falgarone, E., France, K., Fuente, A., Gerin, M., Giesen, T. F., di Giorgio, A. M., Goicoechea, J. R., Goldsmith, P. F., Güsten, R., Harris, A., Helmich, F., Herbst, E., Hily-Blant, P., Jacobs, K., Jacq, T., Joblin, C., Johnstone, D., Kahane, C., Kama, M., Klein, T., Klotz, A., Kramer, C., Langer, W., Lefloch, B., Leinz, C., Lorenzani, A., Lord, S. D., Maret, S., Martin, P. G., Martin-Pintado, J., McCoey, C., Melchior, M., Melnick, G. J., Menten, K. M., Mookerjea, B., Morris, P., Murphy, J. A., Neufeld, D. A., Nisini, B., Pacheco, S., Pagani, L., Parise, B., Pearson, J. C., Pérault, M., Phillips, T. G., Plume, R., Quin, S.-L., Rizzo, R., Röllig, M., Salez, M., Saraceno, P., Schlemmer, S., Simon, R., Schuster, K., van der Tak, F. F. S., Tielens, A. G. G. M., Teyssier, D., Trappe, N., Vastel, C., Viti, S., Wakelam, V., Walters, A., Wang, S., Whyborn, N., van der Wiel, M., Yorke, H. W., Yu, S., & Zmuidzinas, J. 2010, A&A, 518, L111

Paardekooper, D. M., Bossa, J. B., Isokoski, K., & Linnartz, H. 2014, Rev. Sci. Instrum., 85, 104501

Palumbo, M. E., Baratta, G., Fulvio, D., Garozzo, M., Ioppolo, S., Kanuchova, Z., Leto, G., Sangiorgio, I., & Strazzulla, G. 2011, in IAU Symposium, Vol. 280, The Molecular Universe, ed. J. Cernicharo & R. Bachiller

Pardo, J. R. & Cernicharo, J. 2007, ApJ, 654, 978

Penzias, A. A. 1981, ApJ, 249, 513

Peretto, N., Fuller, G. A., Duarte-Cabral, A., Avison, A., Hennebelle, P., Pineda, J. E.,

André, P., Bontemps, S., Motte, F., Schneider, N., & Molinari, S. 2013, A&A, 555, A112

Petrie, S. 1996, MNRAS, 281, 666

Pety, J., Gratier, P., Guzmán, V., Roueff, E., Gerin, M., Goicoechea, J. R., Bardeau, S., Sievers, A., Le Petit, F., Le Bourlot, J., Belloche, A., & Talbi, D. 2012, A&A, 548, A68

Pety, J., Teyssier, D., Fossé, D., Gerin, M., Roueff, E., Abergel, A., Habart, E., & Cernicharo, J. 2005, A&A, 435, 885

Pickett, H. M., Poynter, R. L., Cohen, E. A., Delitsky, M. L., Pearson, J. C., & Müller, H. S. P. 1998, J. Quant. Spec. Radiat. Transf., 60, 883

Pineau des Forets, G., Flower, D. R., & Chieze, J.-P. 1997, in IAU Symposium, Vol. 182, Herbig-Haro Flows and the Birth of Stars, ed. B. Reipurth & C. Bertout, 199–212

Ponti, G., Morris, M. R., Terrier, R., Haberl, F., Sturm, R., Clavel, M., Soldi, S., Goldwurm, A., Predehl, P., Nandra, K., Bélanger, G., Warwick, R. S., & Tatischeff, V. 2015, MNRAS, 453, 172

Price, R. J., Viti, S., & Williams, D. A. 2003, MNRAS, 343, 1257

Qin, S.-L., Schilke, P., Comito, C., Möller, T., Rolffs, R., Müller, H. S. P., Belloche, A., Menten, K. M., Lis, D. C., Phillips, T. G., Bergin, E. A., Bell, T. A., Crockett, N. R., Blake, G. A., Cabrit, S., Caux, E., Ceccarelli, C., Cernicharo, J., Daniel, F., Dubernet, M.-L., Emprechtinger, M., Encrenaz, P., Falgarone, E., Gerin, M., Giesen, T. F., Goicoechea, J. R., Goldsmith, P. F., Gupta, H., Herbst, E., Joblin, C., Johnstone, D., Langer, W. D., Lord, S. D., Maret, S., Martin, P. G., Melnick, G. J., Morris, P., Murphy, J. A., Neufeld, D. A., Ossenkopf, V., Pagani, L., Pearson, J. C., Pérault, M., Plume,

R., Salez, M., Schlemmer, S., Stutzki, J., Trappe, N., van der Tak, F. F. S., Vastel, C., Wang, S., Yorke, H. W., Yu, S., Zmuidzinas, J., Boogert, A., Güsten, R., Hartogh, P., Honingh, N., Karpov, A., Kooi, J., Krieg, J.-M., Schieder, R., Diez-Gonzalez, M. C., Bachiller, R., Martin-Pintado, J., Baechtold, W., Olberg, M., Nordh, L. H., Gill, J. L., & Chattopadhyay, G. 2010, A&A, 521, L14

Qin, S.-L., Schilke, P., Rolffs, R., Comito, C., Lis, D. C., & Zhang, Q. 2011, A&A, 530, L9

Quan, D., Herbst, E., Corby, J. F., Durr, A., & Hassel, G. 2016, ApJ

Rathborne, J. M., Longmore, S. N., Jackson, J. M., Alves, J. F., Bally, J., Bastian, N., Contreras, Y., Foster, J. B., Garay, G., Kruijssen, J. M. D., Testi, L., & Walsh, A. J. 2015, ApJ, 802, 125

Remijan, A., Snyder, L. E., Liu, S.-Y., Mehringer, D., & Kuan, Y.-J. 2002, ApJ, 576, 264

Remijan, A. J., Markwick-Kemper, A., & ALMA Working Group on Spectral Line Frequencies. 2007, in Bulletin of the American Astronomical Society, Vol. 39, American Astronomical Society Meeting Abstracts, 963

Ren, J. Z., Liu, T., Wu, Y., & Li, L. 2011, MNRAS, 415, L49

Riess, A. G., Filippenko, A. V., Challis, P., Clocchiatti, A., Diercks, A., Garnavich, P. M., Gilliland, R. L., Hogan, C. J., Jha, S., Kirshner, R. P., Leibundgut, B., Phillips, M. M., Reiss, D., Schmidt, B. P., Schommer, R. A., Smith, R. C., Spyromilio, J., Stubbs, C., Suntzeff, N. B., & Tonry, J. 1998, AJ, 116, 1009

Roberge, W. G., Jones, D., Lepp, S., & Dalgarno, A. 1991, ApJS, 77, 287

Rodríguez-Fernández, N. J., Tafalla, M., Gueth, F., & Bachiller, R. 2010, A&A, 516, A98

Rollinde, E., Boissé, P., Federman, S. R., & Pan, K. 2003, A&A, 401, 215

Royster, M. J. & Yusef-Zadeh, F. 2014, in IAU Symposium, Vol. 303, The Galactic Center: Feeding and Feedback in a Normal Galactic Nucleus, ed. L. O. Sjouwerman, C. C. Lang, & J. Ott, 92–93

Rubin, R. H., Swenson, Jr., G. W., Benson, R. C., Tigelaar, H. L., & Flygare, W. H. 1971, ApJ, 169, L39

Rubin, V. C. & Ford, Jr., W. K. 1970, ApJ, 159, 379

Sakai, N., Ikeda, M., Morita, M., Sakai, T., Takano, S., Osamura, Y., & Yamamoto, S. 2007, ApJ, 663, 1174

Sargent, W. L. W., Young, P. J., Lynds, C. R., Boksenberg, A., Shortridge, K., & Hartwick, F. D. A. 1978, ApJ, 221, 731

Sato, F., Hasegawa, T., Whiteoak, J. B., & Miyawaki, R. 2000, ApJ, 535, 857

Sato, Y., Matsumi, Y., Kawasaki, M., Koichi, T., & Bersohn, R. 1995, Journal of Physical Chemistry, 99, 16307

Sault, R. J., Teuben, P. J., & Wright, M. C. H. 1995, in Astronomical Society of the Pacific Conference Series, Vol. 77, Astronomical Data Analysis Software and Systems IV, ed. R. A. Shaw, H. E. Payne, & J. J. E. Hayes, 433

Schilke, P., Walmsley, C. M., Pineau des Forets, G., & Flower, D. R. 1997, A&A, 321, 293

Schlicht, E. 2009, Journal of the Japan Statistical Society, 38, 285

Shklovsky, I. S. 1967, ApJ, 148, L1

Sinclair, M. W., Fourikis, N., Ribes, J. C., Robinson, B. J., Brown, R. D., & Godfrey, P. D. 1973, Australian Journal of Physics, 26, 85

Snow, T. P. & McCall, B. J. 2006, ARA&A, 44, 367

Snyder, L. E., Buhl, D., Zuckerman, B., & Palmer, P. 1969, Physical Review Letters, 22, 679

Snyder, L. E., Kuan, Y.-J., & Miao, Y. 1994, in Lecture Notes in Physics, Berlin Springer Verlag, Vol. 439, The Structure and Content of Molecular Clouds, ed. T. L. Wilson & K. J. Johnston, 187

Solomon, P. M. & Klemperer, W. 1972, ApJ, 178, 389

Sonnentrucker, P., Welty, D. E., Thorburn, J. A., & York, D. G. 2007, ApJS, 168, 58

Stahl, O., Casassus, S., & Wilson, T. 2008, A&A, 477, 865

Sternberg, A. & Dalgarno, A. 1995, ApJS, 99, 565

Swings, P. & Rosenfeld, L. 1937, ApJ, 86, 483

Terrier, R., Ponti, G., Bélanger, G., Decourchelle, A., Tatischeff, V., Goldwurm, A., Trap, G., Morris, M. R., & Warwick, R. 2010, ApJ, 719, 143

Teuben, P., Ip, C. Y., Mundy, L., & Varshney, A. 2013, in Astronomical Society of the Pacific Conference Series, Vol. 475, Astronomical Data Analysis Software and Systems XXII, ed. D. N. Friedel, 263

Thaddeus, P., Gottlieb, C. A., Hjalmarson, A., Johansson, L. E. B., Irvine, W. M., Friberg, P., & Linke, R. A. 1985, ApJ, 294, L49

Tideswell, D. M., Fuller, G. A., Millar, T. J., & Markwick, A. J. 2010, A&A, 510, A85

Tielens, A. G. G. M. & Allamandola, L. J. 1987, in Astrophysics and Space Science Library, Vol. 134, Interstellar Processes, ed. D. J. Hollenbach & H. A. Thronson, Jr., 397–469

Tielens, A. G. G. M., Meixner, M. M., van der Werf, P. P., Bregman, J., Tauber, J. A., Stutzki, J., & Rank, D. 1993, Science, 262, 86

Tsytovich, V. N., Ivlev, A. V., Burkert, A., & Morfill, G. E. 2014, ApJ, 780, 131

Turner, B. E. 1989, ApJS, 70, 539

—. 1993, ApJ, 410, 140

—. 1998, ApJ, 501, 731

Turner, B. E., Terzieva, R., & Herbst, E. 1999, ApJ, 518, 699

Val'tts, I. E., Larionov, G. M., & Bayandina, O. S. 2010, ArXiv e-prints

van der Tak, F. F. S., Belloche, A., Schilke, P., Güsten, R., Philipp, S., Comito, C., Bergman, P., & Nyman, L.-Å. 2006, A&A, 454, L99

Viti, S., Williams, D. A., & O'Neill, P. T. 2000, A&A, 354, 1062

von Procházka, A. A., Remijan, A. J., Balser, D. S., Ryans, R. S. I., Marshall, A. H., Schwab, F. R., Hollis, J. M., Jewell, P. R., & Lovas, F. J. 2010, PASP, 122, 354

Walmsley, C. M. & Ungerechts, H. 1983, A&A, 122, 164

Watt, S. & Mundy, L. G. 1999, ApJS, 125, 143

Whiteoak, J. B. & Gardner, F. F. 1979, MNRAS, 188, 445

Wiesemeyer, H., Thum, C., Morris, D., & Sievers, A. W. 2003, Astronomische Nachrichten Supplement, 324, 24

Wilson, T. L. 1999, Reports on Progress in Physics, 62, 143

Wilson, T. L. & Rood, R. 1994, ARA&A, 32, 191

Wilson, W. E., Ferris, R. H., Axtens, P., Brown, A., Davis, E., Hampson, G., Leach, M., Roberts, P., Saunders, S., Koribalski, B. S., Caswell, J. L., Lenc, E., Stevens, J., Voronkov, M. A., Wieringa, M. H., Brooks, K., Edwards, P. G., Ekers, R. D., Emonts, B., Hindson, L., Johnston, S., Maddison, S. T., Mahony, E. K., Malu, S. S., Massardi, M., Mao, M. Y., McConnell, D., Norris, R. P., Schnitzeler, D., Subrahmanyan, R., Urquhart, J. S., Thompson, M. A., & Wark, R. M. 2011, MNRAS, 416, 832

Winkel, B., Kerp, J., Flöer, L., Kalberla, P. M. W., Ben Bekhti, N., Keller, R., & Lenz, D. 2016, A&A, 585, A41

Wirström, E. S., Bergman, P., Black, J. H., Hjalmarson, Å., Larsson, B., Olofsson, A. O. H., Encrenaz, P. J., Falgarone, E., Frisk, U., Olberg, M., & Sandqvist, A. 2010, A&A, 522, A19

Wolfire, M. G., Hollenbach, D., & McKee, C. F. 2010, ApJ, 716, 1191

Yamada, M., Osamura, Y., & Kaiser, R. I. 2002, A&A, 395, 1031

Young, P. J., Westphal, J. A., Kristian, J., Wilson, C. P., & Landauer, F. P. 1978, ApJ, 221, 721

Zaleski, D. P., Seifert, N. A., Steber, A. L., Muckle, M. T., Loomis, R. A., Corby, J. F., Martinez, Jr., O., Crabtree, K. N., Jewell, P. R., Hollis, J. M., Lovas, F. J., Vasquez, D.,

Nyiramahirwe, J., Sciortino, N., Johnson, K., McCarthy, M. C., Remijan, A. J., & Pate, B. H. 2013, ApJ, 765, L10

Zinchenko, I., Henkel, C., & Mao, R. Q. 2000, A&A, 361, 1079

Zwicky, F. 1933, Helvetica Physica Acta, 6, 110